Laboratory and Astronomical Rotational Spectroscopy

Thesis by
Paul Brandon Carroll

In Partial Fulfillment of the Requirements for the
Degree of
Doctor of Philosphy

CALIFORNIA INSTITUTE OF TECHNOLOGY
Pasadena, California

2018
Defended September 21, 2017

Paul Brandon Carroll
ORCID: 0000-0002-3191-5401

ACKNOWLEDGEMENTS

I am grateful to the many people at Caltech and beyond that got me to Caltech and helped me through my time in grad school. First, thank you to my thesis committee Jack Beauchamp, Dan Weitekamp, Dennis Dougherty, and my advisor Geoff Blake for guiding me through the process. I am also grateful to the rest of my class in the chemistry department for all the fun, adventures, and for being the most memorable class in the department. Julian Edwards, Mike Post, Kris Stone, Carl Blumenfeld, all the members of FC_{60}, my brewing partners Justin Rolando and Joel Schmidt, and so many others made my time at Caltech so fun. Finally I would like to thank my friends and coworkers from Emory, especially Susanna Widicus Weaver for giving me my start in science.

I would also like to thank the many friends that made my time in Pasadena so special. First, and most importantly I want to thank the comically large number of housemates that made my time at home so fun. Our late additions Carolina, Esther, and our honorary member Sam that made the Hill house feel like home. The Marengo house roommates, Nicky, John, Patrick, Nick, and Chase are responsible for many of my favorite memories in Pasadena. The Marengo house was truly a silly place, but it was two incredibly fun year and you are all undoubtedly the reason, thank you. Finally, to my original roommates, Zack Nicolau and Ted Zwang, I am still not sure how or why we got placed together, but it was one of the best things to happen in grad school.

The Blake group members are responsible in one way or another for a great deal of the work presented here, my development as a scientist, and for the wonderful time I spent working at Caltech. I especially want to thank everyone who mentored me through the years. Thank you to Matt Kelley and Dan Holland, the original Blake group members who taught me THz and lasers and welcomed me to the group. Thanks also to Marco Allodi for continuing my education in lasers and THz. Thank you to Nate Crockett who patiently taught me astronomy and astrochemistry. Thank you to Sergio Ioppolo for supporting my curiosity and teaching me high vacuum systems and all things ice chemistry and spectroscopy. Unfortunately we only overlapped for a short time, but thank you to Tony Karam for teaching me so much about electron diffraction in such a short time. I also want to thank everyone who I had the good fortune to overlap with for most of my time in grad school: Marco, Ian Finneran, Brett McGuire, Jacob Good, and our visitors Xander de Vries

and Olivier Auricombe. You all made the day to day work of grad school so much better and taught me plenty. To our newer additions: Alex Froebel, Olivia Wilkins, and Griffin Mead, thank you for everything, I'm comforted knowing the lab is in your capable and well trained hands. I would also like to thank the rest of the Blake group, Alex Lockwood, Dana Anderson, Coco Zhang, Danielle Piskorz, Masha Klescheva, Cam Buzard, and Xaolin Xu for their help and friendship over the years.

Next I want to express my gratitude to my advisor. In my time at Caltech I grew far more than I ever expected and I have Geoff to thank for that. I learned so much about spectroscopy and astrochemistry from Geoff, but more importantly, Geoff taught me how to be a curious and well-rounded scientist and how to think both broadly and deeply about my work. Geoff's door is always open and his philosophy of happy students being productive students meant that my time at Caltech was not only productive but truly happy. Thank you for everything Geoff.

Finally, I want to thank my family. I could not have made it to where I am today without their love and support. Spencer, you have been my friend, constantly challenged me, and are my first and best lab partner. My parents endlessly encouraged me, taught me how to learn, to always strive to be better, gave me my work ethic, and loved me unconditionally through it all, thank you.

ABSTRACT

Rotational spectroscopy is a capable technique with a rich history in a variety of chemical physics applications that is undergoing a renaissance thanks to new approaches and powerful new experimental capabilities. This thesis demonstrates that flexibility by examining multiple uses of rotational spectroscopy from instrument development, analytical chemistry, fundamental chemical physics, and astrochemistry.

In chapter 2 we discuss the development of two novel coherent microwave spectrometers. These low cost instruments have only recently become feasible thanks to the burgeoning development of highly flexible digital electronics. The first instrument is designed for undergraduate teaching labs and can be used to demonstrate many new concepts of coherent spectroscopy that are used in modern spectroscopy. It is a rotational spectrometer and can, therefore, also be used for a variety of basic spectroscopy experiments. The second instrument uses the stability and consistency of waveguides and broadband microwave instruments to measure the rotational spectrum and abundance of isotopologues to high accuracy.

Chapter 3 describes the measurement of the rotational spectrum of the cyclopentanol–water dimer. Using microwave spectroscopy, the spectrum is measured and assigned, and the structure of the dimer is determined. The cyclopentanol–water dimer shows a structure dominated by both strong hydrogen bonding and multiple weaker hydrogen bonds from the hydrocarbon ring. The monomer spectrum is measured, though unassigned due to the strong perturbation from the motion of the ring. Dimerization with water is shown to suppress this motion. This system is shown to be an excellent example of the effect of weak hydrogen bonding on the secondary structure and dynamics of molecular systems.

Chapter 4 moves to astronomical observations of rotational transitions with the detection of a new species: propylene oxide. Measuring the inventory, abundance, and distribution of molecular species provides tests of our understanding of interstellar chemistry. Propylene oxide is an important addition to this inventory because it is the first chiral species detected beyond our solar system. Chiral species play an enormously important role in biology on Earth, and it is believed that interstellar chemistry may contribute to the early inventory of prebiotic species on newly formed planets. The detection of propylene oxide is discussed in the context of the origin

and distribution of chiral molecules in the universe.

Chapter 5 discusses recent data from the Atacama Large Millimeter/Submillimeter Array. The data maps the distribution of CH_3CN isotopologues at incredibly high spatial resolution toward the Orion KL region. The measurement of isotopic ratios in CH_3CN is used to inform our understanding the formation mechanisms of cyanides in star forming regions. More broadly, the maps are used to show the extreme spatial heterogeneity of the region, with numerous dense clumps roughly the size of a solar system, each with their own unique chemical and physical structure that reflects their distinct evolutionary histories.

Finally, chapter 6 discusses the non-detection of trans ethylmethyl ether. Ethylmethyl ether is one of the largest molecules claimed to be detected in the interstellar medium. Due to its size, it is believed to be produced on grain surfaces as a secondary or tertiary product from dissociation of ice constituents. Given its complexity, its abundance may be an important metric of the accuracy of chemical models of ice chemistry. The study claiming its detection reported an unusually high abundance of the species toward W51 e1/e2. Follow up observations and analysis showed that the original detection was mistaken, likely caused by interference from other features.

PUBLISHED CONTENT AND CONTRIBUTIONS

Evangelisti, Luca et al. (2017). "Conformational equilibrium and internal dynamics in the iso-propanol–water dimer". In: *Physical Chemistry Chemical Physics* 19.1, pp. 568–573. DOI: https://doi.org/10.1039/C6CP06315B.
P.B.C. Helped in data acquisition and processing, and manuscript preparation.

Burkhardt, Andrew M et al. (2016). "CSO and CARMA Observations of L1157. II. Chemical Complexity in the Shocked Outflow". In: *The Astrophysical Journal* 827.1, p. 21. DOI: https://doi.org/10.3847/0004-637X/827/1/21.
P.B.C. helped write observing proposal, participated in observations and data processing, and manuscript preparation.

Finneran, Ian A et al. (2016). "Hydrogen bond competition in the ethanol–methanol dimer". In: *Physical Chemistry Chemical Physics* 18.32, pp. 22565–22572. DOI: https://doi.org/10.1039/C6CP03980D.
P.B.C. helped in data acquisition and processing, and and manuscript preparation.

Loomis, Ryan A et al. (2016). "Non-detection of HC11N towards TMC-1: constraining the chemistry of large carbon-chain molecules". In: *Monthly Notices of the Royal Astronomical Society* 463.4, pp. 4175–4183. DOI: https://doi.org/10.1093/mnras/stw2302.
P.B.C. assisted in data processing and manuscript preparation.

McGuire, Brett A et al. (2016). "Discovery of the interstellar chiral molecule propylene oxide (CH3CHCH2O)". In: *Science* 352.6292, pp. 1449–1452. DOI: https://doi.org/10.1126/science.aae0328.
P.B.C. wrote Parkes and GBT observing proposals, participated in observations and data processing, participated in laboratory data acquisition and analaysis, and manuscript preparation.

Carroll, P Brandon et al. (2015). "THE search for a complex molecule in a selected hot core region: A rigorous attempt to confirm trans-ethyl methyl ether toward w51 e1/e2". In: *The Astrophysical Journal* 799.1, p. 15. DOI: https://doi.org/10.1088/0004-637X/799/1/15.
P.B.C. reprocessed and analyzed data and wrote manuscript.

Finneran, Ian A et al. (2015a). "Decade-spanning high-precision terahertz frequency comb". In: *Physical review letters* 114.16, p. 163902. DOI: https://doi.org/10.1103/PhysRevLett.114.163902.
P.B.C. assisted in initial instrument testing and data acquisition, and manuscript preparation.

Finneran, Ian A et al. (2015b). "Hydrogen bonding in the ethanol–water dimer". In: *Physical Chemistry Chemical Physics* 17.37, pp. 24210–24214. DOI: https://doi.org/10.1039/C5CP03589A.
P.B.C. helped in data acquisition and processing, and and manuscript preparation.

Good, Jacob T et al. (2015). “A decade-spanning high-resolution asynchronous optical sampling terahertz time-domain and frequency comb spectrometer”. In: *Review of Scientific Instruments* 86.10, p. 103107. DOI: https://doi.org/10.1063/1.4932567.
P.B.C. assisted in initial instrument testing and data acquisition, and manuscript preparation.

McGuire, Brett A et al. (2015). “CSO and CARMA observations of L1157. I. A deep search for hydroxylamine (NH2OH)”. In: *The Astrophysical Journal* 812.1, p. 76. DOI: https://doi.org/10.1088/0004-637X/812/1/76.
P.B.C. helped write observing proposal, participated in observations and data processing, and manuscript preparation.

McGuire, Brett A et al. (2014a). “A CSO search for l-C3H+: detection in the Orion Bar PDR”. In: *Monthly Notices of the Royal Astronomical Society* 442.4, pp. 2901–2908. DOI: https://doi.org/10.1093/mnras/stu1047.
P.B.C. helped write observing proposal, participated in observations and data processing, and manuscript preparation.

McGuire, Brett A et al. (2014b). “AN OBSERVATIONAL INVESTIGATION OF THE IDENTITY OF B11244 (l-C3H+/C3H–)”. In: *The Astrophysical Journal* 783.1, p. 36. DOI: https://doi.org/10.1088/0004-637X/783/1/36.
P.B.C. helped write observing proposal, participated in observations and data processing, and manuscript preparation.

McGuire, Brett A et al. (2014c). “Ignition of Thermite Using the Potassium Chlorate ?Rocket? Reaction: A Systematic Demonstration of Reaction Chemistry”. In: *Journal of Chemical Education* 92.6, pp. 1117–1120. DOI: https://doi.org/10.1021/ed500522c.
P.B.C. assisted in chemical demonstrations and manuscript preparation.

Finneran, Ian A et al. (2013). “A direct digital synthesis chirped pulse Fourier transform microwave spectrometer”. In: *Review of Scientific Instruments* 84.8, p. 083104. DOI: https://doi.org/10.1063/1.4818137.
P.B.C. assisted in instrument development, instrument control development, data acquisition and processing, and manuscript preparation.

TABLE OF CONTENTS

Acknowledgements . . . iii
Abstract . . . v
Published Content and Contributions . . . vii
Table of Contents . . . ix
List of Illustrations . . . xi
List of Tables . . . xix
Chapter I: Introduction . . . 1
1.1 Laboratory Rotational Spectroscopy . . . 1
1.2 Observational Astrochemistry . . . 3
Chapter II: Development of Microwave Instrumentation . . . 7
2.1 Coiled Waveguide Spectrometer and the Measurement of Site-Specific Isotope Ratios . . . 7
2.2 Development of a Low-Cost Chirped-Pulse Fourier Transform Microwave Spectrometer for Undergraduate Physical Chemistry Lab . . . 16
Chapter III: The Microwave Spectrum and Structure of the Cyclopentanol–Water Dimer . . . 28
3.1 Introduction . . . 28
3.2 Experimental . . . 29
3.3 Spectral Assignment . . . 32
3.4 Discussion . . . 36
3.5 Conclusion . . . 38
Chapter IV: The Discovery of the Interstellar Chiral Molecule Propylene Oxide 40
4.1 Introduction . . . 40
4.2 Observations . . . 41
4.3 Laboratory Spectroscopy . . . 45
4.4 The Observational Model . . . 47
4.5 Measurement of Circular Dichroism . . . 55
4.6 Propanal and Acetone Observations in PRIMOS . . . 59
4.7 Discussion . . . 60
Chapter V: ALMA Observations of CH_3CN Toward Orion KL . . . 66
5.1 Introduction . . . 66
5.2 Observations . . . 68
5.3 Analysis . . . 68
5.4 Results and Discussion . . . 74
5.5 Conclusion . . . 82
Chapter VI: Non Detection of Trans Ethylmethyl Ether Toward W51 . . . 84
6.1 Introduction . . . 84
6.2 Observations . . . 86
6.3 Results and Discussion . . . 88

6.4 Conclusions 95
Appendix A: Arduino Control of the AD9914 107
A.1 Short Version 107
A.2 AD9914 DDS 108
A.3 Construction 108
A.4 ALMA Fitting Code 120
A.5 Pressure Controller Code 157
Appendix B: Machining TOPAS 163

LIST OF ILLUSTRATIONS

Number *Page*

2.1 **Intensity of the $^{12}CH_3OH$ $2_{0,2}$–$3_{-1,3}$ transition as a function of time in the Caltech coiled waveguide CP-FTMW.** The amplitude is taken as the fitted intensity of the transition in a 50000 average acquisition at 50 kHz repetition rate and plotted versus the record number. Error bars are shown as the 1-σ uncertainty in the fitted amplitude. 9

2.2 **Schematic of the Caltech coiled waveguide CP-FTMW spectrometer.** Chirps are generated in the DDS board. The board is clocked by a 4 GHz synthesizer and programmed through an Arduino Uno. The chirp is triggered by a delay generator and mixed with a 8-16 GHz LO. Both the synthesizers are in turn referenced to a 10 MHz Rb frequency standard. The up-converted signal is amplified by a 3W amplifier and broadcast into the cell. A p-i-n switch, triggered by the delay generator closes after the pulse to block noise from the amplifier. Emission is amplified by a low noise amplifier placed behind a protective p-i-n switch also triggered by the delay generator. The emission is down-converted in a second mixer, amplified by an IF amplifier, and detected in a high-speed digitizer 10

2.3 **The measured ^{12}C to ^{13}C ratio of CH_3OH using the Caltech coiled waveguide CP-FTMW.** Each data point represents 25 million acquisitions taken at a repetition rate of 50 kHz. The ^{12}C to ^{13}C ratio is determined by ratio of gaussian fits to the $^{12}CH_3OH$ and $^{13}CH_3OH$ $2_{0,2}$–$3_{-1,3}$ transitions. Error bars are 1σ errors determined from the fitting. 11

2.4 **Nutation spectrum of CH_3OH.** This demonstrates the ability of the instrument to fully saturate strong methanol transitions. Methanol spectra were taken at various excitation powers from 0 – 100% of the maximum excitation power using an AB-BA scheme, where the first acquisition, labeled 'Run 1'(Red), was cycled from 0 to 100% and the second set, labeled 'Run 2' (Black), was taken from 100 to 0%. Data were taken as 10 million acquisitions per point. The amplitude of the excitation pulse was varied by controlling the amplitude of the excitation chirp using an arbitrary waveform generator. The amplitude of the $2_{0,2}$–$3_{-1,3}$ (12178.6 MHz) is shown in the bottom panel and amplitude of the $16_{5,12}$–$17_{4,13}$ (12229.4 MHz) is shown in the top panel. 13

2.5 **The rotational spectrum of the $2_{2,0}$–$2_{2,1}$ transition of HDO from the Caltech waveguide CP-FTMW observed in natural abundance.** The spectrum consists of 10 million averages, taken at a repetition rate of 50 kHz, achieving a signal to noise ratio of 6.5. . . . 14

2.6 **The rotational spectrum of the $2_{0,2}$–$3_{-1,3}$ transition of $^{12}CH_3OH$ (left) and $^{13}CH_3OH$ (right) from the Caltech waveguide CP-FTMW observed in natural abundance.** The spectrum consists of 100 million averages, taken at a repetition rate of 50 kHz. 15

2.7 **Schematic of an original HP Stark modulated absorption cell.** . . 17

2.8 **The full schematic of the initial design of the Caltech CH 6 chirped pulse FTMW system.** SMA connections and cables are shown in black, positive voltage sources and connections are red, negative voltage sources and connections are shown in orange, ground is shown in green, BNC connections are purple, and computer connections and USB connections are blue. All individual components are shown as black boxes, and mixers are shown as circles with an x through the center. Components' model numbers are given inside their boxes. The RF frequencies of the components are shown above each SMA connection and the corresponding power below the SMA connection. 20

2.9 **Time domain data of $^{16}O^{12}C^{32}S$ taken with the Caltech CH 6 spectrometer.** The rapidly decaying oscillation is due to the dephasing of the $^{16}O^{12}C^{32}S$ coherence after excitation. The slow oscillation is due to low frequency instrumental response. 23

2.10 **The block diagram of the Caltech CH 6 chirped pulse FTMW spectrometer.** RF connections are shown in black and computer connections in blue. Individual components are shown as black circles or boxes. A key is given in the bottom left. 24

2.11 **OCS spectra recorded from the Caltech CH 6 CP-FTMW.** The spectra of $^{16}O^{12}C^{32}S$ is shown in panel A, $^{16}O^{12}C^{34}S$ in panel B, $^{16}O^{13}C^{32}S$ in panel C, and $^{16}O^{12}C^{33}S$ in panel D. The spectra of $^{16}O^{12}C^{32}S$ is a sum of 50000 averages, $^{16}O^{12}C^{34}S$ is a sum of 100000 averages, $^{16}O^{13}C^{32}S$ is a sum of 500000 averages, and $^{16}O^{12}C^{33}S$ is a sum of 1000000 averages. Amplitudes are arbitrary and are not the same scale between spectra. 26

3.1 **Block diagram of the Caltech supersonic jet CP-FTMW**. The instrument uses either an AD9914 or arbitrary waveform generator to generate linear frequency chirps for excitation. Later iterations utilized a two horn perpendicular supersonic jet arrangement with no circulator. Figure taken from [50] 30

3.2 **Spectrum of the cyclopentanol–water mixture**. The complete spectrum is shown in panel A. The spectrum after subtraction of the monomer data is shown in panel B in black, while a spectral prediction based on the assigned constants is shown as negative lines with intensity proportional to the expected intensity of the line. The y axes are given as signal to noise ratio (SNR), determined by dividing the spectrum by the RMS of a transition free region in the 13 GHz LO region. 31

3.3 **The structure of the cyclopentanol monomer**. The structure is optimized at the MP2/aug-cc-pVTZ using the Gaussian 09 software package [56]. 33

3.4 **The spectrum of the cyclopentanol monomer.** The spectrum was recorded by taking 10 million averages acquired using a flow of 15 PSI Ar buffer gas. The experimental spectrum is shown in black, and the prediction based on *ab initio* calculations is plotted as negative going vertical lines with length proportional to predicted intensity. Frequency is given in MHz, amplitude is arbitrary. 34

3.5 **Potential energy surface of the OH dihedral angle with respect to the cyclopentanol ring**. 36

3.6 **DR measurements of the $4_{0,4}$–$3_{0,3}$ and $4_{1,4}$–$3_{0,3}$ transitions of the cyclopentanol–water dimer.** The top panel shows the spectrum of the $4_{1,4}$–$3_{0,3}$ with the DR pump set to the $4_{0,4}$–$3_{0,3}$ (13532 MHz). The bottom panel shows the spectrum of the $4_{1,4}$–$3_{1,3}$ and $4_{0,4}$–$3_{0,3}$ with the DR pump set to the $4_{1,4}$–$3_{0,3}$ (13860 MHz). In both panels the spectrum with no DR pulse is shown in green, the spectrum with the DR pulse on is shown in blue, and the difference is shown in red. Frequencies are given in the downconverted IF frequency. 37

3.7 **Structure of the cyclopentanol–water dimer**. The structure is optimized at the MP2/aug-cc-pVTZ using the Gaussian 09 software package [56]. 39

4.1 **The molecular structure of S-propylene oxide (A) and R-propylene oxide (B)**. Carbon, hydrogen, and oxygen atoms are indicated by gray, small white, and red spheres, respectively. 41

4.2 **Observations of the $1_{1,0}$- $1_{0,1}$ (Parkes), $2_{1,1}$- $2_{0,2}$ (GBT), and $3_{1,2}$- $3_{0,3}$ (GBT) transitions of propylene oxide, in absorption, toward the Galactic Center.** The 64 km s^{-1} systematic velocity characteristic of Sgr B2(N) is indicated by a vertical red line. The $1_{0,1} - 1_{1,0}$ transition of propanal is also seen in the Parkes data. Data are given as antenna temperature (T_A^*) as a function of shift from local standard of rest velocity (V_{LSR}), where 0 km s^{-1} is the measured laboratory frequency of the transition[100], and have been Hanning smoothed. . 44

4.3 **Illustration of source structure within the Sgr B2 region.** A) The GBT and Parkes beam probe different portions of the cold molecular shell in front of the bright continuum sources/hot cores within Sgr B2. Molecules in the shell which are not backlit by continuum sources are not seen in absorption. As the schematic of the sky view at right shows, B) The GBT (red) and Parkes (blue) beams probe different continuum sources, with the GBT beam probing only Sgr B2(N), while the Parkes beam also includes most of Sgr B2(M) to the south. 45

4.4 **Laboratory spectrum of propylene oxide.** The spectrum of propylene oxide in an Ar buffer gas from 8 – 18 GHz (4.8 million averages, 20 hour acquisition) 47

4.5 **Laboratory spectra of astronomically-observed propylene oxide transitions.** Laboratory measurement of the three transitions detected astronomically in this work, showing the characteristic A-E methyl rotor splitting (solid blue lines) and Doppler splitting (dashed red lines). Rotational quantum numbers are given in red. 48

4.6 **Model spectrum of propylene oxide toward Sgr B2(N) at the best-fit column density and temperature, and comparison with observations.** The spectrum of propylene oxide at $N_T = 1\times10^{13}$ cm^{-2} and $T_{ex} = 5.2$ K, corrected for background continuum, telescope-specific parameters, and beam dilution effects is shown in the main figure. The observed transitions in PRIMOS are shown in insets (a) and (b), with the model spectra overlaid in red. The next strongest transition has no corresponding receiver (Rx) at the GBT or Parkes, and is marked as such. 53

4.7 **Theoretical prediction of the submillimeter spectrum of propylene oxide, assuming $\mathbf{N_T = 1.3\times10^{15}}$, $\mathbf{T_{ex} = 125K}$.** Source size is taken from Qin 2011 and molecular line parameters from Mesko 2017. The previous observed regions of Cunningham 2007 and Belloche 2013 (84 - 114 GHz) are shown in the inset with the average EMoCA survey RMS (Belloche 2016) indicated as a horizontal line. Transitions in Band 7 are approximately 100x brighter than those at Band 3. 60

4.8 **Model spectrum of acetone toward Sgr B2(N) at the best-fit column density and temperature, and comparison with observations.** The spectrum of acetone at $N_T = 2.1\times10^{14}$ cm^{-2} and $T_{ex} = 6.2$ K, corrected for background continuum, telescope-specific parameters, and beam dilution effects is shown in the main figure. The observed transitions in PRIMOS are shown in black, with the model spectra overlaid in red. 62

4.9 **Model spectrum of propanal toward Sgr B2(N) at the best-fit column density and temperature, and comparison with observations.** The spectrum of propanal at $N_T = 6\times10^{13}$ cm^{-2} and $T_{ex} = 6.2$ K, corrected for background continuum, telescope-specific parameters, and beam dilution effects is shown in the main figure. The observed transitions in PRIMOS are shown in black, with the model spectra overlaid in red. 63

5.1 **A plot of the continuum toward Orion KL.** Both the greyscale and contours plot the continuum. The greyscale is plotted on a log scale using vmin of -0.01 and vmid of 0.1. Contours are at the [-0.0028995 0.00323595 0.0093714 0.01550685 0.0216423] Jy beam^{-1} levels. Red crosses mark continuum sources. Numbers mark peaks identified by Hirota[76]. The synthesized beam is shown in the bottom left. 69

5.2 **Channel map of the $9_{4,6}$–$8_{4,5}$ and $9_{4,5}$–$8_{4,4}$ transitions of CH_2DCN.** Velocity is given from -34.14 kms^{-1} to -42.11 kms^{-1}. The synthesized beam is shown in the bottom left. 70

5.3 **The moment 0 map of $^{13}CH_3CN$ toward Orion KL.** The color and contours show the integrated intensity of the $^{13}CH_3CN$ transitions used in the fit. Red crosses mark the continuum sources identified by Hirota[76]. Contours are at the [0.52, 1.04, 2.09] Jy beam^{-1} levels. The red star indicates the position of source I and the blue diamond marks the position of the hot core.The synthesized beam is shown in the bottom left and a scale bar is shown at the top left. 71

5.4 **The moment 0 map of CH_2DCN toward Orion KL.** The color and contours show the integrated intensity of the CH_2DCN transitions used in the fit. Red crosses mark the continuum sources identified by Hirota[76]. Contours are at the [1.58, 3.17, 6.33] Jy beam^{-1} levels. The red star indicates the position of source I and the blue diamond marks the position of the hot core.The synthesized beam is shown in the bottom left and a scale bar is shown at the top left. 72

5.5 **The derived CH_3CN temperature from the least squares fit of the Orion data cube.** The derived temperature is shown as a color plot and the continuum is shown as peak flux×[$\frac{1}{2}$,$\frac{1}{4}$,$\frac{1}{8}$,$\frac{1}{16}$] contours in grey. The synthesized beam is shown in the bottom left corner. 74

5.6 **The derived CH_3CN column density from the least squares fit of the Orion data cube.** The derived $^{13}CH_3CN$ + CH_2DCN column density is shown as a color plot and the continuum is shown as peak flux×[$\frac{1}{2}$,$\frac{1}{4}$,$\frac{1}{8}$,$\frac{1}{16}$] contours in grey. The synthesized beam is shown in the bottom left corner. 75

5.7 **The derived velocity from the least squares fit of the Orion data cube.** The derived velocity is shown as a color plot and the continuum is shown as peak flux×[$\frac{1}{2}$,$\frac{1}{4}$,$\frac{1}{8}$,$\frac{1}{16}$] contours in grey. The synthesized beam is shown in the bottom left corner. 76

5.8 **The derived line width from the least squares fit of the Orion data cube.** The derived line width is shown as a color plot and the continuum is shown as peak flux×[$\frac{1}{2}$,$\frac{1}{4}$,$\frac{1}{8}$,$\frac{1}{16}$] contours in grey. The synthesized beam is shown in the bottom left corner. 77

5.9 **The derived D to ^{13}C ratio and temperature of CH_3CN toward Orion KL.** A map of the D to ^{13}C ratio is shown in the left panel. A plot of the D to ^{13}C ratio versus the derived temperature is shown in the right panel. The color of the points in the right panel corresponds to the color of the rectangles in the left panel. A continuum contour plot and synthesized beam are shown in the left panel as guides. . . . 80

5.10 **Moment 0 map of vinyl cyanide toward Orion KL.** Continuum is shown as contour plots. A scale bar is shown at the bottom right. The synthesized beam is shown at the bottom left. The blue diamond marks the hot core. Red crosses mark HKKH sources. 81

5.11 **Moment 0 map of CH_3CN v_8=1 toward Orion KL.** Continuum is shown as contour plots. A scale bar is shown at the top left. The synthesized beam is shown at the bottom left. The blue diamond marks the hot core. Red crosses mark HKKH sources. The direction of source I's low velocity flow is shown as a blue arrow. 82

6.1 **A comparison of the previous IRAM 30 m data and the current ARO 12 m data.** All tEME transition frequencies are noted as blue vertical lines of uniform height. The inset shows the tEME $20_{0,20} - 19_{1,19}$ transition multiplet. ARO data is converted to T_{mb} assuming the 5″ source size of [57] 87

6.2 **The 2 mm spectral coverage of the ARO observations toward W51 e1/e2.** Frequencies are given assuming an LSR velocity of 55 km/s. Molecular transitions are labeled for context. tEME transitions are marked by vertical blue lines of uniform height. 88

6.3 **The 3 mm spectral coverage of the ARO observations toward W51 e1/e2.** Frequencies are given assuming an LSR velocity of 55 km/s. Molecular transitions are labeled for context. tEME transitions are marked by vertical blue lines of uniform height. 89

6.4 **The computed LTE peak antenna temperature of individual tEME transitions.** The antenna temperature is based on Equation 6.1 assuming a column density of 2×10^{14} cm^{-2}, velocity width of 3 km s^{-1}, and an excitation temperature of 70 K (Blue) plotted with the reported peak antenna temperature from [57] (Red). An enlarged view showing the weakest reported transition from [57] is shown in the inset. 90

6.5 **200 km s^{-1} windows of the ARO observations of potential tEME transitions toward W51 e1/e2 (Black).** A simulation of tEME at 10 K (Blue) 150 K (Green) and 300 K (Red), assuming ΔV = 3 km s^{-1}, η_B = 1, B = 1, N_T is the best fit column density derived for each temperature. Clearly the $3_{2,1}$ - $2_{1,2}$ and $16_{1,16}$ - $15_{0,15}$ are inconsistent with the $20_{0,20} - 19_{1,19}$ transition. 94

A.1 **An overview of the AD9914.** Green - USB control circuits and pins, Blue - Serial control pins, Red- External trigger and power down control pins, Yellow - DDS clock input and DAC (Chirp) output, Light Blue - AD9914 chip, Purple - USB adapter and power suppler input 108

A.2 **USB micro controller pins.** P204 and P203 should be disabled, P205 should remain enabled to allow external chirp triggering. 109

A.3 **EXTPDCTL, RESET, DROVR, DRHOLD, and DRCTL control pins.** EXTPDCTL must have the signal shorted to ground. 110

A.4 **MIO buffers of the AD9914.** MIO buffers, CS (red box top), SYNC_CLK (Green box top), Serial Clock in (Blue box top) and SYNC_IO (red box bottom), IO_UPDATE (Yellow box bottom), and RESET (White box bottom) 112

A.5 **Wiring diagram for the Arduino Uno.** The individual grounding wires (green) for the SYNC_CLK and SDIO are essential to proper function. The IO_UPDATE and RESET pins can use a common ground with no disruption. 113

B.1 **Diagram of the WRD 750 vacuum adapter.** 164

LIST OF TABLES

Number *Page*

2.1 **Current Components of the Caltech CH6 CP-FTMW.** 25

3.1 **Assigned Rotational Transitions of the Cyclopentanol–Water Dimer.** 35

3.2 **Assigned and *Ab Initio* Rotational Constants of the Cyclopentanol–Water Dimer.** 35

4.1 **Measured laboratory frequencies of the transitions used in this work, and associated observed linewidth broadening.** 47

4.2 **Line parameters resulting from Gaussian Fits to the observed transitions.** Numbers in parenthesis are 1σ standard deviations in units of the last significant digit. 49

4.3 **Observed acetone transitions in PRIMOS.** 61

4.4 **Observed propanal transitions in PRIMOS.** 61

5.1 **The correlator configuration used for the ALMA observations of Orion KL.** 68

5.2 **CH_3CN Transitions used for fit.** 73

6.1 **Observed and calculated intensity of tEME Transitions.** 93

Chapter 1

INTRODUCTION

Spectroscopy is one of the most ubiquitous tools in chemical research. Spectroscopy directly probes the structure and dynamics of matter by measuring the connections between eigenstates of the Hamiltonian. The Hamiltonian is responsible for the structure and interactions of matter with its environment. Spectroscopic measurements are, therefore, a powerful way to understand chemistry and chemical processes. Modern spectroscopy covers an enormous range of techniques spanning the electromagnetic spectrum for a truly staggering variety of applications. Rotational spectroscopy in particular has been developed into a powerful tool for fundamental chemical physics research. Measured rotational transitions are directly related to structure, giving rotational spectroscopy an unparalleled ability to identify molecular species and the minute details of their structure and Hamiltonian.

1.1 Laboratory Rotational Spectroscopy

Rotational transitions depend on the moments of inertia of the molecule, making them exquisitely sensitive to molecular structure[68]. Any change in the moments of inertia of a molecule, from conformational changes to isotopic substitution to differences in bond distances or angles due to vibrational excitation, are readily observable. Because a permanent electric dipole moment and free rotation of the molecule is required for measurement, these observations are limited to gas-phase polar targets. The width of these transitions is typically very small, generally at least 100,000 times smaller than the frequency at which they are observed. This gives large available bandwidths for detection of numerous well-resolved transitions. Often line widths are far better than this due to long coherence times and high-precision electronics used. This makes microwave spectroscopy incredibly sensitive to even tiny perturbations [91]. The sensitivity, flexibility, and precision have made rotational spectroscopy a pervasive method in chemical physics research for nearly a century. The development of new equipment and methodologies over this time, especially the recent development of high speed, easily configurable digital electronics over the past decade, has greatly expanded the capabilities of rotational spectroscopy, enabling the work presented here.

Laboratory microwave spectroscopy originated from a goal of measuring molecular

structure[28], and was bolstered by the development of radar technology, somewhat accidentally at times [66]. With the emergence of suitable instrumentation, microwave spectroscopy has been widely applied to the study of rotational transitions of molecules to such a great extent that the terms microwave and rotational spectroscopy are often used interchangeably [144]; however rotational transitions span an enormous range of frequencies and can be observed from radio frequencies to well into the terahertz (THz, 1×10^{12} Hz). Further advances in microwave technology led to the widespread use of rotational spectroscopy to investigate the structure of gas-phase molecules. The development of cavity based Fourier techniques has further enabled high sensitivity studies of spin interactions, structure of clusters, and isotopologues among other systems[6]. Finally, development of adiabatic or chirped pulse excitation schemes have led to the extension of high sensitivity Fourier techniques to extremely broad band studies capable of detecting numerous species simultaneously, enabling studies of clusters, highly energetic species, and dynamics[19, 103].

Chapters 2 and 3 of this thesis describe the development of new microwave spectroscopy instrumentation and the use of microwave spectroscopy to study molecular clusters, respectively. Recent advances in microwave electronics have drastically lowered the cost of components due to a need to mass produce digital and analog electronics for high bandwidth communications and novel technologies like high resolution radar for self-driving cars. This allows for the construction of research quality instruments at a cost comparable to most other undergraduate teaching instruments. This instrumentation is the direct analog of research instruments used today and incorporates many of the core concepts of modern spectroscopy. This combination makes the instrument a powerful education tool for inquiry-based education. It can also be used for academic research with minor modifications which would allow students to participate in academic research at small institutions. This development is part of an ongoing trend of making cheaper and simpler integrated electronics that will only continue to improve access to and quality of rotational spectroscopy instrumentation. This research is a demonstration of how to exploit this trend to build instrumentation that can be used to demonstrate and teach a wide variety of concepts central to chemical physics.

Adaptation of this technology to new sample preparation methods is also a promising avenue for developing new analytical chemistry techniques. In the second half of chapter 2 the use of a static gas waveguide cell for stable isotope measurement is

discussed. Despite its similarity to NMR, rotational spectroscopy has never enjoyed the same success in analytic chemistry. Only in recent years with the development of chirped pulse techniques has instrumentation been developed that is capable of measuring rotational transitions over a large instantaneous bandwidth at high sensitivity. Even with this development, the supersonic jets used to produce the gaseous samples introduce serious shot noise that precludes the kind of consistency required for analytic chemistry; however, combining this with static waveguide cells can produce far more consistent measurements. A natural target for such an instrument is is non-destructive and site specific stable isotope measurement. Isotopic ratios are an incredibly powerful diagnostic tool for discerning the origin and history of samples. The ability of rotational spectroscopy to identify and easily separate signals from different isotopologues makes it an intriguing alternative, particularly because this can be done in a site-specific manner that is challenging for current techniques. While not complete, the developments made point to a promising future for rotational spectroscopy as a tool for isotopic analysis.

Chapter 3 describes the measurement of the spectrum and determination of the structure of the cyclopentanol–water dimer. The power of rotational spectroscopy to determine precise structures of gas-phase species has been repeatedly applied to the study of dimers, and has yielded the best characterizations of these systems. Gas-phase dimers are the starting point for describing condensed-phase systems critical for chemical reactions. The structure and dynamics of condensed phase systems can be described as a sum of all the two body interactions of the molecules present plus all three body interactions and so on to give a complete representation of the interactions of the liquid or solid. Of these, the two body interactions are of the greatest interest, as the effect of higher order interactions is lessened by screening and the distance dependence of electrostatic interactions. Gas-phase dimers are completely isolated and measurement of their structure gives a description of the purely two body interaction, providing a basis for describing the far more complex many body physics of a condensed-phase system. In this chapter, the spectrum and structure of the cyclopentanol–water dimer is measured. This dimer posses a unique combination of a strong and multiple weak hydrogen bonds. The overall structure of the cyclopentanol ring is dictated by secondary weak hydrogen bonding.

1.2 Observational Astrochemistry

Chapters 4, 5, and 6 focus on the use of radio astronomy for astrochemistry. Chapter four outlines the detection of a new species, propylene oxide, via rotational spec-

troscopy. Chapter 5 describes the use of millimeter interferometry, discussed below, to map the distribution of previously identified CH_3CN and its isotopologues, to better understand how it is formed. Finally, chapter 6 discusses the non-detection of a third species, ethyl-methyl ether and its implications for chemical complexity. All three of these chapters revolve around the central goal of observational astrochemistry: the use of telescopes to measure the composition of the universe. As discussed above, this is frequently using radio to terahertz instruments, broadly referred to as radio astronomy, which almost universally measure rotational transitions. There are many important reasons for this. First, the universe is essentially transparent at radio frequencies [111]. This allows the detection of species throughout the interstellar medium (ISM), particularly in dense molecular cores where they are a formed. Second optical and infrared transitions in isolation may be molecule specific, however in the complex mixtures of the ISM, it is impossible to disentangle the mixture of signals found and identify the individual components [3]. Finally, at the temperatures typical of the ISM, molecules are too cold to spontaneously emit at frequencies above a few terahertz, making them impossible to detect unless they have a bright background source behind them, or are detected by direct emission through radio astronomy. There are, of course, many exceptions to this. Indeed, the first molecular detections in the ISM, were done in the optical [2]. More recent detections of H_3^+[101], C_{60}^+[54], detection of gravitational waves[1], and the continuing detection of molecules in exoplanetary atmospheres [94], highlight this fact. Nevertheless, of the nearly 200 molecules detected in the interstellar medium, only a handful have been observed through anything other than radio astronomy.

Chapters 4 and 6 describe the detection of a new molecular constituent of the ISM, propylene oxide, and the non-detection of another, ethylmethyl ether, respectively. The detection of these species is a first step in understanding the chemical processes that shape our universe. Molecular inventories depend on a complex network of chemical reactions and measuring the molecular inventory of a region provides a benchmark for our understanding of the network [60]. Of particular interest is the chemistry of molecular clouds where radiation fields are sufficiently attenuated to allow for the formation of molecules[136]. Molecular clouds span a wide range of sizes and masses, but often exist as high-mass clouds that act as the birthplace of numerous stars typical of the initial mass function[42]. These clouds collapse to form a protostar and eventually a young star with a protoplanetary disk around it. This system further evolves to a planetary system. Throughout this process, material is processed and evolves, and the final composition of the solar system inherits, to

some degree, the chemistry of its parent molecular cloud [29]. Moreover, the remnants of the solar nebula are incorporated into comets and meteors that may then be accreted by nascent planets delivering even more organic material formed in the parent cloud[27]. Thus, astrochemistry is intimately linked with the evolution toward planetary systems and may play a key role in shaping their volatile content, which is key to the potential origins of life on these systems. There are likely over one million Earth-like planets in the habitable zone of stable solar systems in our galaxy[129]. Understanding the chemistry that governs their potential content is, therefore, an important area of research. The first steps towards this goal are better understanding the inventory of molecular clouds and its link to the dynamical processes shaping this inventory.

Interferometric Radio Astronomy

A major challenge of radio astronomy is the relatively modest resolution achievable. The Rayleigh criteria for circular apertures limits the resolution of a single collector telescope to 1.22λ/D, where D is the diameter of the collector. For optical telescopes, even simple hobby telescopes can achieve sub arcsecond resolution. However for modern radio telescopes, which are multimillion dollar feats of engineering, the largest aperture instruments are orders of magnitude lower. The solution to this is to use interferometers. The operating principal for these instruments is relatively straightforward. Rather than construct an unfeasibly large aperture instrument, a series of much smaller more manageable collectors are built. The signal from each collector is then coherently recombined to produce an interference, referred to as a baseline, that can be Fourier transformed to give the spatial distribution. The effective diameter, D, of the instrument is then the separation between collectors, allowing for far higher spatial resolution. Furthermore, by incorporating multiple collectors, a more complete measurement of the spatial distribution can be made because the distance between different sets of collectors must naturally vary. This is further enhanced by observing for a long period of time because the relative motion of the Earth and source changes the orientation of each baseline, to provide a more complete sampling of the full spatial distribution of the source. These instruments are used in the optical and infrared as well, but were first developed for radio astronomy [16, 127], and are more commonly used in the radio due to the ease with which radio antennas can be constructed and the far simpler processes of coherent correlation with radio frequency electronics. In recent years radio frequency interferometry has made huge leaps with the construction of the Very Large

Array (VLA), Submillimeter Array (SMA), NOrthern Extended Millimeter Array (NOEMA)/Plateu de Bure interferometer, and the Atacama Large Millimeter/Submillimeter Array (ALMA). These facilities are now capable of imaging sources with enormous sensitivity, spatial and spectral resolution, and bandwidth.

The application of interferometry to astrochemistry is and will continue to be incredibly important. Imaging provides essentially the same information on molecular content as single dish measurements, but does so with spatial information, producing a spectrum at each point. Astrochemistry is not a static process. The universe, in particular star forming regions where material is assembled into solar systems is a dynamic process. Gradients in temperature, density, and energy input exist over short scales the size of solar systems, or smaller to thousands of astronomical units or more, producing heterogenous and time-dependent chemical evolution[74]. Single-dish observations, while a powerful tool for astrochemistry, provide only a small fraction of the information of an interferometer. Chemical and physical modeling based solely on this information requires very simplistic assumptions. The rapid expansion of radio interferometers, especially ALMA, has provided some of the most exciting advances in our understanding of astrochemistry. The high angular resolution has allowed for the first detection of organic species [147] and CO snow line [118] in protoplanetary disks. It has also enabled the detection of many new species included the first detection of branched carbon chains [10]. Chapter 5 will discuss the use of ALMA to detect organic species toward the Orion nebula at unprecedentedly high angular resolution and spectral sensitivity. The observations described in chapter five show a kinematically and chemically rich and complex region. These observations, completed in only thirty minutes, are the obvious next step in understanding the structure of planetary systems as the form and the role astrochemistry plays in determining the volatile budgets of these systems, and are an example of the studies that will be possible in the coming decades.

Chapter 2

DEVELOPMENT OF MICROWAVE INSTRUMENTATION

2.1 Coiled Waveguide Spectrometer and the Measurement of Site-Specific Isotope Ratios

One of the great aspirations of the rotational spectroscopy community has been the proliferation of the technique and its adaptation to analytical chemistry. Rotational spectroscopy's ability to easily separate individual rotational states of different conformers, isomers, and isotopologues makes it a potentially powerful tool for analyzing complex mixtures. This has been a large driver for the interest in adapting rotational spectroscopy for analytical chemistry. One interesting application is the use of rotational spectroscopy to measure isotopic ratios. Measurement of isotopic ratios is a versatile and highly sensitive tool that can be used for a variety of analytical purposes from forensic identification [92], to paleothermometry [61], to determining the potential biogenic origin of organic species[8]. Such measurements can be greatly improved through the simultaneous measurement of isotopic fractionation from multiple isotopes, termed clumped isotope measurements[148]. Finally, these techniques can be applied to subunits of a molecule to determine site-specific isotopic ratios [113]. With these analyses, complex molecules whose subunits have distinct origins can be distinguished through measurement of the unique isotopic ratio at each site[135]. The ultimate goal of such measurements is the determination of the full isotopic anatomy of the molecule. This is typically done using some form of mass spectrometry. Depending on the fragmentation method employed, substantial structural information is lost, making full determination challenging or impossible. Application of other techniques, most notably NMR, has been able to determine single substitutions in a site-specific manner, but requires 100's of mg's of sample[135]. Therefore an ongoing challenge is to develop techniques capable of such measurements, and rotational spectroscopy is a plausible solution to this challenge.

The general goal of this project is to test the capabilities of rotational spectroscopy to achieve this experiment. This requires the measurement of multiple rotational transitions, at least one from each isotopologue, which are likely separated by several MHz. The obvious choice is to use chirped pulse Fourier transform microwave

spectroscopy (CP-FTMW)[19]. This technique combines the sensitivity of traditional cavity-based FTMW techniques[6] with high speed electronics to cover orders of magnitude more bandwidth. This allows for the detection of widely separated transitions of isotopologues, as well as the detection of multiple isotopologues[22], and even the detection of multiple isotopologues for multiple species in complex mixtures. The challenge is to do this in a way that minimizes systematic noise, in order to allow for the quantitative measurement of isotopic ratios. Traditionally sample is measured by exciting supersonic expansion seeded with sample in a vacuum chamber. This expansion adiabatically cools the molecules, resulting in a substantial improvement in signal due to the $T^{\frac{3}{2}}$ scaling of the rotational partition function. Unfortunately, there is strong variability in expansion, modulating the relative intensities. This issue is exacerbated by the generally low repetition rates used. Typically expansions are run at 10 Hz or less, with 40-80 excitation-detection cycles per expansion. This results in an effective shot noise that limits the uncertainty in the intensities to $\sim$ 20%, despite much higher raw signal to noise. The obvious solution to this is to use a waveguide CP-FTMW. These instruments work on the same principles as supersonic jet CP-FTMW instruments, but substitute low pressure static gas cells made of microwave waveguide for the supersonic jet and vacuum chamber[121]. Because the gas is static, there is, in theory, no variability in the sample conditions and the experiment can be run at repetition rates in excess of 50 kHz. The drawback of this approach is that the intensity of measured transitions is much lower due to the large room temperature partition function. Thus, waveguide CP-FTMW may be a viable technique for measuring the isotopic anatomy of gasses, however it is not obvious that it is possible. The goal of this project is to test the feasibility of waveguide CP-FTMW's ability to measure isotopic ratios in a site-specific manner.

The instrument consists of a single 10 m coiled WRD 750 waveguide cell, chosen to maximize power density and bandwidth. A schematic of the instrument is given in Figure 2.2 The cell volume is of order 1 L, so that at an operating pressure of 5 mTorr, less than 1 μmol of sample is needed. Sample and vacuum are coupled in through two custom WRD 750 adapters, the dimensions and dimensions of which are given in Appendix Figure B.1. These adapters are sealed at the front with 0.15mm mica windows (2spi.com part no: #01872-CA) and TorrSeal. Radiation is coupled into and out of the cell through WRD750 to SMA adapters. Sample pressure is maintained by first baking the cell with heating tape under vacuum to reduce degassing or virtual leaks. Once cleared, the vacuum line is shut and the

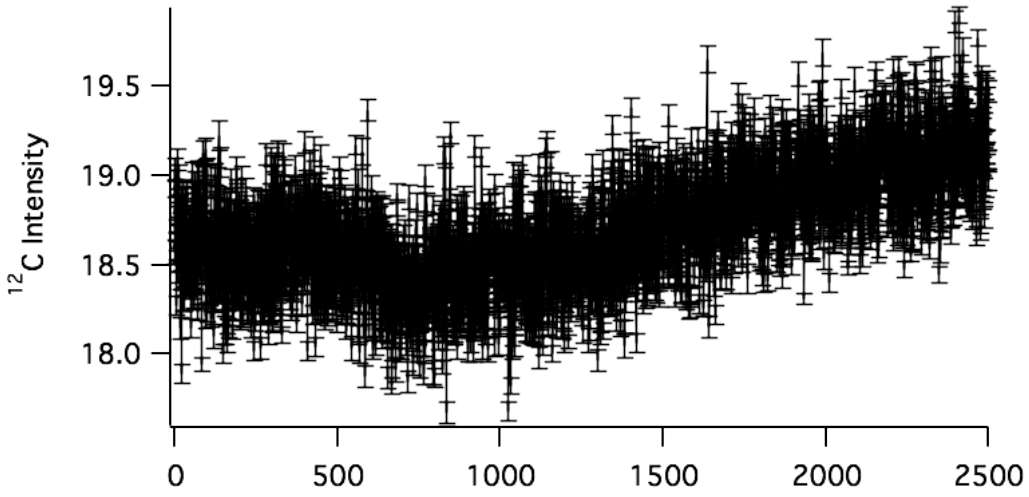

Figure 2.1. Intensity of the $^{12}CH_3OH$ $2_{0,2}$–$3_{-1,3}$ transition as a function of time in the Caltech coiled waveguide CP-FTMW. The amplitude is taken as the fitted intensity of the transition in a 50000 average acquisition at 50 kHz repetition rate and plotted versus the record number. Error bars are shown as the 1-σ uncertainty in the fitted amplitude.

cell is filled with sample to ~ 50 mTorr and manually pumped out to 5 mTorr. This also has the effect of coating the walls of the cell with a small amount of additional sample, so that as virtual leaks increase the cell pressure and sample is pumped out, it is replaced by additional sample, rather than contaminant, which extends the time the experiment can run without losing signal. Pressure is maintained at ~ 5 mTorr using an active feedback system. This consists of an Arduino Uno, a hobby servo motor, and a KJL 275800 digital pressure gauge. Pressure is read out by the Arduino and fed into a simple proportional-derivative loop control system that adjusts the position of a valve between the cell and the vacuum line. The code used to accomplish this is given in the Appendix An early example of the intensity variability achieved is shown in Figure 2.1. This was subsequently improved through faster loops, but the long-term stability proved to be a challenge unless the cell was thoroughly baked prior to data acquisition due to the large hysteresis in the valve used and the limited range of motion of the servo.

The microwave electronics are extremely similar to those used in [50]. Briefly a linear 0 – 2 GHz chirp is generated using a AD9914 direct digital synthesis (DDS) board, clocked at 4 GHz by a Valon 5008 synthesizer (+7dBm). The board is programmed by an Arduino Uno, the program and details of this process are given

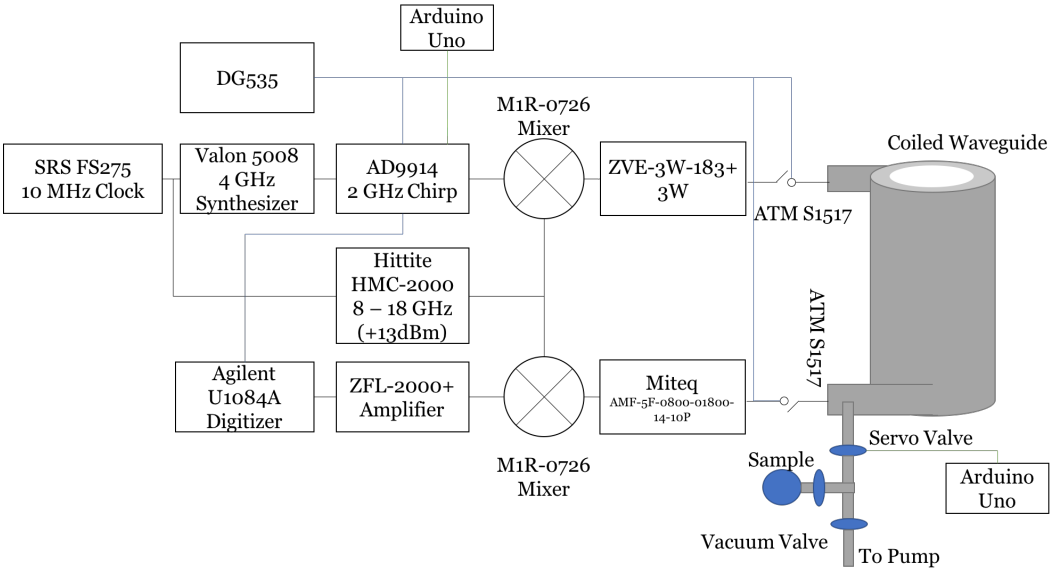

Figure 2.2. Schematic of the Caltech coiled waveguide CP-FTMW spectrometer. Chirps are generated in the DDS board. The board is clocked by a 4 GHz synthesizer and programmed through an Arduino Uno. The chirp is triggered by a delay generator and mixed with a 8-16 GHz LO. Both the synthesizers are in turn referenced to a 10 MHz Rb frequency standard. The up-converted signal is amplified by a 3W amplifier and broadcast into the cell. A p-i-n switch, triggered by the delay generator closes after the pulse to block noise from the amplifier. Emission is amplified by a low noise amplifier placed behind a protective p-i-n switch also triggered by the delay generator. The emission is down-converted in a second mixer, amplified by an IF amplifier, and detected in a high-speed digitizer

in the appendix Section A. The chirp is mixed with a local oscillator (LO) from a Hittite HCM-2000 (+13dBm) using a M1R-0726 mixer. Both the LO and 4 GHz clock are referenced to a 10 MHz FS 275 Rb frequency standard. The chirp is then amplified using a 3W amplifier (ZVE-3W-183+) and broadcast into the waveguide. Noise broadcast by the amplifier is suppressed by a ATM S1517 p-i-n switch that opens during the excitation pulse. Emission is detected at the other end of the cell after the excitation pulse is blocked by a second ATM S1517 switch. Unlike the instrument described in [50], there is no diode limiter used because the switch is capable of directly handling a 3W load. The emission is amplified by an AMF-5F-0800-01800-14-10P amplifier, and down-converted using the same LO and a second M1R-0726 mixer. It is then further amplified by a ZFL-2000+ intermediate frequency (IF) amplifier and digitized by an Agilent U1084A digitizer using custom C code built on the original Acqiris drivers. A schematic of the full setup is shown in Figure 2.2.

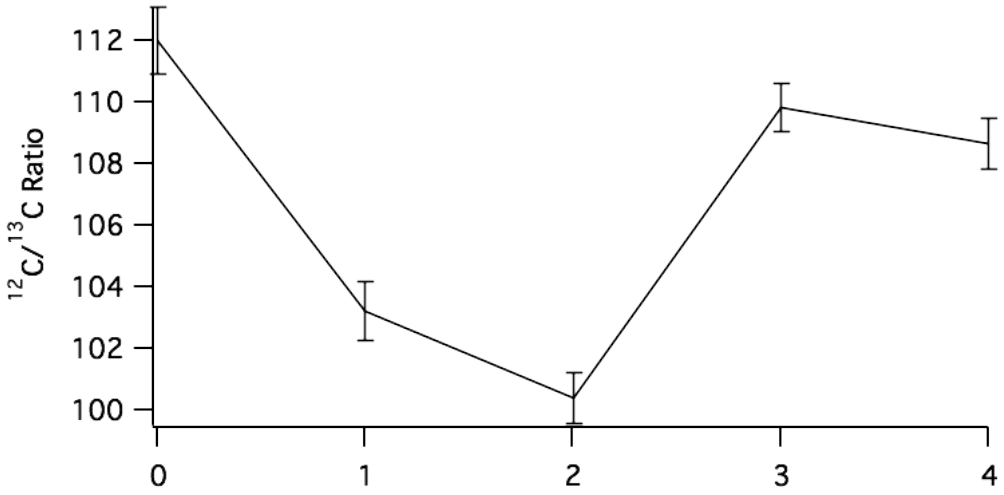

Figure 2.3. The measured ^{12}C to ^{13}C ratio of CH_3OH using the Caltech coiled waveguide CP-FTMW. Each data point represents 25 million acquisitions taken at a repetition rate of 50 kHz. The ^{12}C to ^{13}C ratio is determined by ratio of gaussian fits to the $^{12}CH_3OH$ and $^{13}CH_3OH$ $2_{0,2}$–$3_{-1,3}$ transitions. Error bars are 1σ errors determined from the fitting.

Once the instrument is set up, the measurement of ^{12}C to ^{13}C ratio is a relatively straightforward process. Data is simply acquired and averaged in the time domain and then Fourier transformed. Unlike other double sideband experiments, there is no deconvolution of the Fourier transform, as the transitions of interest are already identified and there is no contamination from other transitions. The ratio is calculated by fitting the line shape of each transition and taking the ratio. In order to test the ability of the instrument to measure the ^{12}C to ^{13}C ratio, successive acquisitions were taken over a fifteen minute period. Individual scans of one thousand averages were combined into one million average waveforms in the time domain and Fourier transformed. The resulting ratios were computed using the $2_{0,2}$–$3_{-1,3}$ transition of CH_3OH and are shown in Figure 2.3, and an example spectrum is shown in Figure 2.6. The derived ratio is higher than expected, and can be explained by optical depth effects discussed below. The variation is of order 10%, as would be expected for a ratio dominated by the low signal to noise ratio of the ^{13}C transition. This test demonstrates the ability of the coiled waveguide system to provide relatively stable measurements of rotational spectra. Indeed, the intensity of ^{12}C is better than 3% over short periods where the pressure stabilization is stable, and appears to be entirely dominated by system noise. This suggests that with better sample stability the intensities and therefore ratios are entirely dominated by the signal to noise ratio

that can be achieved.

Sensitivity

The spectrum of the $2_{2,0}$–$2_{2,1}$ transition of HDO collected in the waveguide spectrometer is shown in Figure 2.5. These data were taken over a 3.3 minute period, resulting in a signal-to-noise ratio (SNR) of ~ 6.5, though the uncertainty in the amplitude can be improved somewhat through fitting of the full line shape. Achieving part per hundred or part per thousand level sensitivity requires both suppression of systematic variation to this level and SNR >100 or > 1000. This would imply that to achieve a SNR of 100 an acquisition time of ~ 13 hours is required for HDO. This presents a serious challenge for this technique, and there is an obvious need for increased sensitivity. Unfortunately, there are few options available with the current instrumentation. Increasing sample density is only marginally helpful, as the collision rate increases linearly with pressure, resulting in significant broadening and corresponding loss in SNR. This is partially compensated for by an increased repetition rate, however this quickly becomes insufficient. In general the best SNR is achieved at pressures of 5–10 mTorr. Similarly, an increase in the cell length is not particularly helpful because the 10m cell currently used is roughly at the optically thick limit for absorption. Increases in amplifier power or reduction in excitation bandwidth can help for weaker transitions; however, as shown in Figure 2.4, stronger methanol transitions fully saturate near 50% power. Curiously, both the transitions used for the test are *b*-type, with the weaker transition, $16_{5,12}$–$17_{4,13}$, having a stronger transition dipole moment by a factor of two. Furthermore, both transitions used, $16_{5,12}$–$17_{4,13}$ and $2_{0,2}$–$3_{-1,3}$, are within 50 MHz of each other. It is therefore unlikely that the instrument response has changed significantly over this small frequency. Therefore, in the case of methanol, the most reasonable explanation is that the cell is near the optically thick limit. This would explain both the lack of full Rabi cycling in Figure 2.4, and the unusually high ^{12}C to ^{13}C ratio derived. This suggests that the cell is not operating in the $\pi/2$ limit and reduction in sample concentration coupled with higher excitation power could provide more accurate data and higher dynamic range data, and could somewhat enhance the SNR by increasing the $^{13}CH_3OH$ signal.

Some improvements in detection amplifier noise are possible, either through cooling of the cell and amplifier, or by simply using a lower noise figure amplifier. Unfortunately, the current amplifier has a noise figure near 1.0 dB, and it is difficult to find wide-band amplifiers capable of improving this. Finally, it might be possible

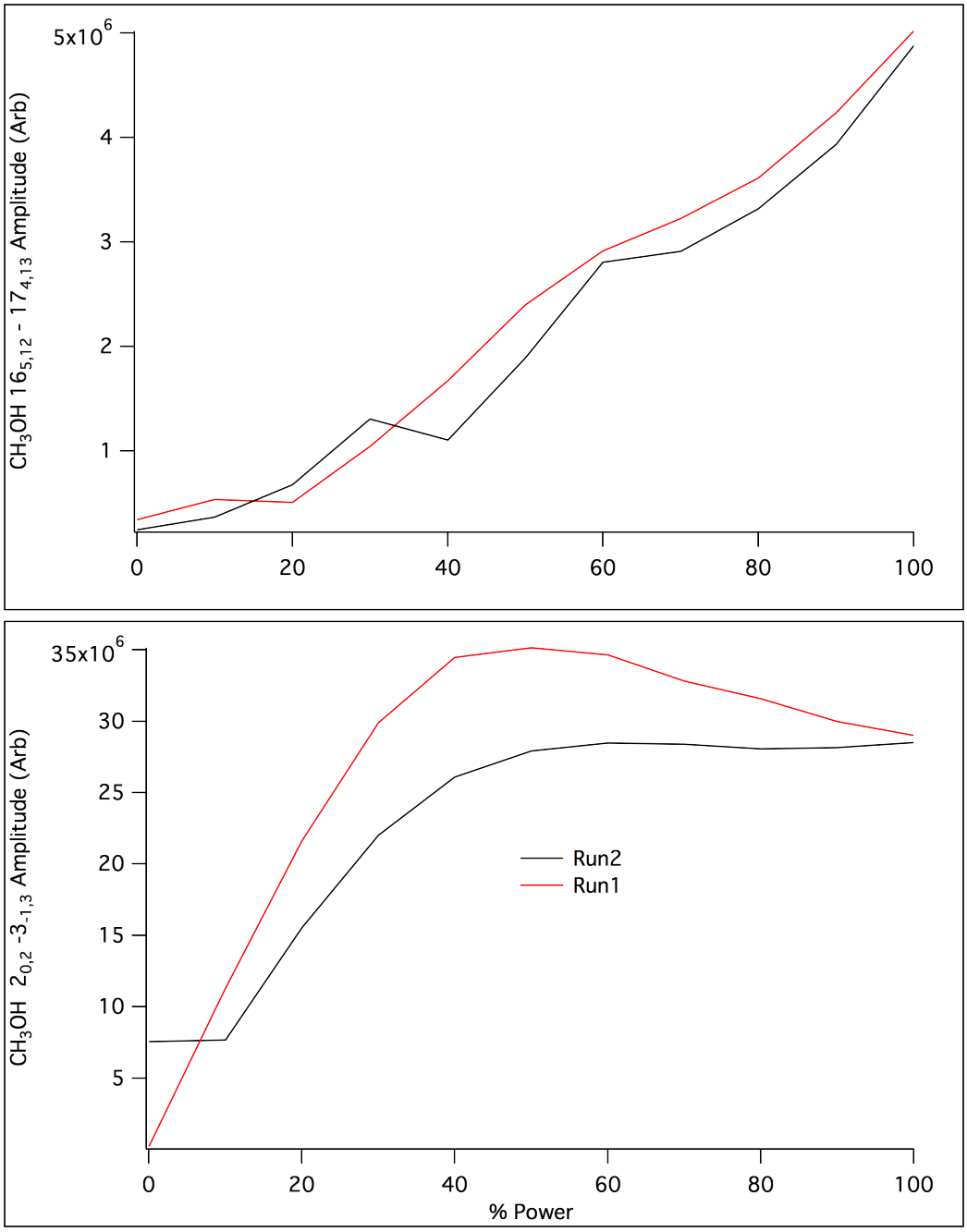

Figure 2.4. Nutation spectrum of CH_3OH. This demonstrates the ability of the instrument to fully saturate strong methanol transitions. Methanol spectra were taken at various excitation powers from 0 – 100% of the maximum excitation power using an AB-BA scheme, where the first acquisition, labeled 'Run 1'(Red), was cycled from 0 to 100% and the second set, labeled 'Run 2' (Black), was taken from 100 to 0%. Data were taken as 10 million acquisitions per point. The amplitude of the excitation pulse was varied by controlling the amplitude of the excitation chirp using an arbitrary waveform generator. The amplitude of the $2_{0,2}$–$3_{-1,3}$ (12178.6 MHz) is shown in the bottom panel and amplitude of the $16_{5,12}$–$17_{4,13}$ (12229.4 MHz) is shown in the top panel.

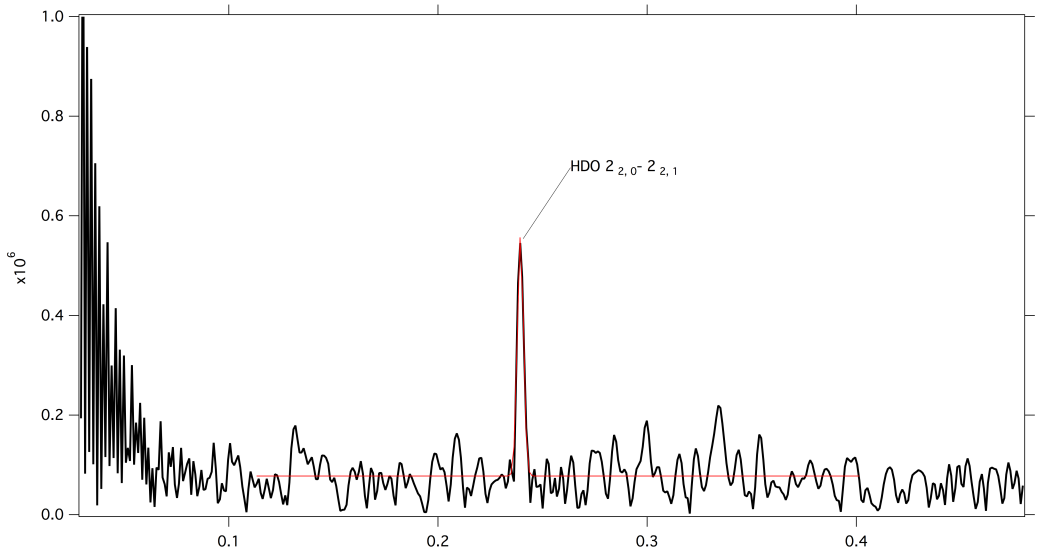

Figure 2.5. The rotational spectrum of the $2_{2,0}$–$2_{2,1}$ transition of HDO from the Caltech waveguide CP-FTMW observed in natural abundance. The spectrum consists of 10 million averages, taken at a repetition rate of 50 kHz, achieving a signal to noise ratio of 6.5.

to target somewhat brighter transitions. The HDO transition shown in Figure 2.5 has an absorption cross section of 4.1×10^{-6} nm ^{2} MHz and an abundance-weighted cross section of $\sim8\times10^{-9}$ nm ^{2} MHz. Strong transitions for ^{13}C abundance-weighted transitions are of order 10^{-9} nm ^{2} MHz for smaller species such as acetaldehyde or methanol [114]. Targeting even larger species will be hindered by large partition functions. Therefore, this is a reasonable limitation for most target species, implying that direct measurement of deuterium fractionation in organic species will not be feasible with this technique, precluding clumped isotope measurements[46], nor will measurements of very low dipole species such as CH_3D or ^{18}OCO [44, 59].

The most obvious solution is the use of buffer gas cells. These sources, originally developed as a source of slow molecular beams for traps, work by flowing pre-cooled helium atoms into a 5-10 K cell. Helium is cryopumped out of the cell by a 4 K stage to maintain a helium density of $\sim10^{14}$ cm^3 [24]. Sample is continuously flowed in independently where it is thermalized through collisions. These cells offer several advantages over the more traditional pulsed jet supersonic sources. First, they can achieve higher sample densities than pulsed molecular beams [83, 112]. Second, because they are continuous, the repetition rate of buffer gas cell experiments is limited only by measurement time, which is 100 to 1000 times faster than typical jet experiments [19], and also compatible with CW measurements. Finally, the

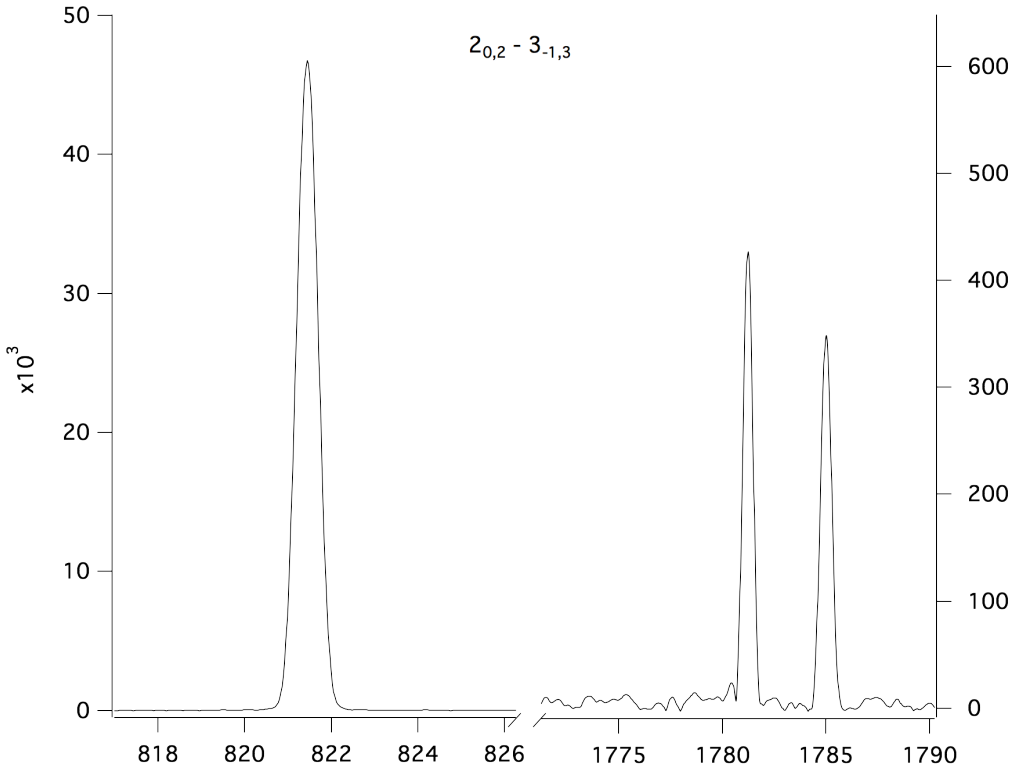

Figure 2.6. The rotational spectrum of the $2_{0,2}$–$3_{-1,3}$ transition of $^{12}CH_3OH$ (left) and $^{13}CH_3OH$ (right) from the Caltech waveguide CP-FTMW observed in natural abundance. The spectrum consists of 100 million averages, taken at a repetition rate of 50 kHz.

principal source of noise in microwave experiments is thermal background and amplifier noise. Operating at 10 K directly reduces detection amplifier noise and detecting against a 10 K background substantially reduces background noise. This combined with the buffer gas cell's ability to achieve cold rotational temperatures typical of supersonic jets makes buffer gas cells a potential avenue to improve sample density and sensitivity, while maintaining high repetition rate. The sample system should be capable of delivering similar or stability to that of the waveguide cell due to the active pumping used. Similarly it should be adaptable to liquid or gas sampling systems, and with proper gas handling design it should be possible to recover and recycle sample for rare samples.

In summary, this project aimed to test the feasibility of waveguide CP-FTMW instruments to measure the isotopic anatomy of samples as a possible new tool for analytical chemistry. As expected, the waveguide-based instrument showed superior stability and relative intensities to traditional supersonic jet systems. The

ability of the system to measure site-specific isotopic ratios, while not in doubt, was nevertheless demonstrated. The precision of the instrument to measure the ^{12}C to ^{13}C ratio of CH_3OH was shown to be ~10%, partially limited by SNR. Variable power tests suggest that amplitudes of stronger transitions of $^{12}CH_3OH$ are limited by optical depth rather than raw SNR, while ^{13}C transitions are purely SNR limited. This suggests that ^{12}C to ^{13}C ratio variability is at least partially tied to sample abundance variation and the leak rate of the waveguide coupled with the pressure control system. SNR-limited precision is shown to be ~1% Measurements of both CH_3OH and HDO show that even with minimal sample variation, SNR will likely be a significant challenge for more detailed isotopic anatomy studies. An alternative method utilizing buffer gas cooling cells is briefly discussed as a promising technique.

2.2 Development of a Low-Cost Chirped-Pulse Fourier Transform Microwave Spectrometer for Undergraduate Physical Chemistry Lab

Introduction

Rotational spectroscopy is a well-established and flexible technique for physical chemistry labs. It provides an interesting and intuitive way to relate structure to spectroscopy and may be used to study numerous effects relevant to an undergraduate or introductory graduate-level physical chemistry course. Recent advances in cutting-edge high speed electronics for next-generation communications networks have also led to greatly increased performance for less expensive systems. The result is that off-the-shelf components are now capable enough to be used for modern rotational spectroscopy, and it is now possible to construct an instrument that would have once been considered a cutting edge research instrument for a relatively low cost. The technological and economic forces driving this development are unlikely to slow in the near future, and the cost of the instrument demonstrated here should be even less in the coming years. This presents educators with the opportunity to combine rotational spectroscopy with modern Fourier transform techniques. This adds the ability to demonstrate key principles of modern spectroscopy like coherence, Fourier transforms, time domain methods, density matrix formalism, dephasing, broadening, and collision theory to an already well-developed physical chemistry lab.

Spectroscopy is a cornerstone of modern physical chemistry, providing a method of directly probing atomic and molecular Hamiltonians, measuring kinetics, dynamics, thermodynamic properties, and molecular structure[134]. As such, a thorough

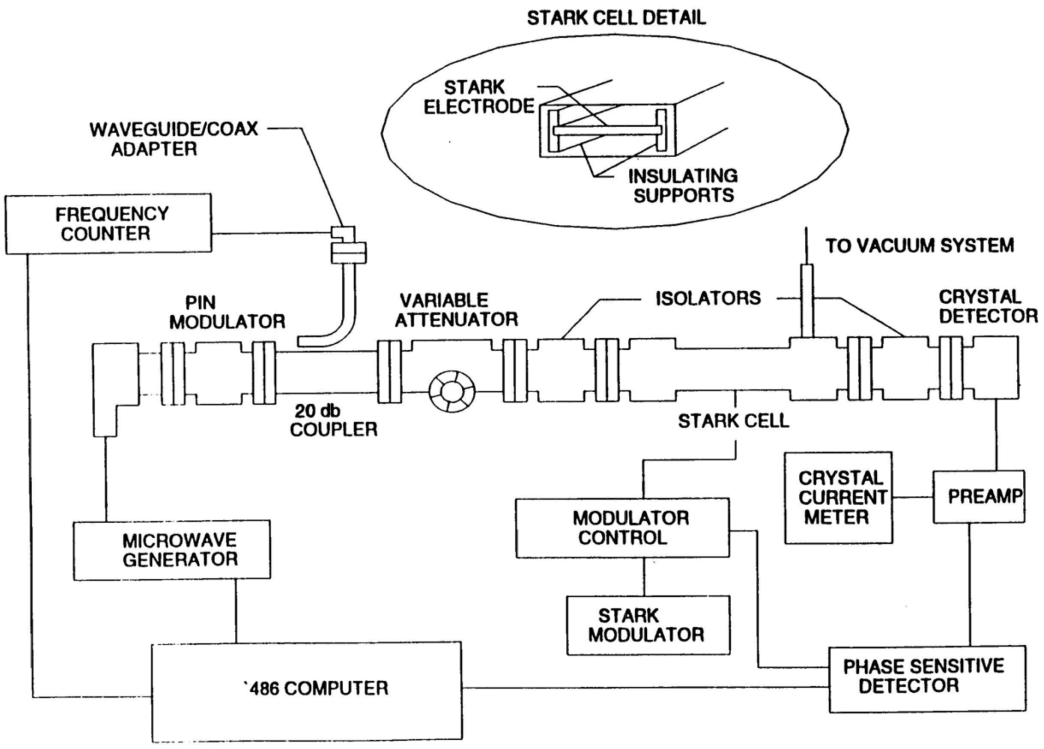

Figure 2.7. Schematic of an original HP Stark modulated absorption cell.

understanding of modern spectroscopy is key to physical chemistry education in order to develop, test, and contextualize many key concepts. Rotational spectroscopy is particularly well suited to this. Observed rotational transitions provide direct structural information that is easily relatable to numerous fundamental concepts in both classical physics and quantum mechanics[13].

Rotational spectroscopy is extremely versatile and may be used to demonstrate numerous fundamental spectroscopic concepts, making it ideal for physical chemistry lab experiments. Moreover, rotational transitions are directly related to molecular structure[68]. Further observation of multiple isotopologues enables very accurate structural determination. Measurement of rotational transitions of vibrationally excited states as well as a determination of centrifugal distortion constants may be used to demonstrate the core concepts of vibrational potentials and vibration-rotation interaction. Perturbations of rotational transitions from external electric fields from a Stark cell or internal fields generated by nuclei with quadrupole moments give significant insight into electronic structure of molecules. Frequency shifts caused by coupling of internal motions to the overall rotation provide further insight into molecular structure, the potentials associated with the motion, and low frequency vibrational modes of the molecule.

With such a wide range of available experiments, rotational spectroscopy has been a staple of many physical chemistry curriculums for several decades. A common apparatus based on a continuous wave (CW) source coupled to a waveguide cell and crystal detector is shown in Figure 2.7 [72]. Measurements are made as a simple Beer's law experiment by slowly sweeping the frequency of a CW light source and measuring the absorption as a function of frequency. This apparatus, based on the HP 8460A spectrometer [72], is relatively straightforward to construct and maintain and is both stable and robust. This is primarily a result of using solid-state electronics to generate and detect all radiation used in the experiment. Furthermore all optical propagation is carried out with either cables or waveguide, which require no alignment. The primary limitations of the instrument are its scanning speed, sensitivity, and cost. The microwave synthesizers predominantly used in the apparatus have limited scan speeds, may need an external frequency counter, and can be prohibitively expensive. Power variations from the microwave source, noise from the crystal detector, and the inherent limitations of direct absorption measurements all limit the sensitivity and increase the time needed for the experiment.

Here we present an alternative to the traditional Beer's law microwave spectrometer that offers significant increases in scanning speed, sensitivity, and versatility over traditional spectrometers at an overall cost (~$7000) significantly less than a comparable direct absorption microwave spectrometer. To accomplish this we use recent advances in radio frequency (RF) integrated circuits (ICs) to construct a chirped pulse Fourier transform microwave spectrometer. Fourier transform microwave spectrometers offer several advantages over direct absorption spectrometers both in performance and in educational potential. The key difference between microwave direct absorption spectrometers and FTMW spectrometers is in the nature of the measurement. Whereas a direct absorption spectrometer relies on measuring a small change in the absorption of a continuous or slowly modulated source, a FTMW experiment detects emission from the sample following a short excitation pulse. This configuration offers two important performance advantages. First, emission is recorded in the absence of any background excitation, reducing power broadening and significantly increasing sensitivity. Second the bandwidth of the excitation and emission are large enough to excite multiple transitions in a single excitation. This combined with the high repetition rates of the instrument results in rapid data acquisition, lowering the time needed to complete experiments or the detection of less abundant species through signal averaging. The spectrometer also offers several educational advantages over its direct absorption counterpart. In FTMW

experiments the free induction decay (FID) resulting from emission is recorded in the time domain and Fourier transformed to give the frequency spectrum. This provides an excellent demonstration of absorption and emission processes as well as an introduction to time-domain spectroscopy. The enhanced sensitivity minimizes sample consumption and allows for the detection of species with lower abundances or weaker transitions, expanding the range of experiments the instrument is capable of performing. The ability of the instrument to acquire broad spectra in a single excitation event also significantly improves the accuracy of measured intensities, allowing for more quantitative analysis of transitions intensities.

Instrument Design and Principles of Operation

The goal of the instrument design is to construct a fully functional FTMW instrument at a cost that is reasonable for undergraduate physical chemistry labs. The complete instrument schematic is shown in Figure 2.8. This is accomplished by using newly developed, low-cost digital electronics in combination with existing Stark cells. The Stark cell itself is a vacuum-tight cell with a sample inlet, a Stark electrode, and adapters to couple radiation in and out. This project simply replaced the components connected to the Stark cell. The cell itself is unmodified, with the Stark electrode and sample inlet and pumping system left as is.

The instrument's electronics consist of three main components: chirp generation, excitation broadcast, and emission detection, a block diagram of which is shown in Figure 2.10. The first, chirp generation is relatively simple, involving a 4 GHz clock, a frequency standard, and a direct digital synthesis (DDS) board. Implementation of these boards and details of their operation have been given elsewhere [50] and practical details are discussed in Appendix section A. Briefly, chirps, specifically linear frequency ramps of the form shown in Equation 2.1, are generated in the AD9914 board. This is done by quickly increasing output frequency, described by a frequency tuning word, of a high bandwidth digital to analog converter (DAC) on each cycle of a provided external clock signal, resulting in a chirp with an instantaneous frequency given by Equation 2.2, where α is the sweep rate of the chirp. The external clock is a simple 4 GHz sine wave produced by a frequency synthesizer that uses a 10 MHz temperature stabilized crystal oscillator as a reference. This subsystem receives a start signal from the timing control, discussed below, generates a chirp, starting from 0 Hz and ramping to its final value, typically 100 MHz for these experiments, in $\sim 1\mu$s, and then sends out a timing pulse indicating the completion of the chirp.

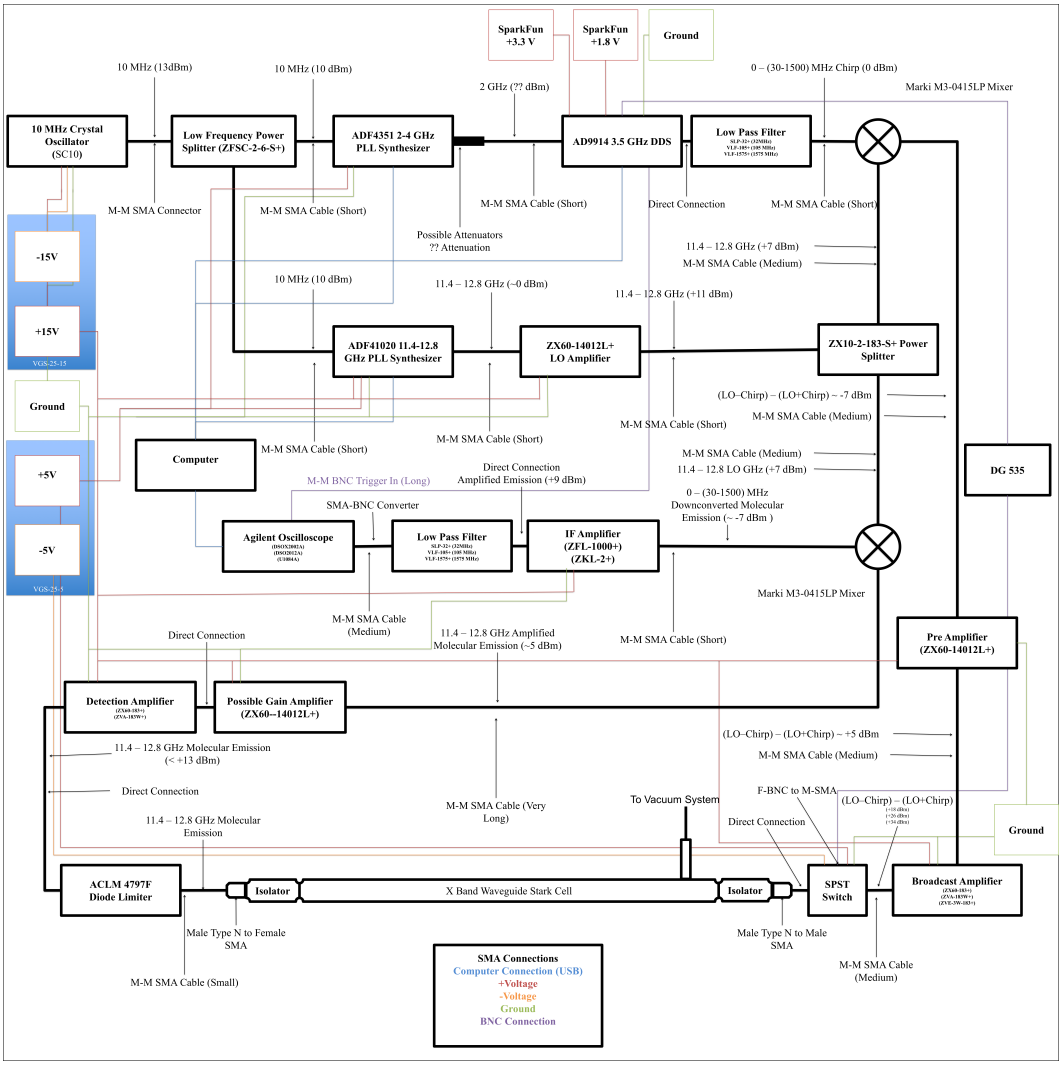

Figure 2.8. The full schematic of the initial design of the Caltech CH 6 chirped pulse FTMW system. SMA connections and cables are shown in black, positive voltage sources and connections are red, negative voltage sources and connections are shown in orange, ground is shown in green, BNC connections are purple, and computer connections and USB connections are blue. All individual components are shown as black boxes, and mixers are shown as circles with an x through the center. Components' model numbers are given inside their boxes. The RF frequencies of the components are shown above each SMA connection and the corresponding power below the SMA connection.

$$E(t) = E_{max} e^{i(\omega_0 t + 1/2 \alpha t^2)} \tag{2.1}$$

$$\omega_{inst} = \frac{d}{dt}\left(\omega_0 t + \frac{1}{2}\alpha t^2\right) = \omega_0 + \alpha t \tag{2.2}$$

The second section, excitation broadcast, takes the 0–100 MHz chirp, and converts it to a higher frequency, amplifies it, and couples it to the cell where it can excite molecular transitions. This is done in three steps. First the chirp is up-converted by heterodyne up conversion. This is done by mixing the chirp with a fixed frequency signal, the local oscillator (LO) in a mixer. Mixers are electrical components that respond to the square of the input field, as shown in Equation 2.3. When two fields are applied, this results in multiple outputs. Of importance to this instrument are the fields produced at the sum and difference of the input. For up-conversion, this results in two chirps, from (LO-100MHz) to LO, and LO to (LO+100 MHz), that are referred to as the lower and upper sideband respectively. We therefore choose our LO frequency to be near, but for reasons that will be clear later, not exactly at the frequency of our target line. This up-converted pulse is then amplified to provide sufficient power, and broadcast into the cell. Finally, once the excitation is complete, a trigger pulse closes a p-i-n switch placed after the amplifier to prevent amplifier noise from interfering with the experiment. This p-i-n switch consists of p-type, intrinsic, and n-type semiconductors stacked together. When forward biased, carrier injection from the p and n-type semiconductors makes it an effective conductor, while under no bias, the stack is a resistor. This allows the diode to be switched from conductor to resistor as fast as an electric field can be applied or removed, typically of order 10s to 100s of ns. Once broadcast into the cell, the pulse interacts with the sample.

$$\begin{aligned} S(t) &\propto e(t)^2 \\ S(t) \propto \frac{1}{2}(E_1^2 + E_2^2) &+ \frac{1}{2}[E_1^2 cos(2\omega_1 t) + E_2^2 cos(2\omega_2 t)] \\ &+ E_1 E_2 cos[(\omega_1 t + \omega_2 t) + (\phi_1 + \phi_2)] \\ &+ E_1 E_2 cos[(\omega_1 t - \omega_2 t) + (\phi_1 + \phi_2)] \end{aligned} \tag{2.3}$$

Sample excitation results in a coherence between two states $|a\rangle$ and $|b\rangle$ when any portion of the chirp is resonant with the frequency ω_0 of the transition between the two states. This coherence results in a macroscopic polarization P of the sample

that is given by Equation 2.4, which may derived from simple time dependent perturbation theory[13]. This polarization is caused by the rotational levels of ΔN = N_b-N_a molecules having rotational wavefunctions having the same phase, i.e. rotating in phase. A group of molecules which each posses a permanent dipole moment, all rotating in phase have an ensemble dipole moment that also rotates, analogous to classical field-induced polarization of a material. This polarization will then emit a field with a power per unit volume given by $\frac{1}{2}\Delta N(\omega_0)\mu\bar{\epsilon}$, where $\bar{\epsilon}$ is the emitted field. The constants a and b for states $|a\rangle$ and $|b\rangle$ describe the coefficients for each state, whose populations are given by $|a^2|$ and $|b^2|$. The value of these coefficients can be derived from time-dependent perturbation theory and their value is given by Equation 2.5, where ω_r is the Rabi frequency of the transition. Thus, the induced polarization of a chirp can be easily calculated by assuming that the chirp is a linear combination of a series of narrow-band excitation pulses. This can be related to the observed emission after accounting for the dephasing of the sample.

$$P(t) = \langle \Psi(\mathbf{r},t)|\, \mu\, |\Psi(\mathbf{r},t)\rangle = \mu[ab^* \exp(+i\omega_0 t) + a^* b exp(-i\omega_0 t)] \tag{2.4}$$

$$\begin{aligned} a(t) &= \cos\left[\frac{1}{2}\left(\frac{\mu\epsilon}{\hbar}\right)t\right] = \cos\frac{\omega_r}{2} \\ b(t) &= -i\sin\left[\frac{1}{2}\left(\frac{\mu\epsilon}{\hbar}\right)t\right] = -i\sin\frac{\omega_r}{2} \end{aligned} \tag{2.5}$$

The field decays through dephasing, that is the loss of phase coherence in the sample. This occurs through two effects: loss of population as the sample equilibrates and the phase of molecules being changed. The first effect, described as T_1, is identical to T_1 dephasing in ultrafast optical and infrared measurements [71], and spin-lattice relaxation in NMR, and is the result of population decay. The second, T_2, is a result of scrambling of individual phases of molecules in the ensemble. This can be caused by a variety of effects including non-homogeneous excitation fields, proper motion of the sample, and collisions with other molecules or the cell, the last of which is the dominant dephasing mechanism for waveguide cells [69], and is the rotational analogue of spin-spin dephasing in NMR. Combined the field decays with the phenomenological decay constant T_2, given in Equation 2.6, which combines the pure dephasing time T_2', itself a sum over all dephasing effects discussed above, and the population relaxation from levels $|a\rangle$ and $|b\rangle$. An example of the emitted field and its decay is shown in Figure 2.9.

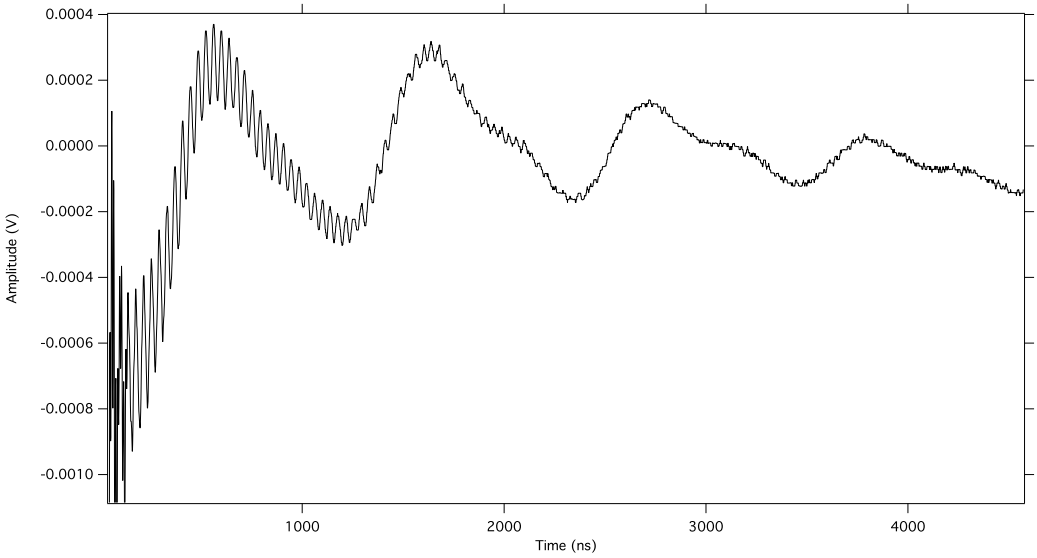

Figure 2.9. Time domain data of $^{16}O^{12}C^{32}S$ taken with the Caltech CH 6 spectrometer. The rapidly decaying oscillation is due to the dephasing of the $^{16}O^{12}C^{32}S$ coherence after excitation. The slow oscillation is due to low frequency instrumental response.

$$\frac{1}{T_2} = \frac{1}{T_2'} + \frac{1}{2}\left(\frac{1}{T_{1a}} + \frac{1}{T_{1b}}\right) \tag{2.6}$$

To detect the emission, it must be converted it to a lower frequency that is more easily detected. The emitted radiation is coupled out of the cell from a second antenna placed at the other end of the cell and detected. This is done in the third part of the instrument. First the signal passes through a diode limiter, which uses diodes to attenuate any signal with power over a threshold, while passing any less intense signal only mildly attenuated. This protects the downstream electronics from damage. The emitted radiation is then amplified and down-converted by reversing the process of up-conversion. To do this, we use the reverse process, and down convert the signal using a second mixer and the same local oscillator. This results in two signals, one at very high frequencies that can be ignored, and a second that varies from 0 - 100 MHz that effectively folds the two sidebands on top of each other. Down-converted frequencies are then observed at a frequency $|LO - \nu|$. To determine the absolute frequency observed, we simply shift the LO by a small amount. For example for a feature in the upper sideband, shifting the LO up in frequency will shift it to a lower observed frequency. Once down-converted, the signal is amplified again and detected as a function of time by an oscilloscope or digitizer. The frequency spectrum is recovered using a Fourier transform.

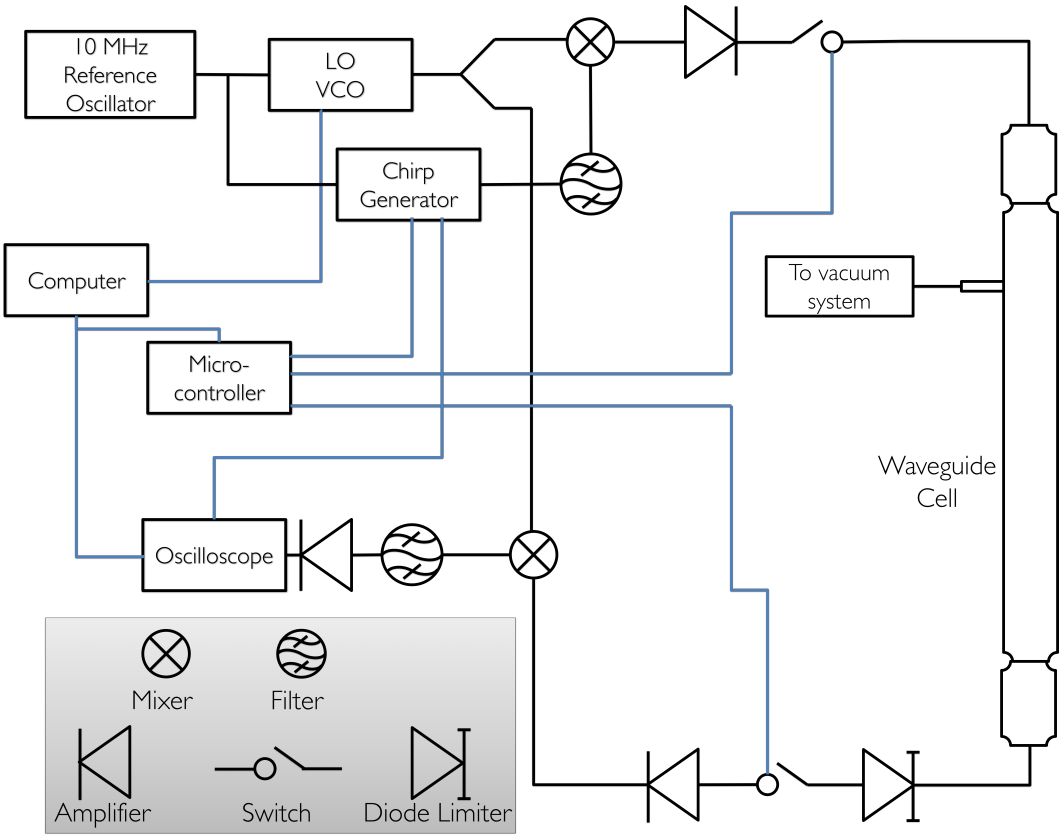

Figure 2.10. The block diagram of the Caltech CH 6 chirped pulse FTMW spectrometer. RF connections are shown in black and computer connections in blue. Individual components are shown as black circles or boxes. A key is given in the bottom left.

The performance of the instrument is demonstrated for the spectrum of OCS. OCS is the prototypical molecular target for physical chemistry laboratory rotational spectroscopy. It has four to five observable isotopologues ($^{16}O^{12}C^{32}S$,$^{16}O^{13}C^{32}S$, $^{16}O^{12}C^{34}S$, $^{16}O^{12}C^{33}S$, and $^{18}O^{12}C^{32}S$), making full structural determination relatively straightforward. It has a vibrationally excited state that is observable at room temperature. Its dipole moment is 0.7 D[120], which makes observation of Stark shifts achievable, and the presence of the ^{33}S nuclei allows for the measurement of hyperfine splitting. This versatility, combined with it's availability and relatively strong transitions due to its linear structure, make it an ideal target. Spectra of various OCS isotopologues were recorded at a pressure of 5 mTorr using the instrument described above. The spectra taken are shown in Figure 2.11.

Table 2.1. Current Components of the Caltech CH6 CP-FTMW.

Item	Description	Price ($)
ADF41020	11.4-12.8 GHz VCO board for LO	150
ZX10-2-183-S+	LO Power Splitter	100
SC10-15-1-J-J-J-SMA	10 MHz Ovenized Quartz Oscillator (SMA Out, ±15V Bias)	390
ZFSC-2-6-S+	Low Frequency Power Splitter (SMA) for 10MHz	60
ADF4351 PLL	2.2 - 4.4 GHz PLL to Clock AD9913	175
AD9914	1.4 GHz DDS Board	600
M3-0415LP	Mixer RF 4-15 GHz +7 dBm L pkg	181 × 2
DSOX2022A	200 MHz 1 GS/s Oscilloscpe	1,575
ZX60-183+	18 dBm, 24 dB Gain 6 - 18 GHz LO Amplifier 6.9 dB NF	170 ×2
ZVA-183W+	26 dBm, 24 dB Gain 0.1 - 18 GHz Receive Amplifier 3 dB NF	1400
ZFL-1000+	+9 dBm, 17 dB Gain 0.1-1000 MHz IF Amplifier	90
ACLM 4797F	+13 dBm Leackage 2W Diode Limiter	254
VLF-190+	190 MHz Low Pass Filter	20×2
33102A-001	SPST PIN Switch, 0.1-18 GHz, 30-40 dB isolation, SMA(f/f/f)	175 × 2
Arduino Controller	Instrument microcontroller	35
Total		7221

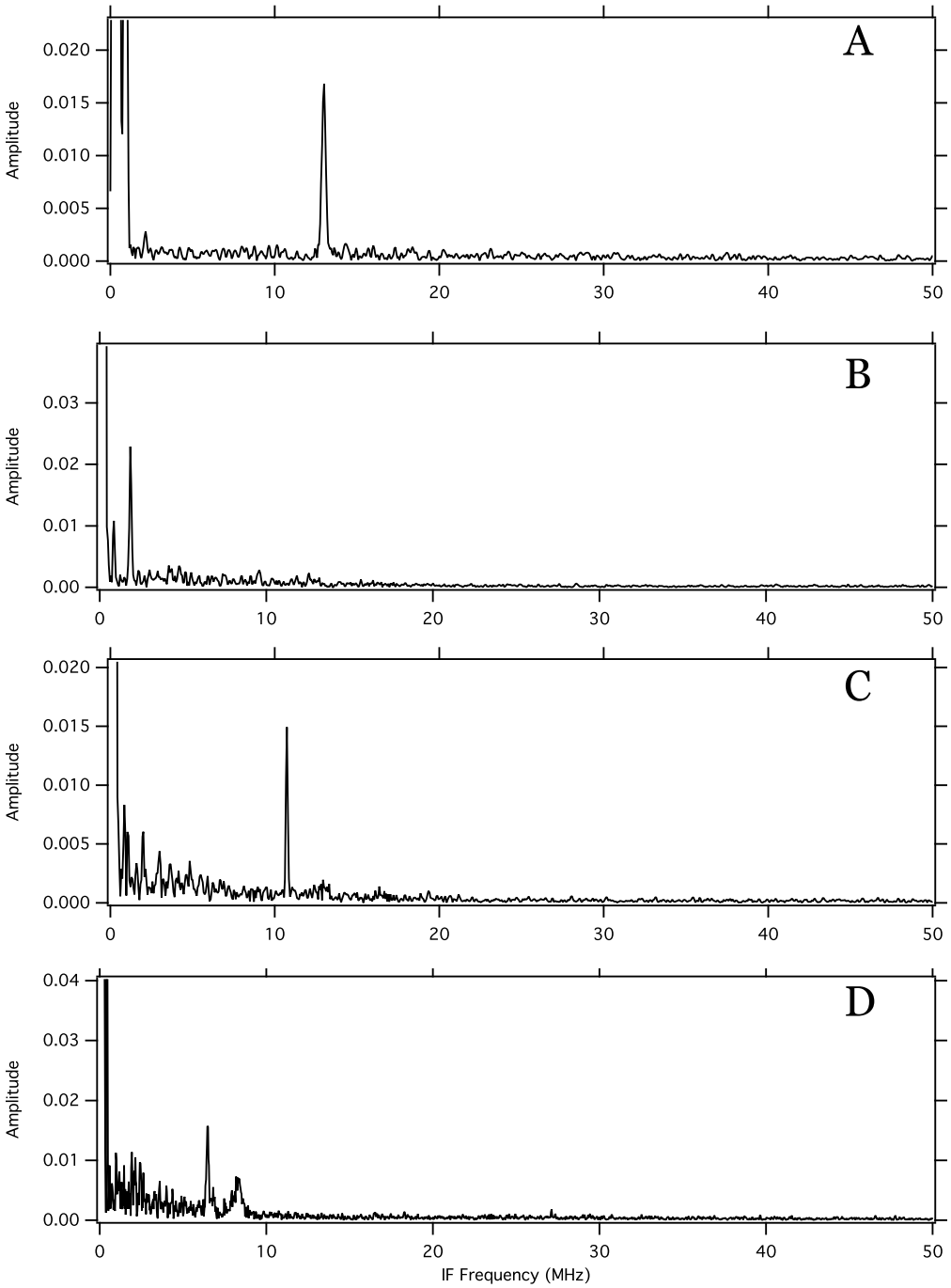

Figure 2.11. OCS spectra recorded from the Caltech CH 6 CP-FTMW. The spectra of $^{16}O^{12}C^{32}S$ is shown in panel A, $^{16}O^{12}C^{34}S$ in panel B, $^{16}O^{13}C^{32}S$ in panel C, and $^{16}O^{12}C^{33}S$ in panel D. The spectra of $^{16}O^{12}C^{32}S$ is a sum of 50000 averages, $^{16}O^{12}C^{34}S$ is a sum of 100000 averages, $^{16}O^{13}C^{32}S$ is a sum of 500000 averages, and $^{16}O^{12}C^{33}S$ is a sum of 1000000 averages. Amplitudes are arbitrary and are not the same scale between spectra.

Conclusion

The design and construction of a low-cost and low-bandwidth waveguide CP-FTMW is demonstrated. Construction of this instrument is enabled by Moore's law-like scaling of bandwidth and corresponding reduction in cost of high-speed digital electronics, and low-cost microwave and RF electronics driven by economies of scale in the telecommunication industry. In total the instrument was constructed for ~$7200. The instrument described is an electronics system that is adaptable to virtually any sample system. For this demonstration, the instrumentation was used with an existing waveguide-based HP Stark cell. Tests show the ability of the instrument to measure the spectrum of $^{16}O^{12}C^{32}S$,$^{16}O^{13}C^{32}S$, $^{16}O^{12}C^{34}S$, and $^{16}O^{12}C^{33}S$. Rotational spectroscopy of OCS makes an excellent target for physical chemistry due to its simplicity, high detectability, and the ability to study a variety of fundamental topics in chemical physics including the Stark effect, rotational spectroscopy and wavefunctions, vibrational modes and partition functions, and nuclear quadrupole moments. Introduction of the CP-FTMW instrumentation adds the augments this by adding new topics time domain spectroscopy and Fourier analysis, coherence and coherent spectroscopy, modern oscilloscopes and RF electronics, and density matrix formalism. Finally, though it remains unexplored at present, the electronics used, the AD9914 in particular, are flexible. In principle, it should be possible to switch the system from a time domain chirp to a frequency, or amplitude modulated CW system with minimal modification. This would enable more traditional direct absorption experiments that utilize lock-in amplifiers, and make it an incredibly general instrument for physical chemistry education.

Chapter 3

THE MICROWAVE SPECTRUM AND STRUCTURE OF THE CYCLOPENTANOL–WATER DIMER

3.1 Introduction

Hydrogen bonding plays a major role in a variety of chemical and physical processes in terrestrial chemistry. Of these, hydrogen bonds with water are paramount, due to water's abundance and role as 'universal solvent' in Earth's chemistry. Hydrogen bonds come in a variety of strengths from strong, e.g. F–H$\cdots$O–H, to weak e.g. C–H$\cdots$O–H or O–H$\cdots\pi$. While strong hydrogen bonds are obviously the largest single contribution to hydrogen bonding interactions, weaker C–H$\cdots$O–H or O–H$\cdots\pi$ bonds are an important part of the solvation of organic species and have a significant effect on the structure and dynamics of solvated organic species[39]. Measuring the structure of hydrogen bonded complexes can provide insight into the bonding potentials of these interactions, which is critical to understanding specific systems and to building a more complete and general understanding of hydrogen bonding. An obvious starting point for these studies is isolated dimers. Molecular dimers are the simplest hydrogen bonded systems and their study can reveal the isolated pairwise interactions, serving as a basis for understanding more complex systems[45].

Rotational spectroscopy has proven to be a powerful tool for the study of hydrogen bonding. Because rotational spectroscopy is sensitive to the moments of inertia of a molecule or complex, it is an inherently structurally sensitive technique[68]. With the incorporation of isotopologue measurements it is possible to determine atomic positions in a molecule or cluster to sub-angstrom precision[22]. This precision can be used to definitively determine the nature of the interaction e.g. van der Waals or hydrogen bond, and provides important benchmarks for theoretical calculations and methods[140, 141]. In recent years the development of chirped pulse Fourier transform microwave (CP-FTMW) spectroscopy has greatly increased the speed at which rotational spectra can be acquired, enabling rapid and blind searches for the spectra of clusters[19]. This has led to renewed interest in the study of several hydrogen bonded complexes including the ethanol–water dimer[52], the propanol–water dimer[48], and the ethanol–methanol dimer [53]. These measure-

ments have revealed two simple motifs that appear to be common in these systems: (1) water-donor alcohol-acceptor structures are energetically favored and therefore the dominant contribution to the interaction energy, and (2) secondary structure is determined by weaker C–H$\cdots$O–H interactions. An important question is to what degree these weaker interactions affect the overall structure. To better understand this question we have studied the cyclopentanol–water dimer, which is an extreme case of C–H$\cdots$O–H interactions with both an alcohol group and four C–H groups available for hydrogen bonding to a single water.

3.2 Experimental

All data were taken using the Caltech supersonic jet CP-FTMW, which has been previously described [50]. An instrument schematic is shown in Figure 3.1. Briefly 0–2 GHz chirps are generated from a direct digital synthesis (DDS) board, and up-converted with a local oscillator (LO) from a microwave synthesizer. The up-converted double sideband chirp is amplified in a solid-state amplifier to ~60 W and broadcast into the chamber where it excites the sample. The low noise detection amplifier is protected by a diode limiter and p-i-n switch. Once the excitation pulse has faded, molecular emission is amplified by the detection amplifier and down-converted using the same LO used for up-conversion. The down-converted signal is further amplified and then digitized by a high-speed digitizer. The double sideband up- and down-conversion system makes absolute frequencies impossible to determine from a single LO setting, so two sets of data are taken for each LO setting, one at the LO itself, and a second at the LO+10 MHz. Together the datasets can be used to determine the absolute frequency of any feature, as long as the spectra is sufficiently sparse, a condition that is met for supersonic jet instruments.

Cyclopentanol was purchased from Sigma Aldrich (99%) and used without further purification. Cyclopentanol–H_2O mixture was prepared by flowing 50 PSI Ar carrier gas through a two step pickup line. Ar is first flowed through a water pickup region, loaded with room temperature deionized water. The Ar–water mixture is then flowed into a lightly heated (~60 °C) reservoir nozzle filled with cyclopentanol. This arrangement was shown to produce the largest cyclopentanol–water dimer signal, and is the reverse of the arrangement that was used with other alcohol–water complexes [48, 52]. This is likely due to the much lower vapor pressure of cyclopentanol. Data were taken at three LO settings, 10 GHz, 13 GHz, and 16 GHz, with a second scan at a 10 MHz offset for each LO setting. To complete the scan, 100,000 averages were taken at each setting from lowest to highest. This cycle was repeated

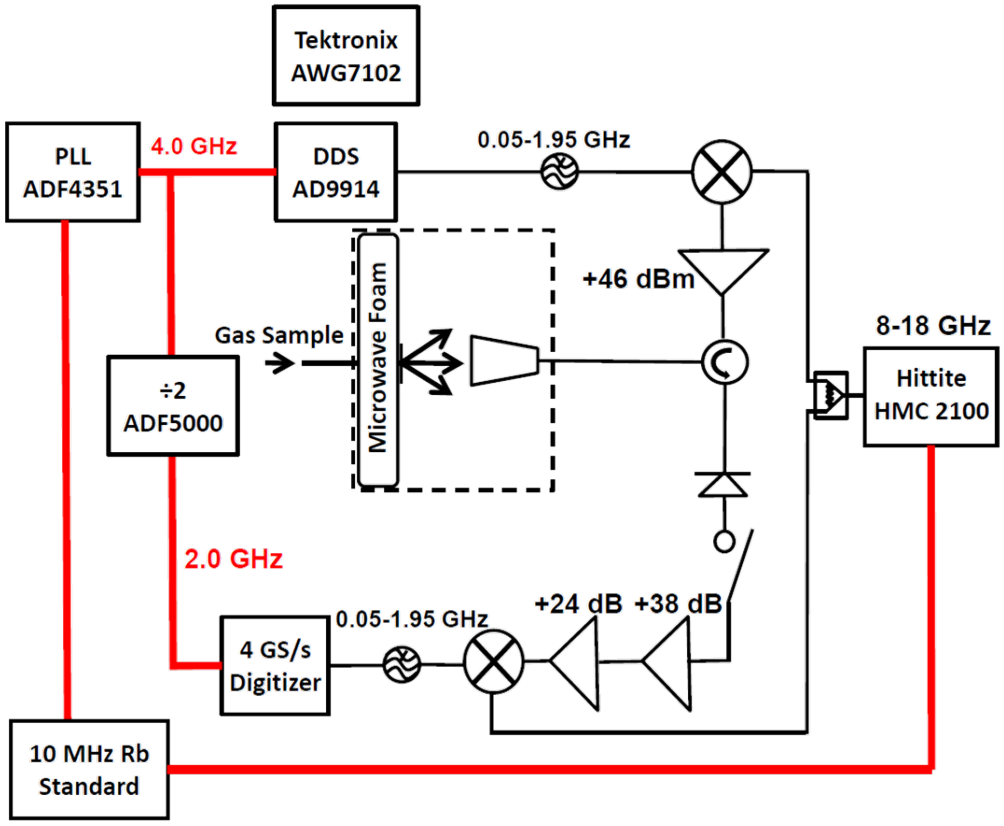

Figure 3.1. Block diagram of the Caltech supersonic jet CP-FTMW. The instrument uses either an AD9914 or arbitrary waveform generator to generate linear frequency chirps for excitation. Later iterations utilized a two horn perpendicular supersonic jet arrangement with no circulator. Figure taken from [50]

until 10 million averages were acquired at each setting using a custom Python script. The 16 GHz LO setting was found to have lower amplitude, in both noise and signal, than the other two settings. This is caused by the lower coupling efficiency of the X band waveguide horn used. The data were then averaged in the time domain and Fourier transformed and deconvolved with a custom Python script to give the spectrum shown in Figure 3.2. After spectral assignment, the data were reprocessed. To improve SNR, each individual scan was Fourier transformed and the amplitude of water dimer, cyclopentanol monomer, and if possible the cyclopentanol–water dimer was recorded. These values were used to create a normalized weight for each scan, which was then applied to each scan in the time domain. The weighted time domain scans were then reaveraged and Fourier transformed.

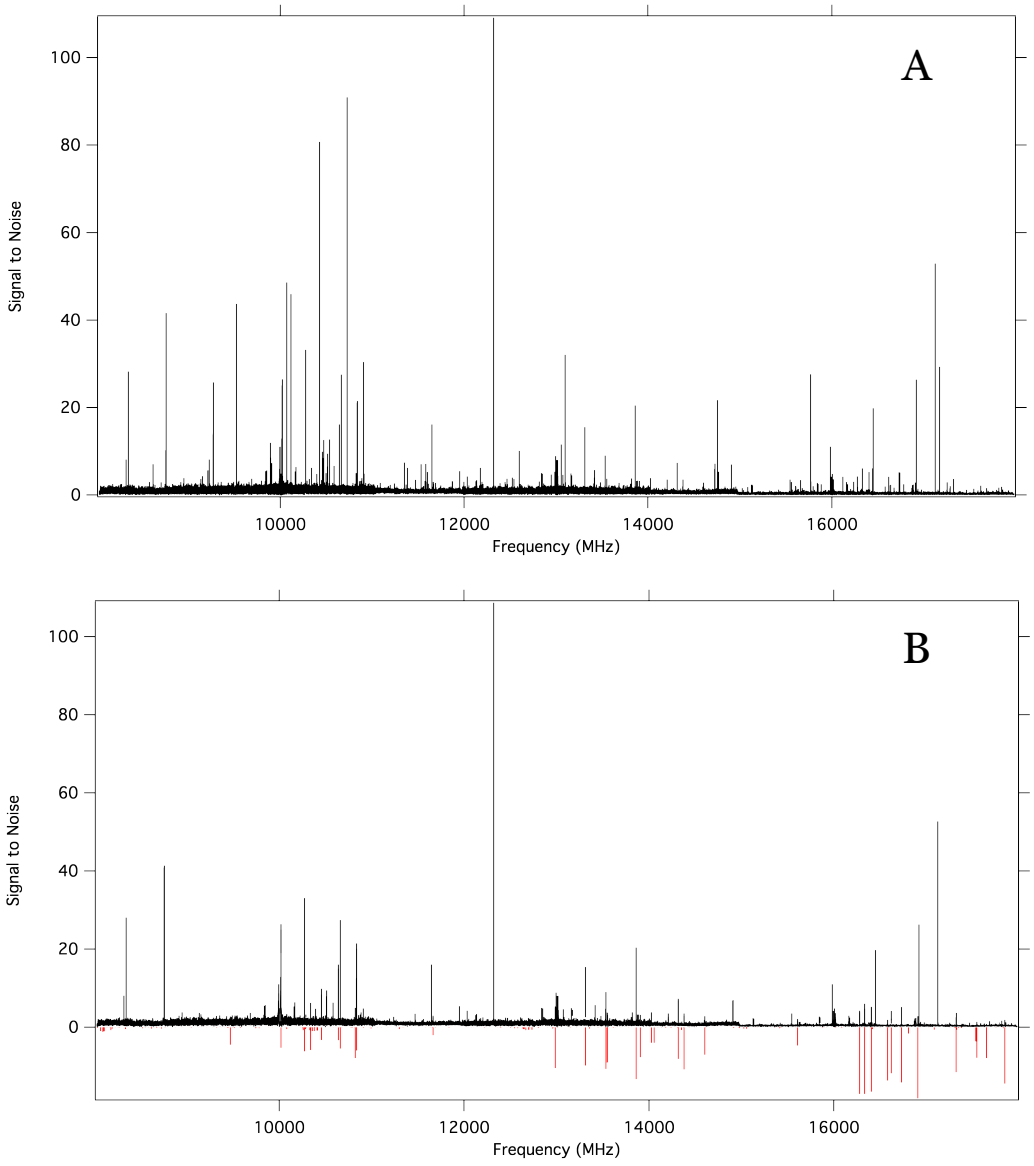

Figure 3.2. Spectrum of the cyclopentanol–water mixture. The complete spectrum is shown in panel A. The spectrum after subtraction of the monomer data is shown in panel B in black, while a spectral prediction based on the assigned constants is shown as negative lines with intensity proportional to the expected intensity of the line. The y axes are given as signal to noise ratio (SNR), determined by dividing the spectrum by the RMS of a transition free region in the 13 GHz LO region.

Cyclopentanol Monomer Spectrum

Typically spectra of mixtures are dominated by the spectra of the monomer constituents, with weaker contributions from the homo- and heterodimers. For water mixtures at the high pressures used in this study, the water dimer is also significant. The monomer and homodimer peaks are often already measured and not of interest and therefore must be accounted for to prevent false assignment. This is usually a simple process since the monomer spectra is known and assigned, however this was not the case for cyclopentanol. Despite being a small, volatile, readily available, and easily measurable species, its pure rotational spectrum has to the best of our knowledge never been measured or assigned. his is somewhat surprising, however it is likely due to the complex internal rotation of the molecule. Analogous to the case of tetrahydrofuran (THF)[119], the C_5 ring undergoes a set of coupled bending or ring puckering motions that effectively rotate around the ring, referred to as a pseudorotation. Splitting caused by this potential significantly complicates the rotational spectrum, and has required extensive study to firmly assign the spectrum of THF. Cyclopentanol posses a similar pseudorotational potential, but is complicated slightly by the presence of the OH group. The structure of the monomer is shown in Figure 3.3. In order to prevent incorrect assignment of cyclopentanol monomer lines to the dimer, a spectrum of only the monomer was recorded. This spectrum consists of 10 million averages taken using a reservoir nozzle filled with monomer, with 15 PSI Ar carrier gas. The spectrum as well as the prediction based on the *ab initio* structure is shown in Figure 3.4. It was later noticed that a small amount of the cyclopentanol–water dimer was present in the spectrum, likely due to contamination from ambient moisture.

3.3 Spectral Assignment

The spectra assignment was done by first removing lines from the monomer reference spectra. This initially resulted in problems due to incorrectly removed cyclopentanol–water dimer lines present in the monomer spectra from water contamination either in the system or the cyclopentanol sample. The spectrum before and after removal is shown in Figure 3.2 panels A and B respectively. The resulting spectrum still has several strong lines due to the water dimer which were left in due to their low number and distance from predicted cyclopentanol–water dimer transitions. The spectrum was fit using the AUTOFIT program [131]. The initial guess for AUTOFIT was taken from *ab initio* calculations of the cyclopentanol–water lowest energy conformer using the MP2 method and aug-cc-pVTZ basis set with verytight

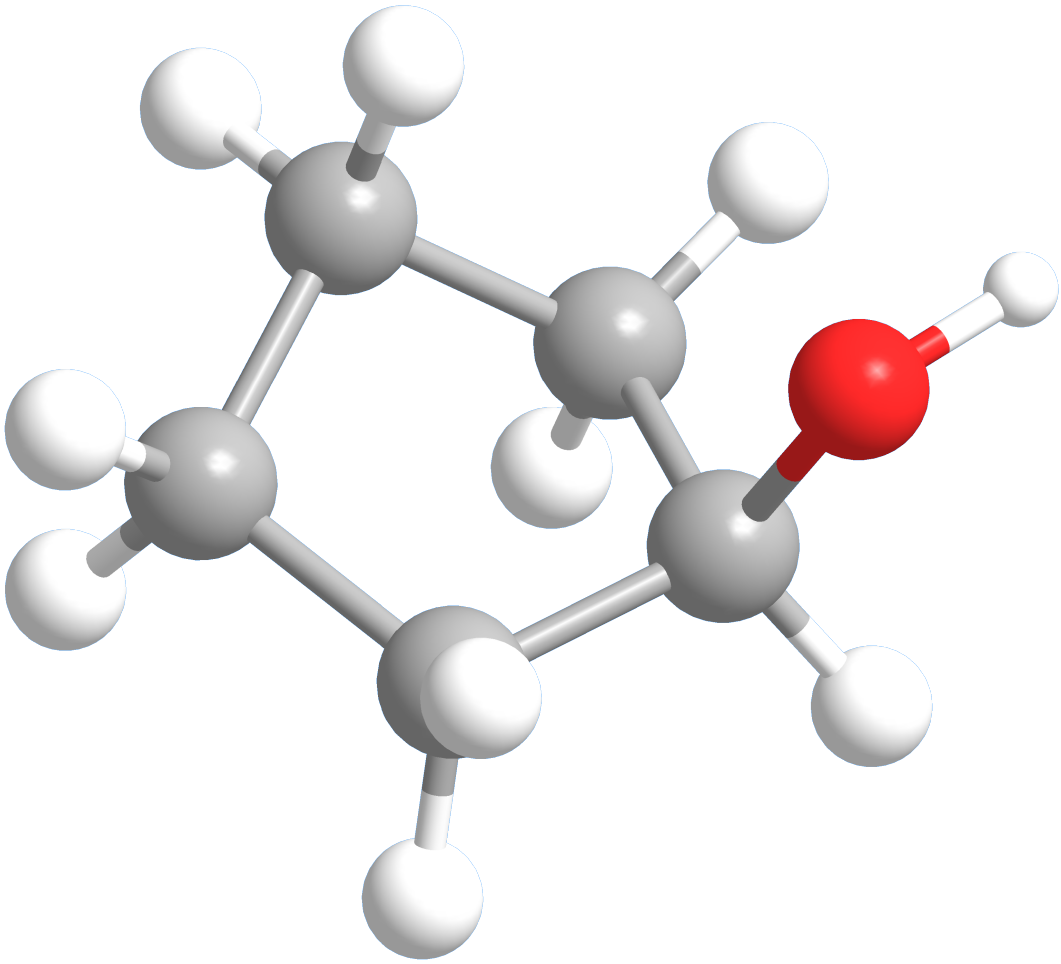

Figure 3.3. The structure of the cyclopentanol monomer. The structure is optimized at the MP2/aug-cc-pVTZ using the Gaussian 09 software package [56].

convergence criteria using the Gaussian 09 software package[56], the structure of which is shown in Figure3.7. Further anharmonic frequency calculations at the same level were used to confirm the optimized structure was a potential energy minimum and to compute distortion constants. The full *ab initio* constants are given in Table 3.2. Due to the very low SNR achieved, AUTOFIT initially struggled to find an acceptable fit, despite *ab initio* calculations that are reasonably accurate. This is caused by a larger than typical number of possible experimental lines found at low SNR, several transitions that were unfortunately close to the LO, and higher than usual variation in signal strength for several transitions. Nevertheless, a solution was found by varying the initial conditions of the AUTOFIT algorithm. The transitions fit are a- and b-type transitions from J = 2 – J = 5, limited by both spectral coverage and SNR. No c-type transitions were observed, in good agreement with the extremely small c-type dipole moment that results from the nearly symmetric struc-

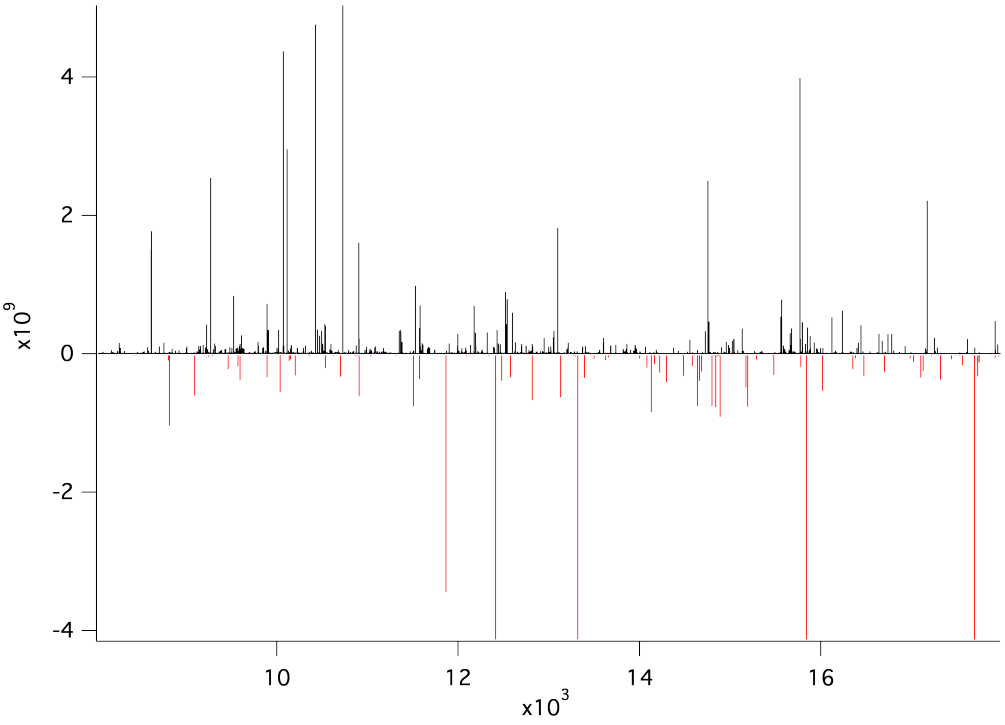

Figure 3.4. The spectrum of the cyclopentanol monomer. The spectrum was recorded by taking 10 million averages acquired using a flow of 15 PSI Ar buffer gas. The experimental spectrum is shown in black, and the prediction based on *ab initio* calculations is plotted as negative going vertical lines with length proportional to predicted intensity. Frequency is given in MHz, amplitude is arbitrary.

ture of the complex. The transitions fit are given in Table 3.1. The transitions were fit with the SPFIT program using the Watson A reduction in the I^r representation. The results of the fit are give in Table 3.2.

Double Resonance

In order to confirm the assignment of the cyclopentanol–water dimer spectrum, double resonance (DR) measurements were performed. Initially this was done using an arbitrary waveform generator by programming in a second single-frequency pulse 400ns duration pulse after the chirp. Later, due to equipment failure, this was changed to use a microwave synthesizer. This was accomplished by adding a power combiner and combining the continuous wave (CW) single frequency from the synthesizer with the output of the DDS prior to amplification and adjusting the switch timing. The frequency of the single frequency tone was chosen to be resonant with a target transition. The effect of this is to generate a coherence using the chirped pulse, and then scramble this coherence with the CW tone. This scrambling results

Table 3.1. Assigned Rotational Transitions of the Cyclopentanol–Water Dimer.

$J'_{K_a,K_c} - J''_{K_a,K_c}$	Frequency (MHz)
$4_{1,4} - 3_{1,3}$	13312.3863
$4_{0,4} - 3_{0,3}$	13532.3883
$4_{1,4} - 3_{0,3}$	13860.0503
$4_{2,2} - 3_{2,1}$	14315.4703
$3_{0,3} - 2_{0,2}$	10274.8923
$3_{2,1} - 2_{2,0}$	10639.8963
$2_{2,0} - 1_{1,1}$	10661.0143
$3_{2,2} - 2_{2,1}$	10457.4223
$3_{1,3} - 2_{0,2}$	10822.5664
$3_{1,2} - 2_{1,1}$	10835.9132
$2_{2,1} - 1_{1,0}$	10338.7557
$3_{0,3} - 2_{1,2}$	9470.5339
$4_{0,4} - 3_{1,3}$	12984.7796
$3_{2,2} - 2_{1,1}$	13550.1124
$4_{1,3} - 3_{1,2}$	14378.5526
$5_{1,4} - 4_{2,3}$	15606.6512
$5_{0,5} - 4_{1,4}$	16403.8591
$5_{1,5} - 4_{1,4}$	16580.5572
$4_{2,3} - 3_{1,2}$	16619.6262
$5_{0,5} - 4_{0,4}$	16731.5617
$5_{1,5} - 4_{0,4}$	16908.1272
$5_{2,4} - 4_{2,3}$	17322.1705
$5_{3,3} - 4_{3,2}$	17544.7769
$5_{1,4} - 4_{1,3}$	17847.6977

Table 3.2. Assigned and *Ab Initio* Rotational Constants of the Cyclopentanol–Water Dimer.

	Ab Initio	Experimental
A\MHz	2894.691	2911.035(83)
B\MHz	1863.648	1880.135(49)
C\MHz	1599.266	1605.745(56)
-Δ_J\kHz	-2.0169815	-2.38(113)
-Δ_K\kHz	-1.3608014	–
-Δ_{JK}\kHz	0.88752646	–
-δ_J\kHz	-0.44248328	–
-δ_K\kHz	0.67903132	–
μ_a\D	1.77	–
μ_b\D	2.05	–
μ_c\D	0.05	–
N_{lines}		24
σ\kHz		24.49

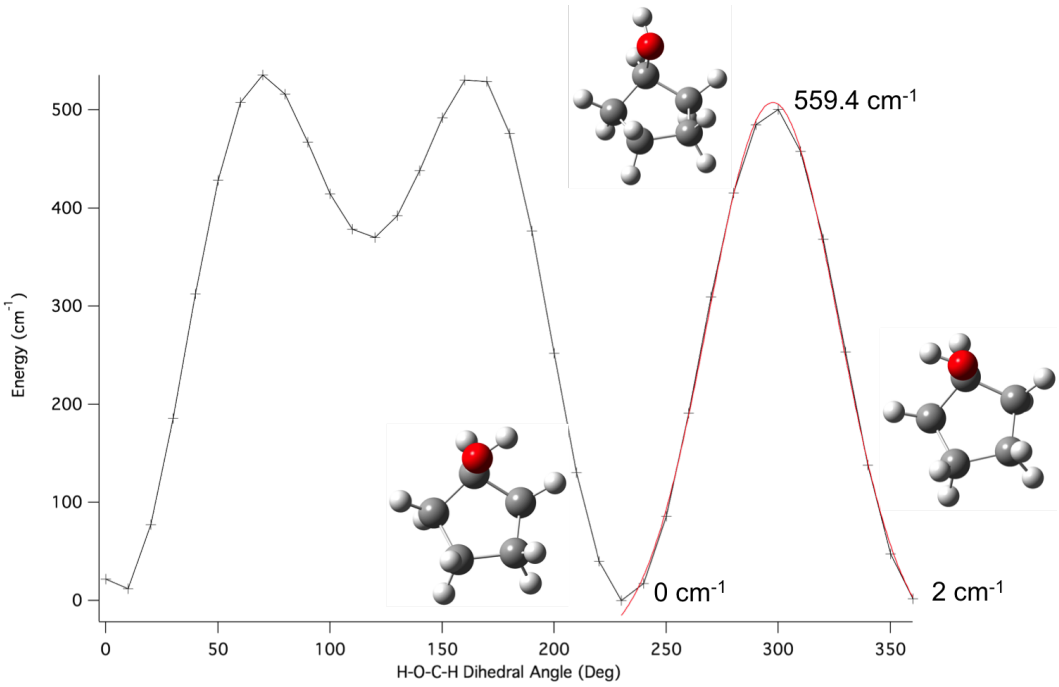

Figure 3.5. Potential energy surface of the OH dihedral angle with respect to the cyclopentanol ring.

in a strong attenuation of emission for any rotational transitions that share a level with the targeted transition, and is analogous to hole burning experiments done in the optical and infrared. This attenuation is then monitored as in any other CP-FTMW experiment. To confirm the levels assigned were correct, two double resonance experiments were carried out: first pumping the $4_{0,4}$–$3_{0,3}$ transition, and then the $4_{1,4}$–$3_{0,3}$; the results of these two experiments are shown in Figure 3.6. Pumping the $4_{0,4}$–$3_{0,3}$ clearly modulates the transition assigned to the $4_{1,4}$–$3_{0,3}$, however no other linked transitions are observable within the excitation bandwidth. Similarly, pumping the $4_{1,4}$–$3_{0,3}$ clearly modulates the transition assigned to the $4_{0,4}$–$3_{0,3}$ and to the $4_{1,4}$–$3_{1,3}$. This shows that these transitions are connected and shows that a-type and b-type transitions are connected, demonstrating that the two ladders are connected and not incorrectly asigned.

3.4 Discussion

The structure of the cyclopentanol–water dimer is largely as expected, and is in keeping with the previous studies of alcohol water complexes. The more acidic water acts as the proton donor to form a water-donor alcohol-acceptor complex, a motif seen in previous alcohol–water and mixed alcohol complexes[48, 52, 53, 140]. The secondary hydrogen bonds also play a significant role. The optimized

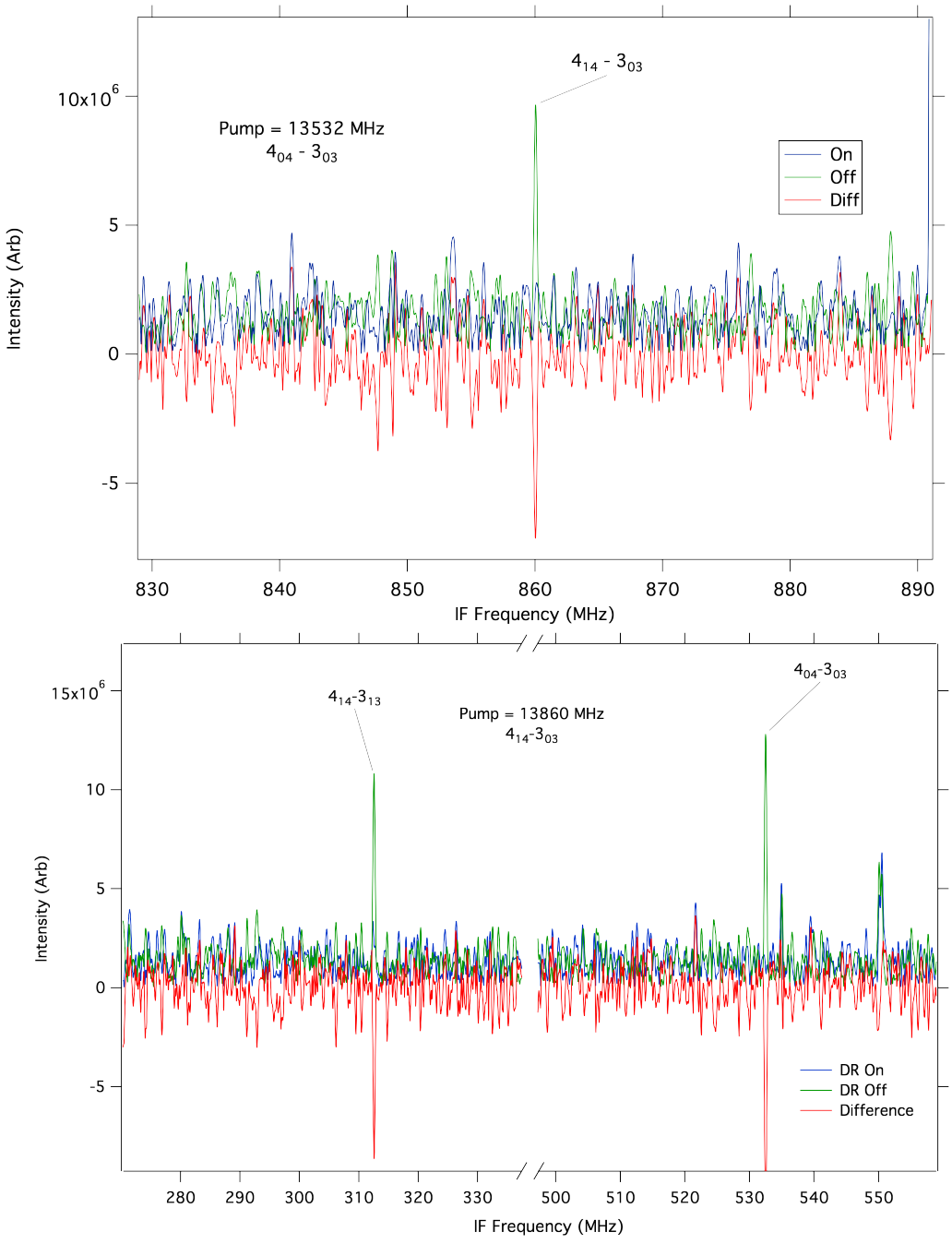

Figure 3.6. DR measurements of the $4_{0,4}$–$3_{0,3}$ and $4_{1,4}$–$3_{0,3}$ transitions of the cyclopentanol–water dimer. The top panel shows the spectrum of the $4_{1,4}$–$3_{0,3}$ with the DR pump set to the $4_{0,4}$–$3_{0,3}$ (13532 MHz). The bottom panel shows the spectrum of the $4_{1,4}$–$3_{1,3}$ and $4_{0,4}$–$3_{0,3}$ with the DR pump set to the $4_{1,4}$–$3_{0,3}$ (13860 MHz). In both panels the spectrum with no DR pulse is shown in green, the spectrum with the DR pulse on is shown in blue, and the difference is shown in red. Frequencies are given in the downconverted IF frequency.

structure is shown in Figure 3.7. Of the four possible weak hydrogen bonds, three form significant interactions with the water's oxygen. This is largely limited by the ring strain of the cyclopentanol, which prevents the final C–H$\cdots$O–H due to ring strain. The calculated bond distances are 2.81, 2.71, and 3.19 Å. This is in line with the values derived for both ethanol–water and propanol–water. Also of interest is the lack of splitting in the rotational spectrum. The cylcopentanol monomer spectrum is strongly perturbed by the pseudorotation of the C_5 ring, however the cyclopentanol–water dimer shows no evidence of splitting. This is caused by the strong water-C–H interaction that raises the pseudorotation barrier high enough to make the splitting unobservable at the experimental resolution of 50 kHz. The presence of this mode is invoked to explain the heat capacity of cyclopentanol solids [86]. The suppression of this vibrational mode is an excellent example of the potential effects of complexation on macroscopic properties.

3.5 Conclusion

The rotational spectra of both cyclopentanol and the cyclopentanol–water dimer have been measured for the first time. The spectrum of the monomer is shown to be complex and well beyond an asymmetric rotor, likely due to pseudorotation of the C_5 ring. The spectrum of the cyclopentanol–water dimer is assigned. A total of 24 a- and b-type transitions from J=2 – J=5 are assigned to the dimer with an RMS of 25 kHz. *Ab Initio* calculations show that the primary structure of the dimer is guided by a O–H$\cdots$O–H hydrogen bond, while the secondary structure of the ring is dominated by C–H$\cdots$O–H interactions. This represents an extreme case of weak hydrogen bonding and highlights the role of secondary interactions in structure and properties of hydrogen bonded complexes.

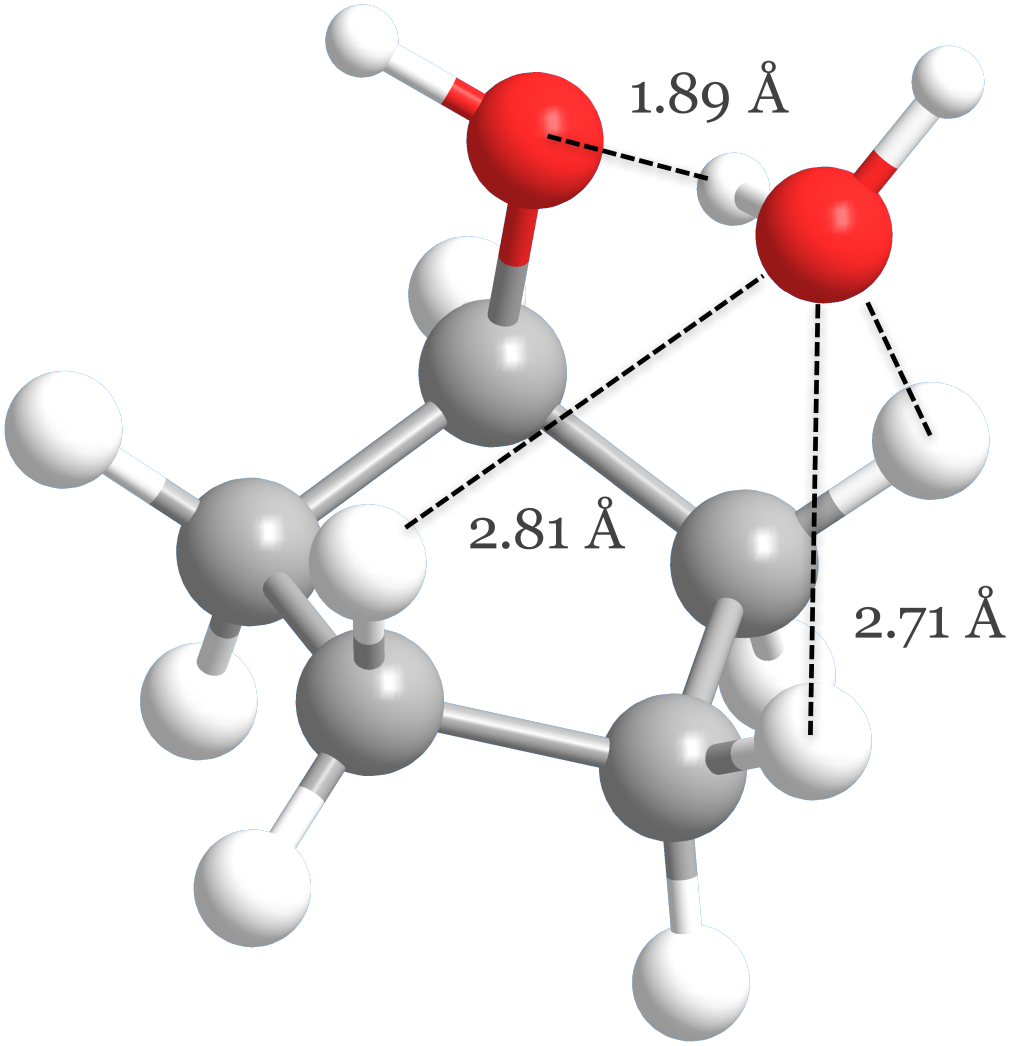

Figure 3.7. Structure of the cyclopentanol–water dimer. The structure is optimized at the MP2/aug-cc-pVTZ using the Gaussian 09 software package [56].

Chapter 4

THE DISCOVERY OF THE INTERSTELLAR CHIRAL MOLECULE PROPYLENE OXIDE

4.1 Introduction

This chapter outlines the detection of the first chiral species discovered in the interstellar medium: propylene oxide. The importance of chiral molecules to biology and the emergence of homochirality is discussed. The detection is bolstered by a robust model of the Sgr(B2)N continuum emission and propylene oxide's absorption of that continuum. This discussion explains the origin of the observed propylene oxide absorption in detail; however, it is worth saying plainly these observations were only made possible through the unique combination of very high molecular abundances in the cold shell around an extremely bright and non-thermal continuum source. Additional laboratory spectroscopy, and ancillary astronomical observations of two propylene oxide structural isomers, acetone and propanal, are presented. Since the original publication, several followup searches for propylene oxide have been conducted using the Green Bank Telescope(GBT) and Australia Telescope Compact Array (ATCA). These searches are discussed briefly. These results are used to contextualize and motivate future submillimeter searches for propylene oxide and other simple chiral species. An additional discussion on feasibility is added to the discussion of the detection of enantiomeric excess by circular dichroism. Finally, a discussion of alternative methods of inferring enantiomeric excess from radio observations particularly using the next generation very large array (ngVLA) is given.

The origin of homochirality is a key mystery in the study of our cosmic origins[115]. While homochirality is itself evolutionarily advantageous[98], the mechanism for the selection of one iso-energetic enantiomer over another is uncertain. Many routes to homochirality have been proposed through the amplification and subsequent transfer of a small primordial enantiomeric excess (e.e. hereafter). Disentangling these possible mechanisms requires that we understand the potential sources from which an e.e. may arise. The oldest material on which e.e. data have been taken in the laboratory are meteoritic samples [47], yet, the provenance of this e.e. remains a matter of considerable debate[62]. Material in molecular clouds from which planetary

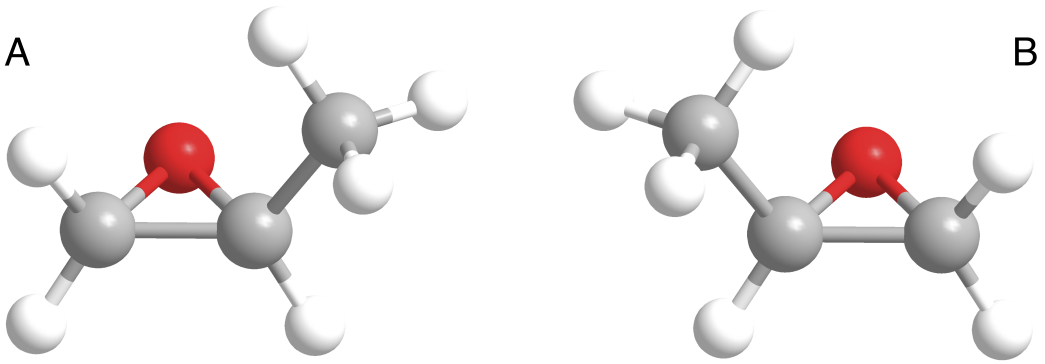

Figure 4.1. The molecular structure of S-propylene oxide (A) and R-propylene oxide (B). Carbon, hydrogen, and oxygen atoms are indicated by gray, small white, and red spheres, respectively.

systems form is processed through circumstellar disks[30], and can subsequently be incorporated into planet(esimal)s[26]. Thus, a primordial e.e. found in the parent molecular cloud may be inherited by the fledgling system. Constraining the origin of e.e. found in meteorites therefore requires the determination of the possible contributions of primordial e.e., and thus the detection of a chiral molecule in these environments.

4.2 Observations

For the past fifty years, radio astronomy has been the primary method for studying the gaseous, complex molecular content of interstellar clouds. In this regime, observed spectral features correspond to fine structure transitions of atoms, or pure rotational transitions of polar molecules, that can uniquely identify their carrier. The observations presented here were taken toward the Sagittarius B2 North (Sgr B2(N)) molecular cloud, the pre-eminent source for new complex-molecular detections in the interstellar medium (ISM).

Propylene oxide (Figure 4.1) was initially detected using data from the publicly-available Prebiotic Interstellar Molecular Survey (PRIMOS) project at the Green Bank Telescope (GBT), which provides near frequency-continuous, high-resolution, high-sensitivity spectral survey data toward Sgr B2(N) from 1 - 50 GHz[109]. The full observational details, data reduction strategy, and analysis of the PRIMOS observations presented here have been previously reported (*13*), and will not be discussed further. PRIMOS provides near-continuous frequency coverage of Sgr B2(N) from 1 – 50 GHz at high sensitivity (RMS~3 – 9 mK) and spectral resolution ($\Delta\nu \sim 25$ kHz) using the 100-m Robert C. Byrd Green Bank Telescope

(GBT). PRIMOS data are fully-reduced and made publicly available with no proprietary period. More information on how to obtain full data sets is available online at http://www.cv.nrao.edu/~aremijan/PRIMOS/, and large portions of the survey, as well as many others, are available through the **S**pectral **Li**ne **S**earch **E**ngine (SLiSE) at http://www.cv.nrao.edu/~aremijan/SLiSE/. Additionally, several hours of archival GBT observations (GBT Project AGBT06B-006) fortuitously covered the 12.8 GHz transition of propylene oxide. These data were reduced in the same way as the PRIMOS data, and used to further bolster the signal-to-noise of the line.

Observations with the Parkes Radio Telescope were conducted over a total of 9 nights from 30 April 2015 – 19 May 2015. The target coordinates for the observations were the same as those for the PRIMOS observations: right ascension = $17^h47^m19.8^s$, declination = -28°22′17.0″ (J2000). Spectra were acquired in position-switching mode, with the off-position located 1° offset in latitude with a switching cycle of 5 minutes. Pointing accuracy was checked by facility staff and converged to ∼5″ accuracy. The Parkes K_u-band receiver was used with a system temperature of ∼80 K across the band. The backend was an 8 MHz bandwidth, 1 kHz resolution Digital Filter Bank.

The quasar ICRF J193925.0-634245 was used for absolute flux calibration. Scans were collected in dual-polarization mode; these were averaged to increase the sensitivity of the observations. Background flux was removed from the scans using a 5th-order polynomial fit to the baseline. The resulting spectra were then binned and Hanning smoothed to a resolution of ∼0.6 km s^{-1}. Finally, an instrumental noise feature, or 'birdy,' was removed at ∼12069.8 MHz.

For such weak features there is a possibility that even small systematic response (e.g. standing waves) may obscure or even be mistaken for genuine molecular absorption. In order to ensure all absorption features were real, each feature was re-observed at a shifted rest frequency such that the target frequency was shifted within the passband. For Parkes observations, these tests were carried out concurrently with the observations described above in the same manner. The additional GBT observations were carried out over four sessions from 20 August 2015 to 16 September 2015 (GBT project AGBT15A-493). Observations were conducted in position-switching mode, with the off-position located 1° offset in azimuth with a switching cycle of 4 minutes. Pointing accuracy was checked and corrected every ∼ 2 hrs using the nearby continuum source PKSJ 1833-2103. The $2_{11} - 2_{02}$ and $3_{12} - 3_{03}$ lines were observed simultaneously using the GBT K_u-band receiver and the VEGAS spectrometer in its

187.5 MHz bandwidth mode. For both Parkes and GBT observations, the targeted transition(s) were successfully reproduced, and were appropriately shifted within the passband. Therefore, the features cannot be attributed to IF or passband response, and must be from the target source at the specified rest frequencies.

Based on our model of rotationally-cold propylene oxide absorbing against the Sgr B2(N) continuum, only three transitions are predicted to have appreciable intensity above the survey noise floor: the b-type Q-branch $1_{1,0} - 1_{0,1}$, $2_{1,1} - 2_{0,2}$, and $3_{1,2} - 3_{0,3}$ transitions at 12.1, 12.8, and 14.0 GHz (λ = 2.478, 2.342, and 2.141 cm), respectively. The $1_{1,0} - 1_{0,1}$ line at 12.1 GHz is obscured by radio frequency interference (RFI) at the GBT, however clear absorption signatures are observed from the $2_{1,1} - 2_{0,2}$, and $3_{1,2} - 3_{0,3}$ transitions (Figure 4.2).

These features may be sufficient for a detection on their own at these wavelengths, however we endeavored to confirm the detection by observing the $1_{1,0} - 1_{0,1}$ line at 12.1 GHz using the Parkes Radio Telescope, which does not suffer from RFI in the region of the line. The data confirm the presence of a feature at the same velocity ($\sim$ 64 km s^{-1}) as the transitions from PRIMOS, as well as fortuitously detecting a nearby feature of propanal, a structural isomer of propylene oxide (Figure 4.2). The far-larger Parkes beam ($\sim$115″ vs 60″) encompasses a much larger sample of environments, inhomogeneously-broadening the observed transition and incorporating a second, distinct $\sim$46 km s^{-1} component not seen by the GBT beam, but previously observed in the material surrounding Sgr B2 (Figure 4.3)[85].

A fit to the observations using a single excitation temperature for propylene oxide finds a column density of $N_T = 1 \times 10^{13}$ cm^{-2} and a rotational excitation temperature of T_{ex} = 5 K [100]. While an excitation temperature of 5 K is indeed the best-fit to the data, we note that the most rigorous constraint on T_{ex} is from the non-detection at higher-frequencies in PRIMOS, giving an upper limit of $\sim$35 K. Changes in T_{ex} significantly affect N_T, and model parameters which fit the data nearly as well are possible for excitation conditions between T_{ex} = 5–35 K. These models all reproduce the observed features from the GBT and Parkes, and are consistent with the non-detection of propylene oxide at 3 mm; under these conditions, no transitions of propylene oxide would be detectable in the reported observations[36].

A search of spectral line catalogues reveals no reasonable interfering transitions from other molecular species. Propylene oxide is an asymmetric rotor with modest rotational constants, and therefore has numerous ($\sim$450) transitions that fall within the PRIMOS data. For lower excitation temperatures ($T_{ex} \approx$ 10-35 K), at most

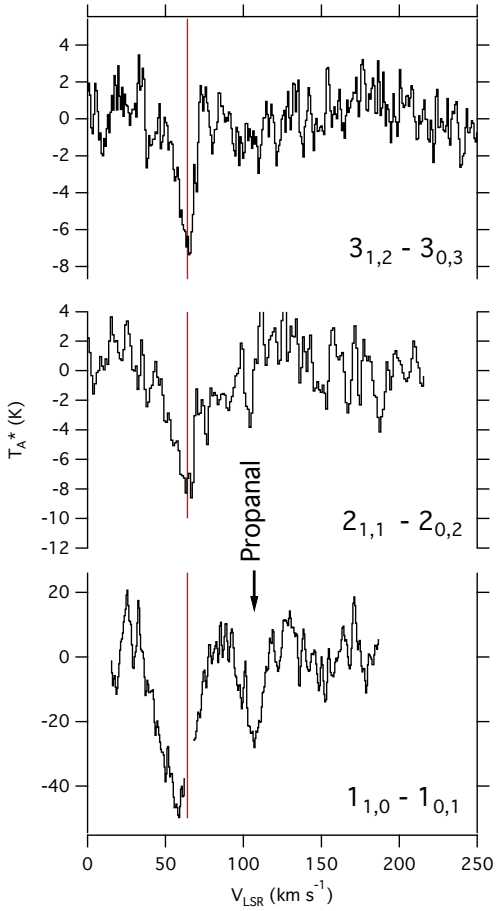

Figure 4.2. Observations of the $1_{1,0}$- $1_{0,1}$ (Parkes), $2_{1,1}$- $2_{0,2}$ (GBT), and $3_{1,2}$- $3_{0,3}$ (GBT) transitions of propylene oxide, in absorption, toward the Galactic Center. The 64 km s^{-1} systematic velocity characteristic of Sgr B2(N) is indicated by a vertical red line. The $1_{0,1} - 1_{1,0}$ transition of propanal is also seen in the Parkes data. Data are given as antenna temperature (T_A^*) as a function of shift from local standard of rest velocity (V_{LSR}), where 0 km s^{-1} is the measured laboratory frequency of the transition[100], and have been Hanning smoothed.

80 have have an intensity ≥1% of the strongest predicted line. Of these, ∼13% are unobservable due to a lack of available receivers at the GBT. Inspection of the entire PRIMOS data set showed no absorption or emission features attributable to propylene oxide at any of these frequencies but the three listed above, in good agreement with the model and the sensitivity of the survey.

This detection is complementary to the upper limit placed by [36] on the non-detection of warm, compact propylene oxide at T_{ex} = 200 K toward Sgr B2(N) at mm-wavelengths using the Mopra Telescope. This search was sensitive only to a warm population of propylene oxide, however, and resulted in a non-detection with

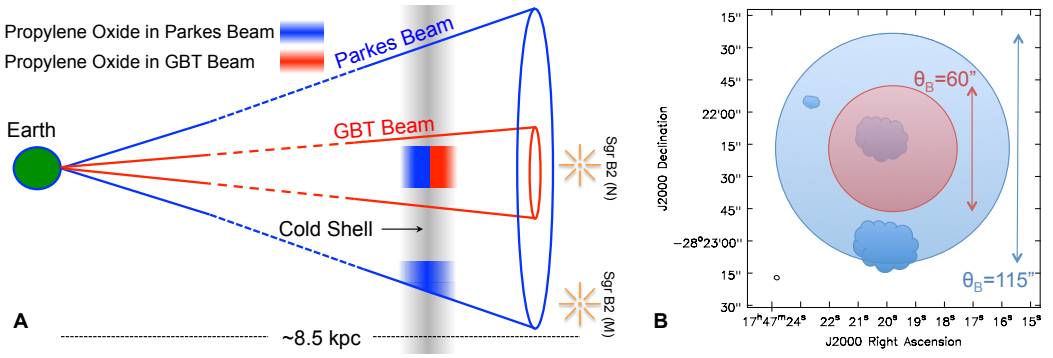

Figure 4.3. Illustration of source structure within the Sgr B2 region. A) The GBT and Parkes beam probe different portions of the cold molecular shell in front of the bright continuum sources/hot cores within Sgr B2. Molecules in the shell which are not backlit by continuum sources are not seen in absorption. As the schematic of the sky view at right shows, B) The GBT (red) and Parkes (blue) beams probe different continuum sources, with the GBT beam probing only Sgr B2(N), while the Parkes beam also includes most of Sgr B2(M) to the south.

an upper limit column density of 6.7×10^{14} cm^{-2} for an excitation temperature of T_{ex} = 200 K and compact source size (5″) such as that expected for gas associated with the embedded protostellar clusters/hot cores in this cloud[36].

In sources with strong background continuum, of which Sgr B2(N) is a prominent example, many rotationally-cold, high dipole moment species are observed almost exclusively in absorption against the continuum source, as shown in Figure 4.3. Because of the exceptionally low line densities, only two to five well-measured centimeter-wavelength spectral features are needed to securely claim a detection (see, e.g., [78, 82, 102]). This stands in stark contrast to mm-wave detections, particularly toward Sgr B2(N), where dozens of lines are typically required. Based on a statistical analysis of the line density in our observations of Sgr B2(N), we find that the likelihood of three random features falling within three resolution elements of the propylene oxide transitions to be $\leq 6{\times}10^{-8}$[100].

4.3 Laboratory Spectroscopy

The cm-wave spectrum of propylene oxide is complicated by coupling of the internal rotation of the methyl group to the overall rotation of the molecule. This splits each rotational level into a non-degenerate A state and a doubly degenerate E state. The high barrier to internal rotation (2710 cal/mole; 0.1175 eV) produces small splittings, $\sim$ 100 kHz, for low J transitions such as those observed here. These internal rotation-driven splittings will be unresolved for astronomical observations

toward Sgr B2(N), but will contribute appreciably to the observed line width. The pure rotational spectrum of propylene oxide has been previously measured and assigned[75, 142]. However, due to linewidth and resolution limits in this (previous) work, the treatment of the splittings was insufficient for determining the contribution of this splitting to the astronomical linewidth. We have therefore re-measured these spectra using a state-of-the-art free jet microwave spectrometer.

Specifically, laboratory spectra were collected from 8–18 GHz using a direct digital synthesis (DDS)-based, chirped-pulse Fourier transform microwave (CP-FTMW) spectrometer. Details of the instrument have been published elsewhere[51]. Briefly, a linear frequency sweep (0 – 2 GHz, 1 μs duration) chirped pulse is generated by a DDS card. This pulse is then upconverted by mixing with a local oscillator (8–18 GHz), amplified (to 50 W), and broadcast by a waveguide horn into the chamber to interact with the sample. Propylene oxide, sometimes referred to as methyl oxirane, (>99% purity), was purchased from Alfa Aesar, and used without further purification. The sample was prepared by flowing 1 atm of Ar through a sealed reservoir containing ~5 mL of propylene oxide, and introduced into the vacuum chamber through a pulsed adiabatic expansion.

After excitation by the microwave pulse, the weak molecular free induction decay (FID) was collected using the same microwave horn, amplified (+38 dB), down-converted, and recorded with a high speed digital-to-analog converter (4 GSa/s). The expansion coupled with the coaxial excitation-detection geometry employed produces a rotationally cold (~3 K) gas with a slight asymmetry in the blended Doppler doublet. This limits the frequency uncertainty in the measured line centers to 20 kHz.

The use of the same local oscillator (LO) for both up and downconversion gives double sideband spectra, thus the absolute the frequency of any emission cannot be determined from a single scan. To determine absolute frequencies, a second scan is recorded at a slightly shifted (LO+10 MHz) LO frequency. The deconvolved broad-band spectrum is shown in Figure 4.4 using a 10 microsecond FID. To resolve the A-E splitting, we followed up with targeted measurements using a 130 microsecond FID (Figure 4.5). Each peak is a doublet of doublets; the A-E methyl rotor splitting is ~100 kHz, while the Doppler splitting from the jet expansion is ~50 kHz. Fit frequencies are given in Table 4.1.

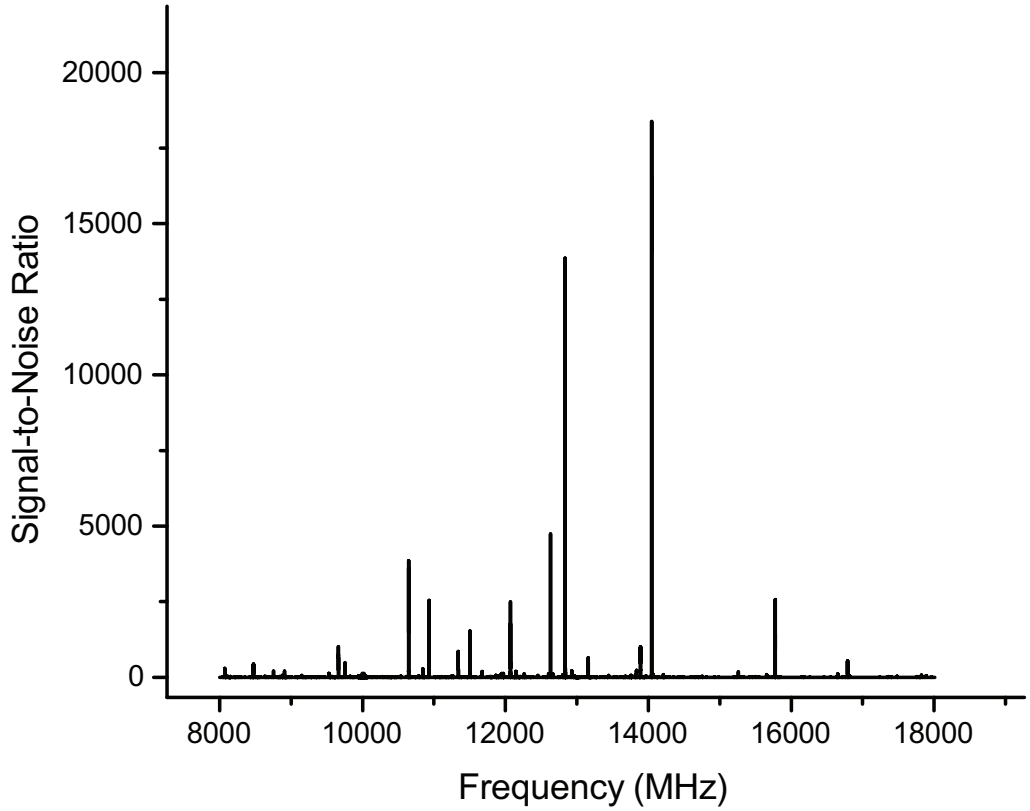

Figure 4.4. Laboratory spectrum of propylene oxide. The spectrum of propylene oxide in an Ar buffer gas from 8 – 18 GHz (4.8 million averages, 20 hour acquisition)

Table 4.1. Measured laboratory frequencies of the transitions used in this work, and associated observed linewidth broadening.

$J'_{K_aK_c} - J''_{K_aK_c}$	Symmetry	Frequency (MHz)	ΔV (km s^{-1})
$1_{10} - 1_{01}$	E	12072.384(20)	2.4
	A	12072.479(20)	2.4
$2_{11} - 2_{02}$	E	12837.292(20)	2.1
	A	12837.381(20)	2.1
$3_{12} - 3_{03}$	E	14047.715(20)	1.9
	A	14047.806(20)	1.9

4.4 The Observational Model

To determine a column density and rotational temperature for propylene oxide, we follow the convention of [82], using Equation 4.1 to calculate the column density N_T, given a rotational partition function Q_r, upper state energy E_u, rotational excitation temperature T_{ex}, transition frequency ν, line strength $S\mu^2$, observed intensity ΔT_A^*,

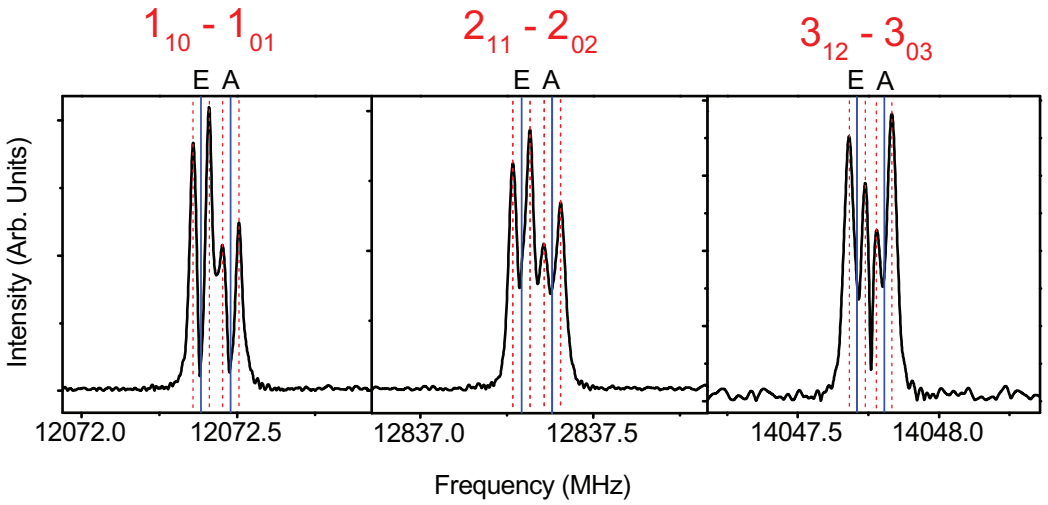

Figure 4.5. Laboratory spectra of astronomically-observed propylene oxide transitions. Laboratory measurement of the three transitions detected astronomically in this work, showing the characteristic A-E methyl rotor splitting (solid blue lines) and Doppler splitting (dashed red lines). Rotational quantum numbers are given in red.

linewidth ΔV, telescope efficiency η_B, and background temperature T_{bg}.

$$N_T = \frac{Q_r e^{E_u/kT_{ex}}}{\frac{8\pi^3}{3k}\nu S\mu^2} \times \frac{\frac{1}{2}\sqrt{\frac{\pi}{ln(2)}}\frac{\Delta T_A^* \Delta V}{\eta_B}}{1 - \frac{e^{h\nu/kT_{ex}}-1}{e^{h\nu/kT_{bg}}-1}} \tag{4.1}$$

We make the assumption that all propylene oxide states can be described by a single excitation temperature equal to T_{ex}. We stress that this assumption does not imply that the molecule is necessarily in thermal equilibrium with the gas; T_{ex} is not assumed to be equal to the ambient gas kinetic temperature, a condition often described as Local Thermodynamic Equilibrium, or LTE. The excitation of molecules in Sgr B2(N), especially those in the cold absorbing layer(s) such as propylene oxide, rarely can be described by the gas kinetic temperature; yet a single-excitation model often describes such species well [82, 96, 153].

The rotational partition function, Q_r, is often calculated according to a high-temperature approximation, given by Equation 4.2, where σ is a unitless symmetry parameter, T_{ex} the excitation temperature (K), and A, B, and C, the rotational constants of the molecule (MHz) (c.f. [67]), which offers excellent values down to modestly-low temperatures.

$$Q_r = \left(\frac{5.34 \times 10^6}{\sigma}\right)\left(\frac{T_{ex}^3}{ABC}\right)^{1/2} \tag{4.2}$$

Molecules seen in absorption toward Sgr B2(N), however, often are characterized by T_{ex} values as low as 6–8 K [80, 82], in which case direct summation of the energy levels is required, as given in Equation 4.3 (c.f. [67]).

$$Q_r = \frac{1}{\sigma} \sum_{J=0}^{J=\infty} \sum_{K=-J}^{K=J} (2J+1) e^{-E_{J,K}/kT_{ex}} \tag{4.3}$$

For asymmetric molecules like propylene oxide, the symmetry parameter $\sigma = 1$. In this study, we directly sum the rotational states using Equation 4.3 to determine Q_r, however, we note that at the temperatures under consideration, the error in Equation 4.2 is only 1.3% at 6 K and drops below 0.1% by 40 K.

The $S\mu^2$ value is the intrinsic line strength S_{ij} multiplied by the square of the transition dipole moment μ, which in the case of the pure rotational transitions considered here is simply the permanent electric dipole moment μ along the principal axis of the transition. The S_{ij} factors are intrinsic quantum mechanical properties determined from the J and K values of the transition; a thorough reference tabulation is available [143]. The dipole moments μ_a, μ_b, and μ_c were taken from [142] as 0.95, 1.67, and 0.56 Debye, respectively.

The observed intensities, ΔT_A^*, and linewidths, ΔV, were obtained by fitting a single Gaussian lineshape to the observed transitions (for PRIMOS observations), or a pair of Gaussians (for Parkes observations). In either case, the observed signals are well-fit. The results are given in Table 4.2. Given the uncertainties, we adopted a uniform linewidth of 13 km s^{-1} when considering the PRIMOS transitions. We note a trend of decreasing linewidth with increasing frequency, which we attribute to a combination of the decreasing beam size encompassing less inhomogeneous environments, and the decreasing broadening due to internal rotation as J-values increase.

Table 4.2. Line parameters resulting from Gaussian Fits to the observed transitions. Numbers in parenthesis are 1σ standard deviations in units of the last significant digit.

	Component 1			Component 2		
Transition	v_o (km s^{-1})	ΔT_A^* (mK)	ΔV (km s^{-1})	v_o (km s^{-1})	ΔT_A^* (mK)	ΔV (km s^{-1})
$1_{1,0} - 1_{0,1}$	59.3(18)	-45(3)	19.6(33)	45.5(23)	-13(9)	9.9(57)
$2_{1,1} - 2_{0,2}$	61.4(7)	-7.4(5)	15.8(20)	...	...	...
$3_{1,2} - 3_{0,3}$	63.0(8)	-6.8(6)	11.6(14)	...	...	...

The lines were fit, and the column density and temperature determinations conducted, using the laboratory frequencies (ν) determined without explicitly treating the splitting of the rotational levels due to internal motion because the splitting is not resolved in our observations. This splitting does, however, contribute a non-negligible amount to the total linewidth of the observed features: 2.4, 2.1, and 1.9 km s^{-1} at 12.1, 12.8, and 14.0 GHz, respectively.

The telescope beam efficiency (η_b) was calculated explicitly at each frequency across the PRIMOS band using Equation 4.4 (c.f. [81]).

$$\eta_b = -15.52 \times 10^{-5}\nu^2 - 22.59 \times 10^{-4}\nu + 0.98 \tag{4.4}$$

As we also include the observations of [36] in our analysis, which were acquired with the MOPRA telescope, we take an average value of $\eta_b = 0.44$ uniformly across the 3 mm MOPRA observational window [90].

The background temperature (T_{bg}) plays a critical role in the accurate modeling of molecular excitation for transitions searched for in the PRIMOS observations, in particular for those molecules which are seen in absorption. This is readily apparent if Equation 4.1 is re-stated as Equation 4.5, below (c.f. [82]).

$$N_T = \frac{Q_r \frac{1}{2}\sqrt{\frac{\pi}{ln(2)}}\frac{\Delta T_A^* \Delta V}{\eta_B}}{\frac{8\pi^3}{3h}(T_{ex} - \frac{T_{bg}}{\eta_B})S\mu^2(e^{-E_l/kT_{ex}} - e^{-E_u/kT_{ex}})} \tag{4.5}$$

Here, it is clear from the $T_{ex} - \frac{T_{bg}}{\eta_B}$ term that for values of $T_{ex} < T_{bg}$, T_A^* must be negative (in absorption) for N_T to remain positive. As the observed propylene oxide transitions are in absorption, it is therefor critical to constrain T_{bg} in Sgr B2(N) at the frequencies observed. In this case, a model must first be adopted to describe the overlap of the GBT beam with the background continuum emission structure at each frequency.

The structure of Sgr B2(N) is complex, with a compact (~5″) hot molecular core surrounded by a more extended, colder molecular shell [81]. The background continuum structure against which molecules in this shell absorb is ~20″ in diameter (see, e.g., Fig. 3*b* of [104]). For the purposes of this study, we assume this 20″ source size for the cold molecular material, and explicitly calculate the spatial overlap of these regions with the GBT beam as its size varies across the frequency coverage. The geometry-corrected source size is then used to determine a correction factor (B) to observed intensities for beam dilution effects, according to Equation 4.6,

where θ_s and θ_b are the source and beam sizes, respectively. This is then applied as required to both peak line intensities (ΔT_A^*) and to the background continuum levels, as described below.

$$B = \frac{\theta_s^2}{\theta_s^2 + \theta_b^2} \tag{4.6}$$

The background continuum temperature at 85 points across the PRIMOS frequency coverage was established by [81]. These continuum measurements range from more than 100 K at low frequencies to several Kelvin above the CMB near 45 GHz, although these measurements are not corrected for any assumed source geometry or beam dilution effects. The authors attribute this to non-thermal continuum in the source. We adopt their measurements of the continuum for these calculations, but correct them for the overlap of the assumed source size of the continuum-emitting region with the GBT beam in the PRIMOS observations. We expect this correction to be valid to frequencies as low as ~10 GHz, below which the GBT beam is sufficiently large that it will encompass additional emitting regions. At that point, the beam dilution correction factor used here will no longer account for the full size of the emitting regions within the beam, and the continuum will be over-estimated in increasing degree.

The effect of this frequency-dependent continuum on the observed intensities of transitions, both in emission and in absorption, is significant. While the relative populations of the energy levels for a molecule at a single excitation temperature are still described by a Boltzmann distribution, the observed relative intensities of the transitions between those levels are not. This is most straightforward to understand looking at absorption transitions. The standard analysis of relative intensities from a molecule whose population is described by a Boltzmann distribution at a single excitation temperature provides predicted absorption depths (i.e. percent absorption). The measured (observed; ΔT_A^*) value is not, however, directly comparable, as the background against which a 10% absorptive transition at 45 GHz is absorbing is not the same as the background against which a 1% absorptive transition at 10 GHz is absorbing. Thus, the predicted absolute absorption spectrum for propylene oxide in the PRIMOS observations will present different relative intensities between transitions, due to this non-constant background, than a simple percentage absorption spectrum.

Model Results

Using the model described above, we have performed a least-squares analysis of our data, taking into account the two observed transitions in PRIMOS, and all transitions covered by PRIMOS but for which no features are seen, as well as those transitions in the coverage of the survey conducted by [36]. Due to the large difference beam size, telescope-specific parameters, receiver efficiencies, and calibration uncertainties, the Parkes transition was not included in the analysis quantitatively. The results of the analysis provide a set of models for column density and temperature which are consistent with our observations, meaning that given the frequency coverage and sensitivity of the PRIMOS observations and those of [36], only the transitions we have detected are expected to be present above the noise level of the observations. The best-fit model for the datasets, including both detected and non-detected lines in the PRIMOS observations and those of [36], is for a column density of 1×10^{13} cm^{-2} and an excitation temperature of $T_{ex} = 5.2$ K. A simulated spectrum under these conditions is shown in Figure 4.6, while insets (a) and (b) show simulations of the model overlaid on the observational spectra.

The uncertainties for the Gaussian-fitted parameters given in Table 4.2 are not the dominant source of uncertainty in our analysis. To quantitatively determine the uncertainty in the column density and excitation temperature, we have followed the approach of [31], which takes into account uncertainty in the baseline offset, the local rms noise level, the absolute flux calibration, the pointing error, error in the beam filling factor due to uncertainty in the source size, and, in our case, the uncertainty in the determined continuum level. We make conservative estimates of these quantities in our analysis, and assume a 20% uncertainty in the absolute flux calibration, 2″ uncertainty in the pointing, a 20% uncertainty in the source size, and a 20% uncertainty in the continuum level. Given the sparsity of spectral features, we assume no contribution to the error from the removal of the baseline.

Given these uncertainties, and combined with the two fitted transitions from PRIMOS, there are a range of models which fit the observed transitions, and non-detected transitions, nearly as well spanning excitation temperatures as high as ~35 K. Nevertheless, a column density of 1×10^{13} cm^{-2} and an excitation temperature of $T_{ex} = 5.2$ K are indeed the best-fit to our observations, although there are a wide range of models which remain consistent with both the detected and non-detected lines from our observations and those with the MOPRA telescope[36].

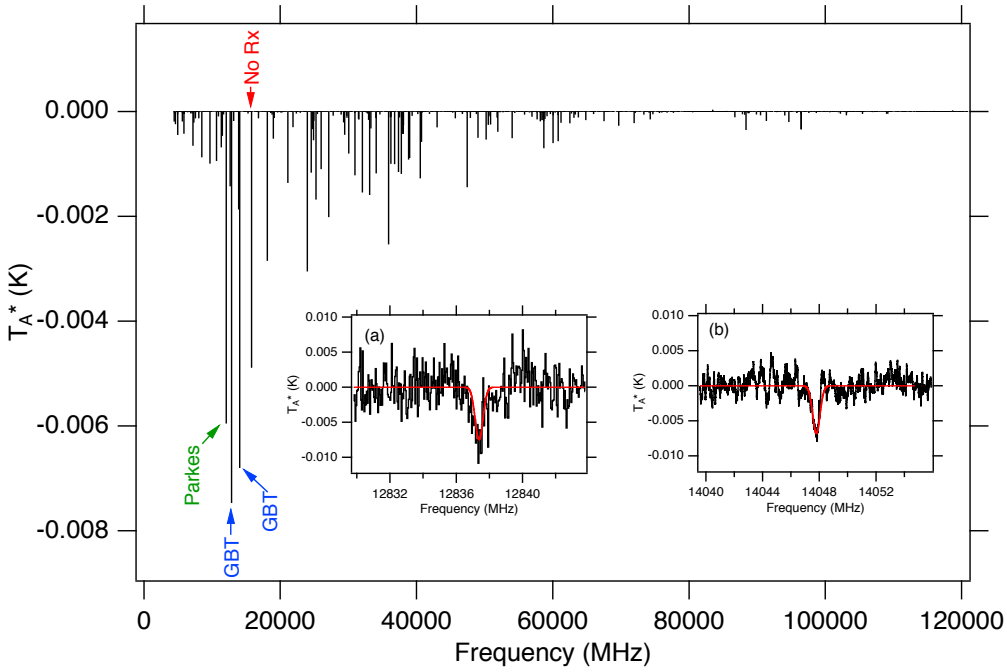

Figure 4.6. Model spectrum of propylene oxide toward Sgr B2(N) at the best-fit column density and temperature, and comparison with observations. The spectrum of propylene oxide at $N_T = 1 \times 10^{13}$ cm^{-2} and $T_{ex} = 5.2$ K, corrected for background continuum, telescope-specific parameters, and beam dilution effects is shown in the main figure. The observed transitions in PRIMOS are shown in insets (a) and (b), with the model spectra overlaid in red. The next strongest transition has no corresponding receiver (Rx) at the GBT or Parkes, and is marked as such.

Astronomical Statistical Analysis

The low line density in the cm-wave region of the spectrum allows for the definitive identification of new molecules from far fewer transitions than are required in the (sub-)mm region. This is especially true in the case of Sgr B2(N), where at frequencies >100 GHz, broad line-widths, high degrees of molecular-complexity, and large column densities contribute to an essentially baseline-free, completely line-confused spectrum. To illustrate the relative line densities of these two frequency regimes, we have compared our PRIMOS observations around 13 GHz to a selection of spectra toward Sgr B2(N) from the Barry E. Turner Legacy survey taken with the NRAO 12 m telescope on Kitt Peak (accessible at http://www.cv.nrao.edu/~aremijan/PRIMOS). The frequency windows were chosen to provide equivalent coverage in velocity space (~6000 km s^{-1}) in both scans.

In the Turner Survey, which has an RMS of ~14 mK, there are ~315 lines at 3σ or above, with a resulting line density of ~1 line per 10 MHz (~1 line per 20 km s^{-1}).

Herschel HIFI and ALMA data have even lower noise floors and are essentially line-confusion limited at all frequencies. Typical linewidths in this source are 8 – 25 km s^{-1} FWHM, making significant line blending inevitable [80, 82, 96, 153]. To claim a detection of a line in the presence of blending, however, the components must be separated by at least their FWHM[139], and the coincidence of lines separated by this criterion is greatly reduced in such crowded spectra. Thus detections at (sub-)mm wavelengths regularly require dozens or hundreds of lines to be secure, and fitting techniques must explicitly account for line blending.

In the PRIMOS survey, there are ∼26 lines above 3σ in the same ∼6000 km s^{-1} window, resulting in a similar line density of ∼1 line per 10 MHz in frequency space. In velocity space, however, the line density drops to ∼1 line per 230 km s^{-1}. With an average line separation > 10 times the linewidth, there is almost no chance for coincidental overlap. Thus as long as the assignments of laboratory spectra are robust, molecular detections at cm wavelengths require only a few (2 – 5) lines to be secure.

The lack of line confusion in the PRIMOS survey allows for further quantitative constraints on the likelihood of a spurious detection (*13*). Previous observations gave a propylene oxide column density upper limit of $\leq 6.7 \times 10^{14}$ cm^{-2}, so we may conservatively only consider features between −100 mK and +100 mK. If we further restrict ourselves to only absorption features, as would be expected for a rotationally cold molecule toward a strong background source, the number of candidate features is ∼ 0.28 per 10 MHz. For this line density, the probability of finding a feature coincident with a propylene oxide transition rest frequency, defined conservatively as being within twice the largest source FWHM, 50 km s^{-1} (2.2 MHz), is ∼ 0.06. The likelihood of three such coincidences is then $\sim 2\times10^{-4}$.

The high resolution of our observations provides even further constraint, as all three observed transition peaks fall within 3 resolution elements (73.2 kHz or 1.7 km s^{-1}) of the measured laboratory transition frequency. For the given line density, the likelihood of a single coincident transition falling no more than 73.2 kHz from the rest frequency is ∼ 0.004, and the likelihood of three transitions all occurring within this window is $\sim 6 \times 10^{-8}$.

Finally, although a wide range of linewidths are observed toward Sgr B2(N), the two transitions measured with the GBT show nearly identical linewidths, providing further evidence that the transitions are truly related, and are not spurious. As previously noted, the Parkes data samples a substantially different total population

and its linewidth cannot be directly compared.

4.5 Measurement of Circular Dichroism

The most straightforward method available for astronomical detection of e.e. is circular dichroism. Circular dichroism (CD), or preferential absorption of left- or right-handed circularly polarized light (CPL), manifests itself as a change in the difference in the electric field of left versus right-handed CPL, commonly referred to as the Stokes V parameter, that follows the absorption profile of the observed (in this case, propylene oxide) features. In principle, detection of e.e. requires two CD measurements. First is a quantitative laboratory measurement of CD to relate e.e. to an observed CD, while second, and most critically, is a polarization-sensitive astronomical observation to detect CD.

For laboratory measurements, this requires experimental measurement and quantification of CD for each of the transitions in question. In the present case this would require laboratory absorption measurement of CD for the cm-wave propylene oxide transitions at 12.1,12.8, and 14.0 GHz. To date, CD has been shown in a laboratory setting from the ultraviolet to the mid-infrared. Extension to the microwave, or radio region, has been studied theoretically[128]. These studies conclude that such measurements should be feasible, although they have not yet been experimentally demonstrated. Such measurements would then enable quantitative analysis of polarization-sensitive astronomical observations of CD discussed below.

Modern radio telescopes, especially unblocked off-axis designs such as the GBT, are capable of highly-accurate, polarization-sensitive observations across wide frequency windows, simultaneously determining the polarization state at each observed frequency (e.g.[99]). Briefly, this is achieved by using receivers that simultaneously detect the electric field of two orthogonal polarizations. The in-phase (0°) and quadrature-phase (90°) components of the electric field for each polarization are then separated and digitized. Appropriate combinations of these four signals are then used to fully determine the polarization state at each frequency within the observed pass band, producing a Stokes vector (discussed below) at each frequency. Acquiring accurate, phase-calibrated, data across large pass bands requires careful calibration, but is regularly achieved by properly designed radio receivers [126]. Such observations are vital both for detection of circular dichroism and to distinguish other effects that may change the polarization state of the detected light, obfuscating potential CD signals.

In astronomical observations, there are two potential sources of confusion for the detection of circular dichroism: non-resonant effects, i.e. those that do not require light at a frequency corresponding to transitions between states of a molecule, and resonant effects that do. First are macroscopic or non-resonant effects, e.g. Faraday rotation or dust scattering. For such effects, small changes in frequency produce effectively no difference in the effect on the polarization[41]. In the present observations, the linewidth is ~ 700 kHz, at frequencies of several GHz, making the difference between on and off resonance is extremely small ($\sim 10^{-5}$). Therefore any non-resonant effect that alters the polarization at the frequency of the absorption will have the same effect in non-absorption channels and this effect can be corrected by comparison of the polarization on and off resonance.

The second possible source of confusion is resonant effects. Because resonant effects are specific not only to a molecule, but to a transition between states of a particular molecule, they occur only in the narrow region where a molecule absorbs or emits. Effects that produce changes in linear polarization, e.g. the Goldreich-Kylafis effect[65], are readily distinguished from circular dichroism, as they produce changes in linear, rather than circular polarization, which is distinct from CD. The plausible effect other than circular dichroism to produce changes in circularly polarized light is the Zeeman effect. In this scenario an applied magnetic field lifts the degeneracy of the m sublevels, and positive m sublevels interact preferentially with one handed of circularly polarized light, while negative m sublevels interact with the opposite handedness. This too is easily distinguished from circular dichroism. In order to produce non-canceling circular polarization, the Zeeman splitting must be spectrally-resolved. Spectrally-resolved Zeeman splitting produces distinct peaks with circular polarizations of opposite sign. Conversely, circular dichroism produces a single peak of a single sign[125, 128].

Furthermore, observing a wide bandwidth allows for additional tests to prevent false positives and constrain polarization effects. By observing one of several achiral species originating from the same region as propylene oxide, e.g. propanal or acetone, it can be confirmed that there are no resonant molecular effects or observational artifacts causing changes in the polarization. Higher order effects such as the Cotton-Mouton effect, quadratic field induced optical activity, and the magnetochiral effect scale nonlinearly with static magnetic field and, given the modest measured field strengths toward Sgr B2(N), are not considered[35, 146].

For astronomical observations, it is then critical to demonstrate that CD produces

observable polarization effects that are distinct from other potential effects, and is therefore an astronomically observable effect. The polarization state of light can be completely specified by four parameters, commonly chosen to be the four Stokes parameters, I, Q, U, and V, where I is the total intensity, Q is linear polarization, U is 45° linear polarization, and V is circular polarization. This is often written as a vector $\mathbf{S}$ = [I,U,Q,V]. Using these vectors, any polarization-altering effect may evaluated using the so-called Mueller matrices[9]. For on and off-resonance observations, the polarization vectors will be of the form $\mathbf{V}' = \mathbf{M}_{los}\cdot\mathbf{V}$, where $\mathbf{V}$ is some initial Stokes vector, $\mathbf{M}_{los}$ is a Mueller matrix describing subsequent polarization changes along the line of sight, and $\mathbf{V}'$ is the Stokes vector measured by the telescope. In the absence of CD, the Stokes vector is exactly as above, while on resonance and additional term describing CD must be included. The resulting vector is then given by $\mathbf{V}'' = \mathbf{M}_{los}\cdot\mathbf{M}_{CD}\cdot\mathbf{V}$. The difference between on and off resonance observations, $\mathbf{V}''$-$\mathbf{V}'$, is given by $\mathbf{M}_{los}\cdot\mathbf{V}$-$\mathbf{M}_{los}\cdot\mathbf{M}_{CD}\cdot\mathbf{V} = \mathbf{M}_{los}$(V-$\mathbf{M}_{CD}\cdot\mathbf{V}$). If these two vectors are identical the difference is zero, and they are indistinguishable, as is the effect of circular dichroism. This expression is zero for two conditions, if the kernel of $\mathbf{M}_{los}$ is not null, or if $\mathbf{V}$ is an eigenvector of $\mathbf{M}_{CD}$, with eigenvalue 1. The first condition can only be met if the line-of-sight transmittance is zero, i.e. if there is complete absorption along the line of sight. For the second condition $\mathbf{M}_{CD}$ has eigenvectors [1,0,0,1], [0,1,0,0], [0,0,1,0], [1,0,0,-1][9]. Of these four vectors, only two can be physically meaningful, corresponding to the pure circularly polarized states. $\mathbf{M}_{CD}$ has eigenvalue 1 only for complete transmittance. The result is that the only valid eigenvector for $\mathbf{M}_{CD}$ with eigenvalue 1 is completely transmitted pure circular polarization. Thus the only two cases in which the on and off resonance Stokes vectors are indistinguishable are total absorption or the absence of any CD, meaning that CD must produce a distinct Stokes vector.

From this analysis it is clear that observations at a frequency where CD occurs and where it does not must produce distinct results, and careful measurements may thus identify CD in observations. In the case of the present observations however, a meaningful measurement of the Stokes vector is not possible. This is principally due to a lack of polarization calibration. Even extremely well-designed receivers such as those at the GBT may introduce significant polarization artifacts through a variety of effects, including polarization side lobes, beam squint, and non-orthogonal response [126]. These effects have dependence on frequency, position angle throughout observations, altitude and azimuth coordinates of the dish, and even cable length, and therefore necessitate great care to accurately determine

Stokes vectors and prevent detection of spurious polarization effects.

There is one final consideration for the detection of astronomical CD: the strength of the effect. The strength of this effect will determine both the signal to noise ratio and polarization sensitivity required for the detection of CD. To date, there has never been a measurement of rotational CD. Thus, a complete and robust estimate of the observability of CD requires a laboratory measurement. Due to the lack of availability of this measurement, the only recourse is to use existing theoretical measurements. Rotational CD has been discussed extensively []. This work derives both the absolute absorption strengths and the dissymmetry parameter, which is a ratio of the CD strength to the linear absorption strength, which is the simplest parameter to use to compare with the current observations. The dissymmetry parameters calculated for propylene oxide are only available for J = 0–10 transitions. For these parameters the dissymmetry parameter varies from 10^{-8}–10^{-5}. These values pose a serious problem for the astronomical observation of CD. They imply that signal-to-noise ratios in excess of 10^5 are likely required for detection of CD. This does assume that the noise power is isotropic in its polarization, which is the case for receiver noise-dominated observations. Achieving such high signal to noise ratios is possible with modern radio telescopes, but requires far higher abundances. Feasibly detecting CD would require massive change of target signal. This could be accomplished by improving signal by increasing the collecting area of the telescope, targeting a region with a higher column density of target molecule, or using a target molecule with both high abundance and lower dissymmetry parameters. Simply improving the receiver sensitivity is unlikely to be able to enable CD, as current instruments are already often within an order of magnitude of the quantum limit, and there is not sufficient improvement to be had with receiver sensitivity alone. Likely, detection of CD will be achieved through improvement of all of these factors.

One of the most obvious routes to higher signal to noise is to work at higher frequencies. Detection of high frequency millimeter or submillimeter transitions necessitates a warmer population and the use of higher noise temperature receivers, however the improvement in signal strength more than outweighs this. As an example, the simulated spectrum of propylene oxide assuming a column density of $N_T = 1.3\times10^{15}$ and T_{ex} = 125K is shown in Figure 4.7. A second option is to target other simple chiral species that may be both more abundant and have more favorable dissymmetry. The obvious target is monodeuterated ethylene oixde (CH_2OCHD). For highly deuterium enriched regions, this species could be as or more abundant

than propylene oxide. Furthermore, this species has more favorable dissymmetry parameters which are more robustly determined. It should be noted, however, that while none of these dissymmetry parameters are well determined, general theories of optical activity suggest that the dissymmetry parameters derived are reasonable, or perhaps optimistic[]. Moving to target denser regions, either through better source selection or the use of interferometry could boost the column density by orders of magnitude. Finally, the use of next-generation telescopes, specifically the high frequency square kilometer array, would improve the raw collecting area by 10^4 over the GBT.

These factors may be sufficient to enable the astronomical detection of CD, however, they are speculative in many regards. A more practical, though less informative, approach is to correlate chiral species abundance with the spatial distribution of polarized light within a region. Using the ngVLA, high-sensitivity observations to map the distribution of a chiral species could be generated. Comparison with optical maps and fluxes used with laboratory photo-destruction cross-sections could place limits on the amount of enantiomeric enrichment achievable. This relies on several assumptions including cospatial molecules and emission, and the length of time under irradiation. This method would therefore produce a large uncertainty in its outcome, but would be the first constraint on enantioenrichment in molecular clouds[]. Large enrichments have been observed in amino acids found in meteorites, and its origins remain unclear []. Using reasonable guesses, it may be possible to set upper limits below the values observed in meteorites. This would require the assumption that conclusions drawn from current molecular clouds are applicable to the formation of our own solar system, but again such observations would be extremely useful in furthering our understanding of chemical processing beyond the molecular cloud stage and the origins of homochirality.

4.6 Propanal and Acetone Observations in PRIMOS

We have examined the PRIMOS dataset for transitions of acetone and propanal. We find 18 clear, unblended transitions of acetone (Table 4.3), and 11 similarly distinct transitions of propanal (Table 4.4). All transitions were observed in absorption, and parameters derived by single-Gaussian fits to the lines were determined. We use the method described above to fit a column density and temperature to these species using these observed transitions, but note that we make no effort to refine the physical models from those used for propylene oxide. A static linewidth of 12 km s^{-1} was used for acetone, and a linewidth of 9 km s^{-1} for propanal. The source

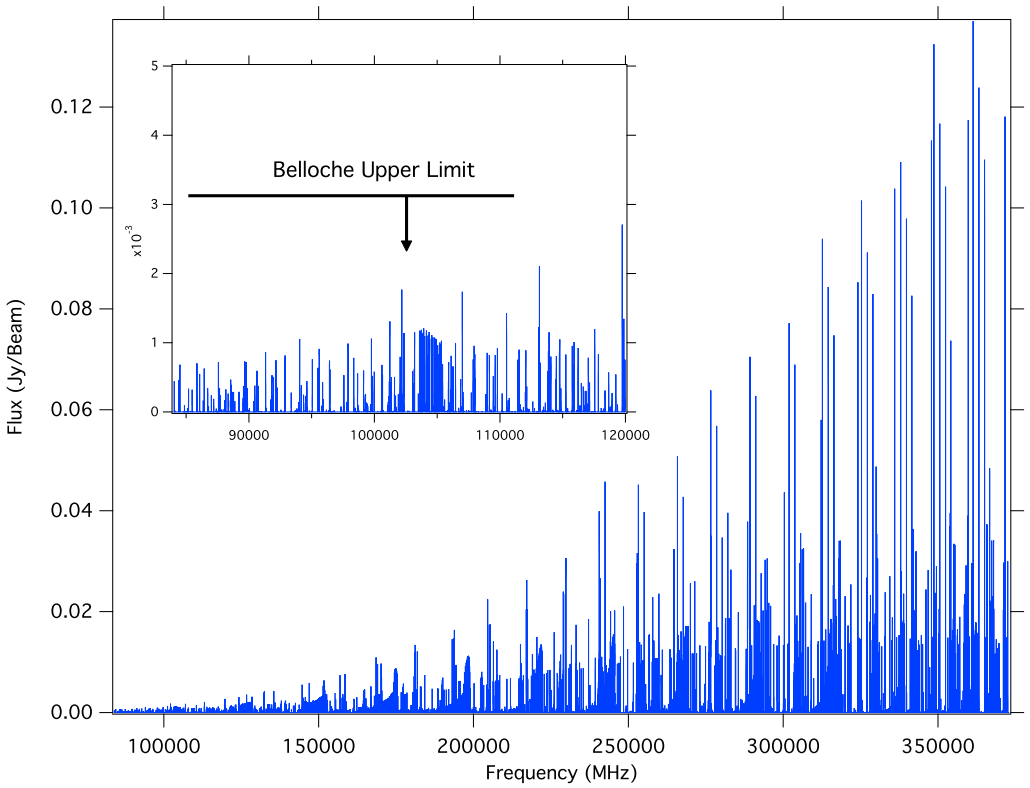

Figure 4.7. Theoretical prediction of the submillimeter spectrum of propylene oxide, assuming N_T = 1.3×10^{15}, T_{ex} = 125K. Source size is taken from Qin 2011 and molecular line parameters from Mesko 2017. The previous observed regions of Cunningham 2007 and Belloche 2013 (84 - 114 GHz) are shown in the inset with the average EMoCA survey RMS (Belloche 2016) indicated as a horizontal line. Transitions in Band 7 are approximately 100x brighter than those at Band 3.

size was taken as 20″ in both cases.

The models derived here reproduce the observed intensities to within a factor of ~2 (Figures 4.8 and 4.9), and the uncertainties in these parameters should be taken to be of this order. Further, for acetone in particular, a warm component is known to be present within the PRIMOS beam, but was not explicitly treated in this analysis. Thus, while the derived values are useful for qualitative comparisons with each other and propylene oxide, a more rigorous treatment than the single population, single excitation-temperature model used here, although beyond the scope of this work, would refine the results.

4.7 Discussion

Taken together, the GBT and Parkes observations provide strong evidence of cold, low-abundance propylene oxide toward the Sgr B2 cloud complex, in excellent

Table 4.3. Observed acetone transitions in PRIMOS.

$J'_{K_a,K_c} - J''_{K_a,K_c}$	Frequency (MHz)	ΔT_A^* (mK)	ΔV (km s^{-1})
$3_{2,1} - 3_{1,2}$ AE	10731.360(9)	-33.0(9)	16.5(6)
$4_{3,1} - 4_{2,2}$ EE	11569.943(4)	-60(3)	14.9(9)
$4_{3,1} - 4_{2,2}$ EA	11583.080(5)	-13(3)	10(3)
$4_{3,1} - 4_{2,2}$ AA	11585.245(3)	-11(2)	10(3)
$5_{4,1} - 5_{3,2}$ EE	14263.975(5)	-28.7(8)	15.8(6)
$5_{4,1} - 5_{3,2}$ AA	14276.816(6)	-18.6(7)	14.8(9)
$4_{2,2} - 4_{1,3}$ EE	18654.309(4)	-29.7(8)	12.7(4)
$3_{1,2} - 3_{0,3}$ AA	20454.895(4)	-9(1)	12(2)
$3_{2,2} - 3_{1,3}$ EE	22413.051(3)	-12.2(5)	8.8(4)
$2_{0,2} - 1_{1,1}$ AA	22793.262(3)	-7.5(7)	12(2)
$2_{0,2} - 1_{1,1}$ EE	22800.382(2)	-32.2(7)	11.8(3)
$4_{3,2} - 4_{2,3}$ EE	23469.238(4)	-18.4(7)	12.2(5)
$4_{3,2} - 4_{2,3}$ AA	23549.025(4)	10.7(9)	10.7(9)
$2_{1,2} - 1_{0,1}$ AA	24916.487(3)	-7.3(9)	9(1)
$3_{1,3} - 2_{0,2}$ EE	34092.973(3)	-23(2)	11.6(9)
$2_{2,1} - 1_{1,0}$ AE	35371.432(5)	-13(2)	8(1)
$2_{2,1} - 1_{1,0}$ EE	35381.289(4)	-43(1)	17.8(7)
$2_{2,1} - 1_{1,0}$ AA	35468.174(5)	-22(2)	6.8(9)

Numbers in parentheses are 1σ uncertainties in units of the last significant digit. A and E labels designate torsional sub-levels.

Table 4.4. Observed propanal transitions in PRIMOS.

$J'_{K_a,K_c} - J''_{K_a,K_c}$	Frequency (MHz)	ΔT_A^* (mK)	ΔV (km s^{-1})
$2_{0,2} - 1_{1,1}$	10098.84(5)	-14.3(8)	21(1)
$4_{1,3} - 4_{0,4}$	19182.410(4)	-8.3(8)	5.8(8)
$2_{1,2} - 1_{1,1}$	19690.51(5)	-18.2(4)	10.2(3)
$2_{0,2} - 1_{0,1}$	20875.19(5)	-8.6(5)	8.7(5)
$3_{0,3} - 2_{1,2}$	21451.62(5)	-17.0(7)	9.0(4)
$2_{1,1} - 1_{1,0}$	22279.26(5)	-8.6(9)	3.8(4)
$4_{2,2} - 4_{1,3}$	29618.95(5)	-28(1)	13.8(9)
$3_{2,1} - 3_{1,2}$	31002.20(5)	-13(2)	6.8(9)
$4_{0,4} - 3_{1,3}$	32897.82(5)	-13(2)	6(1)
$3_{1,3} - 2_{0,2}$	39061.03(5)	-21(1)	10.6(8)
$4_{1,4} - 3_{1,3}$	39177.132(5)	-20(1)	12(2)

Numbers in parentheses are 1σ uncertainties in units of the last significant digit.

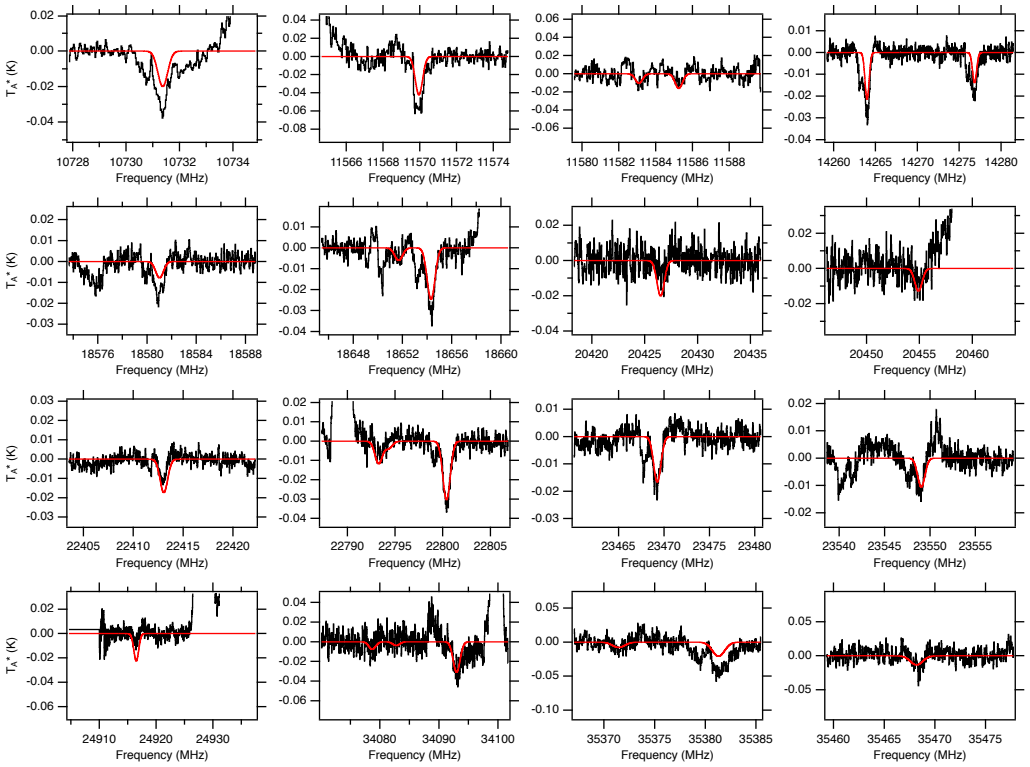

Figure 4.8. Model spectrum of acetone toward Sgr B2(N) at the best-fit column density and temperature, and comparison with observations. The spectrum of acetone at $N_T = 2.1 \times 10^{14}$ cm^{-2} and $T_{ex} = 6.2$ K, corrected for background continuum, telescope-specific parameters, and beam dilution effects is shown in the main figure. The observed transitions in PRIMOS are shown in black, with the model spectra overlaid in red.

agreement with previously established upper limits, as well as with previous observations of complex organic molecules. Indeed, many of the complex organics seen toward Sgr B2(N) are found not in or near the hot cores, but, like propylene oxide, in a cold, extended shell around the source. In these regions, molecules are often liberated into the gas phase via non-thermal, shock-driven, desorption, resulting in colder, spatially-extended gas-phase populations that are often more abundant than predicted by standard warm-up models [124]. This is consistent with the observation that the structurally-similar ethylene oxide is consistently found to have low excitation temperatures (11 – 35 K), well below the temperature of the surrounding grains[84], with the detections of glycolaldehyde[82], ethanimine[96], and propylene oxide's structural isomers propanal[78] and acetone[100] in this region, and with the general pattern of shock-driven liberation of complex molecules in the so-called central molecular zone[124].

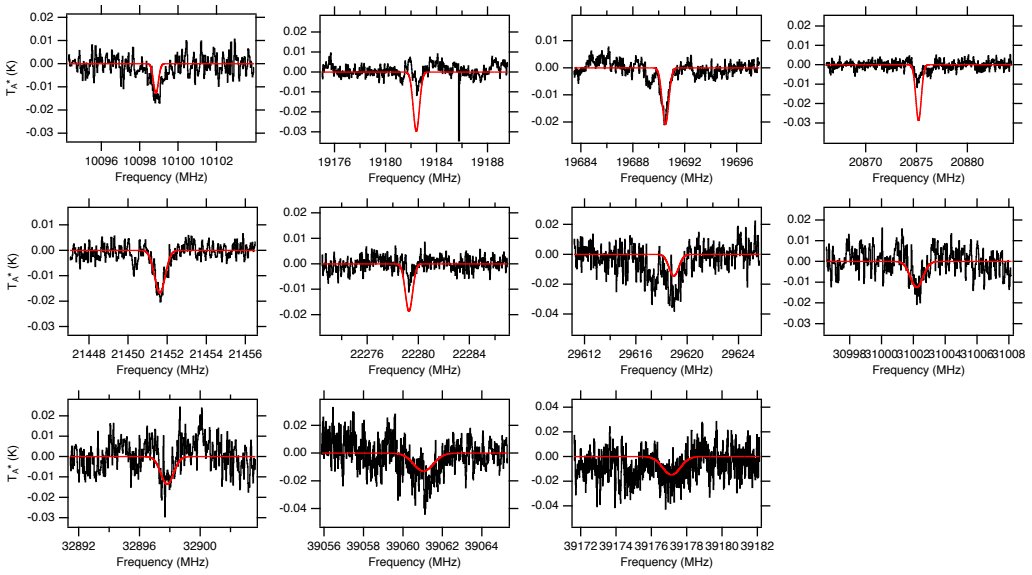

Figure 4.9. Model spectrum of propanal toward Sgr B2(N) at the best-fit column density and temperature, and comparison with observations. The spectrum of propanal at $N_T = 6 \times 10^{13}$ cm^{-2} and $T_{ex} = 6.2$ K, corrected for background continuum, telescope-specific parameters, and beam dilution effects is shown in the main figure. The observed transitions in PRIMOS are shown in black, with the model spectra overlaid in red.

From a chemical perspective, the presence of propylene oxide in Sgr B2(N) is not surprising. Propylene oxide is the third species of the C_3H_6O family detected toward this source. Its structural isomers, propanal (CH_3CH_2CHO) [78] and acetone ($(CH_3)_2CO$) [138], are both seen toward Sgr B2(N), and propylene oxide is not the first epoxide found in the ISM. Ethylene oxide (CH_2OCH_2) is structurally similar to propylene oxide, differing by only a methyl group, and has been detected toward numerous massive star-forming regions including Sagittarius B2(N)[40, 84]. In the case of acetone, [12] report a column density of $N_T = 1.49 \times 10^{17}$ cm^{-2}, but for a warm population with $T_{ex} = 100$ K that peaks at the position of the hot core. In the detection of propanal, column densities were not determined[78].

To determine the relative populations of these molecules in the cold shell around Sgr B2(N), we have used the same procedure as for propylene oxide. We find that a column density of $N_T = 6 \times 10^{13}$ cm^{-2} with $T_{ex} = 6.2$ K reproduces the 11 propanal transitions observed in the full PRIMOS dataset , to within a factor of ∼2. Similarly, using 18 detected lines of acetone in PRIMOS, we find a column density of $N_T = 2.1 \times 10^{14}$ cm^{-2} with $T_{ex} = 6.2$ K reproduces these features within a factor of ∼2. The best-fit $T_{ex} = 5$ K for propylene oxide is in remarkably good agreement with

these values, which due to the larger number of observed transitions over a wider frequency range for propanal and acetone are much more rigorously-constrained. T_{ex} up to 35 K for propylene oxide are formally allowed in the propylene oxide fit, due to loose constraints stemming from the narrow range of energy levels covered in a narrow frequency window. However, the best-fit T_{ex} = 5 K is significantly bolstered by the similar conditions exhibited by the acetone and propanal populations.

All three members of the C_3H_6O family are then detected in absorption in the PRIMOS data at remarkably similar excitation conditions, suggesting they likely occupy the same cold, shocked region surrounding Sgr B2(N). Propanal and acetone are thermodynamically favored over propylene oxide, residing 22.7 and 30.8 kcal mol^{-1} (0.98 and 1.33 eV) lower in energy, respectively [93]. But, while the relative column densities derived here do roughly follow the pattern of increasing abundance with increasing stability, chemistry in molecular clouds is largely kinetically-controlled, rather than thermodynamically, and relative abundances do not regularly follow thermodynamic patterns [73, 97]. The recent detections of acetone and propanal at an abundance ratio of three to one in comet 67P/Churyumov-Gerasimenko show that members of the C_3H_6O family also feature prominently in the volatile organic content of comet nuclei, and the remarkably similar ratios to those observed toward Sgr B2(N) suggest that such kinetically-controlled routes to both species are widespread, and not isolated to extraordinary interstellar sources[64].

The leading models for the production and enhancement of an e.e. in the interstellar medium likely act over timescales far longer than the delivery of complex organic material to the planet-forming region of disks[5, 43, 107]. A number of mechanisms have been proposed for gas-phase routes in the ISM to create such a primordial e.e. While beta decay-related chemistry has been proven to generate slight chiral asymmetries [43] that would be universal in nature, perhaps the most intriguing route, astronomically, is enantiomerically-selective photochemistry induced by circularly-polarized light (CPL) [107]. Here, the chirally-sensitive chemical reaction networks would be stochastically driven on the spatial scales of giant molecular cloud complexes. Toward the Orion Nebula cluster, for example, significant CPL patterns capable of producing e.e. do not extend over the entire protostellar cluster, but have been detected over regions large compared to individual protoplanetary disks [5]. We have rigorously examined the possible mechanisms for determining an e.e., and concluded that the standard, total power observations shown here cannot determine whether such an e.e. exists in the case of propylene oxide, but that high precision,

full polarization state measurements can, in principle. Critically, the detection of gas-phase propylene oxide toward the Galactic Center provides a molecular target for such observations, and demonstrates that interstellar chemistry can reach sufficient levels of complexity to form chiral species in environments with the physical conditions required to produce an enantiomeric excess.

Chapter 5

ALMA OBSERVATIONS OF CH_3CN TOWARD ORION KL

5.1 Introduction

The Orion Kleinmann-Low (KL) nebula is the archetype and best-studied high-mass star forming region in the Milky Way. At a distance of 414 pc [105] it is also the closest. High mass star forming regions produce the majority of stellar systems and are some of the most molecularly rich sources studied [74, 155]. It has been proposed that the Earth and many other solar systems formed in a similar region[20]. Material made in these star forming regions may be inherited by solar systems born in these regions [29]. Therefore the chemistry observed toward these regions may be an important contributor to the molecular inventory of solar systems and planets.

The chemistry occurring in star forming regions is remarkably complex. Both gas-phase and condensed grain surface chemistry combine to produce a wide range of molecular species[74]. The interplay between gases, grain surfaces, and the system's structure and dynamics makes it extremely difficult to model accurately, and even simple species can have highly complex formation driven by large networks of chemical reactions. A better understanding of these formation pathways is critical for developing a robust picture of chemistry in the interstellar medium (ISM). An obvious starting point is the formation of cyanides. Recent observations of Orion KL with the *Herschel* telescope show that cyanides consistently trace warmer gas[33, 34]. There are two likely explanations for this. First that cyanides are formed more efficiently in gas-phase reactions at warmer temperatures and are therefore found to be more abundant in warmer gas. Second, that cyanides are more difficult to liberate from grain surfaces, and therefore formed cold and only found in the gas phase at warmer temperatures. These scenarios are impossible to distinguish with single dish observations, however there is a difference that may be exploited to determine how cyanides are formed: formation temperature. This can be used by noting that at lower temperatures the zero point energy difference favors C–D over C–H bonds. Therefore the D to H ratio can be used as a thermometer for the formation temperature of cyanides.

In order to differentiate the mechanisms, it is necessary to correlate temperature and D to H ratio. If the D to H ratio is independent of the temperature of the region, it

must be due to low-temperature grain surface chemistry. If the D to H ratio is anti-correlated with temperature, the species must be formed directly at that temperature, showing that it is indeed a product of gas-phase chemistry. In particular, CH_3CN is an excellent target. It is highly abundant, its isotopologues are easily observable, and it shows a strong warm component. In order to distinguish these scenarios, the temperature and D to H ratio must be measured at spatial scales over which heating is expected to occur. For self-luminous hot cores like the one proposed to exist in Orion KL, this is hundreds of AU. This therefore requires both extremely high angular resolution and sensitivity. The recent completion of the Atacama Large Millimeter/Submillimeter Array (ALMA) enables such observations toward Orion KL through long baseline submillimeter interferrometry.

Orion KL is one of the best studied and one of the most chemically rich star forming regions, with spatial and chemical heterogeneity that make it a unique source[15]. Orion was recently subjected to an enormous explosive event approximately 500 years ago, producing a near isotropic high velocity outflow [7]. This event is believed to originate from a dynamic interaction between radio source I and the Becklin–Neugebauer (BN) object, a $\sim$10 $M_\odot$ B star, the most likely scenario being ejection of BN from the trapezium (Θ^1 Orinis), and interaction with an existing molecular cloud complex[116]. Such a scenario creates an incredibly heterogeneous and dynamic environment. As a result the region is spatially complex, forming a large cavity with clumps of dense gas and dust elongated along the northeast southeast axis surrounding the cavity. Farther to the south is the relatively quiescent compact ridge. The two major features of the nebula are source I, and BN. BN is located to the northwest, traveling this direction away from the region at 24 kms^{-1} and is bright from the optical to radio wavelengths, although the region around BN is relatively isolated. By contrast, source I appears to be embedded within the millimeter emitting dust on the western inner wall of the cavity. Source I is believed to be a massive protostar with a circumstellar disk, and is the source of a low velocity outflow with a 315° position angle. To the east of source I is the molecularly-rich Orion KL hot core. Beyond this, numerous other sources have been identified by IR[37, 133], millimeter [49, 149] and submillimeter[76] imaging. Throughout the rest of the chapter, the point sources identified by submillimeter imaging at similar resolution by Hirota et al. [76], designated by the HKKH notation, are used as points of reference, as they are detected at similar resolution in the present observations.

Table 5.1. The correlator configuration used for the ALMA observations of Orion KL.

Species	Rest Frequency (GHz)	Channels	Resolution (kHz)
CH_2DCN $9_{1,8}$–$8_{1,7}$	156.970282	960	488.281
CH_2DCN $9_{5,5}$–$8_{5,4}$	156.236135	1920	488.281
CH_2DCN $9_{1,9}$–$8_{1,8}$	155.614895	960	488.281
$^{13}CH_3CN$ 8_3–7_3	142.901396	3840	488.281

5.2 Observations

Observations of Orion KL were taken in ALMA Cycles 1, 2, and 3 For all observations, the pointing center was set to α_{J2000} = $05^h35^m14^s.5$, δ_{J2000} = -05°22'30".9. Cycle 1 observations consist of short baseline, 0.34 km (170kλ) observations, utilizing 36 antennas, spanning two local oscillator settings. The correlator configuration is summarized in Table 5.1. Cycle 2 observations consisted of 33 antennas with a maximum baseline of 1.5km (825kλ), covering the first local oscillator. Cycle 3 observations covered the second local oscillator with 3.2 km (1.6Mλ) maximum baseline and 44 antennas. Calibration was completed using standard CASA calibration pipeline scripts using CASA 4.3.1 for Cycle 1 and 2 observations, and CASA 4.7.0 for Cycle 3 data. Despite substantial spectral line contamination, continuum subtraction was done in the u-v plane using the `uvcontsub` task in CASA. Images were produced using the `CLEAN` task in CASA, using a robust parameter of 0.5. Due to limited u-v sampling, significant artifacts were present in the dirty images. `CLEAN` regions were chosen conservatively based on the strongest emission and confirmed with previous observations [55]. The resulting images had an RMS of ~5 mJy (2.4 K) and resolutions ranging from 1.2 to 0.2 arcseconds. The resulting continuum image is shown in Figure 5.1. The derived continuum is in good agreement with previous high resolution ALMA images [76].

5.3 Analysis

To determine the column densities and temperature of methyl cyanide isotopologues as a function of position, data were fit pixel-by-pixel across a 11″ ×13″ region at the center of the map. We focus on Cycle 2 observations, as these are the only long-baseline observations that simultaneously observed both CH_2DCN and $^{13}CH_3CN$. Because these species are observed simultaneously, the uncertainties in quantities derived from relative fluxes, e.g. temperature or D to ^{13}C ratio, should be dominated by thermal noise, rather than calibration uncertainties, as

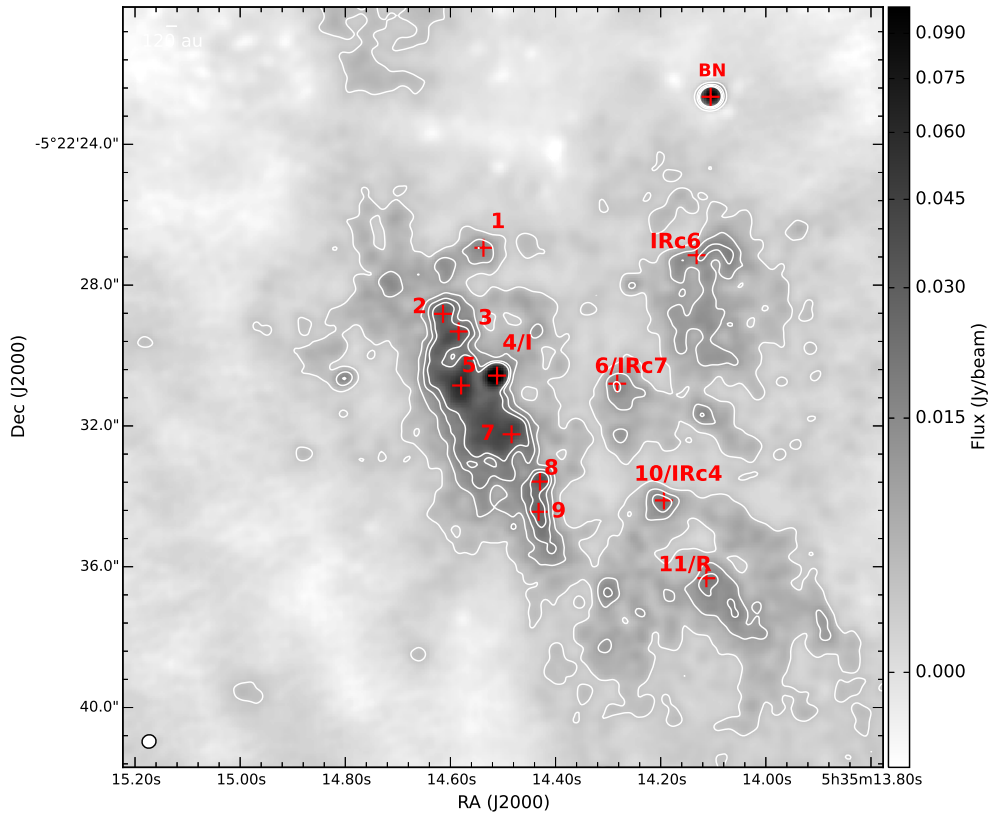

Figure 5.1. A plot of the continuum toward Orion KL. Both the greyscale and contours plot the continuum. The greyscale is plotted on a log scale using vmin of -0.01 and vmid of 0.1. Contours are at the [-0.0028995 0.00323595 0.0093714 0.01550685 0.0216423] Jy beam^{-1} levels. Red crosses mark continuum sources. Numbers mark peaks identified by Hirota[76]. The synthesized beam is shown in the bottom left.

would be the case for separate observations of each species. Additionally, the combination of substantial overlap with CH_3CN transitions, and inherent differences in calibration and array configuration, limit the usefulness of Cycle 3 observations, which observed $CH_3^{13}CN$. The Cycle 2 observations have a resolution of 0.33″ ×0.35″ with a maximum recoverable scale of ∼4″ .There is substantial material at spatial scales greater than 4″ toward Orion KL [149] whose flux will be resolved out. The goal of these observations is to resolve spatial structure on scales commensurate with circumstellar disks which lay within radii typically associated with abundance enhancements brought on by heating from embedded protostars as modeled by so called "jump models" [18, 130]. These observations therefore do not give a complete

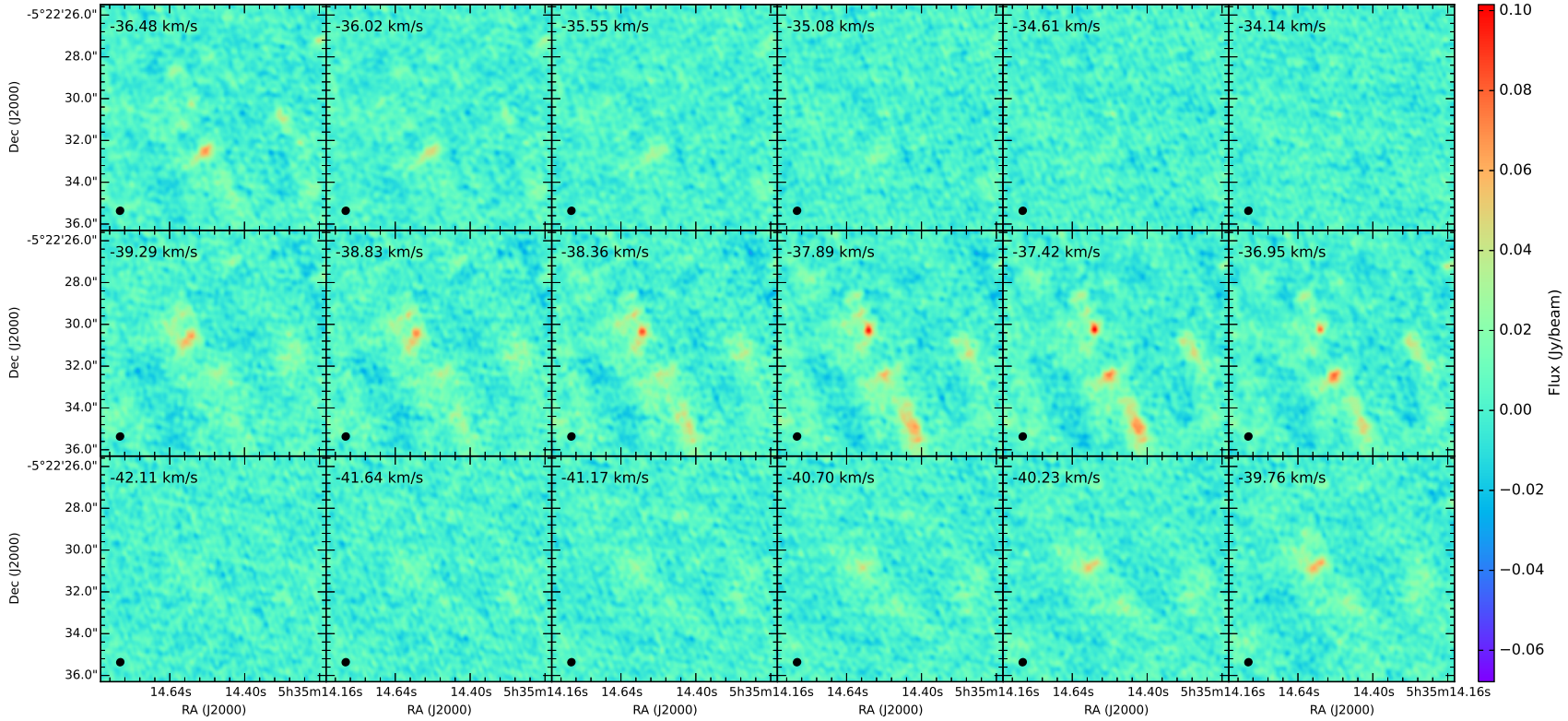

Figure 5.2. Channel map of the $9_{4,6}$–$8_{4,5}$ and $9_{4,5}$–$8_{4,4}$ transitions of CH_2DCN. Velocity is given from -34.14 kms^{-1} to -42.11 kms^{-1}. The synthesized beam is shown in the bottom left.

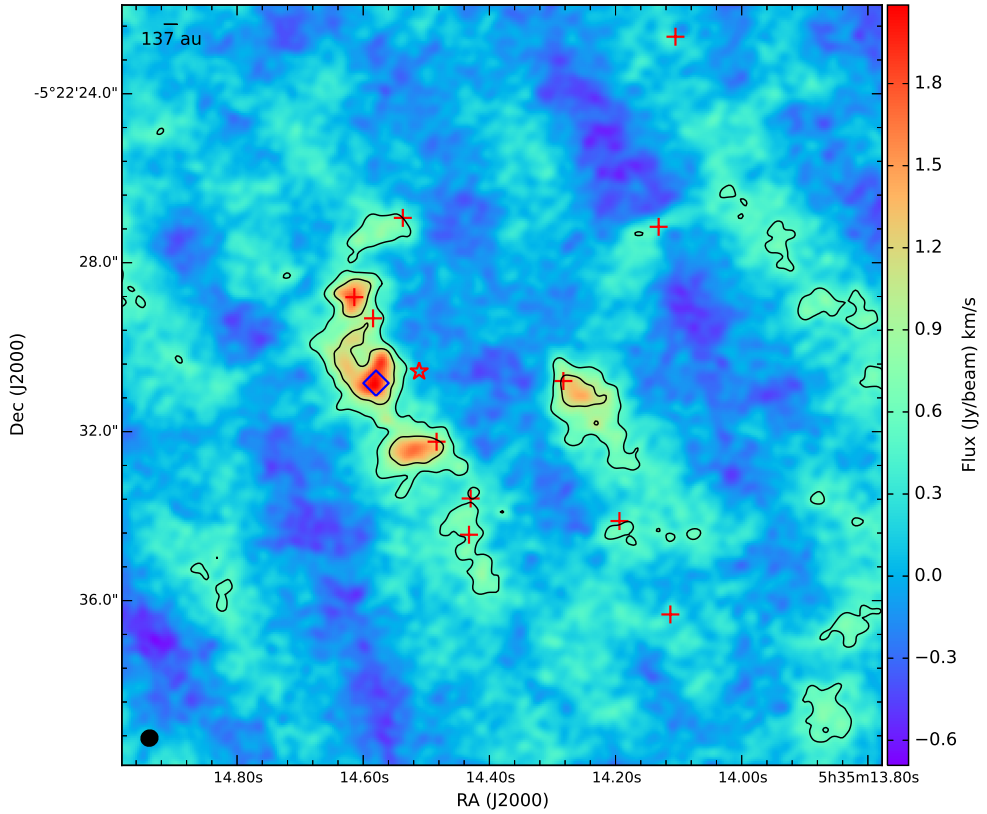

Figure 5.3. The moment 0 map of $^{13}CH_3CN$ toward Orion KL. The color and contours show the integrated intensity of the $^{13}CH_3CN$ transitions used in the fit. Red crosses mark the continuum sources identified by Hirota[76]. Contours are at the [0.52, 1.04, 2.09] Jy beam^{-1} levels. The red star indicates the position of source I and the blue diamond marks the position of the hot core.The synthesized beam is shown in the bottom left and a scale bar is shown at the top left.

picture of CH_3CN toward Orion KL, but instead focus only on the material present at small spatial scales that is relevant to elucidating the origins of CH_3CN .

Fitting was done by extracting spectra in a single synthesized beam centered on each pixel in succession, and performing a fit at each point. For some regions, the presence of small additional continuum flux not fully subtracted during imaging was removed separately for each subband as a constant offset determined from a line-free region of the spectrum. To prevent erroneous fit results, only pixels with CH_2DCN flux greater than three times the local RMS were included. Excitation temperature, velocity, width, and column density of $^{13}CH_3CN$ and CH_2DCN species were determined

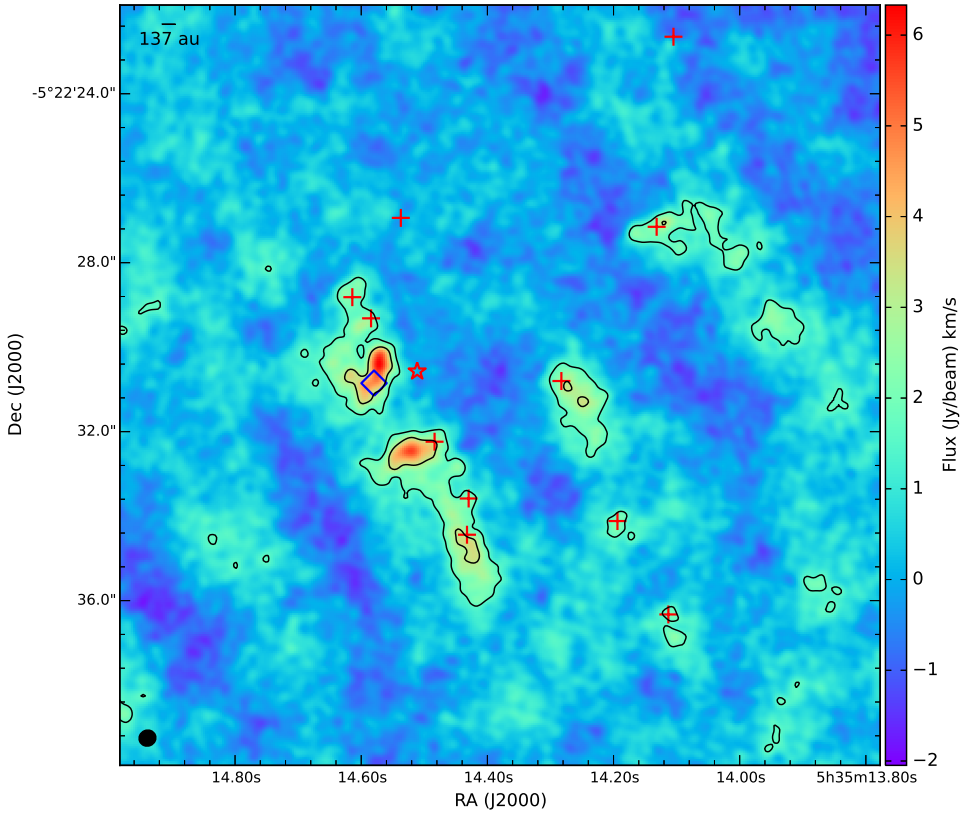

Figure 5.4. The moment 0 map of CH_2DCN toward Orion KL. The color and contours show the integrated intensity of the CH_2DCN transitions used in the fit. Red crosses mark the continuum sources identified by Hirota[76]. Contours are at the [1.58, 3.17, 6.33] Jy beam^{-1} levels. The red star indicates the position of source I and the blue diamond marks the position of the hot core.The synthesized beam is shown in the bottom left and a scale bar is shown at the top left.

simultaneously by least squares fitting. It was assumed that both $^{13}CH_3CN$ and CH_2DCN have the same velocity, line width, and excitation temperature, and the same value was used for both species. Spectra were modeled using Equation 5.1,where N_T is the column density in cm^{-2}, I_v is the flux density in Jy/beam, dv is given in km/s, Q is the rotational partition function, E_u is the upper state energy in K, T_{ex} is the rotational excitation in K, ν is the transition frequency in GHz, and $S\mu^2$ is the transition dipole moment in Debye^2, convolved with a single gaussian lineshape, using the molecular parameters in Table 5.2. B is given by the equation B= $\Omega_S(\Omega_S + \Omega_B)$, where Ω_S and Ω_B are the solid angle of the source and beam respectively. Given the small angular scales, we assume the source completely fills

Table 5.2. CH_3CN Transitions used for fit.

Species	Transition	Rest Frequency (MHz)	Upper State Energy (K)	$S_{ij}\mu^2$ D^2	log(A) $\log(s^{-1})$
$^{13}CH_3CN$	8_7–7_7	142793.94160	381.29879	57.68051	-4.24039
$^{13}CH_3CN$	8_6–7_6	142828.80880	288.39069	215.33644	-3.96901
$^{13}CH_3CN$	8_5–7_5	142858.33610	209.74043	149.96124	-3.82485
$^{13}CH_3CN$	8_4–7_4	142882.51140	145.36583	184.56079	-3.73447
$^{13}CH_3CN$	8_2–7_2	142914.85	59.49889	230.69417	-3.63728
CH_2DCN	$9_{1,9}$–$8_{1,8}$	155614.87	42.74	136.60057	-3.50121
CH_2DCN	$9_{1,8}$–$8_{1,7}$	156970.26	43.06	136.59778	-3.48992
CH_2DCN	$9_{2,7}$–$8_{2,6}$	156304.638	59.08	131.48	-3.51206
CH_2DCN	$9_{3,6}$–$8_{3,5}$	156278.889	54.588	86.03938	-3.54140
CH_2DCN	$9_{3,7}$–$8_{3,6}$	156278.85	54.588	86.03938	-3.54140
CH_2DCN	$9_{4,5}$–$8_{4,4}$	156259.7696	123.77664	110.98263	-3.51206
CH_2DCN	$9_{4,6}$–$8_{4,5}$	156259.7696	123.77664	110.98263	-3.51206
CH_2DCN	$9_{5,5}$–$8_{5,4}$	156236.13200	172.28359	95.61108	-3.65097
CH_2DCN	$9_{5,4}$–$8_{5,3}$	156236.13200	172.28359	95.61108	-3.65097
CH_2DCN	$9_{6,3}$–$8_{6,2}$	156207.55840	231.55057	76.83619	-3.74615
CH_2DCN	$9_{6,4}$–$8_{6,3}$	156207.55840	231.55057	76.83619	-3.74615

the beam at all positions. Only the transitions listed in Table 5.2 were used for the fit. Several other transitions of both species are detected in our observations, but were not included in the fit due to substantial blending with other lines.

$$N_T = 2.04 \times 10^{20} \frac{\int I_v dv Q e^{\frac{E_u}{T_{ex}}}}{B\theta_a\theta_b\nu^3 S\mu^2} \tag{5.1}$$

The results of fitting are shown in Figures 5.5 and 5.6. In general, these results are in good agreement with previous observations of CH_3CN toward Orion KL[33]a. Fitable emission is clearly detected toward the hot core, SMA1/HKKH7, HKKH7 and 8, the compact ridge or HKKH 11, IRC7 or HKKH6, and IRc6. Spatially, the emission is consistent with previous cyanide observations [14, 149]. All fitted regions show smooth gradients in the derived parameters, with some exceptions, notably the line width of the HKKH 11, changing rapidly due to high noise, and several edge pixels toward SMA 1 nearly reaching the width limit of the fitting routine. Furthermore, the kinematic structure matches the channel maps.

The derived temperature structure is qualitatively in agreement with both ammonia mapping with the VLA [63] and millimeter CARMA imaging[149], with the highest temperatures found toward the hot core, with progressively lower temperatures

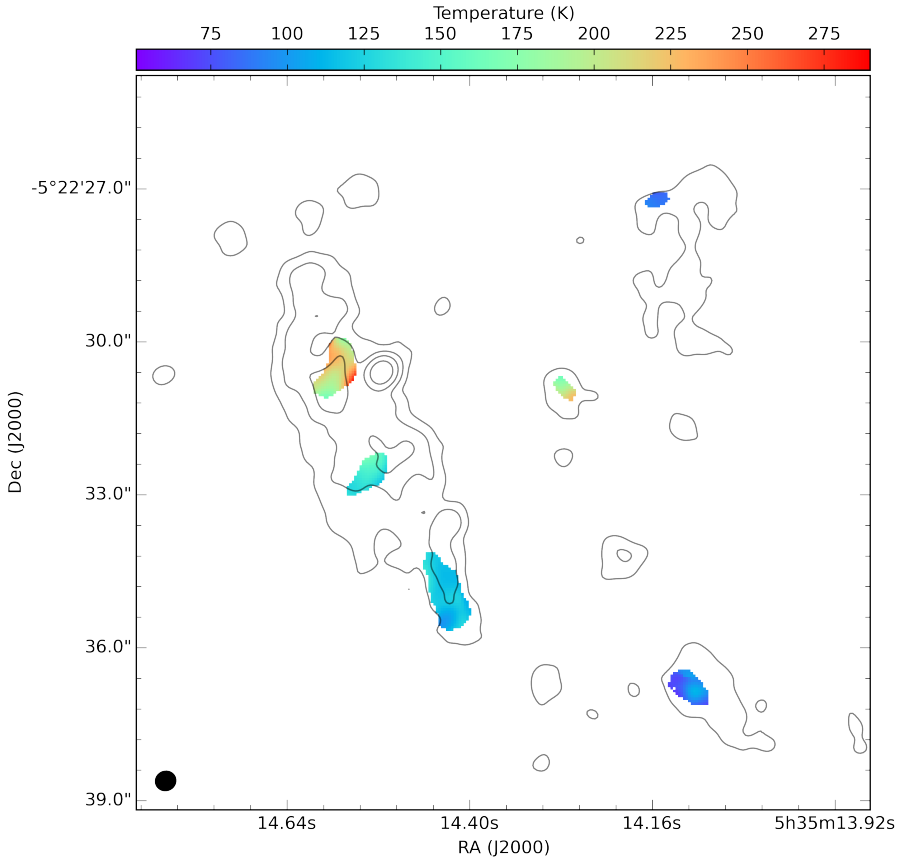

Figure 5.5. The derived CH_3CN temperature from the least squares fit of the Orion data cube. The derived temperature is shown as a color plot and the continuum is shown as peak flux×$[\frac{1}{2},\frac{1}{4},\frac{1}{8},\frac{1}{16}]$ contours in grey. The synthesized beam is shown in the bottom left corner.

to the south west. The absolute temperatures differ from both high resolution ammonia observations [63] and single dish Herschel measurements [32]. This can be reconciled by noting that [63] detected substantially higher excitation transitions that would require unrealistically high column densities to detect with the present observations, and that [32] used a single dish telescope that was far more sensitive to extended structure.

5.4 Results and Discussion

The most striking result of the analysis is that Orion KL's many regions are unique. Aside from the more general complex-scale dynamics observed here and elsewhere, each source appears to be inhomogeneous. While this result should be to some

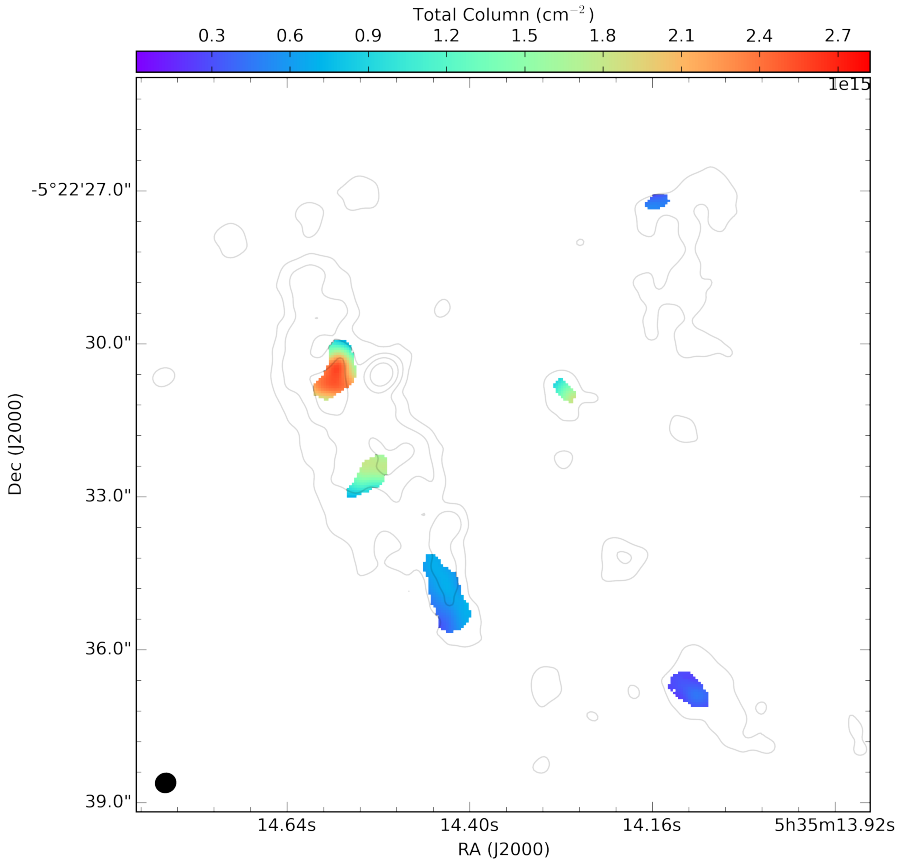

Figure 5.6. The derived CH_3CN column density from the least squares fit of the Orion data cube. The derived $^{13}CH_3CN$ + CH_2DCN column density is shown as a color plot and the continuum is shown as peak flux×$[\frac{1}{2},\frac{1}{4},\frac{1}{8},\frac{1}{16}]$ contours in grey. The synthesized beam is shown in the bottom left corner.

degree expected, it highlights a serious challenge for current and future astrochemical studies: even in the hot core phase, molecular clouds show spatial and chemical heterogeneity that must be accounted for to properly model the source. Moreover, these sources are not isolated and regions between should show a smooth transition between the regions. Future observations with higher sensitivity could trace this lower abundance material and further our understanding how these regions interact. This information would be extremely useful in better understanding the dynamics of the region.

IRc6 and IRc7 are detected with a source size that cannot be deconvolved from the synthesized beam. IRc7 shows a northeast-southwest gradient in temperature, column, velocity, and linewidth. The highest column densities, temperatures, and

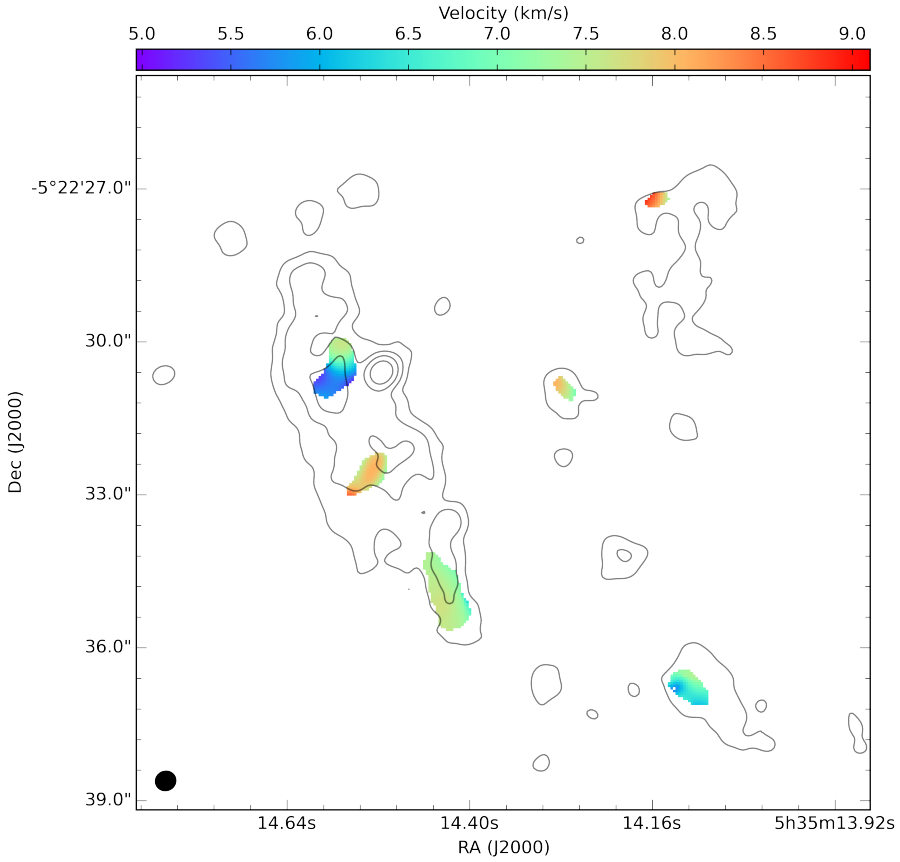

Figure 5.7. The derived velocity from the least squares fit of the Orion data cube. The derived velocity is shown as a color plot and the continuum is shown as peak flux×[$\frac{1}{2}$,$\frac{1}{4}$,$\frac{1}{8}$,$\frac{1}{16}$] contours in grey. The synthesized beam is shown in the bottom left corner.

line width are found at the southeast. The velocity gradient may suggest rotation about a common center of mass with the northwest end rotating away from the observer; however this is difficult to reconcile with the ~50 K temperature gradient observed, and may instead be a clump experiencing an external sheering force. The temperature gradient would imply external heating despite, the fact that the source is cospatial with the peak of the mid IR emission peak associated with IRc7. IRc6 by contrast is essentially homogeneous in all respects. Spatially it is closely aligned with IRc6E, rather than IRc6 or the peak of the millimeter emission near IRc6. HKKH 10 similarly shows little spatial variation, although there is some variation in its northeastern corner caused by low flux.

The peak toward HKKH8/9 appears to be kinematically homogeneous, with slight

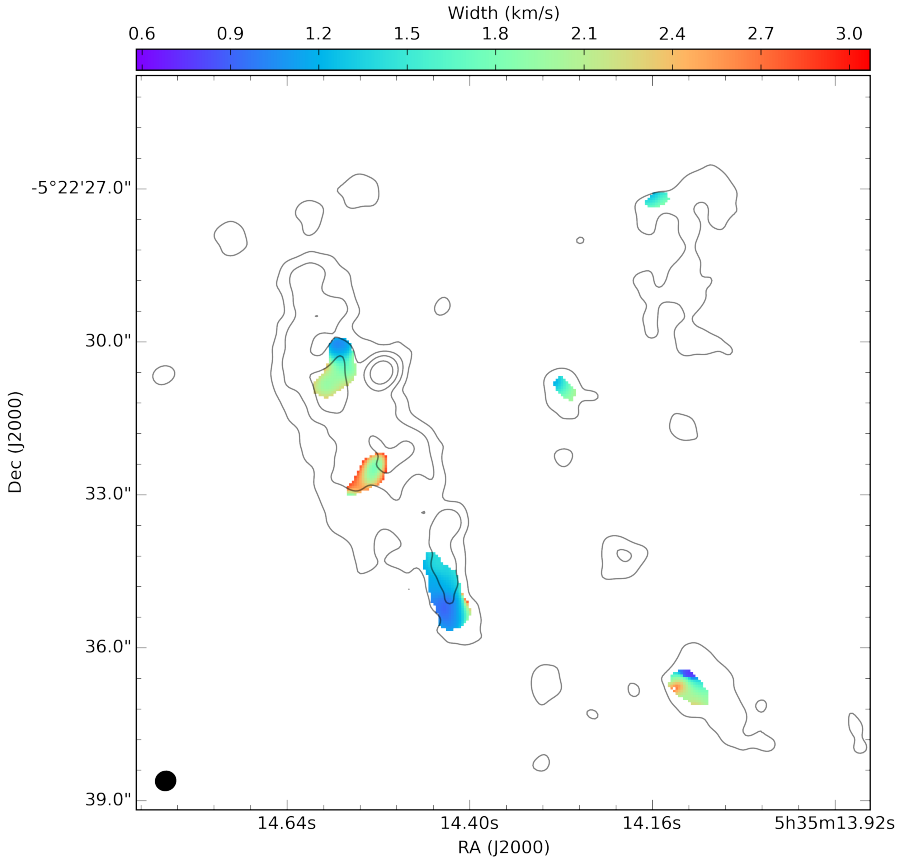

Figure 5.8. The derived line width from the least squares fit of the Orion data cube. The derived line width is shown as a color plot and the continuum is shown as peak flux×$[\frac{1}{2},\frac{1}{4},\frac{1}{8},\frac{1}{16}]$ contours in grey. The synthesized beam is shown in the bottom left corner.

east-west red shift and a corresponding modest decrease in width. There is a small peak in column density in the center of the region. The temperature varies from 100–125 K with small temperature increases near the northern and southern ends of the region, and a small increase in the center. The region is not cospatial with HKKH 8/9 and is located south and west of both, and not associated with the millimeter continuum. SMA1/HKKH7 is kinematically unusual. It appears to have a radial red shift, with lower velocities found at the outer edges of the region. This lower velocity outer region also has a far wider velocity width. Somewhat counterintuitively, both the column density and temperature are not correlated with the kinematic structure. Both column density and temperature increase from southwest to north east. As with the case of HKKH 8/9, this clump of gas is not completely cospatial with either

the millimeter continuum or SMA1. The spatial dependence of the temperature and column density gradient would make sense if the clump were being externally heated by SMA1, with a more turbulent outer shell.

Finally, the hot core is the strongest source of CH_3CN emission and the most structurally interesting region. Kinematically the region is unusual. It has a curved northwest-southeast shape with a velocity gradient that follows this structure. Each velocity component has a size that cannot be deconvolved from the synthesized beam, as shown in the channel maps in Figure 5.2. The velocity gradient is ~ 2 kms^{-1} red shifting to the north. Interestingly, the increase corresponds with decreasing distance to the SiO outflow from source I [117]. There has been considerable debate surrounding the origin of heating within Orion KL, in particular the hot core [38, 154]. Arguments have been made both for and against a self-luminous hot core. The velocity gradient towards the outflow may be the result of an interaction between the outflow and the hot core. The temperature gradient that goes from a hot exterior to cooler middle would support this hypothesis, though the origin of the heating on side of the hot core facing away from source I is less clear. Similarly, the increased velocity width and column density farther from the outflow may be a result of CH_3CN destruction as the region interacts with the source I outflow.

Finally, the results of the D to ^{13}C ratios are give in Figure 5.9. There are six regions with sufficient flux of both $^{13}CH_3CN$ and CH_2DCN to produce reliable D to ^{13}C ratios, the hot core, source n/HKKH 7, HKKH8/9, IRc4/HKKH10, IRc7/HKKH 6, and IRc6. The derived D to ^{13}C ratios vary from 1.0–0.5, assuming a galactic ^{12}C to ^{13}C of 68 [106], this gives very high values for the deuterium fractionation within the Orion KL complex, exceeding several other estimates [110]. Each source within the field of view shows its own unique behavior, analogous to that observed in the kinematic and abundance measurements discussed above, however there are few strong correlations between these variables. While the observed fractionation is extremely high, the source to source variations are very small compared to the enhancement over the cosmic value of 1^{-5}. This shows that despite the local mechanisms that may be modifying the enrichment, the overall enhancement in CH_3CN is large and as a whole, the CH_3CN toward the Orion KL complex evolved at very low temperatures. Despite this, there is a trend to lower deuterium enrichment at higher temperatures. This effect is small, roughly a factor of two, compared with the three orders of magnitude enhancement in fractionation. Still the trend is observed, and is even observed in several regions within Orion KL. IRc6 shows an essentially con-

stant deuterium fractionation, despite its temperature gradient, implying its material is unprocessed. The lack of an obvious temperature gradient in IRc6, HKKH8/9, or HKKH11 makes them difficult to interpret. The large spread in fractionation toward HKKH8/9 and HKKH11could be due to heavy reprocessing of some material, or differences in the formation of parts of these sources. Both scenarios are plausible given the spatial heterogeneity of the sources. HKKH7/SMA1 shows the clearest gradient fractionation gradient. The deuterium fraction drops quickly as the gas heats as it moves closer to the source I outflow and SMA1. This material is being actively reprocessed and appears to be one of the most chemically active regions in Orion KL. Finally, the hot core is again puzzling. The highest fractionation is observed toward the northern region. This part of the hot core is closest to the source I outflow. The spatial structure of the fractionation is correlated to the kinematic structure of the hot core, and suggests that the fractionation observed is a physical, rather than chemical effect, e.g. more complete grain mantle evaporation.

One curious result is the deuterium fractionation toward HKKH1. Comparing the moment 0 maps of $^{13}CH_3CN$ and CH_2DCN shown in Figure 5.3 and Figure 5.4 respectively, it is clear that though they have the same general spatial distribution, there is a strong deuterium depletion toward HKKH 1. While less extreme, there is also a strong depletion toward HKKH 2. The generally low SNR of either species toward HKKH 1/2 makes fitting meaningful D/H ratios impossible. Furthermore, the relatively high noise level of the observations makes it difficult to put strong upper limits on the CH_2DCN abundance, however assuming a T_{rot} of 150 K, the ratio is ~1:50. A second interesting feature of this region is the abundance of vibrationally excited species. Figures 5.11 and 5.10 show the moment 0 maps of CH_3CN v_8=1 and C_2CHCN v_{15}=1. The CH_3CN v_8=1 distribution clearly peaks toward the hot core and HKKH2/3, though it does extend to HKKH1. C_2CHCN on the other hand peaks farther north towards HKKH 2/3 and HKKH 1. These two species have similar upper state energies and critical densities, making it unlikely that this is caused purely by differences in excitation [17, 88].

This distinction is intriguing and suggests an origin for the depletion of CH_2DCN toward HKKH 1. The lack of an obvious excitation mechanism implies a chemical explanation. Vinyl cyanide is unsaturated and produced either directly in the gas-phase or through successive hydrogenation, or through gas-phase ion-neutral reactions [23]. The grain surface abundance peaks and then is depleted by further hydrogenation to ethyl cyanide or evaporation. Conversely, CH_3CN is the terminal

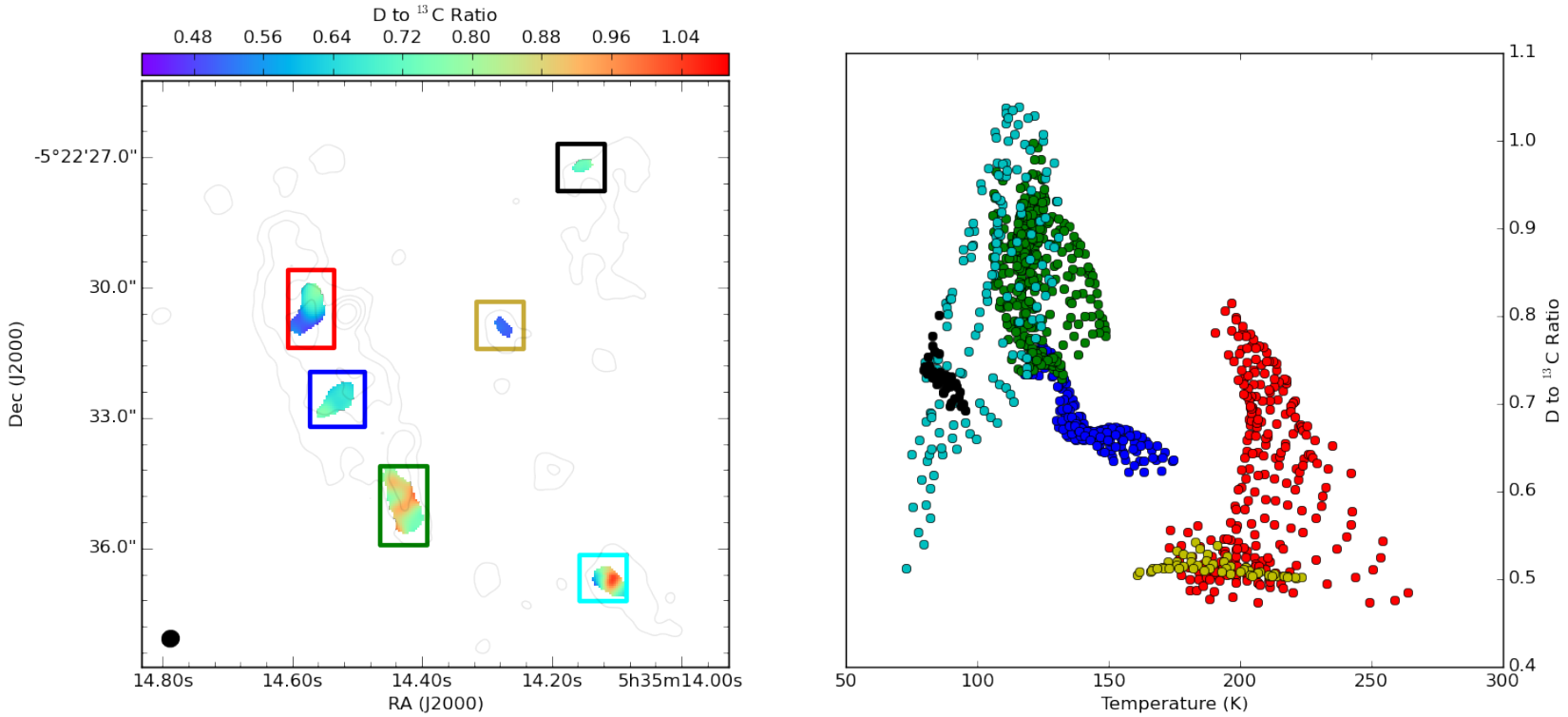

Figure 5.9. The derived D to ^{13}C ratio and temperature of CH_3CN toward Orion KL. A map of the D to ^{13}C ratio is shown in the left panel. A plot of the D to ^{13}C ratio versus the derived temperature is shown in the right panel. The color of the points in the right panel corresponds to the color of the rectangles in the left panel. A continuum contour plot and synthesized beam are shown in the left panel as guides.

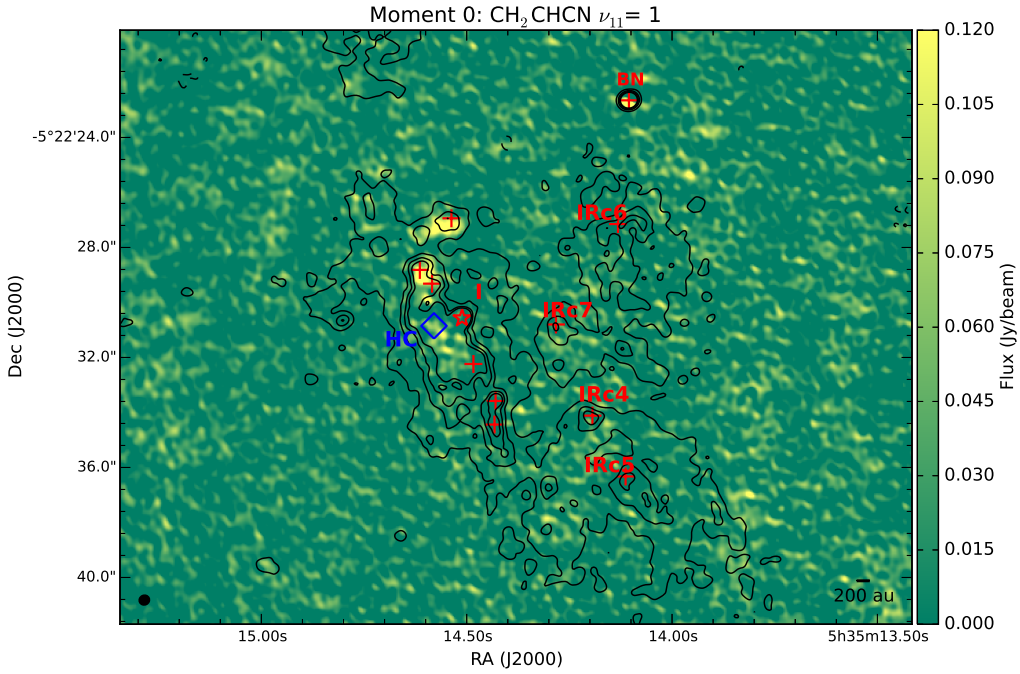

Figure 5.10. Moment 0 map of vinyl cyanide toward Orion KL. Continuum is shown as contour plots. A scale bar is shown at the bottom right. The synthesized beam is shown at the bottom left. The blue diamond marks the hot core. Red crosses mark HKKH sources.

species in grain surface hydrogenation. This would suggest that HKKH 1 is a much younger and more heavily ablated source, while the hot core and HKKH 2/3 are still warm, but substantially older or less heavily processed by the environment. This scenario would also explain the relatively low deuterium abundance in CH_3CN observed in HKKH 1. A young or heavily processed source would show a D/H ratio much closer to that expected from its kinetic temperature, as is the case in HKKH 1 and to a lesser extent HKKH 2/3. The question is then: *why is there such an abrupt change in physical conditions moving north from the hot core?* From Figures 5.1,5.3,5.4 there is very little material between HKKH 1 and source I or BN, and it may be more heavily irradiated. HKKH 1 is not directly along the axis of the source I outflow, but is reasonably close [117]. HKKH 2/3, show moderate

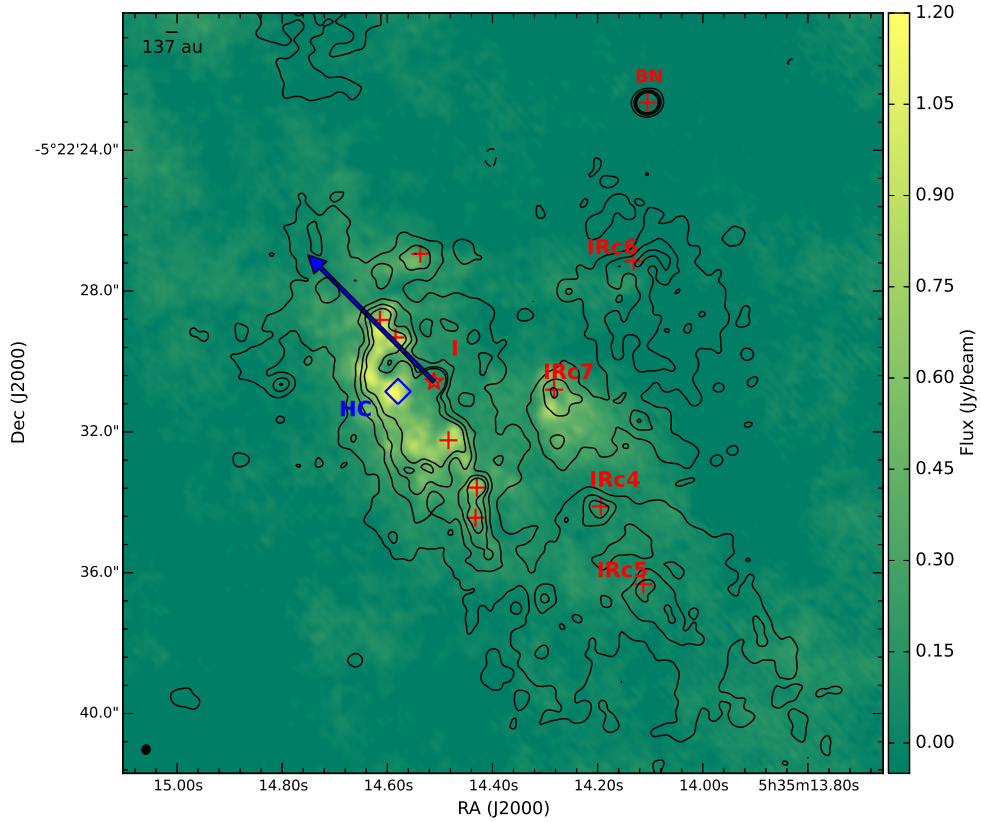

Figure 5.11. Moment 0 map of CH_3CN v_8=1 toward Orion KL. Continuum is shown as contour plots. A scale bar is shown at the top left. The synthesized beam is shown at the bottom left. The blue diamond marks the hot core. Red crosses mark HKKH sources. The direction of source I's low velocity flow is shown as a blue arrow.

depletion; however HKKH2 which is farther from both source I and BN shows higher depletion. There is a larger amount of material to potentially shield both sources and the difference in depletion between HKKH 2 and 3 is modest, but this may imply HKKH 2 is not coplanar with the rest of the material associated with the hot core.

5.5 Conclusion

This chapter outlines the observation and mapping of $^{13}CH_3CN$ and CH_2DCN toward Orion KL at unprecedentedly high angular resolution. These observations are incredibly rich, revealing structural, kinematic, and chemical detail at spatial scales of 100's of AU. This chapter discusses only a small fraction of the observations,

as there are likely several theses worth of material in these observations. Fitting of only $^{13}CH_3CN$ and CH_2DCN produced excellent results, automatically mapping these species at each pixel within the complex. The results of this fit show a strong deuterium enhancement across Orion KL, implying that the material was, in general, formed at very low temperatures. This suggests that CH_3CN and cyanides as a whole trace warmer gas toward Orion KL due to a need for higher energy to liberate them into the gas phase. Mapping shows gradients in temperature that are consistent with modest gas-phase reprocessing. Taken together this suggests that Orion KL began as several cold to modestly warm clouds that have been somehwat reprocessed. Mapping also shows a spatially heterogeneous region. Each source has a unique deuterium enhancement, kinematic and temperature structure, and morphology. It is unclear how typical Orion KL is as a massive star forming region; however if it is representative, this level of heterogeneity presents both a serious challenge and enormous opportunity for astrochemistry.

Chapter 6

NON DETECTION OF TRANS ETHYLMETHYL ETHER TOWARD W51

6.1 Introduction

It is quite clear that our understanding of the molecular complexity of interstellar and circumstellar environments is rapidly growing. It is also apparent that our understanding of interstellar molecular synthesis is presently incomplete; observations of new interstellar molecules are currently outpacing the model predictions as to how these interstellar species are formed in astronomical environments. In addition, many searches for interstellar species have focused on complex organic molecules of biological significance, (e.g. [152], [95], [11]). Since the detection of glycolaldehyde ($HOCH_2CHO$) there have been ~60 new molecular species claimed in interstellar and circumstellar environments. Furthermore, a majority of these claimed detections have involved complex organic species including alcohols (vinyl alcohol (CH_2CHOH), [145]; ethylene glycol ($HOCH_2CH_2OH$), [77]); aldehydes (propenal (CH_2CHCHO), propanal (CH_3CH_2CHO), [79]); amino acids (glycine (NH_2CH_2COOH), [89]) sugars (dihydroxyacetone ($CH_2OHCOCH_2OH$), [150]) and ethers ($C_2H_5OCH_3$, hereafter tEME, [57]).

Large organic molecules typically have high line strength ($S_{ij}\mu^2 \geq 50$ D^2), low energy transitions (≤ 50 K) that span the millimeter and submillimeter spectrum (e.g. [21]). Thus, it appears that the unambiguous identification of large molecules would be straightforward given the number of transitions available to search. Yet the detection of new molecules becomes difficult at millimeter and submillimeter wavelengths due in large part to the line confusion of more well-known interstellar species, including isotopic variants. It has been estimated that in the 2 mm and 3 mm windows, there are approximately 10 lines per 100 MHz at sensitivity levels of 10 mK, toward high mass hot molecular cores (HMCs) [70]. In the case of Sgr B2(N-LMH), perhaps the most well studied region to search for new interstellar species, the chance of finding a line at a particular LSR velocity ($\pm$ 2 km s^{-1}) of a measured spectral line frequency is ~40%, assuming simple Gaussian line profiles [70]. Searching a less complicated source than Sgr B2(N-LMH) can partially mitigate this obstacle; however, the problem of coincident spectral features interfering

with the detection of a new interstellar molecule still persists toward any chemically rich source.

The challenges in the identification of a new interstellar species have been reported by [137]. The authors suggest ways to overcome these challenges by assigning a set of criteria that must be met before the identification of a new interstellar molecules is confirmed. These criteria can be summarized as follows: 1) The transition frequencies searched for must be accurate to within a few kHz. In addition, the most favorable transitions to search for are multiply degenerate (if possible), high line strength, and low energy. The criteria of high line strength and low energy depends on the molecule. 2) The LSR velocities between transitions must be consistent. 3) If possible, the transitions of a new molecular species must be separated by any interfering features by the Rayleigh criterion in order to claim that transition. 4) The relative intensities between transitions must be consistent with radiative transfer based on the physical conditions of the region. Finally 5), if possible, connecting transitions at higher and lower quantum numbers to the claimed transition should be detected. These criteria were applied to the claimed detections of glycine ([89]) and dihydroxyacetone ([150]) and both of the claimed detections were rejected ([137] and [4], respectively). Conversely, the criteria were utilized to confirm the detection of glycolaldehyde ([70]) toward Sgr B2(N-LMH) at the 99.8% confidence level. As demonstrated by [137] and [4], the detection of a large organic molecule based on even 10 to 20 transitions can be tenuous.

In 2005, an extensive survey was performed by Fuchs and colleagues to search for interstellar trans-ethyl methyl ether, $C_2H_5OCH_3$, toward several high mass HMCs [57]. This work was motivated by the previously reported observation of a single tEME transition towards Orion KL and W51 e1/e2 ([25]). As a result of their survey, a detection of tEME was claimed toward the high mass star forming region W51 e2.

This would make tEME the fourth largest molecule to be detected in the interstellar medium (ISM). The three molecules larger than tEME, $HC_{11}N$, C_{60}, and C_{70}, posses symmetry that greatly facilitates their detection. However, tEME lacks such symmetry. Determination of the tEME abundance therefore has important implications for the limits of chemical complexity and detection in the ISM. Additionally, tEME is believed to be produced by the same chemical reactions, summarized in Equation 1, that produce dimethyl ether, a molecule detected in numerous environments in the ISM [1]. Therefore, tEME is the next logical progression in ether synthesis from

[1] R = CH_3 for dimethyl ether formation and CH_3CH_2 for tEME

dimethyl ether. If confirmed, the detection of tEME would represent a significant advance in our understanding of complex molecule formation.

$$\begin{aligned} \mathrm{ROH} + \mathrm{H_3^+} &\rightarrow \mathrm{ROH_2^+} + \mathrm{H_2} \\ \mathrm{ROH_2^+} + \mathrm{CH_3OH} &\rightarrow \mathrm{CH_3ORH^+} + \mathrm{H_2O} \\ \mathrm{CH_3ORH^+} + e^- &\rightarrow \mathrm{CH_3OR} + \mathrm{H} \end{aligned} \tag{1}$$

In this work, we attempted and failed to confirm the detection of tEME toward W51 e1/e2 using the 12 m Telescope of the Arizona Radio Observatory (ARO) in the 2 mm and 3 mm atmospheric windows, and further report on an extensive search for this species toward the high mass star forming region Sgr B2(N-LMH) with the GBT. We additionally reanalyzed the original detection in the context of the [137] criteria and show that the reported column density and temperature of [57] are not reproducible based on their observations. Furthermore, no transitions of tEME were conclusively observed toward either W51 e1/e2 or Sgr B2(N-LMH) in the present ARO and GBT data. Our work therefore calls into question the initial detection of tEME toward W51 e1/e2.

6.2 Observations

The observations using the ARO 12 m telescope, located on Kitt Peak, were conducted during the period of October 2006 to April 2007. The receivers used were dual-channel, cooled SIS mixers, operated in single-sideband mode with at least 20 dB of image rejection. The back ends used were (1) 256-channel filter banks with 500 kHz and 1 MHz resolution, and (2) a millimeter autocorrelator in the 390.5 kHz resolution mode. All spectrometers were configured in parallel mode to accommodate both receiver channels. The temperature scale, T_R^* , was determined by the chopper-wheel method, corrected for forward spillover losses. Conversion to radiation temperature T_R is then $T_R = T_R^*/\eta_c$, where η_c is the corrected beam efficiency. Twelve new transitions of tEME covering the range 91 GHz to 168 GHz were studied; over this frequency range, the beam size was 73″ to 38″ and the beam efficiency varied from 0.9 to 0.7. A comparison of the present observations and those from [57] is given in Figure 6.1. A key concern is that the larger beam size of the ARO 12 m telescope may result in beam dilution of potential tEME flux. To assess this possibility, observational frequencies were chosen to partially overlap with those from [57]. From Figure 6.1, it is likely that both observations sample

similar regions, however, the 12 m ARO beam weights more heavily to larger spatial scales than does the IRAM 30 m. The fact that the feature at 150845 MHz attributed by [57] to the $20_{0,20}$ - $19_{1,19}$ transition of tEME is slightly stronger in the ARO data indicates a non-compact source size. The complete observations from the ARO 12 m are shown in Figure 6.2 and 6.3.

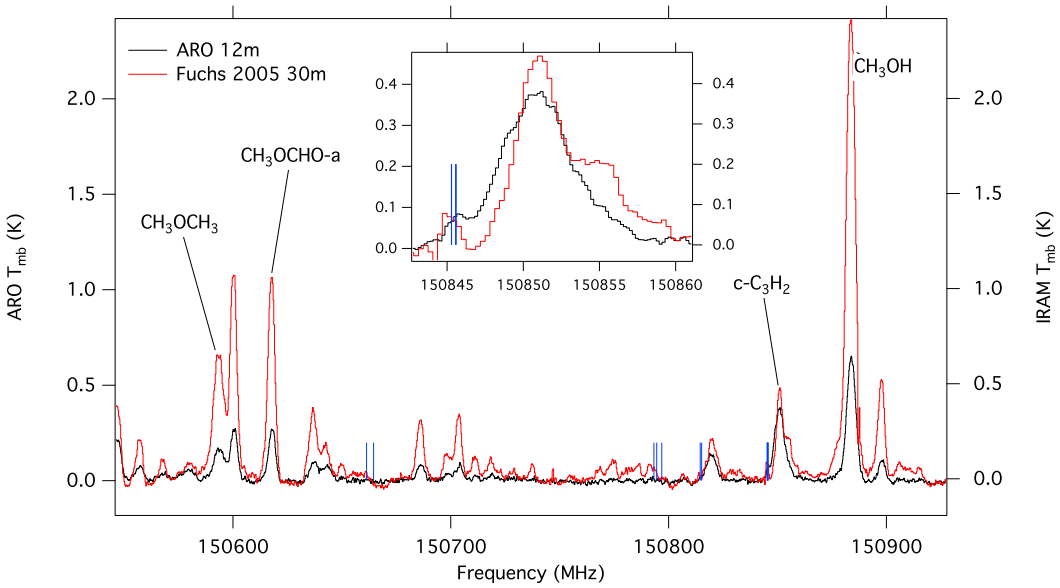

Figure 6.1. A comparison of the previous IRAM 30 m data and the current ARO 12 m data. All tEME transition frequencies are noted as blue vertical lines of uniform height. The inset shows the tEME $20_{0,20} - 19_{1,19}$ transition multiplet. ARO data is converted to T_{mb} assuming the 5″ source size of [57] and η_m = 0.75.

The observations of Sgr B2 (N) were taken using the National Radio Astronomy Observatory (NRAO) Robert C. Byrd 100 m Green Bank Telescope as part of the **PR**ebiotic **I**nterstellar **MO**lecular **S**urvey (PRIMOS). Observations began in 2008, and are continually updated.[2] These observations provide nearly continuous high-sensitivity, high-resolution data from 1 GHz to 50 GHz of the Sgr B2(N-LMH) region (α[J2000] = $17^h47^m19.8^s$, δ[J2000] = -28°22′17″). A complete description of the PRIMOS observations can be found in [108]. Two tEME transitions at 25.3 GHz and 30.5 GHz were fortuitously covered while searching for other molecules; the telescope beamwidths were ∼30″ and ∼25″ , with corresponding beam efficiencies of 0.7 and 0.6, at those frequencies, respectively.

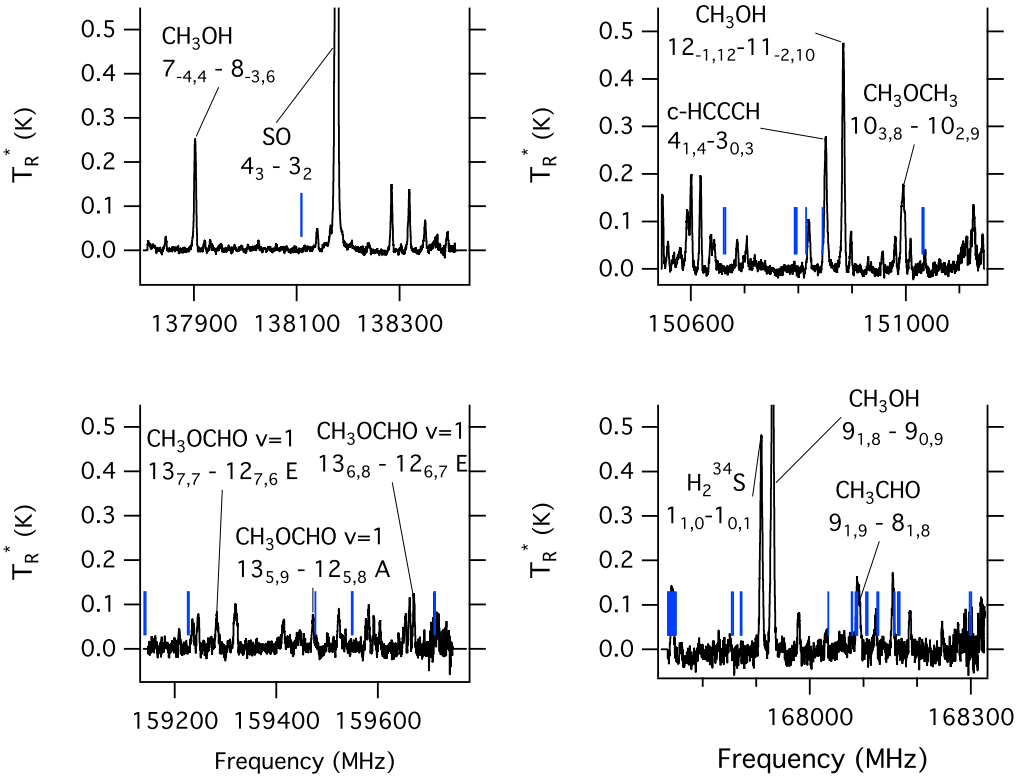

Figure 6.2. The 2 mm spectral coverage of the ARO observations toward W51 e1/e2. Frequencies are given assuming an LSR velocity of 55 km/s. Molecular transitions are labeled for context. tEME transitions are marked by vertical blue lines of uniform height.

6.3 Results and Discussion

Analysis of Previous tEME Observations

Following the criteria of [137], we begin by attempting to verify the previously-reported detection of tEME toward W51 e2. We first consider the possibility that tEME is not well described by an LTE model. While experimental collisional cross-sections are not available, a rough collisional cross section based on molecular geometry and Van der Waals radii gives critical densities of order $\sim 10^3$ - 10^4 cm^{-3}. Reported densities toward W51 e2 are 10^3 - 10^7 cm^{-3} [132, 151], suggesting that tEME transitions should be well described by an LTE approximation. This is supported by the observation that emission from many large species toward W51 is well described by LTE [87]. We therefore conclude that an LTE model is appropriate.

A simple first test is to compare the expected local thermodynamic equilibrium

[2]The PRIMOS data set is available at <http://www.cv.nrao.edu/~aremijan/PRIMOS/>

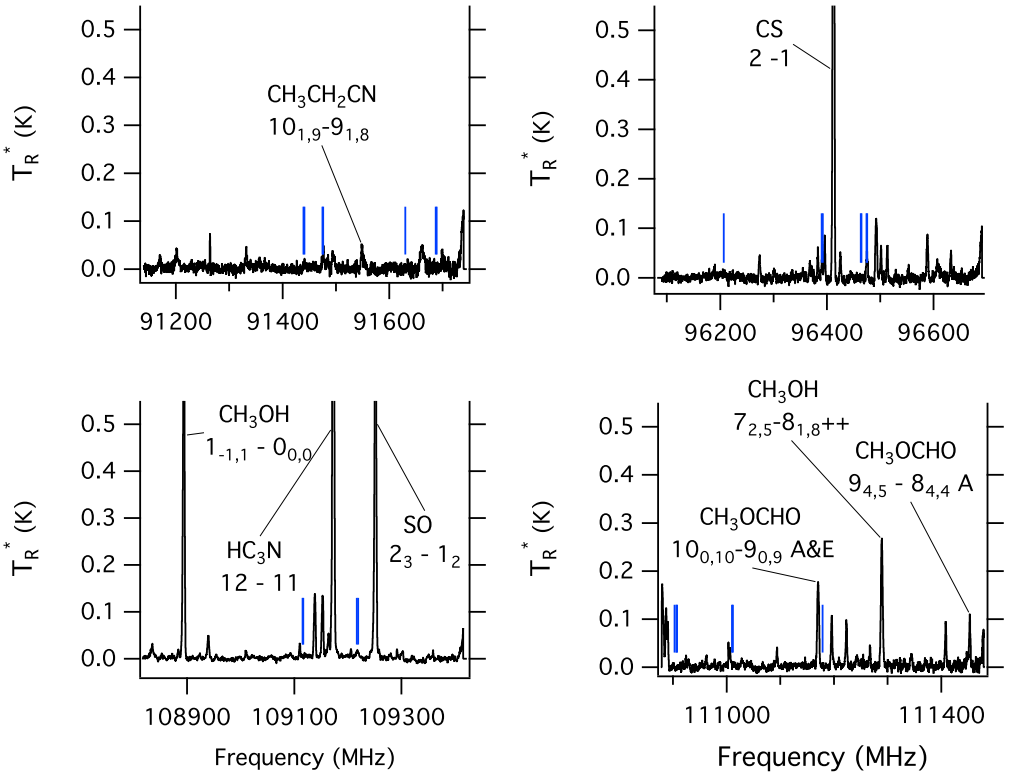

Figure 6.3. The 3 mm spectral coverage of the ARO observations toward W51 e1/e2. Frequencies are given assuming an LSR velocity of 55 km/s. Molecular transitions are labeled for context. tEME transitions are marked by vertical blue lines of uniform height.

(LTE) antenna temperatures with the reported intensity of tEME transitions. From [122], the LTE antenna temperature is related to column density and temperature by Equation 2, where E_U is the upper state energy of the transition (K), Q_r is the rotational partition function, ν is the transition frequency (MHz), S is the line strength, μ is the dipole moment of the molecule (Debye), $\Delta T_{mb}\Delta V$ is the peak observed intensity (mK) times the full width half max (FWHM) of the line (km s^{-1}), B is the beam dilution factor, Θ_S is the source size, Θ_B is the beam size, and η_B is the beam efficiency of the telescope at ν. That is,

$$N_T = (1.8\times10^{14})\frac{Q_r e^{\frac{E_u}{T_{ex}}}}{\mathrm{B}\nu S\mu^2}\times\frac{\Delta T_{mb}\Delta V}{\eta_B\left(1-\frac{e^{\frac{(4.8\times10^{-5})\nu}{T_{ex}}}-1}{e^{\frac{(4.8\times10^{-5})\nu}{T_{bg}}}-1}\right)},\quad B=\frac{\Theta_S^2}{\Theta_B^2+\Theta_S^2} \tag{6.1}$$

The transition strengths, frequencies, and upper state energies, as well as the ro-

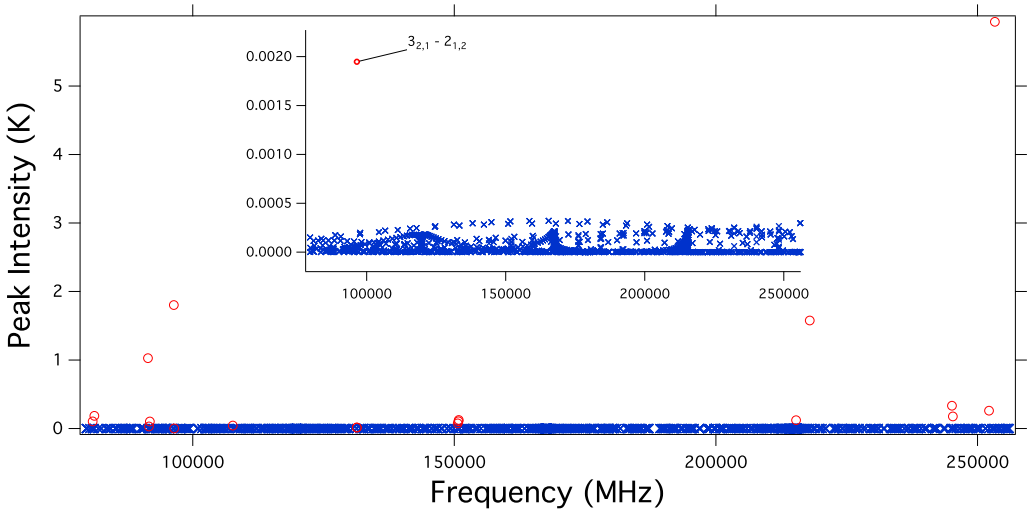

Figure 6.4. The computed LTE peak antenna temperature of individual tEME transitions. The antenna temperature is based on Equation 6.1 assuming a column density of $2{\times}10^{14}$ cm^{-2}, velocity width of 3 km s^{-1}, and an excitation temperature of 70 K (Blue) plotted with the reported peak antenna temperature from [57] (Red). An enlarged view showing the weakest reported transition from [57] is shown in the inset.

tational partition function (Q = 2027.617 $\times$ T$^{3/2}$) and dipole moment (μ_a = 0.146 D & μ_b = 1.165 D) are taken from [58]. While the assumed velocity width is not explicitly given, from Figure 4 of [57] a FWHM of 1.4 MHz at 150.8 GHz, or 2.7 km s^{-1}, may be inferred, in good agreement with previous observations toward W51 e2 [e.g. 123]. Using the reported column density of $2{\times}10^{14}$ cm^{-2} and a rotational temperature of 70 K from [57], as well as a velocity width of 3 km s^{-1}, η_B = 1, a beam filling factor of B = 1, and background temperature of T$_{bg}$ = 2.7 K, the peak intensity values are calculated in the T$_{mb}$ scale using Equation 2 and plotted (blue crosses) against their corresponding observed values (red circles) from [57] in Figure 6.4. The complete list of parameters used and calculated integrated intensities is given in Table 6.1.

It is immediately apparent that the reported transitions from [57] do not match their predicted values. Indeed, *every reported transition should have a peak intensity at least an order of magnitude less than its reported value*. As shown in Table 6.1, the discrepancy is 2 - 4 orders of magnitude for most transitions. In order to be considered valid, the observed intensity of all transitions should match their predicted values, in accordance with criteria 3 from [137]. Accounting for the possibility that the five tEME spin components are blended into a single peak, the

greatest peak intensity observed at the column density and temperature reported by [57] would be the $20_{0,20} - 19_{1,19}$ transition with a peak intensity of 1.4 mK, well below the previously reported intensity of [57] as well as the RMS of both the present and previous observations. Reexamining the data as a whole, we performed an iterative least-squares fit of the data used in Fit II of [57] used to determine the reported column density. This yields a best fit column density of $6{\times}10^{16}$ cm^{-2}. We therefore conclude that the column density of $2{\times}10^{14}$ cm^{-2} derived by [57] is not valid.

A probable explanation for the reported transitions from [57] is interference from coincident transitions of other species. W51 e1/e2 is a rich molecular source and from the present observations of W51 e1/e2, on average there is a transition with peak intensity $\geq$ 25 mK every 6.3 MHz and a transition with peak intensity $\geq$ 15 mK every 3.2 MHz. For transitions near the noise level, this means that there is a strong probability that there will be a coincident transition within twice the FWHM that may be falsely attributed to the new molecule. [57] note that of their observed transitions, only two are free of any interfering transitions. This however is based only on comparison with previously detected species and does not account for the possibility of interference from previously unidentified transitions.

Examining the reported transition frequencies, the difference in the observed and laboratory frequencies varies from -2.0 MHz to 1.46 MHz with a root mean squared value of 926 kHz and a standard deviation of 896 kHz. As these values span a wide range of positive and negative velocity offsets, this cannot be attributed to a systematic difference in the velocity of a single carrier relative to the reported LSR velocity of W51 e2. The laboratory measurements from [58] have uncertainties on the order of tens of kHz, thus this also cannot be attributed to uncertainty in the laboratory frequencies. A possible explanation is low spectral resolution. The previously reported astronomical observations have a resolution that varies from 0.3 MHz to 1.25 MHz. Many of the observed transitions have an observed minus calculated value at or below some or all of these spectral resolutions however, because the resolution of the individual spectra used to calculate these values is not specified, it is impossible to evaluate this possibility for many transitions. It can however be noted that four ($\sim$ 21 %) of the transitions have an observed frequency that differs from its laboratory measurement by $\geq$ 1.25 MHz and are therefore likely not associated with tEME emission.

Analysis of ARO Observations

An alternative approach is to examine all tEME transitions covered by the present ARO observations. As a starting point, we assume a column density of 1.3×10^{16} cm^{-2} such that the emission at the $20_{0,20} - 19_{1,19}$ tEME transition is reproduced for an excitation temperature of 70 K. A simulation can be made of the resulting tEME line intensities, as shown in Figure 6.5. It is clear in this modeling that several transitions with predicted peak intensities well above the RMS of the observations are clearly absent. To satisfy criteria 4 of [137], there should be no absent transitions. In fact, an excitation temperature of 70 K cannot satisfy this criteria unless the column density is sufficiently low that all observed transitions have peak intensities below the RMS of the observations. Considering other excitation temperatures (10 K - 300 K) and column densities (1×10^{12} cm^{-2} - 1×10^{16} cm^{-2}) does not improve the situation. It becomes apparent that, in order not to have “missing" lines, the tEME column density must be sufficiently low enough that all observed transitions are below the RMS of the observations from [57] as well as the present observations, and thus not detectable in either observation.

An additional concern is the effect of beam dilution. Fuchs et al. assume a source size of $5''$. At 145 GHz, the ARO beam is $\sim 43''$, corresponding to a beam dilution factor 6.67 times higher than that of the IRAM 30 m at the same frequency. If this source size is correct, the present ARO observations would be up to a factor of 6.67 less sensitive. However, examining the only transition covered by both observatories, the $20_{0,20} - 19_{1,19}$ tEME transition and 150845 MHz (Figure 6.1), after comparing both ARO and IRAM 30 m observations in the T_{mb} scale, assuming a $5''$ source size, it is clear that the flux observed at this frequency does not decrease when observed with a larger beam, indicating that it cannot arise from a compact source. Therefore a beam dilution factor of 6.67 cannot apply. Furthermore, the column density from Fit II of [57] would still produce transitions clearly visible in the ARO observations.

With no reliably identified tEME transitions, we determine an upper limit to the column density towards W51 e1/e2 using the current observations. As dimethyl ether and tEME are thought to form from similar processes, it is plausible to assume that they should have similar excitation conditions in a source. From [87], the derived rotational temperature of dimethyl ether towards W51 e1/e2 is 85 K. The strongest tEME transition in the current observations at 85 K that has no obvious interfering transitions is the $12_{0,12} - 11_{0,11}$ transition. This transition is not detected,

Table 6.1. Observed and calculated intensity of tEME Transitions.

Transition $J'_{K_a,K_c} - J''_{K_a,K_c}$	ν (MHz)	S_{ij}	E_u (K)	N_{Lines}	Observed $\int T_{mb}d\nu$ K km s^{-1}	Calculated $\int T_{mb}d\nu$ K km s$^{-1}\times10^3$
$11_{2,10} - 11_{1,11}$	80881.71 - 80883.6	5.195	30.1	5	0.09	0.3695
$24_{1,23} - 24_{0,24}$	81198.23 - 81199.22	10.268	118.5	5	0.16	0.2073
$35_{3,32} - 35_{2,33}$	91439.39 - 91441.26	27.608	255.2	5	1.0	0.0891
$34_{2,32} - 34_{1,33}$	91630.26 - 91631.17	21.850	237.1	5	0.03	0.09149
$37_{3,34} - 37_{2,35}$	91811.70 - 91813.40	29.637	283.7	5	0.1	0.06386
$29_{3,26} - 29_{2,27}$	96390.20 - 96392.55	20.487	179.1	5	1.85	0.2067
$3_{2,1} - 2_{1,2}$	96463.73 - 96464.85	1.545 - 1.639	6.9	5	0.002	0.1936[3]
$22_{3,19} - 22_{2,20}$	107655.40 - 107658.06	13.199	108.3	5	0.05	0.4089
$7_{2,5} - 6_{1,6}$	131349.80 - 131351.62	2.306	15.4	5	0.02	0.3284
$15_{1,15} - 14_{0,4}$	131372.62 - 131373.11	9.858	46.7	5	0.02	0.8986
$34_{4,30} - 34_{3,31}$	150661.35 - 150664.55	20.064	248.7	5	0.12	0.1170
$13_{6,x} - 14_{5,y}$[4]	150793.24 - 150797.40	1.289	76.6	10	0.17	0.088
$20_{0,20} - 19_{1,19}$	150845.28 - 150845.58	14.283	80.4	5	0.20	0.9231
$19_{5,z} - 19_{4,15}$[5]	215324.99 - 215327.56	3.487 - 9.519	102.2	6	0.28	0.6436[6]
$28_{0,28} - 27_{1,27}$	217940.65 - 217940.76	22.586	154.7	5	3.66	0.7299
$16_{3,14} - 15_{2,13}$	245103.55 - 245106.43	4.994	62.9	5	0.46	0.6735
$31_{1,31} - 30_{0,30}$	245274.09 - 245274.22	25.712	188.8	5	0.87	0.5748
$17_{3,15} - 16_{2,14}$	252188.29 - 252191.14	5.191	69.5	5	0.70	0.6556
$28_{2,27} - 27_{1,26}$	253307.71 - 253308.94	12.415	161.0	5	16.01	0.4264
$4_{1,3} - 4_{0,4}$[7]	25335.53 - 25336.17	4.386	5.1	5		
$9_{1,8} - 9_{0,9}$	30561.87 - 30562.54	8.335	18.2	5		

Observed integrated intensities are taken from [57]

Computed integrated intensities are for a single transition. The maximum observable integrated intensity can be obtained by $\int T_{mb}d\nu_{max} = \int T_{mb}d\nu \times N_{Lines}$

x-y deontes 7-9, 7-10, 8-9, or 8-10.

z denotes either 14 or 15.

Computed using the average value of S_{ij}

Parameters used to derive upper limits for PRIMOS data

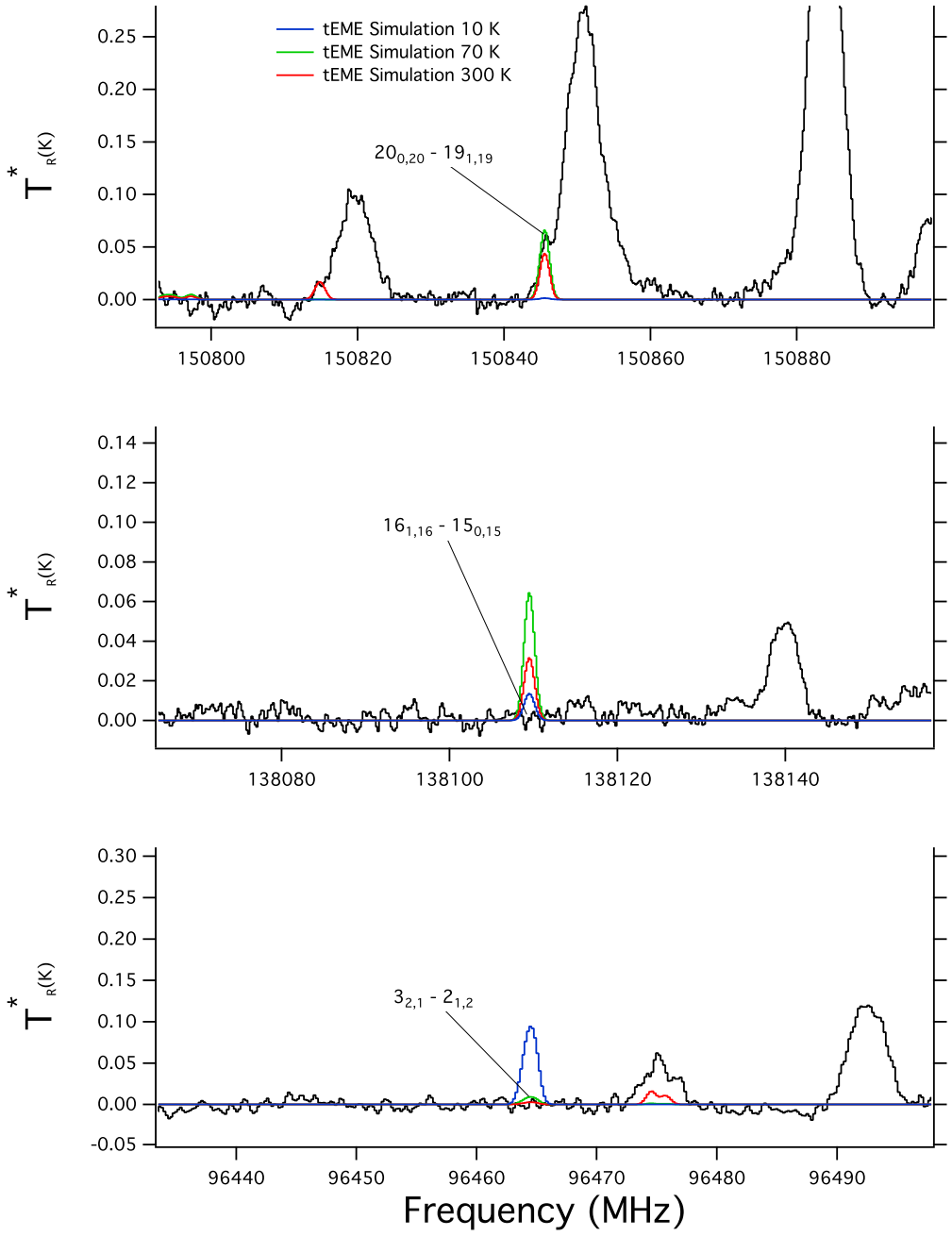

Figure 6.5. 200 km s^{-1} windows of the ARO observations of potential tEME transitions toward W51 e1/e2 (Black). A simulation of tEME at 10 K (Blue) 150 K (Green) and 300 K (Red), assuming ΔV = 3 km s^{-1}, η_B = 1, B = 1, N_T is the best fit column density derived for each temperature. Clearly the $3_{2,1}$ - $2_{1,2}$ and $16_{1,16}$ - $15_{0,15}$ are inconsistent with the $20_{0,20}$ – $19_{1,19}$ transition.

but the RMS at this frequency can be used to determine an upper limit. Using Equation 2 and a velocity width of 3 km s^{-1}, an upper limit of $\leq 1\times10^{15}$ cm^{-2}

can be derived for tEME, assuming all five components are blended into a single transition.

Finally we assess the possibility of detecting tEME in Sagittarius B2 (N-LMH). Using data from the PRIMOS project toward Sgr B2 (N-LMH), we have searched for possible tEME transitions. Several peaks coincident with tEME transitions were located, however several tEME transitions of similar predicted intensity show no emission, indicating that these features are simply coincidental. We therefore use the RMS at the strongest predicted transition to set an upper limit. Molecules detected toward Sgr B2 (N-LMH) show a wide range of excitation temperatures. No tEME transitions are detected, making it impossible to determine an excitation temperature. We therefore compute the upper limit at 10 K and 85 K. At 10 K, the strongest transition with no interfering features is the $4_{1,3} - 4_{0,4}$ transition, while at 85 K the strongest feature would be the $9_{1,8} - 9_{0,9}$ transition. The RMS at each transition frequency in the PRIMOS data is 4.5 mK and 11 mK, respectively. Using Equation 6.1 and assuming a beam efficiency of 0.8, the molecular parameters given in Table 6.1, and a velocity width of 13 km s^{-1}, the upper limits for the column density of tEME towards Sgr B2 (N-LMH) are $\leq 2.1 \times 10^{15}$ cm^{-2} and $\leq 1.7 \times 10^{16}$ cm^{-2}, respectively.

6.4 Conclusions

Rigorous application of the criteria for detection of a new molecule as outlined in [137] has again been applied to a claimed detection. As in the case of dihydroxyacetone [4] and glycine [137], these criteria underline the need for a thorough analysis when evaluating the possible detection of new molecules. In the present case, analysis of the previously reported detection of tEME ([57]) calls into question the original detection. Both the LSR velocities and LTE intensities reported in [57] are shown to be inconsistent with the reported column density and temperature, casting doubt on the claimed detection of tEME. Based on previous observations of W51 e1/e2, we instead derive an upper limit five times higher than the previously reported value. We also derive similar upper limits toward Sgr B2 (N-LMH).

BIBLIOGRAPHY

Abbott, Benjamin P et al. (2016). "Observation of gravitational waves from a binary black hole merger". In: *Physical review letters* 116.6, p. 061102.

Adams, Walter S (1948). "The Gaseous Clouds of Interstellar Space". In: *Publications of the Astronomical Society of the Pacific* 60.354, pp. 174–189.

Allamandola, LJ, AGGM Tielens, and JRz Barker (1985). "Polycyclic aromatic hydrocarbons and the unidentified infrared emission bands-Auto exhaust along the Milky Way". In: *The Astrophysical Journal* 290, pp. L25–L28.

Apponi, A. J. et al. (2006). "Investigating the Limits of Chemical Complexity in Sagittarius B2(N): A Rigorous Attempt to Confirm 1,3-Dihydroxyacetone". In: *The Astrophysical Journal Letters* 643, pp. L29–L32. DOI: 10.1086/504979.

Bailey, J et al. (1998). "Circular polarization in star- formation regions: implications for biomolecular homochirality". In: *Science* 281.5377, pp. 672–674. DOI: 10.1126/science.281.5377.672.

Balle, TJ and WH Flygare (1981). "Fabry–Perot cavity pulsed Fourier transform microwave spectrometer with a pulsed nozzle particle source". In: *Review of Scientific Instruments* 52.1, pp. 33–45.

Bally, John et al. (2015). "The Orion fingers: Near-IR adaptive optics imaging of an explosive protostellar outflow". In: *Astronomy & Astrophysics* 579, A130.

Barker, James F and Peter Fritz (1981). "Carbon isotope fractionation during microbial methane oxidation". In: *Nature* 293.5830, pp. 289–291.

Bass, Michael et al. (2010). *Handbook of Optics, Third Edition Volume I: Geometrical and Physical Optics, Polarized Light, Components and Instruments(Set)*. 3rd ed. New York, NY, USA: McGraw-Hill, Inc. ISBN: 0071498893, 9780071498890.

Belloche, Arnaud et al. (2014). "Detection of a branched alkyl molecule in the interstellar medium: iso-propyl cyanide". In: *Science* 345.6204, pp. 1584–1587.

Belloche, A. et al. (2008). "Erratum: Detection of amino acetonitrile in Sgr B2(N)". In: *Astronomy and Astrophysics* 492, pp. 769–773. DOI: 10.1051/0004-6361:20079203e.

Belloche, A. et al. (2013). "Complex organic molecules in the interstellar medium: IRAM 30 m line survey of Sagittarius B2(N) and (M)". In: *Astronomy and Astrophysics* 559, A47, A47. DOI: 10.1051/0004-6361/201321096. arXiv: 1308.5062.

Bernath, Peter F (2015). *Spectra of atoms and molecules*. Oxford university press.

Beuther, H et al. (2005). "Line Imaging of Orion KL at 865 μm with the Submillimeter Array". In: *The Astrophysical Journal* 632.1, p. 355.

Blake, Geoffrey A et al. (1987). “Molecular abundances in OMC-1-The chemical composition of interstellar molecular clouds and the influence of massive star formation”. In: *The Astrophysical Journal* 315, pp. 621–645.

Blythe, JH (1957). “A new type of pencil beam aerial for radio astronomy”. In: *Monthly Notices of the Royal Astronomical Society* 117.6, pp. 644–651.

Bocquet, R et al. (1988). “The submillimeter-wave rotational spectrum of methyl cyanide: Analysis of the ground and the low-lying excited vibrational states”. In: *Journal of Molecular Spectroscopy* 127.2, pp. 382–389.

Boonman, AMS et al. (2001). “Highly abundant HCN in the inner hot envelope of GL 2591: probing the birth of a hot core?” In: *The Astrophysical Journal Letters* 553.1, p. L63.

Brown, Gordon G et al. (2008). “A broadband Fourier transform microwave spectrometer based on chirped pulse excitation”. In: *Review of Scientific Instruments* 79.5, p. 053103.

Cameron, AGW et al. (1995). “Massive supernovae, Orion gamma rays, and the formation of the solar system”. In: *The Astrophysical Journal Letters* 447.1, p. L53.

Carroll, P. B., B. J. Drouin, and S. L. Widicus Weaver (2010). “The Submillimeter Spectrum of Glycolaldehyde”. In: *The Astrophysical Journal* 723, pp. 845–849. DOI: 10.1088/0004-637X/723/1/845.

Carroll, P Brandon et al. (2013). “The pure rotational spectrum of glycolaldehyde isotopologues observed in natural abundance”. In: *Journal of Molecular Spectroscopy* 284, pp. 21–28.

Caselli, P, TI Hasegawa, and Eric Herbst (1993). “Chemical differentiation between star-forming regions-The Orion hot core and compact ridge”. In: *The Astrophysical Journal* 408, pp. 548–558.

Changala, P Bryan et al. (2016). “Sensitivity and resolution in frequency comb spectroscopy of buffer gas cooled polyatomic molecules”. In: *Applied Physics B* 122.12, p. 292.

Charnley, S. B., P. Ehrenfreund, and Y.-J. Kuan (2001). “Spectroscopic diagnostics of organic chemistry in the protostellar environment”. In: *Spectrochimica Acta* 57, pp. 685–704.

Chyba, C F et al. (1990). “Cometary delivery of organic molecules to the early Earth.” In: *Science* 249.4, pp. 366–373. DOI: 10.1126/science.11538074.

Chyba, Christopher and Carl Sagan (1992). “Endogenous production, exogenous delivery and impact-shock synthesis of organic molecules: an inventory for the origins of life”. In: *Nature* 355.6356, p. 125.

Cleeton, Claud Edwin and Neil Hooker Williams (1934). "Electromagnetic waves of 1.1 cm wave-length and the absorption spectrum of ammonia". In: *Physical Review* 45.4, p. 234.

Cleeves, L Ilsedore et al. (2014a). "The ancient heritage of water ice in the solar system". In: *Science* 345.6204, pp. 1590–1593.

Cleeves, L Ilsedore et al. (2014b). "The ancient heritage of water ice in the solar system". In: *Science* 345.6204, pp. 1590–1593. DOI: 10.1126/science.1258055.

Crockett, Nathan R et al. (2014a). "Herschel observations of extraordinary sources: Analysis of the HIFI 1.2 THz wide spectral survey toward Orion KL. I. Methods". In: *The Astrophysical Journal* 787.2, p. 112. DOI: 10.1088/0004-637X/787/2/112.

Crockett, Nathan R et al. (2014b). "Herschel observations of extraordinary sources: Analysis of the HIFI 1.2 THz wide spectral survey toward Orion KL. I. Methods". In: *The Astrophysical Journal* 787.2, p. 112.

Crockett, Nathan R et al. (2015). "HERSCHEL OBSERVATIONS OF EXTRAORDINARY SOURCES: ANALYSIS OF THE HIFI 1.2 THz WIDE SPECTRAL SURVEY TOWARD ORION KL II. CHEMICAL IMPLICATIONS". In: *The Astrophysical Journal* 806.2, p. 239.

Crockett, NR et al. (2010). "Herschel observations of EXtra-Ordinary Sources (HEXOS): The Terahertz spectrum of Orion KL seen at high spectral resolution". In: *Astronomy & Astrophysics* 521, p. L21.

Crutcher, R. M. et al. (1996). "H i Zeeman Measurements of the Magnetic Field in Sagittarius B2". In: *The Astrophysical Journal Letters* 462, p. L79. DOI: 10.1086/310031.

Cunningham, M R et al. (2007). "A search for propylene oxide and glycine in Sagittarius B2 (LMH) and Orion". In: *Monthly Notices of the Royal Astronomical Society* 376.3, pp. 1201–1210. DOI: 10.1111/j.1365-2966.2007.11504.x.

De Buizer, James M et al. (2012). "FIRST SCIENCE OBSERVATIONS WITH SOFIA/FORCAST: 6-37 μm IMAGING OF ORION BN/KL". In: *The Astrophysical Journal Letters* 749.2, p. L23.

De Vicente, P et al. (2002). "On the heating source of the Orion KL hot core". In: *The Astrophysical Journal Letters* 574.2, p. L163.

Desiraju, Gautam R and Thomas Steiner (2001). *The weak hydrogen bond: in structural chemistry and biology*. Vol. 9. International Union of Crystal.

Dickens, J E et al. (1997). "Detection of Interstellar Ethylene Oxide (c-C2H4O)". In: *The Astrophysical Journal* 489.2, pp. 753–757.

Draine, B. T. (2011). *Physics of the Interstellar and Intergalactic Medium*.

Draine, Bruce T (2010). *Physics of the interstellar and intergalactic medium*. Princeton University Press.

Dreiling, J M and T J Gay (2014). "Chirally Sensitive Electron-Induced Molecular Breakup and the Vester-Ulbricht Hypothesis". In: *Physical Review Letters* 113.11, pp. 118103–5. DOI: 10.1103/PhysRevLett.113.118103.

Drouin, Brian J et al. (2009). "High resolution spectroscopy of 12CH3D and 13CH3D". In: *Journal of Quantitative Spectroscopy and Radiative Transfer* 110.18, pp. 2077–2081.

Dyke, Thomas R and JS Muenter (1974). "Microwave spectrum and structure of hydrogen bonded water dimer". In: *The Journal of Chemical Physics* 60.7, pp. 2929–2930.

Eiler, John M (2007). "?Clumped-isotope? geochemistry?The study of naturally-occurring, multiply-substituted isotopologues". In: *Earth and Planetary Science Letters* 262.3, pp. 309–327.

Engel, Michael H and S A Macko (1997). "Isotopic evidence for extraterrestrial non-racemic amino acids in the Murchison meteorite". In: *Nature* 389.6648, pp. 265–268. DOI: 10.1038/38460.

Evangelisti, Luca et al. (2017). "Conformational equilibrium and internal dynamics in the iso-propanol–water dimer". In: *Physical Chemistry Chemical Physics* 19.1, pp. 568–573.

Favre, C et al. (2011). "HCOOCH3 as a probe of temperature and structure in Orion-KL". In: *Astronomy & Astrophysics* 532, A32.

Finneran, Ian A et al. (2013a). "A direct digital synthesis chirped pulse Fourier transform microwave spectrometer". In: *Review of Scientific Instruments* 84.8, p. 083104.

Finneran, Ian A et al. (2013b). "A direct digital synthesis chirped pulse Fourier transform microwave spectrometer". In: *Review of Scientific Instruments* 84.8, p. 3104. DOI: 10.1063/1.4818137.

Finneran, Ian A et al. (2015). "Hydrogen bonding in the ethanol–water dimer". In: *Physical Chemistry Chemical Physics* 17.37, pp. 24210–24214.

Finneran, Ian A et al. (2016). "Hydrogen bond competition in the ethanol–methanol dimer". In: *Physical Chemistry Chemical Physics* 18.32, pp. 22565–22572.

Foing, BH and P Ehrenfreund (1994). "Detection of two interstellar absorption bands coincident with spectral features of C60+". In: *Nature* 369.6478, pp. 296–298.

Friedel, DN and SL Widicus Weaver (2012). "Complex Organic Molecules at High Spatial Resolution toward ORION-KL. II. Kinematics". In: *The Astrophysical Journal Supplement Series* 201.2, p. 17.

Frisch, M. J. et al. (2016). *Gaussian 09 Software*. Gaussian.

Fuchs, G. W. et al. (2005). “Trans-ethyl methyl ether in space. A new look at a complex molecule in selected hot core regions”. In: *Astronomy and Astrophysics* 444, pp. 521–530. DOI: 10.1051/0004-6361:20053599. eprint: arXiv:astro-ph/0508395.

Fuchs, U. et al. (2003). “trans-Ethyl Methyl Ether: Assignments and Predictions up to 400 GHz for the Vibrational-Torsional Ground State”. In: *The Astrophysical Journal Supplement* 144, pp. 277–286. DOI: 10.1086/345100.

Gangemi, Francis A (1963). “Effect of Isotopic Substitution on the Dipole Moment of Molecules of Symmetrical Configuration”. In: *The Journal of Chemical Physics* 39.12, pp. 3490–3496.

Garrod, Robin T, Susanna L Widicus Weaver, and Eric Herbst (2008). “Complex chemistry in star-forming regions: An expanded gas-grain warm-up chemical model”. In: *The Astrophysical Journal* 682.1, p. 283.

Ghosh, Prosenjit et al. (2006). “13 C–18 O bonds in carbonate minerals: A new kind of paleothermometer”. In: *Geochimica et Cosmochimica Acta* 70.6, pp. 1439–1456.

Glavin, Daniel P and Jason P Dworkin (2009). “Enrichment of the amino acid L-isovaline by aqueous alteration on CI and CM meteorite parent bodies.” In: *Proceedings of the National Academy of Sciences of the United States of America* 106.14, pp. 5487–5492. DOI: 10.1073/pnas.0811618106.

Goddi, C et al. (2011). “Unveiling sources of heating in the vicinity of the orion BN/KL hot core as traced by highly excited inversion transitions of ammonia”. In: *The Astrophysical Journal Letters* 739.1, p. L13.

Goesmann, F. et al. (2015). “Organic compounds on comet 67P/Churyumov-Gerasimenko revealed by COSAC mass spectrometry”. In: *Science* 349.2. DOI: 10.1126/science.aab0689.

Goldreich, P. and N. D. Kylafis (1981). “On mapping the magnetic field direction in molecular clouds by polarization measurements”. In: *The Astrophysical Journal Letters* 243, pp. L75–L78. DOI: 10.1086/183446.

Gordy, Walter (1983). “Early events and some later developments in microwave spectroscopy”. In: *Journal of Molecular Structure* 97, pp. 17–32.

Gordy, Walter and R L Cook (1984a). *Microwave Molecular Spectra*. 3rd ed. New York: Wiley.

Gordy, Walter and Robert L Cook (1984b). *Microwave Molecular Spectra*. Wiley.

Grabow, Jens-Uwe (2011). “Fourier transform microwave spectroscopy measurement and instrumentation”. In: *Handbook of High-Resolution Spectroscopy*.

Halfen, D. T. et al. (2006). “A Systematic Study of Glycolaldehyde in Sagittarius B2(N) at 2 and 3 mm: Criteria for Detecting Large Interstellar Molecules”. In: *The Astrophysical Journal* 639, pp. 237–245. DOI: 10.1086/499225.

Hamm, Peter and Martin Zanni (2011). *Concepts and Methods of 2D Infrared Spectroscopy*. Cambridge University Press.

Harrington, Howard W., John R. Hearn, and Roger F. Rauskolb (1971). "The Routine Rotational Microwave Spectrometer". In: *Hewlett-Packard Journal* 6, pp. 2–12.

Herbst, Eric and Ewine F. van Dishoeck (2009). "Complex Organic Interstellar Molecules". In: *Annual Reviews of Astronomy and Astrophysics* 47.1, pp. 427–480. DOI: 10.1146/annurev-astro-082708-101654.

Herbst, Eric and Ewine F Van Dishoeck (2009). "Complex organic interstellar molecules". In: *Annual Review of Astronomy and Astrophysics* 47, pp. 427–480.

Herschbach, Dudley R and Jerome D Swalen (1958). "Internal Barrier of Propylene Oxide from the Microwave Spectrum. II". In: *The Journal of Chemical Physics* 29.4, pp. 761–17. DOI: 10.1063/1.1744588.

Hirota, Tomoya et al. (2015). "ALMA Imaging of Millimeter/Submillimeter Continuum Emission in Orion KL". In: *The Astrophysical Journal* 801.2, p. 82.

Hollis, J. M. et al. (2002). "Interstellar Antifreeze: Ethylene Glycol". In: *The Astrophysical Journal Letters* 571, pp. L59–L62. DOI: 10.1086/341148.

Hollis, J. M. et al. (2004a). "Green Bank Telescope Detection of New Interstellar Aldehydes: Propenal and Propanal". In: *The Astrophysical Journal* 610.1, pp. L21–L24. DOI: 10.1086/423200.

Hollis, J. M. et al. (2004b). "Green Bank Telescope Detection of New Interstellar Aldehydes: Propenal and Propanal". In: *The Astrophysical Journal Letters* 610, pp. L21–L24. DOI: 10.1086/423200.

Hollis, J. M. et al. (2006). "Cyclopropenone (*c*-H_2C_3O): a new interstellar ring molecule". In: *The Astrophysical Journal* 642.2, pp. 933–939. DOI: 10.1086/501121.

Hollis, J. M. et al. (2007). "Nonthermal continuum toward Sagittarius B2 (N-LMH)". In: *The Astrophysical Journal* 660.2, p. L125. DOI: 10.1086/518124.

Hollis, Jan M et al. (2004c). "Green bank telescope observations of interstellar glycolaldehyde: low-temperature sugar". In: *The Astrophysical Journal* 613.1, p. L45. DOI: 10.1086/424927.

Hutzler, Nicholas R, Hsin-I Lu, and John M Doyle (2012). "The buffer gas beam: an intense, cold, and slow source for atoms and molecules". In: *Chemical reviews* 112.9, pp. 4803–4827.

Ikeda, M. et al. (2001). "Survey Observations of c-C_2H_4O and CH_3CHO toward Massive Star-forming Regions". In: *The Astrophysical Journal* 560, pp. 792–805. DOI: 10.1086/322957.

Jones, P A et al. (2008). "Spectral imaging of the Sagittarius B2 region in multiple 3-mm molecular lines with the Mopra telescope". In: *Monthly Notices of the Royal Astronomical Society* 386.1, pp. 117–137. DOI: 10.1111/j.1365-2966.2008.13009.x.

Kabo, GJ et al. (1995). "Thermodynamic properties, conformational composition, and phase transitions of cyclopentanol". In: *The Journal of Chemical Thermodynamics* 27.9, pp. 953–967.

Kalenskii, S. V. and L. E. B. Johansson (2010). "Spectral survey of the star-forming region W51 e1/e2 at 3 mm". In: *Astronomy Reports* 54, pp. 1084–1104. DOI: 10.1134/S1063772910120036.

Kisiel, Zbigniew et al. (2009). "The rotational spectrum of acrylonitrile up to 1.67 THz". In: *Journal of Molecular Spectroscopy* 258.1, pp. 26–34.

Kuan, Y.-J. et al. (2003). "Interstellar Glycine". In: *The Astrophysical Journal* 593, pp. 848–867. DOI: 10.1086/375637.

Ladd, Ned et al. (2013). "Beam Size, Shape and Efficiencies for the ATNF Mopra Radio Telescope at 86–115 GHz". In: *Publications of the Astronomical Society of Australia* 22.01, pp. 62–72.

Lamb, Willis E (1956). "Fine structure of the hydrogen atom". In: *Science* 123.3194, pp. 439–442.

Lamprecht, Guenther, Friedrich Pichlmayer, and Erich R Schmid (1994). "Determination of the authenticity of vanilla extracts by stable isotope ratio analysis and component analysis by HPLC". In: *Journal of agricultural and food chemistry* 42.8, pp. 1722–1727.

Lifshitz, Assa and Carmen Tamburu (1994). "Isomerization and decomposition of propylene oxide. Studies with a single-pulse shock tube". In: *The Journal of Physical Chemistry* 98.4, pp. 1161–1170. DOI: 10.1021/j100055a020.

Lockwood, Alexandra C et al. (2014). "NEAR-IR direct detection of water vapor in tau Boötis b". In: *The Astrophysical Journal Letters* 783.2, p. L29.

Loomis, R. A. et al. (2013a). "The Detection of Interstellar Ethanimine (CH_3CHNH) from Observations Taken during the GBT PRIMOS Survey". In: *The Astrophysical Journal Letters* 765, L9, p. L9. DOI: 10.1088/2041-8205/765/1/L9. arXiv: 1302.1121 [astro-ph.GA].

Loomis, Ryan A et al. (2013b). "THE DETECTION OF INTERSTELLAR ETHANIMINE (CH 3CHNH) FROM OBSERVATIONS TAKEN DURING THE GBT PRIMOS SURVEY". In: *The Astrophysical Journal* 765.1, p. L9. DOI: 10.1088/2041-8205/765/1/L9.

Loomis, Ryan A et al. (2015). "Investigating the minimum energy principle in searches for new molecular species—the case of H_2C_3O isomers". In: *The Astrophysical Journal* 799.1, pp. 34–8. DOI: 10.1088/0004-637X/799/1/34.

Lunine, Jonathan (2005). *Astrobiology: A Multi-Disciplinary Approach*. San Francisco, CA: Pearson Education Inc.

Mason, B S et al. (2009). "A LIMIT ON THE POLARIZED ANOMALOUS MICROWAVE EMISSION OF LYNDS 1622". In: *The Astrophysical Journal* 697.2, pp. 1187–1193. DOI: 10.1088/0004-637X/697/2/1187.

Materials and methods are available as supplementary materials on Science *Online*.

McCall, BJ et al. (1999). "Observations of H3+ in dense molecular clouds". In: *The Astrophysical Journal* 522.1, p. 338.

McGuire, Brett A et al. (2012). "Interstellar carbodiimide (HNCNH): a new astronomical detection from the GBT PRIMOS survey via maser emission features". In: *The Astrophysical Journal* 758.2, p. L33. DOI: 10.1088/2041-8205/758/2/L33.

McGurk, JC, TG Schmalz, and WH Flygare (1974). "Fast passage in rotational spectroscopy: Theory and experiment". In: *The Journal of Chemical Physics* 60.11, pp. 4181–4188.

Mehringer, David M et al. (1993). "Radio continuum and radio recombination line observations of Sagittarius B2". In: *Astrophysical Journal* 412, pp. 684–695. DOI: 10.1086/172954.

Menten, KM et al. (2007). "The distance to the Orion Nebula". In: *Astronomy & Astrophysics* 474.2, pp. 515–520.

Milam, SN et al. (2005). "The 12C/13C isotope gradient derived from millimeter transitions of CN: The case for galactic chemical evolution". In: *The Astrophysical Journal* 634.2, p. 1126.

Modica, Paola et al. (2014). "Enantiomeric excesses induced in amino acids by ultraviolet circularly polarized light irradiation of extraterrestrial ice analogs: a possible source of asymmetry for prebiotic chemistry". In: *The Astrophysical Journal* 788.1, pp. 79–11. DOI: 10.1088/0004-637X/788/1/79.

Neill, J. L. et al. (2012a). "Laboratory and Tentative Interstellar Detection of Trans-Methyl Formate Using the Publicly Available Green Bank Telescope Primos Survey". In: *The Astrophysical Journal* 755, 153, p. 153. DOI: 10.1088/0004-637X/755/2/153. arXiv: 1206.6021 [astro-ph.GA].

Neill, Justin L. et al. (2012b). "Laboratory and tentative interstellar detection of *trans*-methyl formate using the publicly available Green Bank Telescope PRIMOS Survey". In: *The Astrophysical Journal* 755.2, p. 153. DOI: 10.1088/0004-637X/755/2/153.

Neill, Justin L et al. (2013). "Deuterated molecules in Orion KL from Herschel/HIFI". In: *The Astrophysical Journal* 777.2, p. 85.

Ossenkopf, V and Th Henning (1994). "Dust opacities for protostellar cores". In: *Astronomy and Astrophysics* 291, pp. 943–959.

Patterson, David and John M Doyle (2012). "Cooling molecules in a cell for FTMW spectroscopy". In: *Molecular Physics* 110.15-16, pp. 1757–1766.

Piasecki, Alison et al. (2016). "Analysis of the site-specific carbon isotope composition of propane by gas source isotope ratio mass spectrometer". In: *Geochimica et Cosmochimica Acta* 188, pp. 58–72.

Pickett, HM et al. (1998). "Submillimeter, millimeter, and microwave spectral line catalog". In: *Journal of Quantitative Spectroscopy and Radiative Transfer* 60.5, pp. 883–890.

Pizzarello, Sandra and Thomas L Groy (2011). "Molecular asymmetry in extraterrestrial organic chemistry: An analytical perspective". In: *Geochimica et Cosmochimica Acta* 75.2, pp. 645–656. DOI: 10.1016/j.gca.2010.10.025.

Plambeck, RL and MCH Wright (2016). "ALMA observations of Orion Source I at 350 and 660 GHz". In: *The Astrophysical Journal* 833.2, p. 219.

Plambeck, RL et al. (2009). "Tracing the bipolar outflow from Orion Source I". In: *The Astrophysical Journal Letters* 704.1, p. L25.

Qi, Chunhua et al. (2013). "Imaging of the CO snow line in a solar nebula analog". In: *Science* 341.6146, pp. 630–632.

Rayon, Victor M and Jose A Sordo (2005). "Pseudorotation motion in tetrahydrofuran: An ab initio study". In: *The Journal of chemical physics* 122.20, p. 204303.

Reinartz, JMLJ and A Dymanus (1974). "Molecular constants of OCS isotopes in the (0110) vibrational state measured by molecular-beam electric-resonance spectroscopy". In: *Chemical Physics Letters* 24.3, pp. 346–351.

Reinhold, B, IA Finneran, and ST Shipman (2011). "Room temperature chirped-pulse Fourier transform microwave spectroscopy of anisole". In: *Journal of Molecular Spectroscopy* 270.2, pp. 89–97.

Remijan, A. J. et al. (2005). "Interstellar Isomers: The Importance of Bonding Energy Differences". In: *The Astrophysical Journal* 632, pp. 333–339. DOI: 10.1086/432908. eprint: arXiv:astro-ph/0506502.

Remijan, A. et al. (2002). "Acetic Acid in the Hot Cores of Sagitarrius B2(N) and W51". In: *The Astrophysical Journal* 576, pp. 264–273. DOI: 10.1086/341627.

Requena-Torres, M A et al. (2006). "Organic molecules in the Galactic center". In: *A&A* 455.3, pp. 971–985. DOI: 10.1051/0004-6361:20065190.

Robishaw, T., E. Quataert, and C. Heiles (2008). "Extragalactic Zeeman Detections in OH Megamasers". In: *The Astrophysical Journal* 680, 981-998, pp. 981–998. DOI: 10.1086/588031. arXiv: 0803.1832.

Robishaw, Timothy and Carl Heiles (2009). "On Measuring Accurate 21 cm Line Profiles with the Robert C. Byrd Green Bank Telescope". In: *Publications of the Astronomical Society of the Pacific* 121.877, pp. 272–294. DOI: 10.1086/597985.

Ryle, M, B Elsmore, and Ann C Neville (1965). "High-resolution observations of the radio sources in Cygnus and Cassiopeia". In: *Nature* 205.4978, pp. 1259–1262.

Salzman, WR (1998). "Circular Dichroism at Microwave Frequencies: Calculated Rotational Strengths for Transitions Up to J = 10 for Some Oxirane Derivatives." In: *Journal of Molecular Spectroscopy* 192.1, pp. 61–68. DOI: 10.1006/jmsp.1998.7677.

Schlaufman, Kevin C (2014). "Tests of in situ formation scenarios for compact multiplanet systems". In: *The Astrophysical Journal* 790.2, p. 91.

Schöier, FL et al. (2002). "Does IRAS 16293–2422 have a hot core? Chemical inventory and abundance changes in its protostellar environment". In: *Astronomy & Astrophysics* 390.3, pp. 1001–1021.

Seifert, Nathan A et al. (2015). "AUTOFIT, an automated fitting tool for broadband rotational spectra, and applications to 1-hexanal". In: *Journal of Molecular Spectroscopy* 312, pp. 13–21.

Shi, H., J.-H. Zhao, and J. L. Han (2010). "Nature of W51e2: Massive Cores at Different Phases of Star Formation". In: *The Astrophysical Journal* 710, pp. 843–852. DOI: 10.1088/0004-637X/710/1/843. arXiv: 1001.1101 [astro-ph.SR].

Shuping, RY, Mark Morris, and John Bally (2004). "A new mid-infrared map of the BN/KL region using the Keck telescope". In: *The Astronomical Journal* 128.1, p. 363.

Simon, DA and JD McQuarrie (1997). *Physical chemistry: a molecular approach*.

Singleton, Daniel A and Michael J Szymanski (1999). "Simultaneous determination of intermolecular and intramolecular 13C and 2H kinetic isotope effects at natural abundance". In: *Journal of the American Chemical Society* 121.40, pp. 9455–9456.

Snow, Theodore P and Benjamin J McCall (2006). "Diffuse atomic and molecular clouds". In: *Annu. Rev. Astron. Astrophys.* 44, pp. 367–414.

Snyder, L. E. et al. (2005a). "A Rigorous Attempt to Verify Interstellar Glycine". In: *The Astrophysical Journal* 619, pp. 914–930. DOI: 10.1086/426677. eprint: arXiv:astro-ph/0410335.

Snyder, Lewis E et al. (2002). "Confirmation of Interstellar Acetone". In: *The Astrophysical Journal* 578.1, pp. 245–255. DOI: 10.1086/342273.

Snyder, LE et al. (2005b). "A rigorous attempt to verify interstellar glycine". In: *Astrophys. J.* 619.2, pp. 914–930. DOI: 10.1086/426677.

Stockman, Paul A et al. (1997). "Microwave rotation-tunneling spectroscopy of the water–methanol dimer: Direct structural proof for the strongest bound conformation". In: *The Journal of chemical physics* 107.10, pp. 3782–3790.

Suzuki, Sakae et al. (1992). "Benzene forms hydrogen bonds with water". In: *Science* 257.5072, pp. 942–945.

Swalen, Jerome D and Dudley R Herschbach (1957). “Internal Barrier of Propylene Oxide from the Microwave Spectrum. I”. In: *The Journal of Chemical Physics* 27.1, pp. 100–10. DOI: 10.1063/1.1743645.

Townes, Charles H (1975). *Microwave Spectroscopy*. Ed. by A L Schawlow and Arthur L Schawlow. New York: Dover Publications.

Townes, Charles H and Arthur L Schawlow (2013). *Microwave spectroscopy*. Courier Corporation.

Turner, B. E. and A. J. Apponi (2001). “Microwave Detection of Interstellar Vinyl Alcohol, CH_2CHOH”. In: *The Astrophysical Journal Letters* 561, pp. L207–L210. DOI: 10.1086/324762.

Wagnière, G. H. (1999). “The magnetochiral effect and related optical phenomena”. In: *Chemical Physics* 245, pp. 165–173. DOI: 10.1016/S0301-0104(99)00023-3.

Walsh, Catherine et al. (2016). “First detection of gas-phase methanol in a protoplanetary disk”. In: *The Astrophysical Journal Letters* 823.1, p. L10.

Wang, David T et al. (2015). “Nonequilibrium clumped isotope signals in microbial methane”. In: *Science* 348.6233, pp. 428–431.

Weaver, Susanna L Widicus and Douglas N Friedel (2012). “Complex Organic Molecules at High Spatial Resolution toward ORION-KL. I. Spatial Scales”. In: *The Astrophysical Journal Supplement Series* 201.2, p. 16.

Widicus Weaver, S. L. and G. A. Blake (2005). “1,3-Dihydroxyacetone in Sagittarius B2(N-LMH): The First Interstellar Ketose”. In: *The Astrophysical Journal Letters* 624, pp. L33–L36. DOI: 10.1086/430407.

Young, L. M., E. Keto, and P. T. P. Ho (1998). “Radiative Transfer Modeling of the Accretion Flow onto a Star-forming Core in W51”. In: *The Astrophysical Journal* 507, pp. 270–280. DOI: 10.1086/306310. eprint: astro-ph/9806058.

Zaleski, D. P. et al. (2013a). “Detection of E-Cyanomethanimine toward Sagittarius B2(N) in the Green Bank Telescope PRIMOS Survey”. In: *The Astrophysical Journal Letters* 765, L10, p. L10. DOI: 10.1088/2041-8205/765/1/L10. arXiv: 1302.0909 [astro-ph.GA].

Zaleski, Daniel P. et al. (2013b). “DETECTION OF E-CYANOMETHANIMINE TOWARD SAGITTARIUS B2(N) IN THE GREEN BANK TELESCOPE PRIMOS SURVEY”. In: *The Astrophysical Journal* 765.1, p. L10. DOI: 10.1088/2041-8205/765/1/L10.

Zapata, Luis A, Johannes Schmid-Burgk, and Karl M Menten (2011). “Orion KL: the hot core that is not a ?hot core?” In: *Astronomy & Astrophysics* 529, A24.

Zinnecker, Hans and Harold W Yorke (2007). “Toward understanding massive star formation”. In: *Annu. Rev. Astron. Astrophys.* 45, pp. 481–563.

Appendix A

ARDUINO CONTROL OF THE AD9914

This is meant to be a guide to the construction and implementation of Arduino control of an AD 9914 DDS evaluation board for generation of linear frequency sweeps. This is version 1.0 and will be incorporated into a larger guide as the full chirped pulse FTMW instrument that utilizes this chirp system is completed. Further information regarding the use of the 9914 can be found in Review of Scientific Instruments (2013) 083104, **84**.

Throughout this guide, several pins/jumpers are referenced, and these are generally referenced in the AD9914 evaluation board guide/schematic. The board is generally well labeled, but the board schematic should be consulted if there is any confusion.

Important: Several critical steps in using the DDS have been omitted from this guide. We found it necessary to remove a single 0 Ω resistor from the evaluation board in order to enable the necessary external triggering of the board. The DDS should also be externally clocked, so a 4 GHz clock is required. A simple PLL is available to handle this. Please see the supplemental section of the RSI paper above for details and instructions. This was initially omitted as it does not directly involve the Arduino control, and will be added in later versions.

A.1 Short Version

This is the quick-start version of the material below. It is recommended that anyone setting up Arduino control of an AD9914 read the entire guide.

1. Setup the AD9914 evaluation board including external clock, as outlined in *Rev. Sci. Intsr.*, (2013),083104, **84**
2. Wire the SDIO/SCLK/IO_UPDATE/RESET outputs to the Arduino as shown in Figure A.5
3. Connect these wires to their counterparts on the AD9914 shown in Figure A.4
4. Compile/Load the Arduino code given below onto the Arduino
5. Set pints P204 and P203 to disable, P205 to enable, shown in Figure A.2
6. Short the signal of EXTPDCTL and DRHOLD to ground using a jumper, shown in Figure A.3

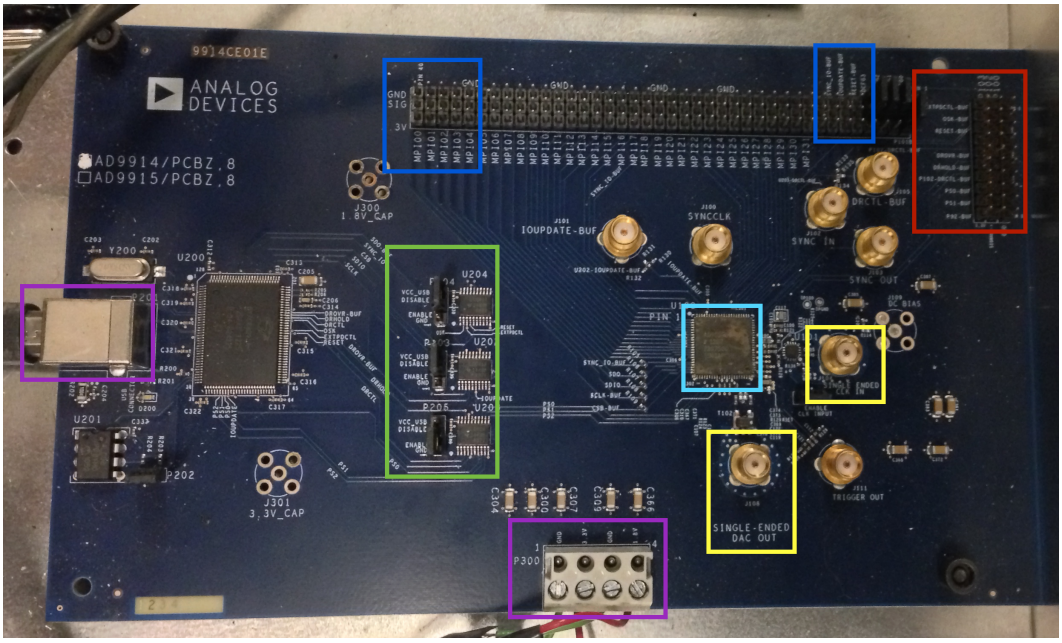

Figure A.1. An overview of the AD9914. Green - USB control circuits and pins, Blue - Serial control pins, Red- External trigger and power down control pins, Yellow - DDS clock input and DAC (Chirp) output, Light Blue - AD9914 chip, Purple - USB adapter and power suppler input

7. Power on the AD9914 and press the reset button on the Arduino
8. Supply a trigger as outlined in the RSI supplement and monitor the chirp output

A.2 AD9914 DDS

To do this we chose an Arduino Uno micro controller board (http://arduino.cc/en/Main/ArduinoBoardUno). The board is cheap, effective, and open source; its software is available on virtually any platform, it has an immense support community, and there are Python libraries for external control.

A.3 Construction

Microcontroller Control of the AD9914

Unlike the PLL synthesizers that can be set and then ignored, or changed fairly rarely, the DDS requires constant attention. While developing the system, we noticed that the phase of the chirps coming from the DDS would slowly drift (this drift is a function of the number of chirps generated, not time), causing our time domain signal to average to something very low. The solution to this is to recalibrate the DDS's digital to analog converter (DAC) approximately every second (because this

is dependent on the number of chirps, not time, this number may need to be lower, 1 - 100ms for very high acquisition rates). This requires sending a DAC calibrate command to the DDS very frequently, something that is not practical with the AD (Analog Devices) DDS control software. The solution is to use a micro controller to send serial commands to the DDS to recalibrate the DAC on a regular basis. A second benefit of this is that the micro controller can be programmed to handle the initial setup of the DDS, which simplifies its use.

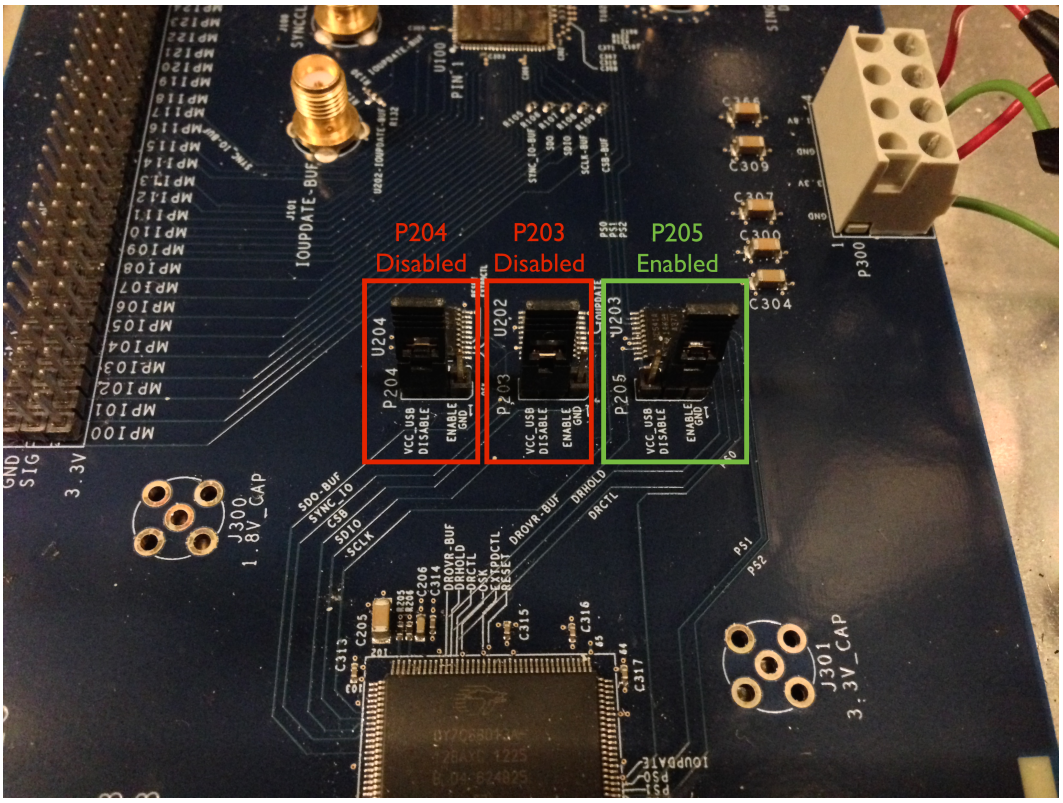

Figure A.2. USB micro controller pins. P204 and P203 should be disabled, P205 should remain enabled to allow external chirp triggering.

The first step is to disable USB control/enable serial control of the DDS. This is done by changing jumpers P203 - 204 to disable. Oddly P205 should remain enabled. This is because the digital ramp status pins, DRSTART and DROVER, the trigger signal to start the chirp, and the output that the chirp has completed (which should be used as the digitizer trigger to minimize phase jitter), respectively, are buffered through the IC associated with P205, and disabling it disables these as well. When this is done, the USB control lines are set to high impedance to prevent the USB controller accidentally sending commands to the AD9914. The side effect of this is that several pins that were being controlled are now floating. Specifically the reset,

SYNCIO, external power down, and chip select are floating, setting them to enable, which makes the board unusable.

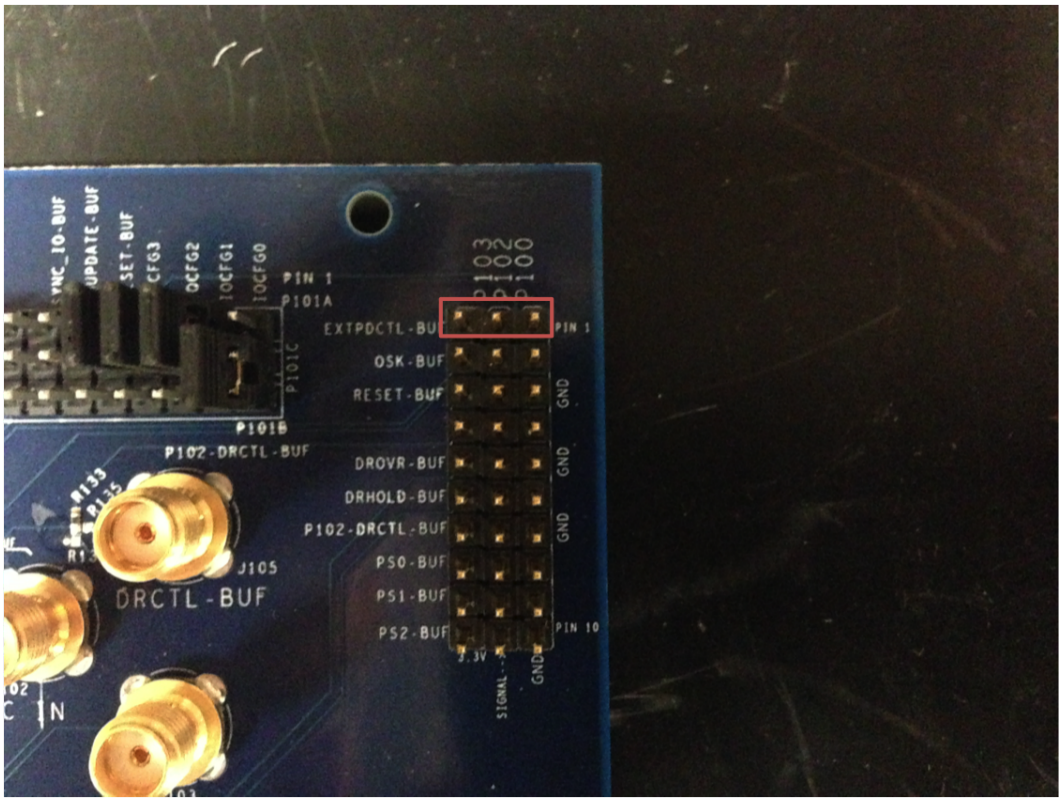

Figure A.3. EXTPDCTL, RESET, DROVR, DRHOLD, and DRCTL control pins. EXTPDCTL must have the signal shorted to ground.

To fix this, the signal line on following pins should be shorted to ground with a jumper to disable them: SYNCIO (Figure A.4), and EXTPDDNCTL (Figure A.3), highlighted in red. Once this is done, the Arduino can be used to control the 9914.

An overview of the Arduino SPI protocol is given (http://arduino.cc/en/Reference/SPI). Briefly, SPI is a simple serial communication protocol supported by the Arduino. When using SPI, several Arduino pins are automatically controlled. Pin 13 is set as the serial clock, and should be linked to the CLK/MIO1 pin on the 9914. Similarly, Pin 12 and Pin 11 are the Master In Slave Out (MISO, essentially data transfer from the 9914 to the Arduino; this feature is not currently used, but could be added to read the state of the 9914 if desired) and Master Out Slave In (MOSI, essentially the pin used to write commands to the 9914) respectively. Pin 12 is not used, but Pin 11 is, and should be connected to the signal line of MPI02. Aside from these mandatory pins, two additional pins are needed to send reset and IO_UPDATE commands to the board. For this project, pins 7 and 4 have been arbitrarily chosen, but any digital

pin on the Arduino not already in use is acceptable. The first pin, the reset pin, can be connected to either of the RESET pins on the 9914. Pin 4 is used to send IO_UPDATE commands to the 9914, and should be connected to the IO_UPDATE BUF pin on the 9914. A full pinout is given in Figure A.5. Finally, the ground pin of the reset, MISO/SDIO, SNYC_CLK, and IO_UPDATE on the AD9914, should be connected to ground on the Arduino.

Once the Arduino is connected, the board can be controlled. The complete code is given below, but a brief explanation is also warranted. The AD9914 is controlled by a set of registers that determine its behavior. Serial commands can be sent to control these register values. Serial control of the 9914 is default most significant bit (MSB) first. This is also default for the Arduino. The serial commands are sent in two phases. First a register address is sent, followed by a series of four bytes. A helpful diagram is given in the 9914 chip guide. Once the 9914 is powered the first command should be a reset command. This is not spelled out in the documentation, but the reset command seems to be necessary to ensure good communication between the boards. Once this is done, the initial register commands can be sent and the registers can be set. The DAC calibration is then sent every second until the Arduino is powered off. One final note is the IO_UPDATE command. The IO_UPDATE command is used to set registers once the command bytes are written. To set registers that control the function of the 9914 the bytes are first written to the 9914, this is the SPI Transfer command. Once the register information is set, it is held in a buffer, but the registers will not be changed until an IO_UPDATE command is sent.

The register values can be worked out from the AD9914 chip documentation, but the 9914 eval board software's debug page is infinitely simpler for accomplishing this. It can also be helpful for testing the board in case of a suspected malfunction.

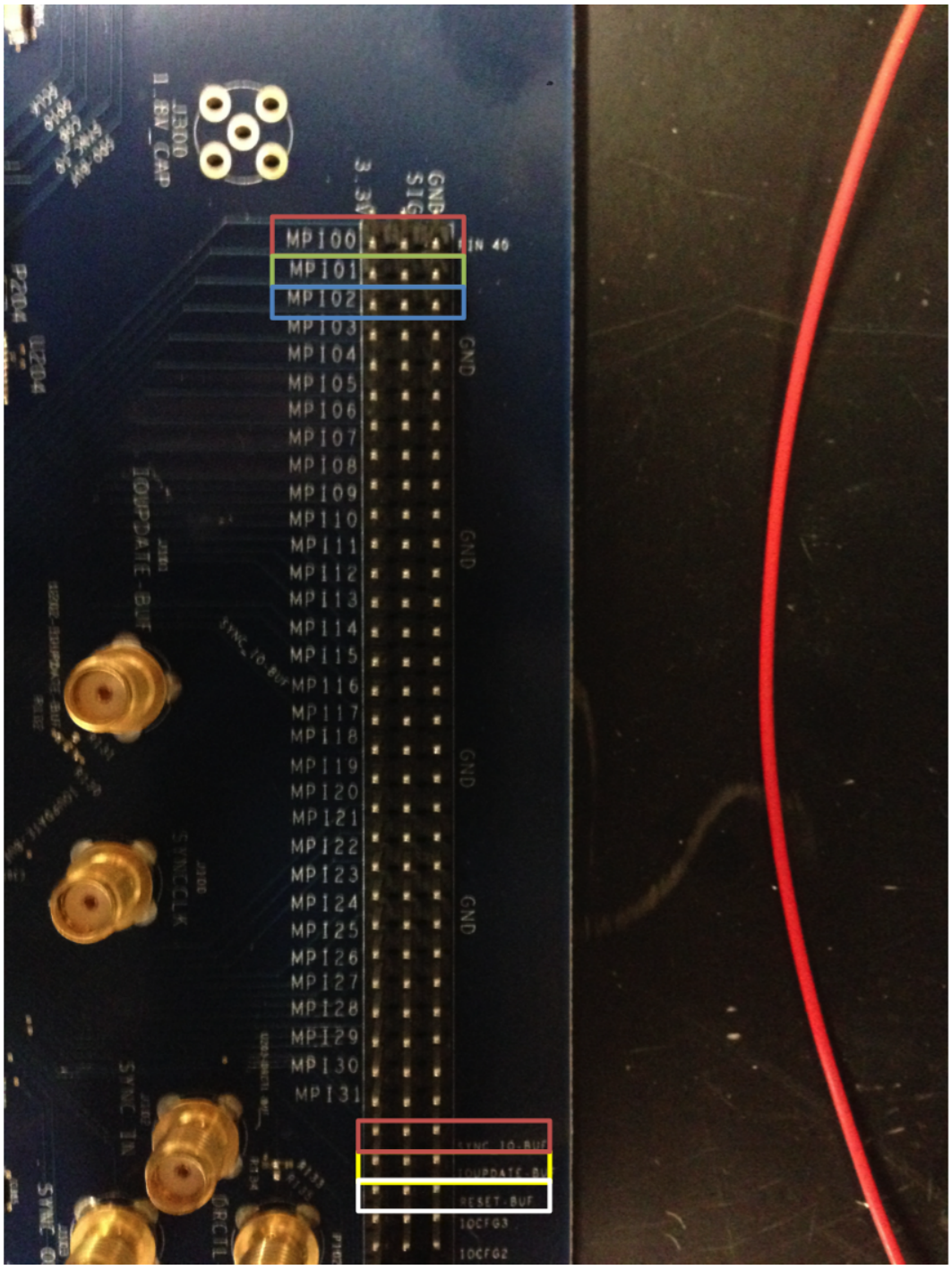

Figure A.4. MIO buffers of the AD9914. MIO buffers, CS (red box top), SYNC_CLK (Green box top), Serial Clock in (Blue box top) and SYNC_IO (red box bottom), IO_UPDATE (Yellow box bottom), and RESET (White box bottom)

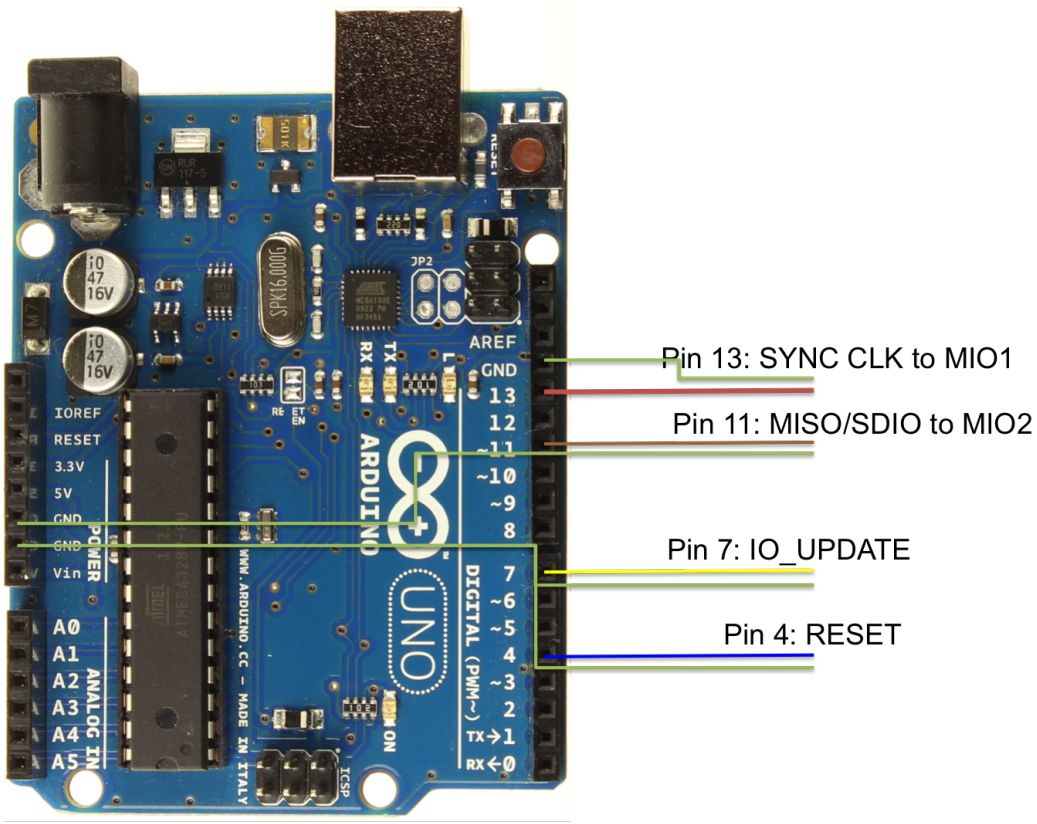

Figure A.5. Wiring diagram for the Arduino Uno. The individual grounding wires (green) for the SYNC_CLK and SDIO are essential to proper function. The IO_UPDATE and RESET pins can use a common ground with no disruption.

Arduino Code

```
#include <SPI.h>

/* A program for control of AD9914 DDS using the 9914's serial
    interface and an Arduino
Written by Brandon Carroll
Creadted 1/9/14
*/


/*See http://arduino.cc/en/Reference/SPI for an explanation of the
    SPI protocol used here
Shockingly, the AD9914 chip documentation is also immensely
    helpful http://www.analog.com/static/imported-files/
    data_sheets/AD9914.pdf
Code is based on: http://arduino.cc/en/Tutorial/
    BarometricPressureSensor
Pin labels are given for the AD9914 chip, followed by their EVAL
    board counterpart, ie Pin 20 on the AD9914 chip is labeled as
    D2, and is accessed by connecting to MIO1 on the EVAL board
Assuming an Arduino Uno is in use, in SPI Mode:
-Pin 13 is the SCLK
-Data from the Arduino to the AD9914 is pin 11 (Arduino:MOSI or
    AD9914: SDIO/Pin 20/D2/MIO1 on the 9914 EVAL)
-Data from the AD9914 to the Arduino (not currently used) is pin
    12 (Arduino:MISO or AD9914: SDO/Pin 19/D3/MIO3 on the 9914
    EVAL)
-Pin 10 is in use by SPI to select which device is in use, not
    needed here, but still reserved by the Arduino, MIO0 on the
    9914EVAL
-Pin 7 is currently used to send the IO Update commands to AD9914
    Pin 86
-Pin 4 is used to send an initial reset command to the 9914,
    suprisingly necessary

Of Note:
-The 9914 used most signifcant bit first (MSB) mode by default.
    This can be changed, but this code assumes MSB operation

Wiring:
For somewhat nonsensical reasons the wiring for the Blake lab
    controller is currently:
Red = Ground
```

```
Green  = SDIO, SCLK, and IO Update (SDIO is labeled with white tape, IO Update has scotch/tan tape, and SCLCK has nothing)
Blue  = Reset
NO LONGER USED:
Yellow =  CS/SS

****The quick setup version:****
For the wires:
There are three that are a green signal and red ground. The unlabeled one is the SYNC_CLK that goes to MDIO1.
The one that says SDIO is the SDIO and goes to MDIO2.
The one with the unlabeled scotch tape is the the IO BUFFER and goes to the IO_UPDATE pin.
All of these are on the longer set of 3 row pin outs, the ones that don't have the trigger in or out cables.

For the jumpers:
The three jumpers to add all short the signal to ground.
The first is MDIO0, just before the SYNC_CLK.
The second and third are on the shorter pin outs with the trigger in and out.
You'll need to jump the EXTCTLPWR or something like it, I'm fairly sure it's the first jumper on the row.
The other is the DRHLD and is between the trigger in and out jumpers. I find it easiest to remove either the trigger jumpers before trying the add this one.

After that set the USB jumpers. If you are standing at the keyboard/ computer the left two jumpers are set to disable the rightmost is set to enable.
That should be everything. Good luck.


*/



/*======Serial Communication parameters======*/
const int IOUpdatePin =  7;  //The pin used to trigger IO Update events
const int ResetPin = 4;      //The pin used to send reset commands
const int CSPin = 10;         //The pin used to handle chip select
```

```
59 /*======Register Addresses======*/
   const byte CFRAddress[] = {0x00,0x01,0x02,0x03};  //Control
      function register addresses
61 //{CFR1, CFR2, CFR3, CFR4}

63 const byte DigitalRampAddress[] = {0x04, 0x05, 0x06, 0x07, 0x08};
       //Digital ramp addresses
   //{Digital Ramp Lower Limit (MHz), DR Upper Limit (MHz), DR Rising
       Step (MHz), DR Falling Step(MHz), DR Step Rate (uS)}
65
   const byte CWToneAddress = 0x0B;  //Address for CW frequency
      tuning word, currently using profile 0
67 const byte USR0Address = 0x1B;

69 /*======Startup register values======*/
   const byte CFR1Start[] = {0x00, 0x01, 0x60, 0x08};
71 const byte CFR2Start[] = {0x00, 0x0C, 0x29, 0x00};
   const byte CFR3Start[] = {0x00, 0x00, 0x19, 0x1C};
73 const byte CFR4Start[] = {0x00, 0x05, 0x01, 0x20};
   const byte DRGStart[] = {0x00, 0x00, 0x00, 0x00};  //Chirp Start
75 //const byte DRGStop[] = {0x00, 0x00, 0x00, 0x00};   //chirp stop
   const byte DRGStop[] = {0x00, 0xA3, 0xD7, 0x0A};   //chirp stop
77 //const byte DRGStepRise[] = {0x00, 0xA3, 0xD7, 0x0A};
   const byte DRGStepRise[] = {0x00, 0x00, 0xD7, 0x17};
79 const byte DRGStepFall[] = {0x00, 0x72, 0x38, 0x4A};
   //const byte DRGRate[] = {0x00, 0x01, 0x00, 0x01};
81 //const byte DRGRate[] = {0x00, 0x03, 0x00, 0x01};
   const byte DRGRate[] = {0x00, 0x01, 0x00, 0x01};
83 const byte ZeroByte = 0x00;
   const byte DACCalEnable[] = {0x01, 0x05, 0x01, 0x20};  //Command
      to enable the DAC Cal, should be 0x01XXXXXX, where X is the
      last 6 digits of CFR4Start
85


87 /*======Variables for controlling the 9914======*/
   //Not currently in use, but may be useful if adjustments to the
      chirp are desired
89 const int ClockFreq = 4000;              //DDS clock frequency in
      MHz
   const float ChirpBandwidth = 2000.0;     //In MHz, a 2 GHz chirp
91 const float ChirpTimeStep = 0.0006;      //Time between chirp steps
       in uS, this is used for both the rise and fall times
```

```
const float ChirpFrequencyStepRise = 9.99999976;  //Rising sweep
    step size in MHz
const float ChirpFrequencyStepFall = 6.971428171;  //Falling sweep
     step in MHz
const float DACCalDelay = 100;  //Time in ms between DAC
    Calibrations


/*======Test Tuning Words======*/
const byte TenMHz[] = {0x00, 0xA3, 0xD7, 0x0A};
const byte FiftyMHz[] = {0x03, 0x33, 0x33, 0x33};
const byte CFR2Test[] = {0x00, 0x84, 0x29, 0x00};


void setup ()
{

  //delay (3000);                  //We will give everything 3s to
    boot up before we start setting up the DDS
  pinMode (IOUpdatePin, OUTPUT); //Set the IO Update Pin to output
  pinMode (ResetPin, OUTPUT);     //Set the Reset pin to output
  pinMode (CSPin, OUTPUT);        //Set the Chip select pin to
    output
  digitalWrite (CSPin, HIGH);     //Set the chip select pin to high
    , ie we aren't communicating with the board right now,
    debatably necessary.
  SPI.begin ();                   //Start the SPI library
  SPI.setClockDivider(SPI_CLOCK_DIV2);  //Set the SPI clock
    divider to 2, default is 4, but the DDS/Arduino can handle 2,
    and it speeds up data transfer
  SPI.setBitOrder(MSBFIRST);             //Set the SPI to MSB first
    , this is the default for SPI and the DDS, but better to be
    safe
  SPI.setDataMode (SPI_MODE0);           //Set the SPI to use clock
     polarity and clock phase 0. I *think* this is the only mode
    that will work, have not tested MODE2/3, MODE1 doesnt seem to
    work

  Send_Reset();  //This is suprisingly very imporant. Even after
    power cycling the DDS a reset command is needed to ensure good
     communication
  Initialize_DDS ();
  Calibrate_DAC ();     //Do an initial DAC cal for funsies
```

```
119
121   /* Test code to check the functionality of the the DDS. It
        should set the DDS to output a 10 MHz tone
      Write_Register (CWToneAddress, TenMHz[0], TenMHz[1], TenMHz[2],
        TenMHz[3]);  //Set the FTW
123   Write_Register (0x1A, 0xC0, 0x00, 0x00, 0x00);  //Set the phase/
        amp
      Send_IO_Update ();
125   */


127
}
129
void loop ()
131 {
int i;
133   i = 0;
      delay (DACCalDelay);  //Wait for some amount of time between DAC
        cals so we don't spam the DDS and lock it up
135   Calibrate_DAC ();      //Send a DAC cal
      i++;
137   if (i > 300000) {  //Reinitialize every 30 min
        Initialize_DDS ();
139     i = 0;
      }
141 }

143 //Register writing function
void Write_Register (byte Register, byte Value1, byte Value2, byte
      Value3, byte Value4)
145 {
int i;
147   digitalWrite (CSPin, LOW);          //Set the chip select to low,
        to tell the DDS we want to send commands
      SPI.transfer(Register);             //The 9914 expects a register
        address first
149   SPI.transfer(Value1);               //Followed by the register
        value
      SPI.transfer(Value2);               //Registers are 4 bytes, but
        we can only send 1 at a time
151   SPI.transfer(Value3);
      SPI.transfer(Value4);
```

```
153   digitalWrite (CSPin, HIGH);          //Set the CS pin high, so the
        DDS will ignore anything on the
}
155
157
159 void Send_IO_Update ()
{
161   digitalWrite (IOUpdatePin, HIGH);  //The IO Update is active on
        logic high, so we send the pin high for an update
      digitalWrite (IOUpdatePin, LOW);   //Then low to end it. The
        delay between rise and fall is many clock cycles, so no delay
        between the high and low commands is needed
163 }

165 void Send_Reset ()
{
167   digitalWrite (ResetPin, HIGH); //The reset is active on logic
        high, so we send the pin high for an update
      digitalWrite (ResetPin, LOW);  //Then low to end it. The delay
        between rise and fall is many clock cycles, so no delay
        between the high and low commands is needed
169 }

171 void Calibrate_DAC ()
{
173   Write_Register (CFRAddress[3], DACCalEnable[0], DACCalEnable[1],
        DACCalEnable[2], DACCalEnable[3]);  //The DAC cal is a two
        step proccess, first we must set the DAC
      Send_IO_Update();
                                            //cal bit to 1, then send
        the IO Update to initiate it
175   Write_Register (CFRAddress[3], CFR3Start[0], CFR3Start[1],
        CFR3Start[2], CFR3Start[3]);              //Then we set the
        DAC cal bit back to low, to prevent the board
      Send_IO_Update();
                                            //from repeatedly
        calibrating. Finally an IO UPDATE to set the bit
177 }

179 void Initialize_DDS ()
{
```

```
181   Send_Reset();
      Write_Register(CFRAddress[0], CFR1Start[0], CFR1Start[1],
       CFR1Start[2], CFR1Start[3]);   //Write the inital control
       registers
183   Write_Register(CFRAddress[1], CFR2Start[0], CFR2Start[1],
       CFR2Start[2], CFR2Start[3]);
      Write_Register(CFRAddress[2], CFR3Start[0], CFR3Start[1],
       CFR3Start[2], CFR3Start[3]);
185   Write_Register(CFRAddress[3], CFR4Start[0], CFR4Start[1],
       CFR4Start[2], CFR4Start[3]);
      Write_Register(USR0Address, 0xE2, 0x00, 0x08, 0x00);      //
       Write the USR register, not sure if this is needed
187   Write_Register(DigitalRampAddress[0], DRGStart[0], DRGStart[1],
        DRGStart[2], DRGStart[3]);  //Set the the start frequency for
       the DRG
      Write_Register(DigitalRampAddress[1], DRGStop[0], DRGStop[1],
       DRGStop[2], DRGStop[3]);      //Set the the stop frequency for
       the DRG
189   Write_Register(DigitalRampAddress[2], DRGStepRise[0],
       DRGStepRise[1], DRGStepRise[2], DRGStepRise[3]);  //Set the
       the DRG rising step size
      Write_Register(DigitalRampAddress[3], DRGStepFall[0],
       DRGStepFall[1], DRGStepFall[2], DRGStepFall[3]);  //Set the
       the DRG falling step size
191   Write_Register(DigitalRampAddress[4], DRGRate[0], DRGRate[1],
       DRGRate[2], DRGRate[3]);                    //Set the the DRG
       step rate
      Send_IO_Update();    //Send the update to set the control
       registers
193 }
```

Code/AD9914.c

A.4 ALMA Fitting Code

```
#########
2 # Changes from v2.6:
# -Simplified and commented numerous things
4 # -Build my own curve_fit for direct access to the least_squares
    calls so we can get better control of the fitting
# -Removed several old optfuncs
6 #
#
8 #
```

```
#
#
#

import os
import sys
sys.path.remove('/home/pcarroll/.local/lib/python2.7/site-packages')
import pylab as plb
import matplotlib.pyplot as plt
import numpy as np
import time
import matplotlib.patches as patches
from scipy.optimize import curve_fit
from scipy import asarray as ar,exp
from scipy.optimize import least_squares
from scipy.linalg import svd
from astropy.io import fits


################## Defining Functions ##################
#Functions are given in no particular order

def CH2DCN_Q(T):
#Empirical partition function from power law fit of splatalogue data, power was fixed to 1.5
#Fitting with the power unconstrained returns a best fit power of 1.5008, so it should be fine
  return 0.359027+1.76783*T**1.5

def C13H3CN_Q(T):
#Empirical partition function from power law fit of splatalogue data, power was fixed to 1.5
#Fitting with the power unconstrained returns a best fit power of 1.5008, so it should be fine
  return 7.087+1.974*T**1.5026

def Build_LTE_Spectrum(NT,Q,T,Width,EUpper,v,Sij,X,Y):
  Intensity = np.zeros_like(EUpper)
  for i in range(0,len(EUpper)):
    Intensity[i] = LTE_Intensity(NT,Q,T,EUpper[i],v[i],Sij[i])
    Render_Spectrum (X,Y,v[i],Intensity[i],Width,0.00001)

```

```
def Build_LTE_Spectrum_Degeneracy(NT,Q,T,Width,EUpper,v,Sij,X,Y,
    Degeneracy):
  Intensity = np.zeros_like(EUpper)
  for i in range(0,len(EUpper)):
    Intensity[i] = LTE_Intensity(NT,Q,T,EUpper[i],v[i],Sij[i])*
    Degeneracy[i]
    Render_Spectrum (X,Y,v[i],Intensity[i],Width,0.00001)

def LTE_Intensity(NT,Q,T,EUpper,v,Sij):
#compute an LTE intensity (technically the integrated intensity)
    for a line based on Remijan et al 2005.
#Currently coded for single dish emission
  C = 4.8E-5
  A = (1-(exp((C*v)/T)-1)/(exp((C*v)/2.7)-1)) #Computing this
    separately for my own sanity, currently hard coding CMB
    background temp
  return (NT*v*Sij*A)/((1.8E+14)*Q*exp(EUpper/T))

def LTE_Intensity_Interferometer(NT,Q,T,EUpper,v,Sij,B,beam):
#compute an LTE intensity (technically the integrated intensity)
    for a line based on Remijan et al 2005 (note: Tony fucked up,
    the listed frequency has to be GHz for this calculation, not
    MHz like it implies in the paper, see his urea paper for proof
    ).
#Currently coded for an interferometer
#This technically returns the integrated intensity of the line,
    assuming an input of Jy/B(which is what ALMA uses. hooray)
#The beam argument should be supplied as bmja*bmin, as listed in
    Tony's paper, it can also, probably more correctly, be thought
     of as beam area, which for a circular/elliptical is not
    explicitly bmaj*bmin, however since the code currently
    extracts square regions, this should be exactly right
#This simplification is done for a small cpu speed up
  return (NT*B*(beam)/(2.04E+20))*((((v/1000.0)**3.0)*Sij)/(Q*exp(
    EUpper/T)))

def Render_Spectrum (X,Y,Center,A,Width,Threshold):
#Render a gaussian spectrum
  c = Width/2.35482
  Temp1 = 2*c*c
  j = len(X)-1
  Cutoff = c*sqrt(2*np.log(A/Threshold)) #The Full width 1/X max
    of a gaussian is 2sqrt(2*ln(X)), should give the onesided
```

```
    cutoff distance
  while (X[j] < (Center-Cutoff)): #Again ALMA data is in velocity
    space so all the pixel by pixel data comes out last to first
    j = j-1
  while (X[j] < (Center+Cutoff)):
    Y[j] = Y[j] + A*exp(-((X[j]-Center)**2)/Temp1)
    j = j-1

def Baseline_Subtract_D (y):
#Function to do a baseline subtraction of an emission-free region.
#Very important to keep the gaussian fitting in check
#Im starting to think this way of doing things is dumb
  RMS = 0.0
  N = 0
  for i in range(141,254):        #Baseline-free region determined
    from averaging over most of the complex
    RMS += y[i]          #ALMA data is spit out in highfrequency
    first
    N+=1
  RMS/=N
  #RMS = sqrt(RMS)
  for i in range(0,len(y)):
    y[i] = y[i]-RMS
  return RMS

def Baseline_Subtract_13C (y):
#Function to do a baseline subtraction of an emission-free region.
#Very important to keep the gaussian fitting in check
#Im starting to think this way of doing things is dumb
  RMS = 0.0
  N = 0
  for i in range(0,200):        #Baseline-free region determined
    from averaging over most of the complex
    RMS += y[i]          #ALMA data is spit out in highfrequency
    first
    N+=1
  RMS/=N
  #RMS = sqrt(RMS)
  for i in range(0,len(y)):
    y[i] = y[i]-RMS
  return RMS

def Baseline_Subtract_D_918 (y):
```

```
#Function to do a baseline subtraction of an emission-free region.
#Very important to keep the gaussian fitting in check
#Im starting to think this way of doing things is dumb
  RMS = 0.0
  N = 0
  for i in range(0,30):          #Baseline-free region determined
   from averaging over most of the complex
    RMS += y[i]          #ALMA data is spit out in highfrequency
    first
    N+=1
  RMS/=N
  #RMS = sqrt(RMS)
  for i in range(0,len(y)):
    y[i] = y[i]-RMS
  return RMS

def Baseline_Subtract_D_919 (y):
#Function to do a baseline subtraction of an emission-free region.
#Very important to keep the gaussian fitting in check
#Im starting to think this way of doing things is dumb
  RMS = 0.0
  N = 0
  for i in range(130,200):          #Baseline-free region determined
    from averaging over most of the complex
    RMS += y[i]          #ALMA data is spit out in highfrequency
    first
    N+=1
  RMS/=N
  #RMS = sqrt(RMS)
  for i in range(0,len(y)):
    y[i] = y[i]-RMS
  return RMS

def MHz_to_Kms (Frequency_MHz,CenterFrequency_MHz):
  #Pretty self explanatory
  return (Frequency_MHz/CenterFrequency_MHz)*3.0E+5

def Kms_to_MHz (Kms,CenterFrequency_MHz):
  #Also pretty self explanatory
  return (Kms/3.0E+5)*CenterFrequency_MHz

def Make_Rotation_Diagram (Frequency,A,Intensities,Nu):
#Not in use, but kept for completeness and possibly error checking
```

```
150   for i in range(0,len(Frequency)):
          Nu[i] = Intensities[i]*1.94359E-14*((Frequency[i]*1.0E+6)
      **2)/A[i]
152
    def Compute_RMS (Start,End,Array):
154   RMS = 0.0
      Channels = 0
156   for i in range(len(Start)):
        for j in range(Start[i],End[i]):
158       RMS += Array[j]*Array[j]

160     Channels += abs(Start[i]-End[i])
      RMS/=Channels
162   RMS = np.sqrt(RMS)
      return RMS
164
    def Compute_RMS_Diff (Start,End,Array1,Array2):
166   RMS = 0.0
      Channels = 0
168   #for i in range(len(Start)):
      for j in range(Start,End):
170     RMS += (Array1[j]-Array2[j])**2.0
      Channels = End-Start
172   RMS/=Channels
      RMS = np.sqrt(RMS)
174   return RMS

176 def Compute_RMS_Diff_Tuple (Start,End,Array1,Array2):
      RMS = 0.0
178   Channels = 0
      for i in range(len(Start)):
180     for j in range(int(Start[i]),int(End[i])):
          RMS += (Array1[j]-Array2[j])**2.0
182     Channels = abs(int(End[i]-Start[i]))
      RMS/=Channels
184   RMS = np.sqrt(RMS)
      return RMS
186
    def Load_Fits_File (FitsName):
188   hdulist = fits.open(FitsName)   #Astropy fits file loader, way
      faster than CASA, that steaming pile of junk, we should be
      loading the entire dataset into RAM
```

```
    data = hdulist[0].data[0]      #Take only the Stokes I data,
     there isnt anything else anyway, but it simplifies things
    header = hdulist[0].header
    hdulist.close()            #Close the data
    data = np.swapaxes(data,0,2)     #Switch the axes so its data[RA
     ][DEC][spectrum]
    return data,header

def Check_Fittable (Spectrum,Threshold,Start,End):
    for i in range(Start,End):
      if (Spectrum[i]>Threshold):
        return 1
    return 0

def Get_Beam (Data,XDim,YDim,CenterX,CenterY,Theta):
    y = np.zeros_like(Data[CenterX][CenterY])
    if ((XDim%2 == 0) or (XDim == 0)):     #Stupid checks, also I'm
     not dealing with even dimensions cause that makes defining a
     center pixel silly
      XDim += 1
    if ((YDim%2 == 0) or (YDim == 0)):     #Stupid checks, also I'm
     not dealing with even dimensions cause that makes defining a
     center pixel silly
      YDim += 1
    XOffset = int(XDim/2)   #Doing this explicitly so it isnt done
     repeatedly, and so its definitely an integer, dam you python
     and your convenient handling of data types for me
    YOffset = int(YDim/2)

    for i in range(XDim):
      for j in range(YDim):
        y += Data[i-XOffset+CenterX][j-YOffset+CenterY]
    y /= (XDim*YDim)
    return y

def Load_Mol_Data (Filename):
    Moldata = plb.loadtxt(Filename,skiprows=1)
    Catalog_Freq = Moldata[:,0]      #Frequencies
    Catalog_Error= Moldata[:,1]      #Cat error, we dont really use
     this but it was here so why not
    Catalog_JPLStr= Moldata[:,2]     #JPL logstr
    Catalog_SijMu = Moldata[:,3]     #Sij values
```

```
222   Catalog_A = Moldata[:,4]       #Einstein A coefficient, not
        necessary
      Catalog_UpperState = Moldata[:,5] #Upper state energies
224   Catalog_Mask = Moldata[:,6]       #To plot or not to plot, that
        is the question and also what this variable does
      Catalog_Degeneracy = Moldata[:,7] #Some CH2DCN lines have two
        lines at the same frequency, so its a hell of a lot easier to
        just fit one line and divide by this number
226
      CatalogLength = 0
228   for i in range(len(Catalog_Mask)):
        if (Catalog_Mask[i] == 1):
230       CatalogLength +=1

232   Catalog = np.zeros((5,CatalogLength)) #Catalog[Frequency(1),
        Upper State Energy(2), SijMu^2(3),Degeneracy(4),Einstein A(5)]
        [Line #=

234   Count = 0
      for i in range(len(Catalog_Freq)):
236     if (Catalog_Mask[i] == 1):
          Catalog[0][Count] = Catalog_Freq[i]
238       Catalog[1][Count] = Catalog_UpperState[i]
          Catalog[2][Count] = Catalog_SijMu[i]
240       Catalog[3][Count] = Catalog_Degeneracy[i]
          Catalog[4][Count] = 10.0**Catalog_A[i]
242       Count += 1

244   return Catalog

246 def Get_Index (Target,Array):
      if (Target > Array[0]):     #Stupid checks, these may appear ass
        backwards, but that's only because the ALMA data is
248     return -1
      if (Target < Array[len(Array)-1]):
250     return -1
      i = 1
252   while (Array[i]>Target):
        i+=1
254   return int(i-1)

256 def Optical_Depth(A,NT,Frequency,T,dV,gu,Q,Eu):
```

```
    #Return the optical depth, using a slightly modified version of
      eq 6 of Goldsmith and Langer
258 #All I did was adjust it to take Einstein A instead of B and
      make it use friendlier units
    #A is in Hz, Nu is in cm^-2, frequency is in MHz, T is in K, and
      dV is in km/s
260 return (exp(4.79924E-5*(Frequency)/(T))-1.0)*(10.0/(dV))*(
      Calculate_Nu (NT,gu,Q,T,Eu))*(A)*((2.99792458E+2)/(Frequency))
      **3.0

262 def Calculate_Nu (NT,gu,Q,T,Eu):
    #Calculates the population in a given upper state for a column
      density and temperature
264 #gu is the upper state degeneracy, which ought to be 2J+1 for a
      rotational transition
    return (NT*gu)/(Q*exp(Eu/T))
266
  def LTE_Interferrometer_OD (A,NT,Frequency,T,dV,gu,Q,Eu,Sij):
268 Tau = Optical_Depth(A,NT,Frequency,T,dV,gu,Q,Eu)
    C = Tau/(1.0-exp(-Tau))
270 return C*LTE_Intensity_Interferometer(NT,CH2DCN_Q(T),T,Eu,
      Frequency,Sij,0.5,BeamSize)

272 def OptFuncC(x, *a):
    #Main optimization function for fitting spectra, it runs fast
      enough for now, but there are faster ways
274 y = np.zeros_like(x)
    sigma = a[0]
276 xoffset = a[1]
    T = a[2]
278 NT1 = a[3]  #Deuterium
    NT2 = a[4]  #13C
280 VelRatio = Catalog_13C[0][0]/Catalog_D[0][0]
    #VelRatio = 1.0
282 for i in range(0,len(Catalog_D[0])):
      y = y + (1.0/sigma*2.35482)*LTE_Intensity_Interferometer(NT1,
      CH2DCN_Q(T),T,Catalog_D[1][i],Catalog_D[0][i],Catalog_D[2][i
      ],0.5,BeamSize)*exp(-(x-Catalog_D[0][i]-xoffset)**2/(2*sigma
      **2))
284 for i in range(0,len(Catalog_13C[0])):
      y = y + (1.0/sigma*2.35482)*LTE_Intensity_Interferometer(NT2,
      C13H3CN_Q(T),T,Catalog_13C[1][i],Catalog_13C[0][i],Catalog_13C
      [2][i],0.5,BeamSize)*exp(-(x-Catalog_13C[0][i]-(xoffset*
```

```
    VelRatio))**2/(2*(sigma*VelRatio)**2))
  for i in range(0,len(Catalog_D_918[0])):
    y = y + (1.0/sigma*2.35482)*LTE_Intensity_Interferometer(NT1,
    CH2DCN_Q(T),T,Catalog_D_918[1][i],Catalog_D_918[0][i],
    Catalog_D_918[2][i],0.5,BeamSize)*exp(-(x-Catalog_D_918[0][i]-
    xoffset)**2/(2*sigma**2))
  for i in range(0,len(Catalog_D_919[0])):
    y = y + (1.0/sigma*2.35482)*LTE_Intensity_Interferometer(NT1,
    CH2DCN_Q(T),T,Catalog_D_919[1][i],Catalog_D_919[0][i],
    Catalog_D_919[2][i],0.5,BeamSize)*exp(-(x-Catalog_D_919[0][i]-
    xoffset)**2/(2*sigma**2))
  return y

def OptFuncC_Offset(x, *a):
  #Main optimization function for fitting spectra, it runs fast
    enough for now, but there are faster ways
  y = np.zeros_like(x)
  sigma = a[0]
  xoffset = a[1]
  Line_Offset = a[2]
  T = a[3]
  NT1 = a[4]  #Deuterium
  NT2 = a[5]  #13C
  for i in range(0,len(Catalog_D[0])):
    #y = y + LTE_Intensity(N1T,CH2DCN_Q(T1),T1,Catalog[1][i],
    Catalog[0][i],Catalog[2][i])*exp(-(x-Catalog[0][i]-xoffset)
    **2/(2*sigma**2))
    y = y + LTE_Intensity_Interferometer(NT1,CH2DCN_Q(T),T,
    Catalog_D[1][i],Catalog_D[0][i],Catalog_D[2][i],0.5,BeamSize)*
    exp(-(x-Catalog_D[0][i]-xoffset-Line_Offset)**2/(2*sigma**2))
  for i in range(0,len(Catalog_13C[0])):
    #y = y + LTE_Intensity(N1T,CH2DCN_Q(T1),T1,Catalog[1][i],
    Catalog[0][i],Catalog[2][i])*exp(-(x-Catalog[0][i]-xoffset)
    **2/(2*sigma**2))
    y = y + LTE_Intensity_Interferometer(NT2,C13H3CN_Q(T),T,
    Catalog_13C[1][i],Catalog_13C[0][i],Catalog_13C[2][i],0.5,
    BeamSize)*exp(-(x-Catalog_13C[0][i]-xoffset)**2/(2*sigma**2))
  return y

def OptFuncNTT(x, *a):
  #Main optimization function for fitting spectra, it runs fast
    enough for now, but there are faster ways
  y = np.zeros_like(x)
```

```
312     #T = a[0]
        T = a[0]
314     NT1 = a[1]   #Deuterium
        NT2 = a[2]   #13C
316     VelRatio = Catalog_13C[0][0]/Catalog_D[0][0]
        xoffset = XOffset_Fix
318     sigma = Sigma_Fix
        for i in range(0,len(Catalog_D[0])):
320       #y = y + LTE_Intensity(N1T,CH2DCN_Q(T1),T1,Catalog[1][i],
          Catalog[0][i],Catalog[2][i])*exp(-(x-Catalog[0][i]-xoffset)
          **2/(2*sigma**2))
          y = y + LTE_Intensity_Interferometer(NT1,CH2DCN_Q(T),T,
          Catalog_D[1][i],Catalog_D[0][i],Catalog_D[2][i],0.5,BeamSize)*
          exp(-(x-Catalog_D[0][i]-xoffset)**2/(2*sigma**2))
322     for i in range(0,len(Catalog_13C[0])):
          #y = y + LTE_Intensity(N1T,CH2DCN_Q(T1),T1,Catalog[1][i],
          Catalog[0][i],Catalog[2][i])*exp(-(x-Catalog[0][i]-xoffset)
          **2/(2*sigma**2))
324       y = y + LTE_Intensity_Interferometer(NT2,C13H3CN_Q(T),T,
          Catalog_13C[1][i],Catalog_13C[0][i],Catalog_13C[2][i],0.5,
          BeamSize)*exp(-(x-Catalog_13C[0][i]-(xoffset*VelRatio))
          **2/(2*(sigma*VelRatio)**2))
        for i in range(0,len(Catalog_D_918[0])):
326       #y = y + LTE_Intensity(N1T,CH2DCN_Q(T1),T1,Catalog[1][i],
          Catalog[0][i],Catalog[2][i])*exp(-(x-Catalog[0][i]-xoffset)
          **2/(2*sigma**2))
          y = y + LTE_Intensity_Interferometer(NT1,CH2DCN_Q(T),T,
          Catalog_D_918[1][i],Catalog_D_918[0][i],Catalog_D_918[2][i
          ],0.5,BeamSize)*exp(-(x-Catalog_D_918[0][i]-xoffset)**2/(2*
          sigma**2))
328     for i in range(0,len(Catalog_D_919[0])):
          #y = y + LTE_Intensity(N1T,CH2DCN_Q(T1),T1,Catalog[1][i],
          Catalog[0][i],Catalog[2][i])*exp(-(x-Catalog[0][i]-xoffset)
          **2/(2*sigma**2))
330       y = y + LTE_Intensity_Interferometer(NT1,CH2DCN_Q(T),T,
          Catalog_D_919[1][i],Catalog_D_919[0][i],Catalog_D_919[2][i
          ],0.5,BeamSize)*exp(-(x-Catalog_D_919[0][i]-xoffset)**2/(2*
          sigma**2))
        return y
332
    def curve_fit_PBC(f, xdata, ydata, p0=None, sigma=None,
        absolute_sigma=False,check_finite=True, bounds=(-np.inf, np.
        inf), method=None,  jac=None, **kwargs):
```

```
334     if p0 is None:
            # determine number of parameters by inspecting the
        function
336         from scipy._lib._util import getargspec_no_self as
        _getargspec
            args, varargs, varkw, defaults = _getargspec(f)
338         if len(args) < 2:
                raise ValueError("Unable to determine number of fit
        parameters.")
340         n = len(args) - 1
        else:
342         p0 = np.atleast_1d(p0)
            n = p0.size
344
        lb, ub = prepare_bounds(bounds, n)
346     if p0 is None:
            p0 = _initialize_feasible(lb, ub)
348
        bounded_problem = np.any((lb > -np.inf) | (ub < np.inf))
350     if method is None:
            if bounded_problem:
352             method = 'trf'
            else:
354             method = 'lm'

356     if method == 'lm' and bounded_problem:
            raise ValueError("Method 'lm' only works for unconstrained
        problems. "
358                          "Use 'trf' or 'dogbox' instead.")

360     # NaNs can not be handled
        if check_finite:
362         ydata = np.asarray_chkfinite(ydata)
        else:
364         ydata = np.asarray(ydata)

366     if isinstance(xdata, (list, tuple, np.ndarray)):
            # `xdata` is passed straight to the user-defined `f`, so
        allow
368         # non-array_like `xdata`.
            if check_finite:
370             xdata = np.asarray_chkfinite(xdata)
            else:
```

```
372             xdata = np.asarray(xdata)

374     # Determine type of sigma
        if sigma is not None:
376         sigma = np.asarray(sigma)

378         # if 1-d, sigma are errors, define transform = 1/sigma
            if sigma.shape == (ydata.size, ):
380             transform = 1.0 / sigma
            # if 2-d, sigma is the covariance matrix,
382         # define transform = L such that L L^T = C
            elif sigma.shape == (ydata.size, ydata.size):
384             try:
                    # scipy.linalg.cholesky requires lower=True to
    return L L^T = A
386                 transform = cholesky(sigma, lower=True)
                except LinAlgError:
388                 raise ValueError("`sigma` must be positive
    definite.")
            else:
390             raise ValueError("`sigma` has incorrect shape.")
        else:
392         transform = None

394     func = _wrap_func(f, xdata, ydata, transform)
        if callable(jac):
396         jac = _wrap_jac(jac, xdata, transform)
        elif jac is None and method != 'lm':
398         jac = '2-point'

400     if method == 'lm':
            # Remove full_output from kwargs, otherwise we're passing
    it in twice.
402         return_full = kwargs.pop('full_output', False)
            res = leastsq(func, p0, Dfun=jac, full_output=1, **kwargs)
404         popt, pcov, infodict, errmsg, ier = res
            cost = np.sum(infodict['fvec'] ** 2)
406         if ier not in [1, 2, 3, 4]:
                raise RuntimeError("Optimal parameters not found: " +
    errmsg)
408     else:
            # Rename maxfev (leastsq) to max_nfev (least_squares), if
    specified.
```

```
410         if 'max_nfev' not in kwargs:
                kwargs['max_nfev'] = kwargs.pop('maxfev', None)
412
            res = least_squares(func, p0, jac=jac, bounds=bounds,
    method=method)
414
            if not res.success:
416             raise RuntimeError("Optimal parameters not found: " +
    res.message)

418         cost = 2 * res.cost  # res.cost is half sum of squares!
            popt = res.x
420
            # Do Moore-Penrose inverse discarding zero singular values
    .
422         _, s, VT = svd(res.jac, full_matrices=False)
            threshold = np.finfo(float).eps * max(res.jac.shape) * s
    [0]
424         s = s[s > threshold]
            VT = VT[:s.size]
426         pcov = np.dot(VT.T / s**2, VT)
            return_full = False
428
        warn_cov = False
430     if pcov is None:
            # indeterminate covariance
432         pcov = zeros((len(popt), len(popt)), dtype=float)
            pcov.fill(inf)
434         warn_cov = True
        elif not absolute_sigma:
436         if ydata.size > p0.size:
                s_sq = cost / (ydata.size - p0.size)
438             pcov = pcov * s_sq
            else:
440             pcov.fill(inf)
                warn_cov = True
442
        if warn_cov:
444         warnings.warn('Covariance of the parameters could not be
    estimated',
                          category=OptimizeWarning)
446
        if return_full:
```

```
448         return popt, pcov, infodict, errmsg, ier
    else:
450         return popt, pcov

452 def prepare_bounds(bounds, n):
    lb, ub = [np.asarray(b, dtype=float) for b in bounds]
454
    if lb.ndim == 0:
456         lb = np.resize(lb, n)

458 if ub.ndim == 0:
        ub = np.resize(ub, n)
460
    return lb, ub
462
def _wrap_func(func, xdata, ydata, transform):
464 if transform is None:
        def func_wrapped(params):
466         return func(xdata, *params) - ydata
    elif transform.ndim == 1:
468     def func_wrapped(params):
            return transform * (func(xdata, *params) - ydata)
470 else:
        # Chisq = (y - yd)^T C^{-1} (y-yd)
472     # transform = L such that C = L L^T
        # C^{-1} = L^{-T} L^{-1}
474     # Chisq = (y - yd)^T L^{-T} L^{-1} (y-yd)
        # Define (y-yd)' = L^{-1} (y-yd)
476     # by solving
        # L (y-yd)' = (y-yd)
478     # and minimize (y-yd)'^T (y-yd)'
        def func_wrapped(params):
480         return solve_triangular(transform, func(xdata, *params
    ) - ydata, lower=True)
    return func_wrapped
482
def Build_Boundaries (Width,Offset,T,NT,WidthLimit,XOffsetLow,
    XOffsetHigh,TLow,THigh,NTLow,NTHigh,NTCount):
484   Guess = []            #Initial guesses
  Bounds = []             #Bounds for fit
486   Bounds.append([])       #Lower bounds aka b[0]
  Bounds.append([])       #Upper bounds aka b[1]
488
```

```
    Guess.append(Width)       #Width initial guess
    Guess.append(Offset)      #xoffset initial guess (in MHz)
    Guess.append(T)         #T
    for i in range(NTCount):
        Guess.append(NT)        #NT[i]

    Bounds[0].append(0.0)     #Width lower limit
    Bounds[1].append(WidthLimit)  #Width upper limit, this is my
        best guess at an upper limit based on fucking around with the
        fits
    Bounds[0].append(XOffsetLow)  #xoffset lower limit
    Bounds[1].append(XOffsetHigh)#xoffset upper limit, this is my
        best guess at an upper limit based on fucking around with the
        fits
    Bounds[0].append(TLow)      #T lower limit
    Bounds[1].append(THigh)     #T upper limit, this is my best guess
        at an upper limit based on fucking around with the fits
    for i in range(NTCount):
        Bounds[0].append(NTLow)     #NT1 lower limit
        Bounds[1].append(NTHigh)      #NT1 upper limit, this is my best
        guess at an upper limit based on fucking around with the fits

    return Guess,Bounds

def Build_XAxis(Header):
    if (Header['CTYPE3'] != 'FREQ      '):
        return -1
    StartX = Header['CRVAL3']
    XStep = Header['CDELT3']
    X = np.zeros(Header['NAXIS3'])
    for i in range(Header['NAXIS3']):
        X = StartX+i*XStep
    return X

###################################
##################  Code Starts Here
SaveData =       True  #Save the data, THIS WILL OVERWRITE THE
    CURRENT DATA UNLESS YOU CHANGE THE FILENAMES BELOW
ErrorCheck =     True  #Check and mask pixels with high error
SecondaryFitting =  False #Perform secondary fitting of the data
PlotErrorMaps =    True  #Plot maps of the error
PlotSecondaryMaps = True  #Plot Velocity and width
PlotPrimaryMaps =    True  #Plot NT and T
```

```
SavePlots =      True  #Save the plots, this just saves literally
    anything you have enabled for plotting
526
StartTime = time.time()    #
528 VLSR = 6.5           #Initial guess at VLSR,
bmaj = 0.38          #Size of the synthesized beam along the major
    axis, units are arcsec
530 bmin = 0.35          #Size of the synthesized beam along the minor
    axis, units are arcsec
BeamSize = bmaj*bmin    #Knocking this calculation out early,
    debatably necessary
532 CellSize = 0.05       #size of a pixel in arcsec
FileName = 'ALMA v2_7'    #Parent file name we'll be using to save
534 BeamPixX = 7         #Pixels to use in X
BeamPixY = 7         #Pixels to use in Y
536 BeamSize = (BeamPixX*BeamPixY)*CellSize**2.0  #Superseding the
    true beam with the actual beam we use
FitThreshold = 0.043#0.052      #Threshold for initial pixel
    testing, we fit if the amplitude of a channel within range is
    above this value
538
WidthGuess =  0.2
540 XOffsetGuess = -3.3
TGuess =     200.0
542 NTGuess =      1.0E+15
WidthLimit =  1.5   #Only the upper limit is specified since by
    definition the width can never be below 0
544 XOffsetLow =  -5.3
XOffsetHigh =    -1.3
546 TLow =       10.0
THigh =      800.0
548 NTLow =      1.0E+7      #Using the same limits for both columns,
    since it really shouldnt matter
NTHigh =     1.0E+20
550 cc  =        2.99792458e10

552 print 'Loading Fits file'
data_13C,header_13C = Load_Fits_File('../13CH3CN/
    Orion_KL_13CH3CN_8_7_Reclean_image.image.fits')
554 data_D,header_D = Load_Fits_File('../Deuterium/
    Orion_KL_CH2DCN_9_8_image.image.fits')
data_D_918,header_D_918 = Load_Fits_File('../Deuterium/
    Orion_KL_CH2DCN_9_18_8_17_image.image.fits')
```

```
556 data_D_919,header_D_919 = Load_Fits_File('../Deuterium/
    Orion_KL_CH2DCN_9_19_8_18_image.image.fits')

558 x_D = plb.loadtxt('../Deuterium/DataCube_135_185_XAxis.txt')  #
    Loading the X axis data, X DATA ARE NOT EVENTLY SPACED IN
    FREQUENCY SPACE
    x_D_918 = plb.loadtxt('../Deuterium/918_XAxis.txt')
560 x_D_919 = plb.loadtxt('../Deuterium/919_XAxis.txt')
    x_13C = plb.loadtxt('../13CH3CN/13CH3CN_XAxis.txt')
562
    print 'Loading molecular line data'
564 Catalog_D = Load_Mol_Data('../Deuterium/CH2DCN Full Cat Band 1.tsv
    ')
    Catalog_D_918 = Load_Mol_Data('../Deuterium/CH2DCN_918.tsv')
566 Catalog_D_919 = Load_Mol_Data('../Deuterium/CH2DCN_919.tsv')
    Catalog_13C = Load_Mol_Data('../13CH3CN/13CH3CN_NoHF.tsv')
568
    #######Map Parameters
570 StartX = 450-256          #Starting pixel in X
    StopX  = 670-256          #Stopping pixel in X
572 StartY = 360-256          #Starting pixel in Y
    StopY  = 620-256          #Stopping pixel in Y
574 SizeX = StopX-StartX        #Total pixels in X
    SizeY = StopY-StartY        #Total pixels in Y, handy for the loops
    tp come
576
    #######Fitting Parameters
578 c,d  =  Build_Boundaries (WidthGuess,XOffsetGuess,TGuess,NTGuess,
    WidthLimit,XOffsetLow,XOffsetHigh,TLow,THigh,NTLow,NTHigh,2)
    c1,d =  Build_Boundaries (WidthLimit,XOffsetGuess,TGuess,NTGuess,
    WidthLimit,XOffsetLow,XOffsetHigh,TLow,THigh,NTLow,NTHigh,2)
580 c2,d =  Build_Boundaries (WidthGuess,XOffsetHigh,TGuess,NTGuess,
    WidthLimit,XOffsetLow,XOffsetHigh,TLow,THigh,NTLow,NTHigh,2)
    c3,d =  Build_Boundaries (WidthGuess,XOffsetGuess,75.0,NTGuess,
    WidthLimit,XOffsetLow,XOffsetHigh,TLow,THigh,NTLow,NTHigh,2)
582 c4,d =  Build_Boundaries (WidthGuess,XOffsetGuess,TGuess,1.0E+14,
    WidthLimit,XOffsetLow,XOffsetHigh,TLow,THigh,NTLow,NTHigh,2)
    c5,d =  Build_Boundaries (WidthGuess,XOffsetGuess,TGuess,1.0E+16,
    WidthLimit,XOffsetLow,XOffsetHigh,TLow,THigh,NTLow,NTHigh,2)
584 c6,d =  Build_Boundaries (WidthGuess,XOffsetLow,75.0,NTGuess,
    WidthLimit,XOffsetLow,XOffsetHigh,TLow,THigh,NTLow,NTHigh,2)
    c7,d =  Build_Boundaries (WidthGuess,XOffsetHigh,75.0,NTGuess,
    WidthLimit,XOffsetLow,XOffsetHigh,TLow,THigh,NTLow,NTHigh,2)
```

```
c8,d =  Build_Boundaries (WidthGuess,XOffsetGuess,350.0,NTGuess,
    WidthLimit,XOffsetLow,XOffsetHigh,TLow,THigh,NTLow,NTHigh,2)
c9,d =  Build_Boundaries (WidthGuess,XOffsetHigh,75.0,NTGuess,
    WidthLimit,XOffsetLow,XOffsetHigh,TLow,THigh,NTLow,NTHigh,2)
c10,d = Build_Boundaries (WidthLimit,XOffsetLow,TGuess,NTGuess,
    WidthLimit,XOffsetLow,XOffsetHigh,TLow,THigh,NTLow,NTHigh,2)
#c11,d = Build_Boundaries (WidthLimit,XOffsetHigh,TGuess,NTGuess,
    WidthLimit,XOffsetLow,XOffsetHigh,TLow,THigh,NTLow,NTHigh,2)
c11 = np.empty(np.shape(c1))
c11[:] = np.nan

a,b  = Build_Boundaries (WidthGuess,XOffsetGuess,TGuess,NTGuess,
    WidthLimit,XOffsetLow,XOffsetHigh,TLow,THigh,NTLow,NTHigh,1)

#######Map Arrays
ParameterMap = np.zeros((SizeX,SizeY,len(c)))
Errors = np.zeros((SizeX,SizeY,len(c)))     #An array to store all
    the errors we will generate for the fitting, using a fixed
    length declaration
RMSMap = np.zeros((SizeX,SizeY))          #An image of the RMS of
    the fit
DtoH = np.zeros((SizeX,SizeY))            #An image of the D/13C
    ratio in the cloud
FractionalError = np.zeros((SizeX,SizeY))
NTMap = np.zeros((SizeX,SizeY))

TemperatureArray = np.zeros(SizeX*SizeY)    #Linear array to track
    the temperature
NTArray1 = np.zeros(SizeX*SizeY)          #Linear array to track the
    column density
NTArray2 = np.zeros(SizeX*SizeY)          #Linear array to track the
    column density
TErrorArray = np.zeros(SizeX*SizeY)         #Linear array to track
    the temperature error
NTErrorArray = np.zeros(SizeX*SizeY)        #Linear array to track
    the column density error
DtoHArray = np.zeros(SizeX*SizeY)         #Linear array to track the
    D ot H ratio
OffsetArray = np.zeros(SizeX*SizeY)         #Linear array to track
    the D ot H ratio
NanArray = np.zeros(len(c))
AvgCov = np.zeros((len(c),len(c)))
DtoHArray2 = np.zeros((6,(SizeX*SizeY)))
```

```
Popts = np.zeros(SizeX*SizeY)

for i in range(len(c)): NanArray[i] = np.nan

########Fit the amplitudes etc of the map
DetectedPixels = 0          #A count of pixels where we decided to fit
Subx_D = x_D[0:1200]        #Making a smaller array for fitting to speed things up
Subx_D_918 = x_D_918[400:600] #Making a smaller array for fitting to speed things up
Subx_D_919 = x_D_919[450:650] #Making a smaller array for fitting to speed things up
Subx_13C = x_13C[1600:2400]   #Making a smaller array for fitting to speed things up
x = np.zeros(len(Subx_D)+len(Subx_13C)+len(Subx_D_918)+len(Subx_D_919))
Residual = np.zeros_like(x)
TotalFitResidual = np.zeros_like(x)
x[:len(Subx_D)] = Subx_D
x[len(Subx_D):len(Subx_D)+len(Subx_13C)] = Subx_13C
x[len(Subx_D)+len(Subx_13C):len(Subx_D)+len(Subx_13C)+len(Subx_D_918)] = Subx_D_918
x[len(Subx_D)+len(Subx_13C)+len(Subx_D_918):] = Subx_D_919


LineChannels = np.zeros((2,len(Catalog_D[0])+len(Catalog_13C[0])+len(Catalog_D_918[0])+len(Catalog_D_919[0])))  #A rough guess at the line channels based on the catalog and LSR LineChannels [Low/High][Line #]
for i in range(len(Catalog_D[0])):
  LineChannels[0][i] = Get_Index (Catalog_D[0][i]-3.5,x)-10
  LineChannels[1][i] = LineChannels[0][i]+20
for i in range(len(Catalog_13C[0])):
  LineChannels[0][i+len(Catalog_D[0])] = Get_Index (Catalog_13C[0][i]-3.5,Subx_13C)-10+len(Subx_D)
  LineChannels[1][i+len(Catalog_D[0])] = LineChannels[0][i+len(Catalog_D[0])]+20
for i in range(len(Catalog_D_918[0])):
  LineChannels[0][i+len(Catalog_D[0])+len(Catalog_13C[0])] = Get_Index (Catalog_D_918[0][i]-3.5,Subx_D_918)-10+len(Subx_D)+len(Subx_13C)
```

```
    LineChannels[1][i+len(Catalog_D[0])+len(Catalog_13C[0])] =
      LineChannels[0][i+len(Catalog_D[0])+len(Catalog_13C[0])]+20
for i in range(len(Catalog_D_919[0])):
    LineChannels[0][i+len(Catalog_D[0])+len(Catalog_13C[0])+len(
      Catalog_D_918[0])] = Get_Index (Catalog_D_919[0][i]-3.5,
      Subx_D_919)-10+len(Subx_D)+len(Subx_13C)+len(Subx_D_918)
    LineChannels[1][i+len(Catalog_D[0])+len(Catalog_13C[0])+len(
      Catalog_D_918[0])] = LineChannels[0][i+len(Catalog_D[0])+len(
      Catalog_13C[0])+len(Catalog_D_918[0])]+20

TemperatureLimitsCount = 0
ColumnLimitsCount = 0
WidthLimitsCount = 0
OffsetLimitsCount = 0

NewResult = 0
NewWidths = 0
NewWidth = 0.0

BetterWidth = 0
RefitChanged = 0
AmplitudeLimit = 0

print 'Starting initial processing'
for i in range(StartX,StopX):
    for j in range(StartY,StopY):
        print "Processing pixel X:"+str(i)+" Y:"+str(j)
        Spectrum_D = Get_Beam (data_D,BeamPixX,BeamPixY,i,j,0.0)
        Spectrum_D_918 = Get_Beam (data_D_918,BeamPixX,BeamPixY,i+256,
      j+256,0.0)
        if (Check_Fittable (Spectrum_D,FitThreshold,680,700) or
      Check_Fittable (Spectrum_D,FitThreshold,860,880) or
      Check_Fittable (Spectrum_D_918,FitThreshold,480,500)):  #Check
       to see that theres some amplitude in at least 1 of 2 regions,
       this speeds up fits immensely, since most pixels are garbage,
       for full images only 5-10% of pixels are useful
            DetectedPixels += 1   #Track useful pixels
            Spectrum_13C = Get_Beam (data_13C,BeamPixX,BeamPixY,i+256,j
      +256,0.0)
            Spectrum_D_919 = Get_Beam (data_D_919,BeamPixX,BeamPixY,i
      +256,j+256,0.0)
            y = np.zeros_like(x)
            SubSpectrum_D = Spectrum_D[0:1200]
```

```
    SubSpectrum_D_918 = Spectrum_D_918[400:600]
    SubSpectrum_D_919 = Spectrum_D_919[450:650]
    SubSpectrum_13C = Spectrum_13C[1600:2400]

    #######Curve Fitting
    RMS_D = Baseline_Subtract_D (SubSpectrum_D)
    RMS_D_918 = Baseline_Subtract_D_918 (SubSpectrum_D_918)
    RMS_D_919 = Baseline_Subtract_D_919 (SubSpectrum_D_919)
    RMS_13C = Baseline_Subtract_13C (SubSpectrum_13C)       # Subtract anything missed by UVContsub in the processing, this is often substantial, and since the fitting function doesnt include a DC offset, it substantially improves the fit

    y[:len(Subx_D)] = SubSpectrum_D
    y[len(Subx_D):len(Subx_D)+len(Subx_13C)] = SubSpectrum_13C
    y[len(Subx_D)+len(Subx_13C):len(Subx_D)+len(Subx_13C)+len(SubSpectrum_D_918)] = SubSpectrum_D_918
    y[len(Subx_D)+len(Subx_13C)+len(SubSpectrum_D_918):len(x)] = SubSpectrum_D_919

    popt,pcov = curve_fit(OptFuncC,x,y,p0=c,bounds=d) #popt[Width,Xoffset,T,NT1,NT2]

    Popts[(j-StartY)+(i-StartX)*SizeY] = np.nan
    if (SecondaryFitting):
      popt1,pcov = curve_fit_PBC(OptFuncC,x,y,p0=c1,bounds=d)
      popt2,pcov = curve_fit_PBC(OptFuncC,x,y,p0=c2,bounds=d)
      popt3,pcov = curve_fit_PBC(OptFuncC,x,y,p0=c3,bounds=d)
      popt4,pcov = curve_fit_PBC(OptFuncC,x,y,p0=c4,bounds=d)
      popt5,pcov = curve_fit_PBC(OptFuncC,x,y,p0=c5,bounds=d)
      popt6,pcov = curve_fit_PBC(OptFuncC,x,y,p0=c6,bounds=d)
      popt7,pcov = curve_fit_PBC(OptFuncC,x,y,p0=c7,bounds=d)
      popt8,pcov = curve_fit_PBC(OptFuncC,x,y,p0=c8,bounds=d)
      popt9,pcov = curve_fit_PBC(OptFuncC,x,y,p0=c9,bounds=d)
      popt10,pcov = curve_fit_PBC(OptFuncC,x,y,p0=c10,bounds=d)
      if (np.isfinite(c11[0])): popt11,pcov = curve_fit_PBC(OptFuncC,x,y,p0=c11,bounds=d)

      Residual0 = y-OptFuncC(x, *popt)
      Residual1 = y-OptFuncC(x, *popt1)
      Residual2 = y-OptFuncC(x, *popt2)
      Residual3 = y-OptFuncC(x, *popt3)
      Residual4 = y-OptFuncC(x, *popt4)
```

```
        Residual5 = y-OptFuncC(x, *popt5)
        Residual6 = y-OptFuncC(x, *popt6)
        Residual7 = y-OptFuncC(x, *popt7)
        Residual8 = y-OptFuncC(x, *popt8)
        Residual9 = y-OptFuncC(x, *popt9)
        Residual10 = y-OptFuncC(x, *popt10)
        if (np.isfinite(c11[0])): Residual11 = y-OptFuncC(x, *
    popt11)

        RMS0 = Compute_RMS_Diff_Tuple (LineChannels[0],
    LineChannels[1],Residual0,y)
        RMS1 = Compute_RMS_Diff_Tuple (LineChannels[0],
    LineChannels[1],Residual1,y)
        RMS2 = Compute_RMS_Diff_Tuple (LineChannels[0],
    LineChannels[1],Residual2,y)
        RMS3 = Compute_RMS_Diff_Tuple (LineChannels[0],
    LineChannels[1],Residual3,y)
        RMS4 = Compute_RMS_Diff_Tuple (LineChannels[0],
    LineChannels[1],Residual4,y)
        RMS5 = Compute_RMS_Diff_Tuple (LineChannels[0],
    LineChannels[1],Residual5,y)
        RMS6 = Compute_RMS_Diff_Tuple (LineChannels[0],
    LineChannels[1],Residual6,y)
        RMS7 = Compute_RMS_Diff_Tuple (LineChannels[0],
    LineChannels[1],Residual7,y)
        RMS8 = Compute_RMS_Diff_Tuple (LineChannels[0],
    LineChannels[1],Residual8,y)
        RMS9 = Compute_RMS_Diff_Tuple (LineChannels[0],
    LineChannels[1],Residual9,y)
        RMS10 = Compute_RMS_Diff_Tuple (LineChannels[0],
    LineChannels[1],Residual10,y)
        if (np.isfinite(c11[0])):RMS11 = Compute_RMS_Diff_Tuple (
    LineChannels[0],LineChannels[1],Residual11,y)

        RMSs = [RMS0,RMS1,RMS2,RMS3,RMS4,RMS5,RMS6,RMS7,RMS8,RMS9,
    RMS10]
        if (np.isfinite(c11[0])): RMSs.append(RMS11)
        popts = [popt,popt1,popt2,popt3,popt4,popt5,popt6,popt7,
    popt8,popt9,popt10]
        if (np.isfinite(c11[0])): popts.append(popt11)
        Opt = np.argmin(RMSs)
        if (Opt != 0):
          RefitChanged+=1
```

```
            print 'Refitting worked: '
736         print 'Original parameters: RMS was: '+str(RMS0)
            print '%e  ' % popt[0]+'%g  ' % popt[1]+'%g  ' % popt
    [2]+'%e  ' % popt[3]+'%e ' % popt[4]
738         print 'Better fit was: improvement was: '+str(abs(RMS0-
    RMSs[Opt])/RMS0)+str(' using fit: ')+str(Opt)
            #print '%e  ' % popts[Opt][0]+'%g  ' % popts[Opt][1]+'%
    g  ' % popts[Opt][2]+'%e ' % popts[Opt][3]+'%e ' % popts[Opt
    ][4]
740
          popt = popts[Opt]
742       if (3.0*np.amax(OptFuncC(x, *popt)) < RMS_D):
            popt = NanArray
744         AmplitudeLimit +=1
          Popts[(j-StartY)+(i-StartX)*SizeY] = Opt
746
        XOffset_Fix = popt[1]
748     Sigma_Fix = popt[0]
        TFix = popt[2]
750     NTOpt,NTCov = curve_fit(OptFuncNTT,x,y,p0=a,bounds=b)
        NTErr = np.sqrt(np.diag(NTCov))
752
        AvgCov += pcov
754     ParameterMap[i-StartX][j-StartY] = popt
        Errors[i-StartX][j-StartY] = np.sqrt(np.diag(pcov)) #Convert
     to proper errors and store them
756     print '%e  ' % popt[0]+'%g  ' % popt[1]+'%g  ' % popt[2]+'
    %e  ' % popt[3]+'%e ' % popt[4]   #Keeping this print call in
    cause it looks cool

758     Residual = y-OptFuncC(x, *popt)           #First compute the
     residual, this is done separately to make it easy to compute
    this pixel's rms
        TotalFitResidual += Residual            #Add this to the map
    -averaged residual
760
#       if (Residual[2089] < -0.015):
762 #       plt.plot(y,'r-')
#         plt.plot(OptFuncC(x,*popt),'b-')
764 #       plt.plot(Residual,'g-')
#         plt.show()
766
```

```
            RMSMap[i-StartX][j-StartY] = Compute_RMS_Diff_Tuple (
        LineChannels[0],LineChannels[1],Residual,y)
768         DtoH[i-StartX][j-StartY] = popt[3]/popt[4]
            TemperatureArray[(j-StartY)+(i-StartX)*SizeY] = ParameterMap
        [i-StartX][j-StartY][2]
770         NTArray1[(j-StartY)+(i-StartX)*SizeY] = ParameterMap[i-
        StartX][j-StartY][3]
            NTArray2[(j-StartY)+(i-StartX)*SizeY] = ParameterMap[i-
        StartX][j-StartY][4]
772         TErrorArray[(j-StartY)+(i-StartX)*SizeY] = Errors[i-StartX][
        j-StartY][2]
            NTErrorArray[(j-StartY)+(i-StartX)*SizeY] = np.sqrt((Errors[
        i-StartX][j-StartY][3]/popt[3])**2.0 + (Errors[i-StartX][j-
        StartY][4]/popt[4])**2.0)*DtoH[i-StartX][j-StartY]#Errors[i-
        StartX][j-StartY][3]
774         DtoHArray[(j-StartY)+(i-StartX)*SizeY] = DtoH[i-StartX][j-
        StartY]
            NTMap[i-StartX][j-StartY] = popt[3]+popt[4]
776
            if ((i-StartX > 25) and (i-StartX < 52) and (j-StartY > 141)
         and (j-StartY < 185)):
778             DtoHArray2[0][(j-StartY)+(i-StartX)*SizeY] = DtoH[i-StartX
        ][j-StartY]
                DtoHArray2[1][(j-StartY)+(i-StartX)*SizeY] = np.nan
780             DtoHArray2[2][(j-StartY)+(i-StartX)*SizeY] = np.nan
                DtoHArray2[3][(j-StartY)+(i-StartX)*SizeY] = np.nan
782             DtoHArray2[4][(j-StartY)+(i-StartX)*SizeY] = np.nan
                DtoHArray2[5][(j-StartY)+(i-StartX)*SizeY] = np.nan
784         elif ((i-StartX > 30) and (i-StartX < 73) and (j-StartY >
        103) and (j-StartY < 135)):
                DtoHArray2[0][(j-StartY)+(i-StartX)*SizeY] = np.nan
786             DtoHArray2[1][(j-StartY)+(i-StartX)*SizeY] = DtoH[i-StartX
        ][j-StartY]
                DtoHArray2[2][(j-StartY)+(i-StartX)*SizeY] = np.nan
788             DtoHArray2[3][(j-StartY)+(i-StartX)*SizeY] = np.nan
                DtoHArray2[4][(j-StartY)+(i-StartX)*SizeY] = np.nan
790             DtoHArray2[5][(j-StartY)+(i-StartX)*SizeY] = np.nan
            elif ((i-StartX > 64) and (i-StartX < 95) and (j-StartY >
        52) and (j-StartY < 103)):
792             DtoHArray2[0][(j-StartY)+(i-StartX)*SizeY] = np.nan
                DtoHArray2[1][(j-StartY)+(i-StartX)*SizeY] = np.nan
794             DtoHArray2[2][(j-StartY)+(i-StartX)*SizeY] = DtoH[i-StartX
        ][j-StartY]
```

```
            DtoHArray2[3][(j-StartY)+(i-StartX)*SizeY] = np.nan
            DtoHArray2[4][(j-StartY)+(i-StartX)*SizeY] = np.nan
            DtoHArray2[5][(j-StartY)+(i-StartX)*SizeY] = np.nan
        elif ((i-StartX > 120) and (i-StartX < 142) and (j-StartY > 134) and (j-StartY < 162)):
            DtoHArray2[0][(j-StartY)+(i-StartX)*SizeY] = np.nan
            DtoHArray2[1][(j-StartY)+(i-StartX)*SizeY] = np.nan
            DtoHArray2[2][(j-StartY)+(i-StartX)*SizeY] = np.nan
            DtoHArray2[3][(j-StartY)+(i-StartX)*SizeY] = DtoH[i-StartX][j-StartY]
            DtoHArray2[4][(j-StartY)+(i-StartX)*SizeY] = np.nan
            DtoHArray2[5][(j-StartY)+(i-StartX)*SizeY] = np.nan
        elif ((i-StartX > 164) and (i-StartX < 192) and (j-StartY > 25) and (j-StartY < 55)):
            DtoHArray2[0][(j-StartY)+(i-StartX)*SizeY] = np.nan
            DtoHArray2[1][(j-StartY)+(i-StartX)*SizeY] = np.nan
            DtoHArray2[2][(j-StartY)+(i-StartX)*SizeY] = np.nan
            DtoHArray2[3][(j-StartY)+(i-StartX)*SizeY] = np.nan
            DtoHArray2[4][(j-StartY)+(i-StartX)*SizeY] = DtoH[i-StartX][j-StartY]
            DtoHArray2[5][(j-StartY)+(i-StartX)*SizeY] = np.nan
        elif ((i-StartX > 154) and (i-StartX < 185) and (j-StartY > 215) and (j-StartY < 242)):
            DtoHArray2[0][(j-StartY)+(i-StartX)*SizeY] = np.nan
            DtoHArray2[1][(j-StartY)+(i-StartX)*SizeY] = np.nan
            DtoHArray2[2][(j-StartY)+(i-StartX)*SizeY] = np.nan
            DtoHArray2[3][(j-StartY)+(i-StartX)*SizeY] = np.nan
            DtoHArray2[4][(j-StartY)+(i-StartX)*SizeY] = np.nan
            DtoHArray2[5][(j-StartY)+(i-StartX)*SizeY] = DtoH[i-StartX][j-StartY]
        else:
            DtoHArray2[0][(j-StartY)+(i-StartX)*SizeY] = np.nan
            DtoHArray2[1][(j-StartY)+(i-StartX)*SizeY] = np.nan
            DtoHArray2[2][(j-StartY)+(i-StartX)*SizeY] = np.nan
            DtoHArray2[3][(j-StartY)+(i-StartX)*SizeY] = np.nan
            DtoHArray2[4][(j-StartY)+(i-StartX)*SizeY] = np.nan
            DtoHArray2[5][(j-StartY)+(i-StartX)*SizeY] = np.nan


        FractionalError[i-StartX][j-StartY] = RMSMap[i-StartX][j-StartY]/(ParameterMap[i-StartX][j-StartY][3]+ParameterMap[i-StartX][j-StartY][4])
```

```
830         if (abs(popt[0]-WidthLimit)< 0.001):
              WidthLimitsCount += 1
832           popt1,pcov = curve_fit(OptFuncC,x,y,p0=[WidthGuess,
    XOffsetLow,240.0,NTGuess,NTGuess],bounds=d)
              popt2,pcov = curve_fit(OptFuncC,x,y,p0=[WidthGuess,
    XOffsetHigh,240.0,NTGuess,NTGuess],bounds=d)
834           print 'New fit: '+str(popt1)
              print 'New fit: '+str(popt2)
836           if ((abs(popt1[0]-WidthLimit)> 0.001) or (abs(popt2[0]-
    WidthLimit)> 0.001)):
                BetterWidth +=1
838           ParameterMap[i-StartX][j-StartY] = NanArray
              Errors[i-StartX][j-StartY] = NanArray
840           RMSMap[i-StartX][j-StartY] = np.nan
              DtoH[i-StartX][j-StartY] = np.nan
842           TemperatureArray[(j-StartY)+(i-StartX)*SizeY] = np.nan
              NTArray1[(j-StartY)+(i-StartX)*SizeY] = np.nan
844           NTArray2[(j-StartY)+(i-StartX)*SizeY] = np.nan
              TErrorArray[(j-StartY)+(i-StartX)*SizeY] = np.nan
846           NTErrorArray[(j-StartY)+(i-StartX)*SizeY] = np.nan
              DtoHArray[(j-StartY)+(i-StartX)*SizeY] = np.nan
848           FractionalError[i-StartX][j-StartY] = np.nan
              NTMap[i-StartX][j-StartY] = np.nan
850         if ((abs(popt[1]-XOffsetLow)< 0.001) or (abs(popt[1]-
    XOffsetHigh)< 0.001)):
              OffsetLimitsCount += 1
852           ParameterMap[i-StartX][j-StartY] = NanArray
              Errors[i-StartX][j-StartY] = NanArray
854           RMSMap[i-StartX][j-StartY] = np.nan
              DtoH[i-StartX][j-StartY] = np.nan
856           TemperatureArray[(j-StartY)+(i-StartX)*SizeY] = np.nan
              NTArray1[(j-StartY)+(i-StartX)*SizeY] = np.nan
858           NTArray2[(j-StartY)+(i-StartX)*SizeY] = np.nan
              TErrorArray[(j-StartY)+(i-StartX)*SizeY] = np.nan
860           NTErrorArray[(j-StartY)+(i-StartX)*SizeY] = np.nan
              DtoHArray[(j-StartY)+(i-StartX)*SizeY] = np.nan
862           FractionalError[i-StartX][j-StartY] = np.nan
              NTMap[i-StartX][j-StartY] = np.nan
864         if ((abs(popt[2]-TLow)< 0.001) or (abs(popt[2]-THigh)<
    0.001)):
              TemperatureLimitsCount += 1
866           ParameterMap[i-StartX][j-StartY] = NanArray
              Errors[i-StartX][j-StartY] = NanArray
```

```
868             RMSMap[i-StartX][j-StartY] = np.nan
                DtoH[i-StartX][j-StartY] = np.nan
870             TemperatureArray[(j-StartY)+(i-StartX)*SizeY] = np.nan
                NTArray1[(j-StartY)+(i-StartX)*SizeY] = np.nan
872             NTArray2[(j-StartY)+(i-StartX)*SizeY] = np.nan
                TErrorArray[(j-StartY)+(i-StartX)*SizeY] = np.nan
874             NTErrorArray[(j-StartY)+(i-StartX)*SizeY] = np.nan
                DtoHArray[(j-StartY)+(i-StartX)*SizeY] = np.nan
876             FractionalError[i-StartX][j-StartY] = np.nan
                NTMap[i-StartX][j-StartY] = np.nan
878           if ((abs(popt[3]-NTLow)< 0.001) or (abs(popt[3]-NTHigh)<
        0.001) or (abs(popt[4]-NTLow)< 0.001) or (abs(popt[4]-NTHigh)<
         0.001)):
                ColumnLimitsCount += 1
880             ParameterMap[i-StartX][j-StartY] = NanArray
                Errors[i-StartX][j-StartY] = NanArray
882             RMSMap[i-StartX][j-StartY] = np.nan
                DtoH[i-StartX][j-StartY] = np.nan
884             TemperatureArray[(j-StartY)+(i-StartX)*SizeY] = np.nan
                NTArray1[(j-StartY)+(i-StartX)*SizeY] = np.nan
886             NTArray2[(j-StartY)+(i-StartX)*SizeY] = np.nan
                TErrorArray[(j-StartY)+(i-StartX)*SizeY] = np.nan
888             NTErrorArray[(j-StartY)+(i-StartX)*SizeY] = np.nan
                DtoHArray[(j-StartY)+(i-StartX)*SizeY] = np.nan
890             FractionalError[i-StartX][j-StartY] = np.nan
                NTMap[i-StartX][j-StartY] = np.nan
892
              c11 = popt
894
#             plt.axis([156200,156310,-0.01,0.05])
896 #             plt.plot(SubSpectrum,'r+-')
#             plt.plot(OptFunc2(Subx, *a), 'b-')
898 #             plt.plot(OptFunc2(Subx, *popt), 'g-')
#             ax = plt.gca()
900 #             ax.get_xaxis().get_major_formatter().set_useOffset(False)
#             plt.show()
902


904           else : #Set the pixel value to nan if we dont use it,
        strangely this simplifies things later
              ParameterMap[i-StartX][j-StartY] = NanArray
906           Errors[i-StartX][j-StartY] = NanArray
              RMSMap[i-StartX][j-StartY] = np.nan
```

```
908         DtoH[i-StartX][j-StartY] = np.nan
            TemperatureArray[(j-StartY)+(i-StartX)*SizeY] = np.nan
910         NTArray1[(j-StartY)+(i-StartX)*SizeY] = np.nan
            NTArray2[(j-StartY)+(i-StartX)*SizeY] = np.nan
912         TErrorArray[(j-StartY)+(i-StartX)*SizeY] = np.nan
            NTErrorArray[(j-StartY)+(i-StartX)*SizeY] = np.nan
914         DtoHArray[(j-StartY)+(i-StartX)*SizeY] = np.nan
            FractionalError[i-StartX][j-StartY] = np.nan
916         NTMap[i-StartX][j-StartY] = np.nan
            DtoHArray2[0][(j-StartY)+(i-StartX)*SizeY] = np.nan
918         DtoHArray2[1][(j-StartY)+(i-StartX)*SizeY] = np.nan
            DtoHArray2[2][(j-StartY)+(i-StartX)*SizeY] = np.nan
920         DtoHArray2[3][(j-StartY)+(i-StartX)*SizeY] = np.nan
            DtoHArray2[4][(j-StartY)+(i-StartX)*SizeY] = np.nan
922         DtoHArray2[5][(j-StartY)+(i-StartX)*SizeY] = np.nan
            c11[:] = np.nan
924         Popts[(j-StartY)+(i-StartX)*SizeY] = np.nan

926 print 'Refitting gave a new velocity '+str(NewResult)+' times'
    print 'Refitting gave a new width '+str(NewWidths)+' times, on
        average the new width was '+str(NewWidth)
928
    print 'I found '+str(WidthLimitsCount)+' pixels at the width limit
        '
930 print 'I found '+str(OffsetLimitsCount)+' pixels at the velocity
        limit'
    print 'I found '+str(TemperatureLimitsCount)+' pixels at the
        temperature limit'
932 print 'I found '+str(ColumnLimitsCount)+' pixels at the column
        limit'

934 print str(AmplitudeLimit)+' amplitude limits hit'

936 print 'Better width: '+str(BetterWidth)
    print 'Refit worked '+str(RefitChanged)+' times'
938
    TotalFitResidual/=DetectedPixels
940
    #######Check the data for obvious errors
942 if (ErrorCheck):
      print 'Map fitting is complete, running qa on maps'
944   WidthErrors = 0
      VelocityErrors = 0
```

```
946 ColumnErrors = 0
    TemperatureErrors = 0
948 for i in range(StartX,StopX):
      for j in range(StartY,StopY):
950     if (np.isfinite(ParameterMap[i-StartX][j-StartY][1])):  #
     Width
          if (3.0*Errors[i-StartX][j-StartY][0] > ParameterMap[i-
     StartX][j-StartY][0]): #Reject pixel if its error is too great
952         ParameterMap[i-StartX][j-StartY] = NanArray
            Errors[i-StartX][j-StartY] = NanArray
954         RMSMap[i-StartX][j-StartY] = np.nan
            DtoH[i-StartX][j-StartY] = np.nan
956         WidthErrors += 1
            break
958       if (3.0*Errors[i-StartX][j-StartY][1] > abs(ParameterMap[i
     -StartX][j-StartY][1])):
            ParameterMap[i-StartX][j-StartY] = NanArray
960         Errors[i-StartX][j-StartY] = NanArray
            RMSMap[i-StartX][j-StartY] = np.nan
962         DtoH[i-StartX][j-StartY] = np.nan
            VelocityErrors += 1
964         break
          if (3.0*Errors[i-StartX][j-StartY][2] > ParameterMap[i-
     StartX][j-StartY][2]):
966         ParameterMap[i-StartX][j-StartY] = NanArray
            Errors[i-StartX][j-StartY] = NanArray
968         RMSMap[i-StartX][j-StartY] = np.nan
            DtoH[i-StartX][j-StartY] = np.nan
970         TemperatureErrors += 1
            break
972       if ((3.0*Errors[i-StartX][j-StartY][3] > ParameterMap[i-
     StartX][j-StartY][3]) or (3.0*Errors[i-StartX][j-StartY][3] >
     ParameterMap[i-StartX][j-StartY][4]) or (ParameterMap[i-StartX
     ][j-StartY][3] < 1.0E+11) or (ParameterMap[i-StartX][j-StartY
     ][4] < 1.0E+11)):
            ParameterMap[i-StartX][j-StartY] = NanArray
974         Errors[i-StartX][j-StartY] = NanArray
            RMSMap[i-StartX][j-StartY] = np.nan
976         DtoH[i-StartX][j-StartY] = np.nan
            ColumnErrors += 1
978         break
```

```
    print 'I found '+str(WidthErrors)+' pixels with an unacceptable
     width error'
    print 'I found '+str(VelocityErrors)+' pixels with an
     unacceptable velocity error'
    print 'I found '+str(ColumnErrors)+' pixels with an unacceptable
      column error'
    print 'I found '+str(TemperatureErrors)+' pixels with an
     unacceptable temperature error'
    print str(WidthErrors+VelocityErrors+ColumnErrors+
     TemperatureErrors)+' total pixels rejected'

    print 'Covariance Matrix:'
    print '\t Width\t\t Velocity\t\t T\t\t NT1\t\t NT2'
    print 'Width: \t %e'% AvgCov[0][0]+'\t %e' % AvgCov[0][1]+'\t %e
     ' % AvgCov[0][2]+'\t %e' % AvgCov[0][3]+'\t %e' % AvgCov[0][4]
    print 'Vel:\t %e' % AvgCov[1][0]+'\t %e' % AvgCov[1][1]+'\t %e'
     % AvgCov[1][2]+'\t %e' % AvgCov[1][3]+'\t %e' % AvgCov[1][4]
    print 'T:\t %e'   % AvgCov[2][0]+'\t %e' % AvgCov[2][1]+'\t %e'
     % AvgCov[2][2]+'\t %e' % AvgCov[2][3]+'\t %e' % AvgCov[2][4]
    print 'NT1:\t %e' % AvgCov[3][0]+'\t %e' % AvgCov[3][1]+'\t %e'
     % AvgCov[3][2]+'\t %e' % AvgCov[3][3]+'\t %e' % AvgCov[3][4]
    print 'NT2:\t %e' % AvgCov[4][0]+'\t %e' % AvgCov[4][1]+'\t %e'
     % AvgCov[4][2]+'\t %e' % AvgCov[4][3]+'\t %e' % AvgCov[4][4]

for i in range(StartX,StopX):
    for j in range(StartY,StopY):
        if (np.isfinite(ParameterMap[i-StartX][j-StartY][1])):  #
    Width
            ParameterMap[i-StartX][j-StartY][0] = MHz_to_Kms (
    ParameterMap[i-StartX][j-StartY][0],header_D['RESTFRQ']*1.0E
    -6)
            ParameterMap[i-StartX][j-StartY][1] = -1.0*MHz_to_Kms (
    ParameterMap[i-StartX][j-StartY][1],header_D['RESTFRQ']*1.0E
    -6)
            #popt[Width,Xoffset,T,NT1,NT2]


######Plot the results
RMSMap = np.swapaxes(RMSMap,0,1)
Errors = np.swapaxes(Errors,0,2)
ParameterMap = np.swapaxes(ParameterMap,0,2)
DtoH = np.swapaxes(DtoH,0,1)
FractionalError = np.swapaxes(FractionalError,0,1)
```

```
1008 NTMap = np.swapaxes(NTMap,0,1)

1010 #Mask all the non-detected pixels, this should greatly simplify
     the maps visually
     ParameterMap = np.ma.masked_where(np.isnan(ParameterMap),
     ParameterMap)
1012 DtoH = np.ma.masked_where(np.isnan(DtoH), DtoH)
     RMSMap = np.ma.masked_where(np.isnan(RMSMap), RMSMap)
1014 Errors = np.ma.masked_where(np.isnan(Errors), Errors)
     FractionalError = np.ma.masked_where(np.isnan(FractionalError),
     FractionalError)
1016 NTMap = np.ma.masked_where(np.isnan(NTMap), NTMap)

1018 FullTime = time.time()
     print 'Mapping complete'
1020 print "I found "+str(DetectedPixels)+" pixels with the line ("+str
     (float(DetectedPixels*100.0)/(SizeX*SizeY))+" %)"
     print 'All processing complete, full execution time:'+str(FullTime
     -StartTime)+'s ('+str((FullTime-StartTime)/60.0)+'min)'
1022



1024
     if (PlotErrorMaps):
1026   ymax = np.argmax(TotalFitResidual)
       ymin = np.argmin(TotalFitResidual)
1028   plt.title('ALMA Fitting v2.7 - Average Residual across all fits'
       )
       plt.plot((1200,1200),(TotalFitResidual[ymin],TotalFitResidual[
       ymax]),'k--')
1030   plt.plot((2000,2000),(TotalFitResidual[ymin],TotalFitResidual[
       ymax]),'k--')
       plt.plot((2200,2200),(TotalFitResidual[ymin],TotalFitResidual[
       ymax]),'k--')
1032   ax = plt.gca()
       ax.get_xaxis().get_major_formatter().set_useOffset(False)
1034   for i in range(len(LineChannels[0])):
         ax.add_patch(patches.Rectangle((LineChannels[0][i],
       TotalFitResidual[ymin]),LineChannels[1][i]-LineChannels[0][i],
       TotalFitResidual[ymax]-TotalFitResidual[ymin],alpha=0.1))
1036
       plt.plot(TotalFitResidual,'b-')
1038   plt.plot(OptFuncC(x, *[0.5,-3.3,200.0,1.0E+15,1.0E+15]),'g-')
       if (SavePlots): plt.savefig('Combined_Fit_Residual.png')
```

```
1040    plt.show()
#
1042 #    plt.title('Fitted column density vs temperature')
#    ax = plt.gca()
1044 #    ax.errorbar(TemperatureArray,NTArray,xerr=TErrorArray,yerr=
    NTErrorArray,fmt='o')
#    plt.show()
1046 #
    plt.title('ALMA Fitting v2.7 - CH2DCN Velocity Error')
1048    plt.pcolormesh(Errors[1], cmap='rainbow')
    cbar = plt.colorbar()
1050    cbar.set_label('km/s')
    plt.show()
1052
    plt.title('ALMA Fitting v2.7 - CH2DCN Width Error')
1054    plt.pcolormesh(Errors[0], cmap='rainbow')
    cbar = plt.colorbar()
1056    cbar.set_label('km/s')
    plt.show()
1058
    plt.title('ALMA Fitting v2.7 - CH2DCN Temperature Error')
1060    plt.pcolormesh(Errors[3], cmap='rainbow')
    cbar = plt.colorbar()
1062    cbar.set_label('K')
    plt.show()
1064
    plt.title('ALMA Fitting v2.7 - CH2DCN Column Error')
1066    plt.pcolormesh(Errors[2], cmap='rainbow')
    cbar = plt.colorbar()
1068    cbar.set_label('cm^-2')
    plt.show()
1070
    plt.plot(TemperatureArray,NTArray1,'bo')
1072    plt.plot(TemperatureArray,NTArray2,'bo')
    plt.show()
1074
    print Popts
1076    print np.shape(Popts)
    plt.hist(Popts,11,range=[0,11])
1078    plt.show()

1080 if (PlotSecondaryMaps):
    plt.title('ALMA Fitting v2.7 - Combined Width Field')
```

```
1082    plt.pcolormesh(ParameterMap[0], cmap='rainbow')
        cbar = plt.colorbar()
1084    cbar.set_label('MHz')
        if (SavePlots): plt.savefig('Combined_Width_Map.png')
1086    plt.show()

1088    plt.title('ALMA Fitting v2.7 - Combined Velocity Field')
        plt.pcolormesh(ParameterMap[1], cmap='rainbow')
1090    cbar = plt.colorbar()
        cbar.set_label('MHz')
1092    if (SavePlots): plt.savefig('Combined_Velocity_Map.png')
        plt.show()
1094
        plt.title('ALMA Fitting v2.7 - Combined RMS Field')
1096    plt.pcolormesh(FractionalError, cmap='rainbow')
        cbar = plt.colorbar()
1098    cbar.set_label('Jy/Beam km/s')
        if (SavePlots): plt.savefig('Combined_RMS_Map.png')
1100    plt.show()

1102    plt.title('ALMA Fitting v2.7 - Total Column')
        plt.pcolormesh(NTMap, cmap='rainbow')
1104    cbar = plt.colorbar()
        cbar.set_label('cm^-2')
1106    if (SavePlots): plt.savefig('Total_Column_Map.png')
        plt.show()
1108
    if (PlotPrimaryMaps):
1110    plt.title('ALMA Fitting v2.7 - Combined Temperature')
        plt.pcolormesh(ParameterMap[2], cmap='rainbow')
1112    cbar = plt.colorbar()
        cbar.set_label('K')
1114    if (SavePlots): plt.savefig('Combined_Temperature_Map.png')
        plt.show()
1116
        plt.title('ALMA Fitting v2.7 - D to H Ratio')
1118    plt.pcolormesh(DtoH, cmap='rainbow')
        cbar = plt.colorbar()
1120    ax = plt.gca()
        ax.add_patch(patches.Rectangle((25,141),53-25,185-141,alpha=0.1,
          facecolor='red'))
1122    ax.add_patch(patches.Rectangle((30,103),73-30,135-103,alpha=0.1,
          facecolor='blue'))
```

```
    ax.add_patch(patches.Rectangle((64,52),95-64,103-52,alpha=0.1,
      facecolor='green'))
    ax.add_patch(patches.Rectangle((120,134),142-120,162-134,alpha
      =0.1,facecolor='yellow'))
    ax.add_patch(patches.Rectangle((164,25),192-164,55-25,alpha=0.1,
      facecolor='cyan'))
    ax.add_patch(patches.Rectangle((154,215),185-154,242-215,alpha
      =0.1,facecolor='black'))
    if (SavePlots): plt.savefig('DtoH.png')
    plt.show()

    plt.title('ALMA Fitting v2.7 - D to H Ratio vs Temperature')
    #plt.plot(TemperatureArray,DtoHArray,'bo-')
    ax = plt.gca()
    #ax.errorbar(TemperatureArray,DtoHArray,xerr=TErrorArray,yerr=
      NTErrorArray,fmt='o')
    #ax.errorbar(TemperatureArray,DtoHArray2[0],xerr=TErrorArray,
      yerr=NTErrorArray,fmt='o')
    #ax.errorbar(TemperatureArray,DtoHArray2[0],xerr=TErrorArray,
      yerr=NTErrorArray,fmt='o')
    ax.errorbar(TemperatureArray,DtoHArray2[0],xerr=TErrorArray,yerr
      =NTErrorArray,fmt='ro')
    #plt.plot(TemperatureArray,DtoHArray2[0],'ro')
    ax.errorbar(TemperatureArray,DtoHArray2[1],xerr=TErrorArray,yerr
      =NTErrorArray,fmt='bo')
    #plt.plot(TemperatureArray,DtoHArray2[1],'bo')
    plt.plot(TemperatureArray,DtoHArray2[2],'go')
    plt.plot(TemperatureArray,DtoHArray2[3],'yo')
    plt.plot(TemperatureArray,DtoHArray2[4],'co')
    plt.plot(TemperatureArray,DtoHArray2[5],'ko')

    if (SavePlots): plt.savefig('DtoHLin.png')
    plt.show()

if (SaveData):
    print 'Saving Data'
    hdulist = fits.open('../13CH3CN/calibrated_final_cont_image.
      image.fits')
    header = hdulist[0].header
    hdulist.close()
    FakeMap = np.zeros((1,1,1024,1024))
    for i in range(1024):
      for j in range(1024):
```

```
1156        if ((i >= StartY+256) and (i < StopY+256) and (j >= StartX
      +256) and (j < StopX+256)):
              FakeMap[0][0][i][j] = DtoH[i-StartY-256][j-StartX-256]
1158        else :
              FakeMap[0][0][i][j] = np.nan
1160    if(os.path.isfile('DtoH.fits')): os.remove('DtoH.fits')
        hdu = fits.PrimaryHDU(FakeMap)
1162    hdu.header = header
        hdu.writeto('DtoH.fits')
1164
        for i in range(1024):
1166      for j in range(1024):
            if ((i >= StartY+256) and (i < StopY+256) and (j >= StartX
      +256) and (j < StopX+256)):
              FakeMap[0][0][i][j] = NTMap[i-StartY-256][j-StartX-256]
            else :
1170          FakeMap[0][0][i][j] = np.nan
        if(os.path.isfile('TotalColumn.fits')): os.remove('TotalColumn.
      fits')
1172    hdu = fits.PrimaryHDU(FakeMap)
        hdu.header = header
1174    hdu.writeto('TotalColumn.fits')

1176    for i in range(1024):
          for j in range(1024):
1178        if ((i >= StartY+256) and (i < StopY+256) and (j >= StartX
      +256) and (j < StopX+256)):
              FakeMap[0][0][i][j] = ParameterMap[2][i-StartY-256][j-
      StartX-256]
1180        else :
              FakeMap[0][0][i][j] = np.nan
1182    if(os.path.isfile('Temperature.fits')): os.remove('Temperature.
      fits')
        hdu = fits.PrimaryHDU(FakeMap)
1184    hdu.header = header
        hdu.writeto('Temperature.fits')
1186
        for i in range(1024):
1188      for j in range(1024):
            if ((i >= StartY+256) and (i < StopY+256) and (j >= StartX
      +256) and (j < StopX+256)):
1190          FakeMap[0][0][i][j] = ParameterMap[1][i-StartY-256][j-
      StartX-256]
```

```
      else :
1192        FakeMap[0][0][i][j] = np.nan
    if(os.path.isfile('Velocity.fits')): os.remove('Velocity.fits')
1194  hdu = fits.PrimaryHDU(FakeMap)
    hdu.header = header
1196  hdu.writeto('Velocity.fits')

1198  for i in range(1024):
      for j in range(1024):
1200    if ((i >= StartY+256) and (i < StopY+256) and (j >= StartX
     +256) and (j < StopX+256)):
          FakeMap[0][0][i][j] = ParameterMap[0][i-StartY-256][j-
     StartX-256]
1202    else :
          FakeMap[0][0][i][j] = np.nan
1204  if(os.path.isfile('Width.fits')): os.remove('Width.fits')
    hdu = fits.PrimaryHDU(FakeMap)
1206  hdu.header = header
    hdu.writeto('Width.fits')
1208
    FullName = FileName+'_TemperatureMap.txt'
1210  fh = open (FullName,'w')
    file_str = ''
1212  for j in range(SizeX):
      for k in range(SizeY):
1214    if (np.isfinite(ParameterMap[2][k][j])):
          file_str+= str(ParameterMap[2][k][j]) + '\t '
1216    else :
          file_str+= str(-1.0) + '\t '
1218    file_str+='\n'

1220  fh.write(file_str)
    fh.close()
1222
    FullName = FileName+'_Column13CMap.txt'
1224  fh = open (FullName,'w')
    file_str = ''
1226  for j in range(SizeX):
      for k in range(SizeY):
1228    if (np.isfinite(ParameterMap[4][k][j])):
          file_str+= str(ParameterMap[4][k][j]) + '\t '
1230    else :
          file_str+= str(-1.0) + '\t '
```

```
1232      file_str+='\n'

1234    fh.write(file_str)
        fh.close()
1236
        FullName = FileName+'_FitRegions.txt'
1238    fh = open (FullName,'w')
        file_str = ''
1240    for j in range(len(TemperatureArray)):
          file_str += str(TemperatureArray[j])+'\t'+str(DtoHArray2[0][j
         ])+'\t'+str(DtoHArray2[1][j])+'\t'+str(DtoHArray2[2][j])+'\t'+
         str(DtoHArray2[3][j])+'\t'+str(DtoHArray2[4][j])+'\t'+str(
         DtoHArray2[5][j])+'\n'
1242    fh.write(file_str)
        fh.close()
1244


1246 ###############Test Code
```

Code/ALMA_Fitting_v2_7.py

A.5 Pressure Controller Code

```
import serial
2 import time
usbport1 = 'COM4'
4 ser2 = serial.Serial(usbport1, 9600, timeout=1, stopbits=1)
usbport2 = 'COM3'
6 ser1 = serial.Serial(usbport2, 9600, timeout=1)
def move(servo, angle):
8   '''Moves the specified servo to the supplied angle.
    Arguments:
10  servo
    the servo number to command, an integer from 1-4
12  angle
    the desired servo angle, an integer from 0 to 180
14  (e.g.) >>> servo.move(2, 90)
    ... # "move servo #2 to 90 degrees"'''
16  if (0 <= angle <= 180):
    ser1.write(chr(255))
18  ser1.write(chr(servo))
    ser1.write(chr(angle))
20  else:
    print "Servo angle must be an integer between 0 and
```

```
  180.\n"
ser2.write("p")#this retrieves the pressure from the pressure
    gauge
x = float(ser2.readline()[0:5])#this selects gauge 1
pressure = x
last_p = pressure
y = 90
move(1,y)
time.sleep(2)
counter = 0
marker = ""
100
while 1:
  counter +=1
  if counter ==180:
    fh = open("pressure_data.txt","a")
    data = str(x)+"\n"
    fh.write(data)
    fh.close
    counter =0
  ser2.write("p")
  x = float(ser2.readline()[0:5])#this selects gauge 1
  print x
  if x>last_p:
    marker = "up"
  if x<last_p:
    marker = "down"
  if abs(pressure-x)<0.1:
    marker = "stable"
  if x<(pressure-0.1) and marker != "up":
    y+=1
    if y>155:
      y=155
    move(1,y)
    time.sleep(.3)
  if x>(pressure+0.1) and marker !="down":
    y+=-1
    if y<20:
      y=20
    move(1,y)
    time.sleep(.3)
  time.sleep(.3)
  last_p = x
```

Code/pressure_control.py

```
/*
 * ------------------------------
 *   MultipleSerialServoControl
 * ------------------------------
 *
 * Uses the Arduino Serial library
 *  (http://arduino.cc/en/Reference/Serial)
 * and the Arduino Servo library
 *  (http://arduino.cc/en/Reference/Servo)
 * to control multiple servos from a PC using a USB cable.
 *
 * Dependencies:
 *   Arduino 0017 or higher
 *     (http://www.arduino.cc/en/Main/Software)
 *   Python servo.py module
 *     (http://principialabs.com/arduino-python-4-axis-servo-
   control/)
 *
 * Created:  23 December 2009
 * Author:   Brian D. Wendt
 *   (http://principialabs.com/)
 * Version:  1.1
 * License:  GPLv3
 *   (http://www.fsf.org/licensing/)
 *
 */

// Import the Arduino Servo library
#include <Servo.h>

// Create a Servo object for each servo
Servo servo1;
Servo servo2;
Servo servo3;
Servo servo4;
// TO ADD SERVOS:
//   Servo servo5;
//   etc...

// Common servo setup values
```

```
int minPulse = 600;   // minimum servo position, us (microseconds)
int maxPulse = 2400;  // maximum servo position, us

// User input for servo and position
int userInput[3];     // raw input from serial buffer, 3 bytes
int startbyte;        // start byte, begin reading input
int servo;            // which servo to pulse?
int pos;              // servo angle 0-180
int i;                // iterator

// LED on Pin 13 for digital on/off demo
int ledPin = 13;
int pinState = LOW;

void setup()
{
  // Attach each Servo object to a digital pin
  servo1.attach(2, minPulse, maxPulse);
  servo2.attach(3, minPulse, maxPulse);
  servo3.attach(4, minPulse, maxPulse);
  servo4.attach(5, minPulse, maxPulse);
  // TO ADD SERVOS:
  //   servo5.attach(YOUR_PIN, minPulse, maxPulse);
  //   etc...

  // LED on Pin 13 for digital on/off demo
  pinMode(ledPin, OUTPUT);

  // Open the serial connection, 9600 baud
  Serial.begin(9600);
}

void loop()
{
  // Wait for serial input (min 3 bytes in buffer)
  if (Serial.available() > 2) {
    // Read the first byte
    startbyte = Serial.read();
    // If it's really the startbyte (255) ...
    if (startbyte == 255) {
      // ... then get the next two bytes
      for (i=0;i<2;i++) {
        userInput[i] = Serial.read();
```

```
83        }
          // First byte = servo to move?
85        servo = userInput[0];
          // Second byte = which position?
87        pos = userInput[1];
          // Packet error checking and recovery
89        if (pos == 255) { servo = 255; }

91        // Assign new position to appropriate servo
          switch (servo) {
93          case 1:
              servo1.write(pos);     // move servo1 to 'pos'
95            break;
            case 2:
97            servo2.write(pos);
              break;
99          case 3:
              servo3.write(pos);
101           break;
            case 4:
103           servo4.write(pos);
              break;
105
    // TO ADD SERVOS:
107 //      case 5:
    //        servo5.write(pos);
109 //        break;
    // etc...
111
          // LED on Pin 13 for digital on/off demo
113       case 99:
            if (pos == 180) {
115           if (pinState == LOW) { pinState = HIGH; }
              else { pinState = LOW; }
117         }
            if (pos == 0) {
119           pinState = LOW;
            }
121         digitalWrite(ledPin, pinState);
            break;
123     }
      }
125 }
```

```
}
```

Code/servo_control.c

Appendix B

MACHINING TOPAS

TOPAS, while having excellent optical and THz transmission (when made properly), has some of the worst physical properties for machining. It is somehow both brittle and gummy, intolerant of many solvents (water however is fine), and not amenable to heating. Because of its excellent transmission however, it is often required for building THz vacuum systems. This requires machining this awful substance. Conventional machining (usually lathing) can be more accurately described as rapidly melting and pushing the polymer out of the way. This is exacerbated by the inability to use oil. Initial attempts to make TOPAS windows were moderately successful...at first. Over timer these windows would develop small cracks at the edges. Small cracks would become bigger cracks and we would lose vacuum. The suspicion, based attempts at making windows, faster and messier than the Caltech machinists, is that the faster/warmer TOPAS is cut, the larger/faster the fractures develop, since you are rapidly heating/cooling the material and it doesn't properly reanneal. Our solution was to cut the TOPAS much slower under water cooling. This yields much higher quality results. The recipe is as follows: **Machine slowly under ice water cooling applied with an acid brush. 0.05" removed per turn. 250 RPM (pressure turn). Feed 0.0024"/rev.**

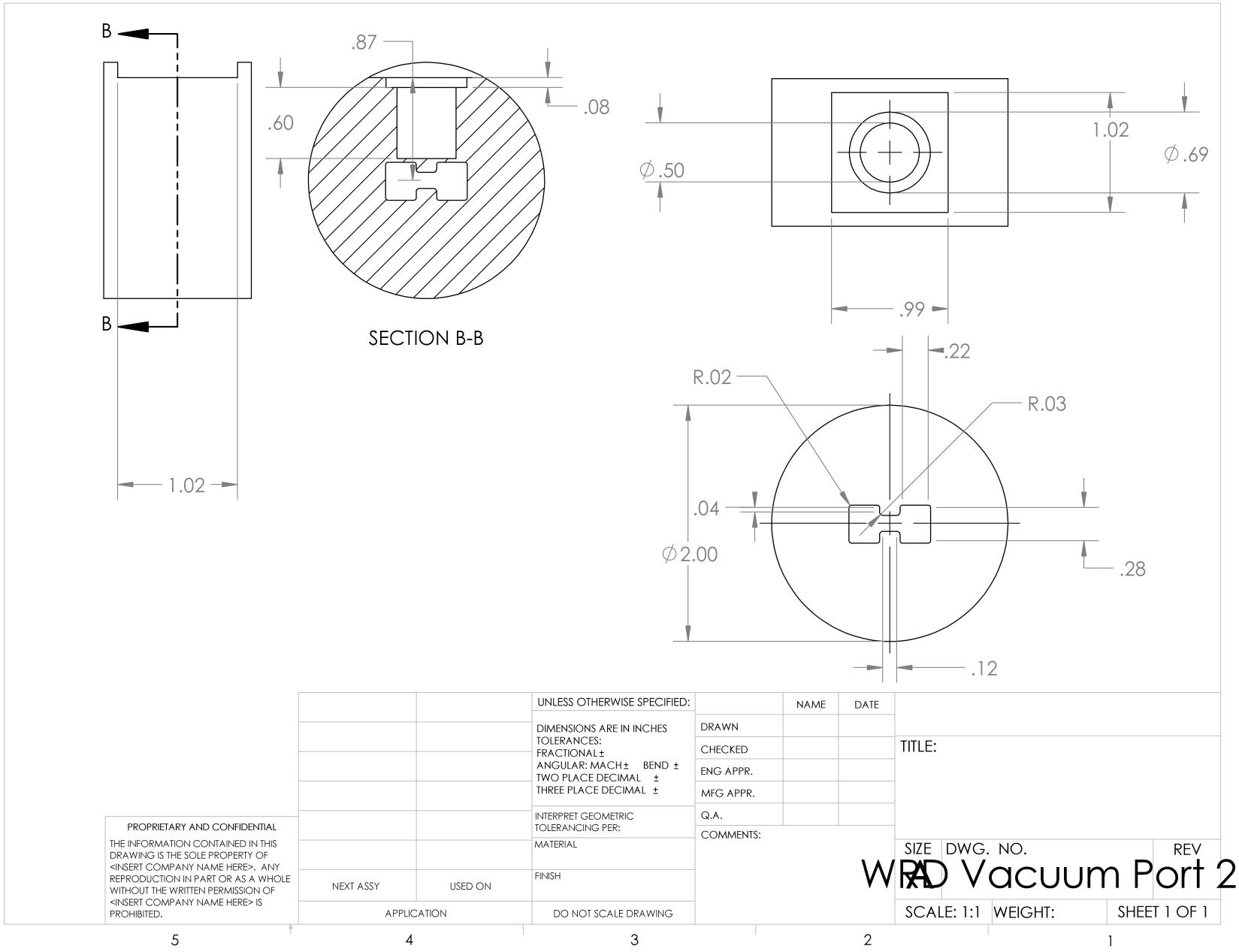

Figure B.1. Diagram of the WRD 750 vacuum adapter.